UNIVERSITÉ DU QUÉBEC À MONTRÉAL

GÉOCHRONOLOGIE ET GÉOCHIMIE DES ROCHES MAFIQUES DU NORD DU CANADA, DU BASSIN DE FURY ET HECLA AU NUNAVUT, ET DU BASSIN DE THULÉ AU GROENLAND : IMPLICATIONS POUR LES LARGES PROVINCES IGNÉES DE MACKENZIE ET FRANKLIN

THÈSE

PRÉSENTÉE

COMME EXIGENCE PARTIELLE

DU DOCTORAT EN SCIENCES DE LA TERRE ET DE L'ATMOSPHÈRE

PAR

FRÉDÉRIC DUFOUR

NOVEMBRE 2022

REMERCIEMENTS

Cette aventure du doctorat aura été pour le coup très intense, comprenant autant de défis à relever tous les jours pendant plus de quatre années. Malgré les difficultés auxquelles j'ai dû faire face, je suis fier d'avoir réussi à traverser cette épreuve et de pouvoir ressortir grandi de cette expérience. Les rêves, les espoirs et le courage qui m'animent sans cesse, m'ont sans nul doute permis de surmonter les obstacles.

Je tiens à remercier en premier lieu mon directeur de thèse, Ross Stevenson qui aura été d'un soutien sans faille au cours de ces quatre années. Je lui exprime toute ma gratitude d'avoir pu me transmettre l'ouverture d'esprit, la persévérance et les connaissances nécessaires pour accomplir cette thèse.

Je remercie également mon co-directeur Joshua Davies pour son accompagnement. Il a été d'une grande aide au cours de ce doctorat et m'aura permis d'appréhender le monde de la géochronologie.

Un grand merci à Galen Halverson pour m'avoir fait confiance, m'avoir donné l'opportunité de prendre part à ce grand projet de recherche, et pour son écoute.

Merci à Thomas Skulski pour son expertise sur les sujets, son aide et son humour.

Merci à toutes les personnes de l'équipe du projet Fury et Hecla qui ont été d'une aide indispensable : David Evans, Wilder Greenman, Mollie Patzke, Angelo dos Santos, Holly Steenkamp, Lorraine Lebeau, Tianran Zhang, Patrick Bovingdon, Alessandro Ielpi, Celine Gilbert.

Merci également aux personnels du laboratoire GEOTOP pour leur assistance au cours des analyses : André Poirier, Julien Gogot, Bassam Ghaleb.

Merci aux professeurs et au personnel du département des Sciences de la Terre et de l'Atmosphère de l'UQAM pour leur aide.

Merci à Elisabeth Lindsey et Nicole Turcot qui ont été d'une aide précieuse pour bien des problèmes.

Un immense merci à ma Rose pour son soutien perpétuel, sa patience et l'espoir qu'elle m'a donné au cours de ce long périple !

Un grand grand merci à mon docteur Williams Limon (Willy) qui a su être la quand il le fallait pour me remonter le moral d'innombrables fois et à tous ces moments partagés !

Merci aussi à Pierre Taillardat, une personne sage qui m'a partagé son énergie et ses conseils.

Merci à Denise Agiman pour le précieux soutien qu'elle m'a apporté !

Merci à Romain, Dominique, Jade, Mehdi N., Mehdi A., Oumy, Agustin, Nantio, Seynabou, Youssoupha, Manon, Karelle, Bruna, Maty, Parfait, Babacar, Atou, Sophia, Mélanie, Irene, Fanta, Lucille, Rocio, Adina, Anissa, Djamilla, Khaoutar, Zineb pour leur soutien.

Merci à En Marche Montréal pour leur soutien, leur bienveillance et les actions menées ensemble !

Merci à la famille scoute pour m'avoir fait grandir et permis de rêver de plein de projets et d'ambitions !

Enfin un grand Merci à ma famille qui a toujours eu les mots pour remonter le moral, à mes parents Pierre et Christiane, à mes frères Sébastien et Emmanuel, à ma grand-mère Annick Priser, à Sophie et Marie, mes neveux et nièces, à mes cousins Cédric et Guillaume, ma tante Marie, et à Excel !

DÉDICACE

Je dédie cette thèse à mes parents, qui ont été d'un soutien inconditionnel durant cette période, et qui m'auront aidé autant qu'ils ont pu depuis la Bretagne. Je leur serai éternellement reconnaissant qu'ils m'aient appris à persévérer dans la vie et à faire les choses bien et respectueusement. Je remercie inconditionnellement ma Rose et Dr. Willy qui m'ont auront soutenu énormément durant ce périple !

AVANT-PROPOS

Cette thèse est présentée sous la forme de trois articles scientifiques rédigés en anglais (chapitres I, II, III), avec une introduction et une conclusion générale en français. Le chapitre II sera soumis sous peu dans le journal Earth and Planetary Science Letters. Les deux autres articles seront soumis pour publication dans des journaux scientifiques révisés par les pairs, tels que Canadian Journal of Earth Sciences pour le chapitre I et ou Precambrian Research pour le chapitre III.

Le premier chapitre intitulé « New whole-rock geochemistry and Nd isotopes highlight the early and late phases of the Mackenzie LIP », a été écrit sous la supervision de Thomas Skulski et Ross Stevenson.

Le deuxième chapitre dénommé « New U-Pb CA-ID TIMS zircon ages implicate the Franklin LIP as the proximal trigger for the Sturtian Snowball Earth event », a été rédigé sous la supervision de Joshua Davies, Wilder Greenman, Thomas Skulski, Galen Halverson et Ross Stevenson.

Le troisième et dernier chapitre intitulé « Major and trace element and Nd isotope compositions reveal low-, and high-Ti provinces in the Franklin LIP indicating changes in lithosphere thickness and Arctic Laurentia tectonics », a été rédigé sous la supervision de Thomas Skulski et Ross Stevenson.

TABLE DES MATIÈRES

REMERCIEMENTS ii

DÉDICACE iv

AVANT-PROPOS v

LISTE DES FIGURES ix

LISTE DES TABLEAUX xiii

LISTE DES ABRÉVIATIONS, DES SIGLES ET DES ACRONYMES xiv

LISTE DES SYMBOLES ET DES UNITÉS xvi

RÉSUMÉ xvii

ABSTRACT xix

INTRODUCTION 1

CHAPITRE 1 NEW WHOLE-ROCK GEOCHEMISTRY AND ND ISOTOPES HIGHLIGHT THE EARLY AND LATE EMPLACEMENT PHASES OF THE MACKENZIE LIP 14

1.1 Introduction 16

1.2 Geological Settings 17

1.2.1 Coppermine River Group 19

1.2.2 Mackenzie dyke swarm and distal correlatives rocks 19

1.2.2.1 Size of the swarm, distribution of dykes and sills and existing age constraints 19

1.2.2.2 Previous work on the chemistry of dykes 24

1.2.2.3 Paleomagnetic data, common paleopole 24

1.3 Methodology 25

1.3.1 Whole-rock geochemistry 25

1.3.2 Sm-Nd analyses 25

1.4 Results 26

1.4.1 Coppermine River Group 26

1.4.2 Mackenzie dyke swarm, distal lavas, and intrusive rocks 31

1.5 Discussion 35

1.5.1 Early Mackenzie magmatism 35

1.5.1.1 Geochemical similarities and contamination in early Mackenzie rocks 35

1.5.1.2 Western extensional tectonic features 38

1.5.1.3 Northeastern crustal stretching and implications on the history of the lower Bylot Supergroup 38

1.5.2 Late Mackenzie magmatism 39

1.5.2.1 Geochemical differentiation 39

1.5.2.2 Emplacement of the late Mackenzie dyke swarm and upper Coppermine sequence 42
1.6 Conclusion 42
1.7 Acknowledgments 43
1.8 References 44

CHAPITRE 2 NEW U-PB CA-ID TIMS ZIRCON AGES IMPLICATE THE FRANKLIN LIP AS THE PROXIMAL TRIGGER FOR THE STURTIAN SNOWBALL EARTH EVENT 52
2.1 Introduction 54
2.2 Materials and Methods 57
2.2.1 U-Pb geochronology 57
2.2.2 Isotopic compilations 58
2.3 Results 59
2.3.1 Sample selection for geochronology 59
2.3.2 U-Pb geochronology 59
2.4 Discussion 62
2.4.1 Bayesian updated ages and combined weighted mean ages 62
2.4.2 Timing of the Franklin event 64
2.4.3 The Franklin LIP as a trigger for Snowball Earth 65
2.4.4 New estimate for the timing of onset of Sturtian glaciation 66
2.4.5 The role of basalt weathering in the onset of Sturtian glaciation 68
2.5 Conclusion 72
2.6 Acknowledgments 72
2.7 References 73

CHAPITRE 3 MAJOR AND TRACE ELEMENT AND ND ISOTOPE COMPOSITIONS REVEAL LOW-, AND HIGH-TI PROVINCES IN THE FRANKLIN LIP INDICATING CHANGES IN LITHOSPHERE THICKNESS AND ARCTIC LAURENTIA TECTONICS 78
3.1 Introduction 80
3.2 Geological settings 81
3.2.1 Natkusiak Formation basalts and sills 81
3.2.2 Distal Franklin basalts, sills and dyke swarm 82
3.3 Methodology 88
3.3.1 Whole-rock geochemistry 88
3.3.2 Sm-Nd analyses 88
3.4 Results 89
3.5 Discussion 99
3.5.1 Evidence for low-, and high Ti provinces associated with the Franklin LIP 99
3.5.2 Fractional crystallization 99
3.5.3 Contamination 99
3.5.4 Partial melting and mantle sources of the Franklin LIP 102

3.5.5 Relationships between the Arctic Laurentia tectonics and geochemical Ti provinciality 103
3.6 Conclusion 106
3.7 Acknowledgments 106
3.8 References 107
CONCLUSION 114
ANNEXE A DONNEES DU CHAPITRE I 116
ANNEXE B DONNEES DU CHAPITRE II 134
ANNEXE C DONNEES DU CHAPITRE III 16
RÉFÉRENCES 26

LISTE DES FIGURES

Figure 1.1: Map of the Mackenzie igneous suites. Colored fields are from Buchan et al. (2010); light brown field is the Coppermine River Group; purple field is the Muskox Intrusion; orange field is the Ekalulia volcanics; the red brown field is the Fortress Gabbros; the dark lines are the Mackenzie dyke swarm. Green fields are the Bylot basins. Red box indicates location of Fig. 1.2. Inset map is the Coppermine River Group modified from Skulski et al. (2018) with lower divisions of the Copper Creek Formation (green field, September Creek member; blue field, Stony Creek member; red field, Burnt Creek member) and the Husky Creek Formation (orange field). Black open star is the proposed Mackenzie plume (Baragar et al., 1996). Blue stars are the U-Pb ages from Table 1.1. CR, Coppermine River; MI; Muskox Intrusion; EV, Ekalulia volcanics. 18

Figure 1.2: Geological map of Fury and Hecla Basin and the Archean basement modified from Dufour et al. (submitted). The Paleozoic rocks and the Fury and Hecla Basin are adapted from Chandler (1988), Long and Turner (2012), and Greenman et al. (2020). The Neoproterozoic Franklin intrusions and the Archean basement are adapted from Steenkamp et al. (2018) and Dufour et al. (2020). Dark star indicates location of the U-Pb ages of the Fury and Hecla dyke and Dybbol sill determined in Dufour et al. (submitted). Inset figure is the stratigraphy of the Fury and Hecla Basin after Chandler (1988) and Greenman et al. (2021). 23

Figure 1.3: SiO_2, MgO, TiO_2 and Fe_2O_3 variations with stratigraphic height in the Coppermine River Group. Data is normalized to 100%..... 28

Figure 1.4: Ce/Yb, Th/Nb and εNd variations with stratigraphic height in the Coppermine River Group. Depleted Mantle is from DePaolo (1981). εNd data is compiled from Griselin et al. (1997) and Day et al. (2013)..... 29

Figure 1.5: Chondrite and Primitive Mantle normalized diagrams with selected Mackenzie data. Normalized values are from McDonough and Sun (1995). A and B are the diagrams of the Coppermine River Group with numbers corresponding to the stratigraphic heights. C and D are the diagrams of the Mackenzie dyke swarm and basalts, sills across Canada and Greenland. 30

Figure 1.6: SiO_2, TiO_2 and Fe_2O_3 variations vs MgO of the Mackenzie dyke swarm and basalts, sills across Canada and Greenland. Data is normalized to 100%. The Nyeboe basalts, Hansen and Savage Point sills data are from this study; the Tweed Lake volcanics are from Sevigny et al. (1991); the Nauyat basalts from Dostal et al. (1989); the basalts and sills of the Cape Combermere Formation from Dawes (2006); the Bear River dykes from Schwab et al. (2004); the Mackenzie dykes are from this study, Gibson et al. (1987) and Ernst and Buchan (2010)..... 33

Figure 1.7: TiO_2, Th/Nb and εNd variations vs Ce/Yb of the Mackenzie dyke swarm and basalts, sills across Canada and Greenland. Data points according to Fig. 1.5. Green bar is the εNd data range of the Coppermine River Group and blue bar is the εNd range of the Muskox Intrusion from Mackie et al. (2009). Depleted Mantle is from DePaolo (1981). 34

Figure 1.8: Initial εNd isotopic compositions vs. Th/Nb ratios. Mixing line is calculated using trace elements and isotopic composition of the Wopmay paragneiss (Day et al., 2008), and a basalt from the Husky Creek Formation. Primitive-mantle values are normalized are from Sun and McDonough (1989)... 37

Figure 1.9: Trace-element modeling results for incongruent dynamic mantle melting for tholeiitic lava from the Husky Creek Formation. The melting model is from Zou and Reid (2001). Melt reaction

coefficients of spinel lherzolite are from Kinzler and Grove (1992), and partition coefficients are from Salters and Stracke (2004), and Shaw (2000). An enriched mantle (Sun and McDonough, 1989) spinel lherzolite with source mineralogy of 0.3cpx:0.15opx:0.52ol:0.03sp was the best fit to model the partial melting. 41

Figure 2.1: Map of the Franklin igneous suites. Red box indicates location of Fig. A2.2, and black box is location of Fig. A2.3. Black lines are the mafic dyke swarm. Black open star is the proposed plume location (Denyszyn et al., 2009a). Filled stars denote U-Pb ages; blue stars are from Heaman et al. (1992); green stars from Denyszyn et al. (2009a, b); purple star is from Macdonald et al. (2010); orange star is from Pehrsson and Buchan (1999); red stars are from this study. NB, Natkusiak basalts; NS, Natkusiak sills..... 56

Figure 2.2 : Concordia diagrams showing the results of U-Pb zircon CA-ID-TIMS geochronology of Fury and Hecla dyke, Dybbol sill, Thule dyke, Steensby Land sill complex (2σ error ellipses). Reported ages are Th-corrected $^{206}Pb/^{238}U$ weighted mean ages. 61

Figure 2.3 : Probability density plots for the ages of the Fury and Hecla and Thule intrusions and onset of the Sturtian glaciation. (A) Updated ages for the dykes and sills based on the observation of cross-cutting relationships, compared with a Monte Carlo estimate for the age for the onset of Sturtian glaciation. (B) Combined weighted mean ages of the sills and the dykes based on the assumption that dykes and sills were the product of two separate pulses of Franklin magmatism. The difference between emplacement ages and onset of Sturtian glaciation is shown by arrows. 63

Figure 2.4 : Timing constraints for the Franklin LIP and the onset of the Sturtian glaciation. (A) $^{206}Pb/^{238}U$ zircon ages (red) and baddeleyite ages (all others) of the Franklin event. Ages are color-coded as in Fig. 2.1. The onset of the Sturtian glaciation is based on our estimated age 717.17 +0.26/-0.33 Ma. SLSC, Steensby Land sill complex. All ages are given with 95% uncertainty. (B) Summary of $\delta^{13}C$ for marine carbonates 725–718 Ma. Grey shading and black lines indicate the 95% uncertainty and mean values from a LOESS smoothing fit. 67

Figure 2.5 : Late Tonian isotopic compilations (830–710 Ma). (A) Summary of $\delta^{13}C$ for marine carbonates. Grey shading and black lines indicate the 95% uncertainty and mean values from a LOESS smoothing fit. Red circles are scaled to estimated erupted LIPs area (Ernst et al., 2021a). G&W-G, Guibei, Willouran and Gairdner; G-K, Gunbarrel and Kangding; MW, Mundine Well; F, Franklin. (B) Summary of the $^{87}Sr/^{86}Sr$ and $^{187}Os/^{188}Os$ records. Green squares are $^{187}Os/^{188}Os$ data, and blue circles are $^{87}Sr/^{86}Sr$ data. 71

Figure 3.1: Map of the Franklin igneous suites modified from Dufour et al. (submitted). Red box indicates location of Fig. 3.2, and black box is location of Fig. 3.3. Black lines are the mafic dyke swarm. Black open star is the proposed plume location (Denyszyn et al., 2009a). Filled stars denote U-Pb ages; blue stars are from Heaman et al. (1992); green stars from Denyszyn et al. (2009a, b); purple star is from Macdonald et al. (2010); orange star is from Pehrsson and Buchan (1999); red stars are from Dufour et al. (submitted). NB, Natkusiak basalts; NS, Natkusiak sills; CL, Clarence Head dykes; LR; Lasard River dykes; SS, Strathcona Sound dykes. Samples locations are color-coded as in the geochemistry plots. 85

Figure 3.2: Geological map of Fury and Hecla Basin and the Archean basement modified from Dufour et al. (submitted). The Paleozoic rocks and the Fury and Hecla Basin are adapted from Chandler (1988), Long and Turner (2012), and Greenman et al. (2020). The Neoproterozoic Franklin intrusions and the Archean basement are adapted from Steenkamp et al. (2018) and Dufour et al. (2021). Red star indicates location of the U-Pb ages of the Fury and Hecla dyke and Dybbol sill. Inset figure is the

stratigraphy of the Fury and Hecla Basin after Chandler (1988) and Greenman et al. (2021). Red circles are sample locations of the Franklin dykes..... 86

Figure 3.3: Geological map of the Thule area is modified from Dufour et al. (submitted) and the Geological Survey of Denmark and Greenland. Inset figure is the stratigraphy of the Thule Basin after Dawes (1997). Samples locations are color-coded similar as the geochemistry plots. 87

Figure 3.4: Total-alkali silica diagram from LeBas et al. (1986). The Fury and Hecla dykes, the Dybbol sills, and the Thule sills and dykes are from this study. The Kikiktat volcanics are from Cox et al. (2015). The Ellesmere-Devon dykes and the Greenland dykes are from Denyszyn (2008). The Coronation sills are from Shellnutt et al. (2004). The Eastern Baffin Island dykes, the northern mainland dykes, the Victoria dykes, and the Aston sill are from Ernst and Buchan (2010). The Natkusiak basalts and sills are from Bédard et al. (2016)..... 92

Figure 3.5: MgO and TiO_2 variations with stratigraphic height in the Natkusiak Formation (data from Bédard et al., 2016). 93

Figure 3.6: Major and trace elements variations diagrams of the Franklin igneous suites. A is the TiO_2/MgO plot. B shows variations of Ni vs Zr after Cocherie (1986). C indicates variations of Zr/Y (partial melting and fractionation) vs Th/Nb (crustal input). D is the classification diagram modified after Pearce and Norry (1979) with variations of Zr/Y vs Zr. OIB, E-, N-MORB, and primitive-mantle (PM) values are from Sun and McDonough (1989)..... 94

Figure 3.7: Alkali (Na_2O + K_2O), Fe_2O_{3T}, MgO (AFM) diagram. Dashed line represents the separation between the tholeiitic and calc-alkaline sub-fields (after Irvine and Baragar, 1971). 95

Figure 3.8: Major, trace element ratios and Nd diagrams. A is the geochemical proxy diagram for melting depth (TiO_2/Yb) and source composition (Nb/Yb) after Pearce (2008). B and C represent the variations of Dy/Yb and $\varepsilon Nd_{718\ Ma}$ vs Ce/Yb. Black lines in B indicate the incongruent dynamic melting model (Zou and Reid, 2001) of garnet lherzolite (gt lherz), spinel lherzolite (sp lherz) and a mixture of 1x garnet and 4x spinel lherzolite (1x gt + 4x sp lherz; Greene et al., 2009). Melt reaction coefficients of spinel lherzolite and garnet lherzolite are from Kinzler and Grove (1992), and Walter (1998). Partition coefficients (Table A3.3) are from Salters and Stracke (2004), and Shaw (2000). Source mineralogy (PM is from Sun and McDonough, 1989) for spinel lherzolite (0.18cpx:0.27opx:0.52ol:0.03sp) is from Kinzler (1997), and for garnet lherzolite (0.34cpx:0.08opx:0.53ol:0.05gt) is from Salters and Stracke (2004). Data are similar to previous figures and are supplemented with those of Beard et al. (2017). OIB, E-, N-MORB, and Primitive Mantle (PM) values are from Sun and McDonough (1989). Depleted Mantle line is from DePaolo (1981). 97

Figure 3.9: Chondrite and Primitive Mantle normalized diagrams of selected Franklin data. Chondrite normalized values are from McDonough and Sun (1995), and Primitive Mantle values are from Sun and McDonough (1989). A and B are the diagrams of the Franklin igneous suites in Alaska, Canada, and Greenland. C and D are the diagrams of the Natkusiak basalts and sills in Victoria Island. The Franklin data are from Beard et al. (2017). The profiles plotted depict the maximum and minimum profiles from a given area. The melting model used in 9A is similar to Fig. 3.8B. Primitive-mantle source is from Sun and McDonough (1989)..... 98

Figure 3.10: Modelling of crustal contamination in the Franklin rocks with initial εNd isotopic compositions vs. Th/Nb ratios. Mixing line with diamond marks is calculated using a mix of trace elements and isotopic composition of Slave Province granodiorites (Yamashita et al., 1999), and a Thule sill. Mixing line with x marks uses a mean of trace elements and isotopic composition of the representative Fury

and Hecla basement rocks (this study, M152, C074, P043 and P110 geochemical compositions are provided in Table A3.4). Primitive-mantle values are normalized are from Sun and McDonough (1989). 101

Figure 3.11: Paleogeographic reconstruction of Rodinia at 720 Ma is modified after Swanson-Hysell (2021) integrating the low-, and high-Ti provinces of the Franklin LIP. Open white star is the proposed plume location (Denyszyn et al., 2009a). 105

LISTE DES TABLEAUX

Tableau 1.1 : Published Mackenzie ages..... 21

Tableau 2.1 : U-Pb zircon $^{206}Pb/^{238}U$ weighted mean ages from the Mount Harper region in the Ogilvie Mountains used to generate an age estimate for the onset of Sturtian glaciation (Macdonald et al., 2010, 2018)..... 66

LISTE DES ABRÉVIATIONS, DES SIGLES ET DES ACRONYMES

$^{87}Sr/^{86}Sr$: Strontium isotope $^{87}Sr/^{86}Sr$ ratio

$^{187}Os/^{188}Os$: Osmium isotope $^{187}Os/^{188}Os$ ratio

CA-ID-TIMS: Chemical abrasion isotope dilution thermal ionization mass spectrometry

CO_2 : Carbon dioxide/ Dioxyde de carbone

DS: Dybbol sill

FH: Fury and Hecla

HFS: High Field Strength

HREE: Heavy Rare Earth Elements

LPI/LIP: Large Province Ignée/ Large Igneous Province

LREE: Light Rare Earth Elements

OIB: Ocean Island Basalt

REE: Rare Earth Elements

Re-Os: Rhenium-Osmium

SLSC: Steensby Land sill complex

TD: Thule dyke

Ti: Titane/Titanium

U-Pb : Uranium-Plomb/Uranium-Lead

$\delta^{13}C : 10^{3} * \left[\frac{\left(\frac{^{13}C}{^{12}C}\right)sample}{\left(\frac{^{13}C}{^{12}C}\right)standard} - 1 \right]$

LISTE DES SYMBOLES ET DES UNITÉS

Mkm^2 : Million de kilomètre carré/Million square kilometre

Ma: Million years ago/Millions d'années

wt. %: Poids pourcentage/weight percentage

RÉSUMÉ

Les larges provinces ignées (LPI) représentent des événements géologiques importants car ils mettent en place de grands volumes de roche ignées sur des grandes distances et en quelques millions d'années. Ces provinces magmatiques sont souvent corrélées à la dislocation des continents et précèdent des changements climatiques globaux. Ainsi cette thèse présente l'étude géochimique et géochronologique des roches mafiques de Mackenzie à ca. 1268 Ma et Franklin à ca. 720 Ma au nord du Canada et nord-ouest du Groenland. La pétrogenèse des roches de ces provinces magmatiques est interprétée en considérant comment les changements dans la chimie des magmas reflète les changements dans la source mantellique et les tectoniques régionales sur des distances de plusieurs milliers de kilomètres des centres des LPI. La thèse fournie aussi de nouvelles contraintes sur la chronologie du magmatisme de Franklin comme un potentiel déclencheur a l'initiation de l'événement du Sturtien de la Terre boule de neige à 717–661 Ma. Il a été évoqué que l'épisode de Franklin a initié la glaciation globale mais la précision des âges du magmatisme de Franklin n'est pas suffisante pour confirmer qu'il a causé la glaciation.

Cette étude a été divisée en trois chapitres.

Le premier chapitre de ce projet de recherche concerne l'étude géochimique des basaltes, filons-couches et filons de Mackenzie. La géochimie totale et les isotopes de Nd des roches ont permis de montrer que l'événement de Mackenzie aurait formé en premier lieu des roches à faible TiO_2 et contaminées par la croute continentale, alignées nord-est à travers l'Arctique, et interprétées comme ayant été mises en place pendant un épisode d'extension crustale. La majorité des autres roches du second groupe de Mackenzie se seraient formées dans un second temps, caractérisées par un enrichissement en TiO_2 et une relative absence de contamination.

Le deuxième chapitre de la thèse porte sur la datation des roches de Franklin et de leur corrélation à la glaciation de la Terre boule de neige. La méthode de datation U-Pb CA ID-TIMS a été utilisée sur des zircons pour déterminer l'âge de deux filons-couche et deux filons au nord-ouest de Baffin Island (Canada) et nord-ouest du Groenland. Ces âges associés à la relation des filons recoupant les filons-couche permettent de montrer que le magmatisme se produit sur 0.53 ±0.58 millions d'années à ca. 718 millions d'années, immédiatement avant la glaciation du Sturtien qui est estimée s'etre mise en place à 717.19 +0.26/-0.33 millions d'années. Le magmatisme coïncide avec une diminution drastique de l'enregistrement des isotopes de carbone des calcaires marins ($\delta^{13}C_{carb}$) juste avant le début de la glaciation du Sturtien démontrant une relation temporelle entre la province ignée de Franklin, les changements globaux du cycle du carbone et le début de la glaciation du Néoprotérozoïque.

Le troisième chapitre de cette étude s'intéresse à la géochimie des roches de l'épisode de Franklin. La géochimie totale et les isotopes de Nd des roches indiquent la présence de provinces géochimiques basées sur la composition en TiO_2 telles que la province du nord-ouest du Laurentien à faible (<2%) TiO_2 et la province du nord-est du Laurentien à TiO_2 élevée (2–6%). Les roches à faible titane sont appauvries en terres rares légères et en éléments incompatibles reflétant des taux de fusion partiels plus élevés d'un manteau lherzolite a spinelle alors que les roches à hautes titanes sont plus enrichies suggérant des faibles taux de fusion partielle d'une lherzolite à grenat. Ces différentes conditions de fusion partielle sont reliées à l'épaisseur de la lithosphère à travers l'Arctique Laurentien, qui aurait été plus mince dans le nord-ouest du Laurentien à la suite de la rupture de Rodinia a 775–720 millions d'années, et inchangée et plus épaisse dans le nord-est du Laurentien.

Cette thèse aura donc apporté une nouvelle compréhension de : (1) magmatisme de Mackenzie et comment la géochimie corrèle avec les événements tectoniques ; (2) l'emplacement rapide l'événement de Franklin et de son rôle comme potentiel déclencheur a la glaciation du Sturtien ; et (3) des changements dans la structure lithosphérique ont influencé la composition géochimique des magmas associés à la LPI de Franklin. Ce travail a contribué à la compréhension des relations entre les larges provinces ignées, et les événements tectoniques et changements environnementaux globaux.

Mots-clés : larges provinces ignées de Mackenzie et Franklin, géochronologie U-Pb, zircons, glaciation du Sturtien, nord du Canada, Fury et Hecla (nord-ouest de l'ile de Baffin), Thulé (nord-ouest du Groenland), Sm-Nd, lithosphère, composition faibles et élevées en TiO_2.

ABSTRACT

Large igneous provinces (LIP) represent important geological events because they emplace large volumes of igneous rocks over vast distances within a few millions of years. These igneous provinces are often correlated with the break-up of continents and precede global climate change events. This thesis presents a geochemical and geochronological study of mafic rocks from the ca. 1268 Ma Mackenzie and the ca. 718 Ma Franklin LIPs in northern Canada and northwestern Greenland. The petrogenesis of the rocks of these LIPs are discussed with respect to how changes in magma chemistry reflect changes in mantle source and regional tectonics over distances of thousands of kilometers from the LIP focal points. The thesis also provides new constraints for the timing of the Franklin LIP and as a potential trigger for the onset of the ca. 717–661 Ma Sturtian Snowball Earth event. Given the close association in time between these two events, it has been widely argued that the Franklin event contributed to the initiation of global glaciation. However, a lack of accurate high-precision geochronology has hampered establishing the timeframe of Franklin magmatism and discerning its precise temporal and possible causative relationship to glaciation.

The thesis is divided into three chapters.

The first chapter of the thesis presents new whole-rock geochemistry and Nd isotope data for Mackenzie dykes and eastern distal basalts of the Fury and Hecla Basin and compare them to previously studied Mackenzie igneous rocks. This compilation reveals that the geochemistry of the Mackenzie rocks varies spatially in relation to changes in tectonic stress regimes. The Mackenzie rocks form two distinct geochemical groups based on major and trace element data, with a group characterized by low TiO_2 and crustal contamination, aligned in a northeasterly direction across the Canadian Arctic, and interpreted to be emplaced during a crustal stretching episode related to an early phase of the Mackenzie magmatism. The second group consists of high TiO_2 and relatively uncontaminated rocks. The differences in the geochemistry of the two groups may reflect changes in the melting regime associated with the Mackenzie mantle plume.

The second chapter of the thesis presents four new chemical abrasion, isotope dilution, thermal ionization mass spectrometry (CA-ID-TIMS) U-Pb zircon ages from mafic intrusions crosscutting the Fury and Hecla and Thule basins in northeastern Canada and northwestern Greenland. These are the first high-precision U-Pb zircon ages reported on the Franklin event and together indicate a pair of Franklin magmatic pulses over 0.53 ±0.58 Ma at ca. 718 Ma, coincident with the carbon isotope record of marine carbonates ($\delta^{13}C_{carb}$), which shows a sharp decline just prior to the onset of Sturtian glaciation. Using available age constraints bracketing the onset of Sturtian glaciation and a simple Bayesian model, we estimate glacial initiation at 717.19 +0.26/-0.33 Ma. This new calibration of global events across the Tonian–Cryogenian boundary

demonstrates a close temporal link between the Franklin LIP, perturbation to the global carbon cycle, and the onset of Neoproterozoic glaciation.

The third chapter presents new whole-rock geochemistry and Nd isotope data for Franklin dykes and sills in northwestern Baffin Island and Greenland, and compare them to previously studied Franklin igneous rocks. This study reveals the presence of geochemical provinces within the Franklin LIP based on the abundance of TiO_2, with rocks from northwestern Laurentia having low-TiO_2 (<2%) compositions, whereas rocks from northeastern Laurentia yield higher (2–6%) TiO_2 contents. The low-Ti rocks exhibit flat to slightly light-REE enriched and incompatible element profiles that are consistent with high degrees of partial melting of a spinel lherzolitic mantle source while the high-Ti rocks are enriched in LREE and incompatible elements, reflecting lower degrees of partial melting of a garnet lherzolitic mantle source. The REE modelling of the least contaminated rocks from these suites indicates that they likely originated from the same Franklin plume material, but that they experienced different conditions of partial melting related to the thickness of the lithosphere across the Arctic Laurentia. The break-up of Rodinia at 775–720 Ma in northwestern Laurentia would have favored extensive thinning of the lithosphere and shallower melting of the mantle, while the lithosphere thickness would have been unchanged in northeastern Laurentia, leading to deeper mantle melting within the garnet stability field.

This thesis provides a new understanding of: (1) the Mackenzie magmatism and how the geochemistry of the rocks correlate with tectonic events; (2) the rapid emplacement of the Franklin event and its role as a proximal trigger for the Sturtian Snowball Earth; and (3) how changes in lithospheric structure influenced the geochemical composition of magmas associated with the Franklin LIP. This work has contributed to understanding the relationship between large igneous provinces, and tectonic and global environmental events.

Keywords: Mackenzie and Franklin large igneous provinces, U-Pb geochronology, zircons, Sturtian glaciation, northern Canada, Fury and Hecla (northwest Baffin Island), Thulé (northwest Greenland), Sm-Nd, lithosphere, low-, and high-TiO_2.

INTRODUCTION

Mise en contexte global

Les larges provinces ignées (LPI) sont des provinces magmatiques qui extrudent des grandes quantités de magma, généralement mafique, sur plus de >0.1 Mkm^2 dans une courte périodes de temps de l'ordre de quelques millions d'années, sont souvent associées aux ruptures des continents et au rifting, et sont fréquemment originaires de plumes mantelliques (Coffin et Eldholm, 1994; Courtillot et al., 1999; Ernst et al., 2005 ; Bryan et Ernst, 2008; Ernst, 2014 ; Ernst et al., 2021 ; Kasbohm et al., 2021). Cependant, plusieurs autres origines pour la formation des LPI ont été proposées impliquant une fusion partielle par décompression en contexte de rifting (White et McKenzie, 1989), d'arrière-arc (Rivers et Corrigan 2000), de convection à la limite des plaques (King et Anderson, 1998) et d'impact météoritique (Jones et al., 2002), alors que les points chauds océaniques semblent être reliés à des anomalies sismiques à la base du manteau inférieur connus sous le nom de province de basse vitesse des ondes S ou superpanaches (Torsvik et al., 2006).

La distribution globale et l'emplacement radial, synchrone des essaims de filons fait des larges provinces ignées un outil important pour reconstruire la paléogéographie et la position relative des continents (Halls, 1987). Les LPI continentales forment principalement des basaltes en trapps, des filons-couche, des intrusions mafiques litées et des essaims de filons. Les grands essaims de filons associés avec les LPIs montrent des réseaux radiants ou linéaires, s'étendent sur des longues distances (>2000 km) à partir du centre de l'essaim comme c'est le cas dans les essaims de filons du Karoo, Mackenzie, Franklin, Atlantique Centre et Paraná-Etendenka (LeCheminant et Heaman, 1989; Heaman et al., 1992; Jourdan et al., 2007; Marzoli et al., 2018; Simões et al., 2019). Les essaims de filons peuvent avoir une direction verticale du magma dans la région focale de la plume, et une direction horizontale au-delà comme vu dans l'essaim de filon de Mackenzie des filons est utilisée pour déterminer la direction du magma (Ernst et Baragar, 1992). La direction des filons indique le champ des anciennes contraintes des blocs continentaux, généralement parallèle à la direction maximale horizontale régionale et contemporaine, et perpendiculaire à la direction d'extension, avec les filons radiants généralement formés avec les plumes mantelliques ou édifices volcaniques, les filons parallèles souvent se mettent en place dans des fractures préexistantes, et les essaims de filons circonférentiel délimitant la plume perpendiculairement (Pollard, 1987; Hou et al., 2010; Ju et al., 2013 ; Ernst et al., 2019; Buchan et Ernst, 2021).

Les LPI prennent leur origine dans le manteau et mettent en place des quantités importantes de roches qui présentent une diversité géochimique, apportant ainsi de nombreuses informations sur la composition du

manteau terrestre. Les éléments majeurs, traces et isotopes des roches reflètent une ou plusieurs sources du manteau (asthénosphère ou plume, lithosphérique sous-continentale, asthénosphère appauvrie) et les processus d'assimilation et de différenciation magmatique (Bryan et Ernst, 2008) comme observe dans les provinces du Karoo, Mackenzie, Paraná et Etendeka. Parmi celles-ci, des larges provinces ignées a faibles et hautes teneurs en titane (Ti) ont été identifiées dans des LPI d'âges différents (Xu et al., 2001; Melluso et al., 2006; Jourdan et al., 2007; Marzoli et al., 2018). Les provinces hautes en Ti résultent soit d'un faible taux de fusion partiel d'une source mantellique profonde non-contaminée, alors que les provinces faibles en Ti sont interprétées comme ayant été contaminées par le manteau lithosphérique sous-continental et/ou de la croute continentale, ou aurait subies des hauts taux de fusion partiel d'une source mantellique peu profonde (Arndt et al., 1993; Xu et al. 2001 ; Wang et al., 2007 ; Bryan et Ernst, 2008).

La mise en place des LPI engendre aussi des grandes perturbations à court ou long terme sur l'environnement global de la Terre telles que des périodes de réchauffement, de refroidissement, des anomalies isotopiques négatives en carbone et des extinctions de masse (Ernst et al., 2021 ; Kasbohm et al., 2021). Les émissions magmatiques de SO_2 peuvent conduire à des refroidissements sur la période de l'éruption (Schaller et al., 2012), alors que les réchauffements de longue durée ($<10^5$ ans) sont causés par la rapide altération des basaltes de trapps (Dessert et al., 2001). L'émission de quantités importantes en CO_2 prédit une anomalie négative en $\delta^{13}C$ correspondant au début d'une phase de réchauffement global, et qui peut aussi etre détectée avec les chutes d'isotopes de $^{87}Sr/^{86}Sr$ et $^{187}Os/^{188}Os$ dans les carbonates marins dû à l'altération des nouveaux basaltes (Ernst et al., 2021).

Contexte géologique

Les roches de cette étude portent sur les LPI de Mackenzie et Franklin (Ernst et al., 2021), et proviennent essentiellement du nord du Canada et des bassins sédimentaires de Bylot (Fig. 0.1 ; Fury et Hecla, Hunting-Aston, Borden et Thulé) situés au nord-est du Canada et au nord-ouest du Groenland. Les bassins de Bylot, d'âge Méso- à Néoprotérozoïque (1270–718 Ma), incluent des roches sédimentaires (grès, schistes argileux) et magmatiques (basaltes, filons-couche et filons) pour des épaisseurs stratigraphiques individuelles comprises entre 3 et 4 km (Long et Turner, 2012).

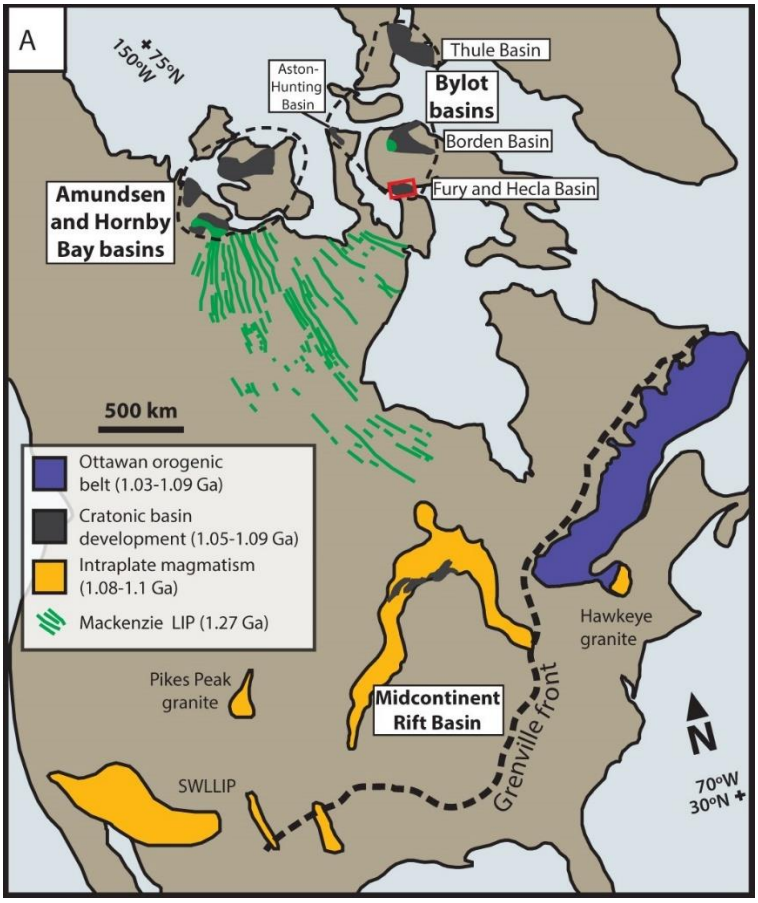

Figure 0.1. Bassins cratoniques Mésoprotérozoïque de Laurentia d'après Greenman et al. (2021).

Mackenzie

La large province ignée de Mackenzie est une des plus grandes LPI de l'histoire de la Terre comprenant essentiellement la grande coulée basaltique du groupe de la rivière Coppermine, l'intrusion stratifiée du Muskox, et un grand essaim de filons au central nord du Canada (Fig. 0.2 ; LeCheminant et Heaman, 1989 ; Ernst et al., 1995 ; Baragar et al., 1996). D'autres roches mises en place plus loin (> 2000 km) sont associées à l'événement de Mackenzie incluant des roches basaltiques et filon-couches ont été mis en place le long de l'essaim de dyke et dans l'archipel Arctique tels que les basaltes du lac Tweed, les gabbros Fortress, et des roches dans les bassins de Bylot (Hoffman, 1988; Sevigny et al., 1991; Fahrig et al., 1981). Le large volume de magma mafique extrudé (~2.90 Mkm^2), une courte période de temps entre 1272–1265 Ma, l'évidence de soulèvement domal et l'essaim de filon convergeant vers le point focal sur l'île de Victoria ont permis d'interpréter que la LPI de Mackenzie est produit à partir de la fusion d'une plume mantellique (LeCheminant et Heaman, 1989; Baragar et al., 1996 ; Ernst et al., 2021). Le soulèvement domal, centré sur l'île de Victoria, a un diamètre de plus de 1000 km, et est supposé avoir causé l'effondrement du graben et

l'extension vers l'extérieur des fractures radiales menant à la formation de l'essaim de filon de Mackenzie (Baragar et al., 1996). Des dykes en Sibérie ont aussi été associés à l'événement de Mackenzie (Ernst et al., 2016).

La tectonique et la paléogéographie de l'Amérique du Nord (continent Laurentia) au Protérozoïque est encore peu comprise. Le continent Laurentia a fait parti du supercontinent Nuna (1900–1300 Ma ; Fig. 0.3 ; Evans et Mitchell, 2011). Des études précédentes ont suggéré que la sédimentation des bassins de Bylot était due à l'ouverture du rift associé à l'événement de Mackenzie a 1268 Ma (Jackson et Ianelli, 1981; LeCheminant et Heaman, 1989). Cependant, des ages Re-Os de 1048 ± 12 Ma et 1046 ± 16 Ma venant de la formation d'Arctic Bay (Gibson et al., 2018), et celui de 1087 ± 6 Ma venant de la formation d'Agu Bay (Greenman et al., 2021) indiquent que la majorité de la stratigraphie du bassin de Borden et de Fury et Hecla datent ultérieurement le magmatisme de Mackenzie de plus de 200 Ma, impliquant la présence d'une importante discontinuité dans le supergroupe de Bylot qui a dû connaître une plus longue histoire géologique (ca. 1270–1050 Ma) et remettant en cause l'hypothèse d'un rifting avec la formation d'un océan.

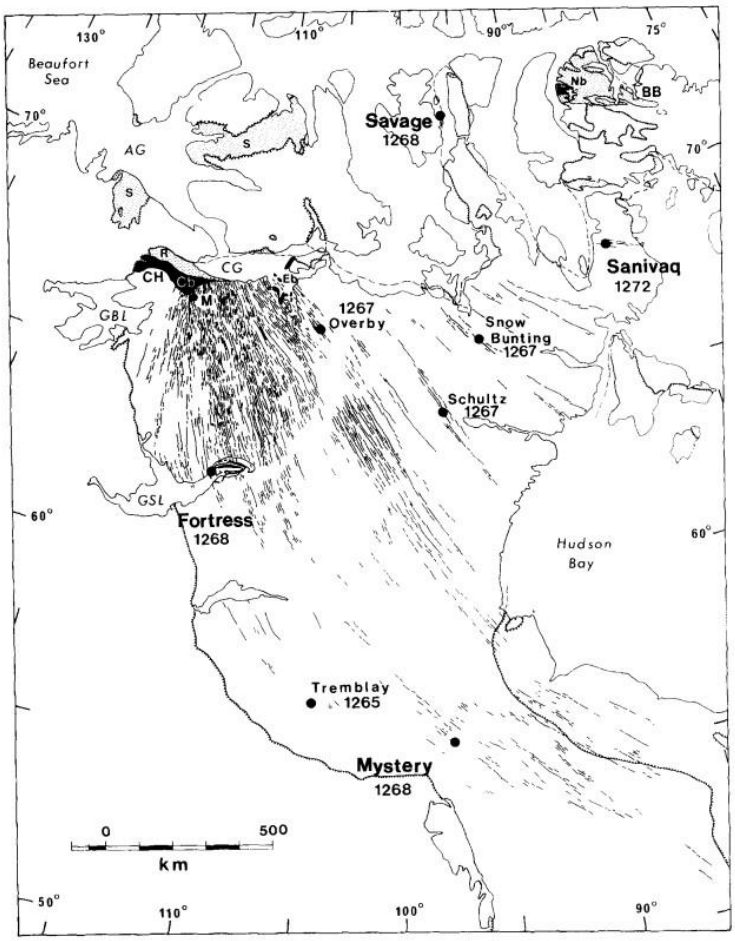

Figure 0.2. Carte de la large province ignée de Mackenzie d'après LeCheminant et Heaman (1993).

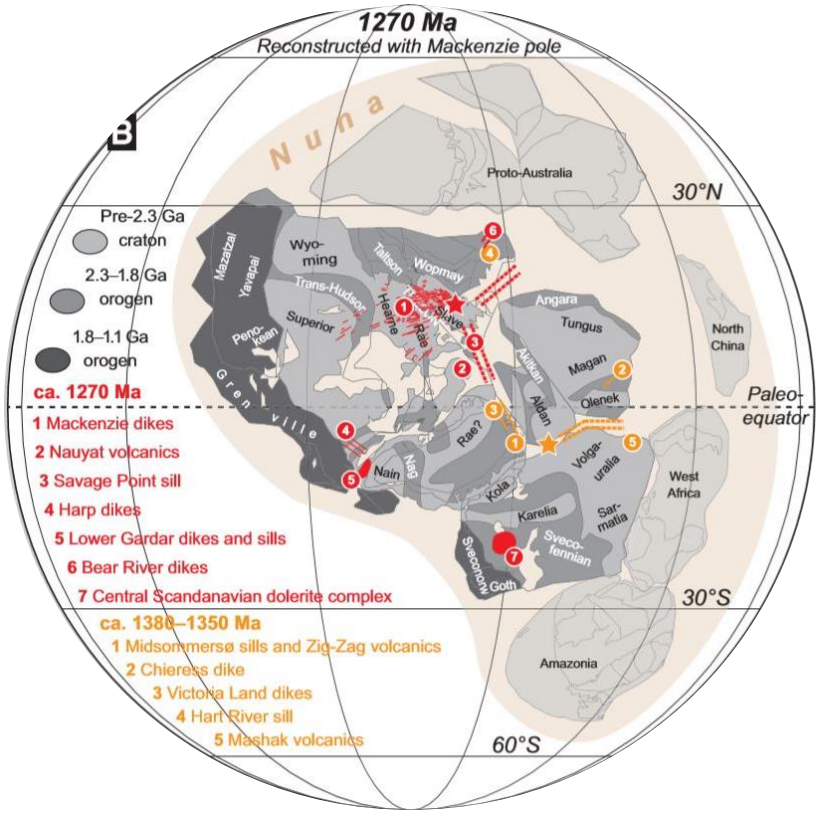

Figure 0.3. Reconstruction du supercontinent Nuna d'après Evans et Mitchell (2011).

Franklin

La large province ignée de Franklin (ca. 718 Ma) est supposée avoir mis en place près de ~2.64 Mkm^2 de roches mafiques (Ernst et al., 2021) incluant les coulées basaltiques et sills de Natkusiak a l'île de Victoria (Fig. 0.4 ; Heaman et al., 1992; Bedard et al., 2016; Beard et al., 2017), les coulées basaltiques de Kikiktat au nord-est de l'Alaska (Cox et al., 2015), et un essaim de filon et filon-couches du nord du Canada au nord-ouest du Groenland (Heaman et al., 1992; Shellnutt et al., 2004; Denyszyn et al., 2009a, b). L'événement de Irkutsk est supposé etre la continuation de Franklin en Sibérie. (Ernst et al., 2016). La LPI de Franklin est une des plus large LPI mise en place pendant la période du Tonien (1000–720 Ma) intervenant à la rupture du supercontinent Rodinia (Ernst et al., 2021). La LPI de Franklin a mis en place un volume important de magma sur une durée de quelques millions d'années, et est caractérisé par une phase de soulèvement observée dans la stratigraphie du groupe de Shaler avant la phase d'extrusion de magma, supportant l'origine d'une plume mantellique (Heaman et al., 1992). Les âges U-Pb, essentiellement des baddeleyites, ont contraint l'événement de Franklin entre 725 et 712 Ma (Heaman et al., 1992; Pehrsson et Buchan, 1999; Denyszyn et al., 2009a, b; Macdonald et al., 2010) et montrent sa longue durée. Cependant, cette durée d'environ 10 Ma est contraire à une typique LPI du Phanérozoïque qui se forment en environ ~1

Ma (Kasbohm et al., 2021), suggérant que soit les roches n'appartiennent pas à l'événement de Franklin ou que certains de ces âges sont inexacts.

L'emplacement des LPI du Phanérozoïque ont été corrélées à des perturbations environnementales globales comprenant des épisodes de réchauffement et de refroidissement, des anomalies négatives d'isotopes de Carbone et des extinctions de masse (Ernst et al., 2021). Il a été proposé que la LPI de Franklin a également perturbé le climat global de la Terre et les cycles biogéochimiques (Cox et al., 2016 ; Macdonald et Wordsworth, 2017). La première glaciation globale du Cryogénien (720–635 Ma), aussi appelée l'épisode de la Terre boule de neige du Sturtian, a débutée vers 717 Ma (Hoffman et al., 1998 ; Macdonald et al., 2010, 2018 ; MacLennan et al., 2018) peu après ou pendant l'épisode de Franklin. Cox et al. (2016) et Goddéris et al. (2003) ont proposé que l'altération des roches de Franklin et celles d'autres LPI du Néoprotérozoïque au niveau des tropiques du supercontinent Rodinia (Denyszyn et al., 2009a) ont mené à une baisse drastique du CO_2 et un refroidissement planétaire catastrophique qui a initié la glaciation du Sturtien. Néanmoins, les ages U-Pb actuels ne permettent pas d'établir une temporalité claire et de déterminer si l'emplacement de Franklin a réellement participé à l'initiation de la glaciation de la Terre boule de neige.

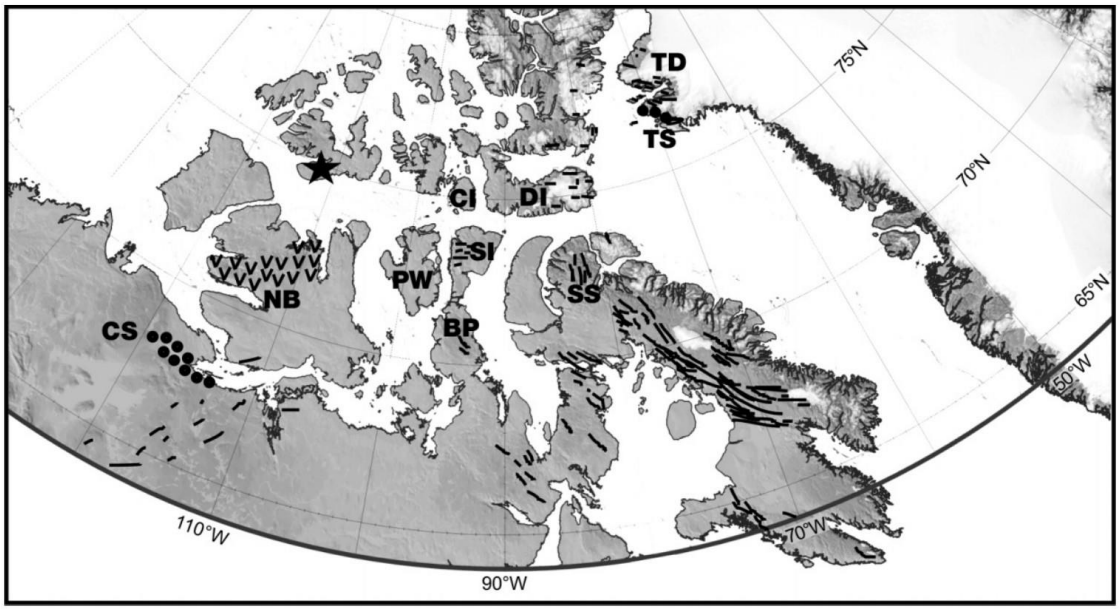

Figure 0.4. Carte de la large province ignée de Franklin d'après Denyszyn et al. (2009a).

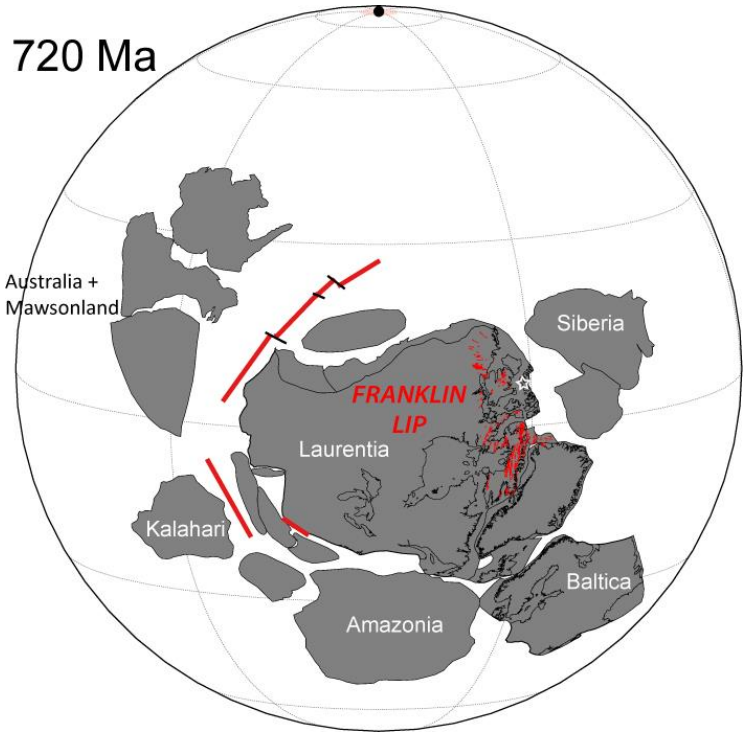

Figure 0.5. Reconstruction paléogéographique de Rodinia à 720 Ma modifié d'après Swanson-Hysell (2021). L'étoile blanche correspond à la localisation du centre de la plume de Franklin (Denyszyn et al., 2009a)

L’approche méthodologique

Géochimie de roche totale

Les éléments majeurs et traces présents dans les roches sont importants à étudier pour comprendre la formation de ces roches et leur origine. On peut ainsi classer les roches selon leur composition géochimique (e.g. alcaline, tholéiitique, calco-alcaline) et observer l’évolution des éléments afin de déterminer si cela reflète un contexte de formation spécifique. Ces éléments permettent également d’étudier la différenciation des roches à travers les processus de cristallisation fractionnée, de fusion partielle et d’assimilation.

Ainsi, la géochimie apporte plusieurs informations sur la compréhension des LPIs. Le magma des LPIs est souvent mafique bien qu’on trouve des LPIs siliciques. Il est possible d’identifier les pulses du magmatisme, de corréler les unités qui sont souvent dispersées sur des grandes distances et de relier la composition de groupes volcaniques à des sous-essaims de filons (e.g. Mackenzie). Afin de contraindre les origines et les source des roches des LPIs, il est intéressant d’utiliser des proxys géochimiques (ratios d’éléments), et particulièrement ceux incluant des éléments incompatibles (Zr, Y, Nb, REE) qui sont généralement immobiles lors de l’altération. Ils permettent de distinguer à travers les unités des LPIs, plusieurs types géochimiques et de suivre le mouvement des groupes de magmas correspondant à la répartition de chaque type géochimique de la large province ignée (Ernst, 2014). Pour ceci on peut étudier dans les LPIs, la distinction des provinces à faible et haute titane (e.g. Karoo, Paraná-Etendenka, CAMP).

Isotopes

Les isotopes d’un même élément chimique partagent le même nombre de protons mais un nombre de neutrons différent. Ils ont des charges similaires mais des masses différentes et se distinguent en isotopes stables et radioactifs. Les isotopes radioactifs, par la désintégration radioactive, se transforment spontanément en d'autres atomes en émettant simultanément des particules de matière et de l'énergie. Ainsi, l’évolution et la distribution des isotopes dans les réservoirs terrestres (manteau, croûte) produits par la désintégration radioactive au cours du temps, font des isotopes radiogéniques des excellents traceurs isotopiques pour caractériser les roches et les processus géologiques à petite et grande échelle. Ainsi, le système isotopique Sm-Nd permet par exemple d’interpréter l’origine de la source des roches et leur pétrogenèse. Les isotopes radiogéniques sont aussi importants pour dater précisément les roches comme c’est le cas avec le système U-Pb. Cette étude se focalise sur l’analyse des isotopes de Sm-Nd et U-Pb.

Géochronologie U-Pb

Le système Uranium-Plomb (U-Pb) est le système isotopique de datation par excellence. Il possède quatre isotopes naturels de Pb stable ^{204}Pb, ^{206}Pb, ^{207}Pb et ^{208}Pb, les trois derniers sont issus respectivement de la désintégration radioactive de ^{238}U, ^{235}U et ^{232}Th impliquant des chaines de décroissance différentes avec plusieurs isotopes intermédiaires. L'U-Pb est l'outil idéal pour dater les roches du fait que les longues durées de demi-vie de ^{238}U ($t_{1/2}$ = 4.5 Ga), ^{235}U ($t_{1/2}$ = 0.7 Ga) et ^{232}Th ($t_{1/2}$ = 14 Ga) et l'incorporation de l'uranium dans plusieurs minéraux datables permettent de contraindre les événements loin dans le temps, et de dater les plus anciennes roches du système solaire. La datation U-Pb peut également fournir plusieurs autres informations avec les zircons renseignant sur les événements comme la cristallisation du magma ou le métamorphisme. En outre, la très-haute précision de l'U-Pb permet de dater les épisodes magmatiques, les extinctions de masse et les événements environnementaux majeurs.

Ainsi, le système U-Pb repose sur les trois équations suivantes :

$$\left(\frac{^{206}Pb}{^{238}U}\right) = (e^{\lambda 238t} - 1)$$

$$\left(\frac{^{207}Pb}{^{235}U}\right) = (e^{\lambda 235t} - 1)$$

$$\left(\frac{^{208}Pb}{^{232}Th}\right) = (e^{\lambda 232t} - 1)$$

La désintégration de deux isotopes du même élément père (^{238}U, ^{235}U) en deux isotopes du même élément fils (^{206}Pb, ^{207}Pb) avec deux demi-vies différentes est la grande force de cette méthode géochronologique, qui permet de calculer deux âges U-Pb indépendants du même échantillon et de connaitre l'âge de cristallisation du minéral si les âges concordent (Schoene, 2014) sur les diagrammes Concordia de Wetherill (^{206}Pb/^{238}U versus ^{207}Pb/^{235}U) et de Tera-Wasserburg (^{238}U/^{206}Pb versus ^{207}Pb/^{206}Pb).

Les minéraux de zircon ($ZrSiO_4$) et baddeleyites (ZrO_2) sont les minéraux les plus emblématiques de la méthode U-Pb. Ils partitionnent fortement l'uranium (Condomines et al., 2003) dans leur structure cristalline et rejettent le plomb, du fait de son incompatibilité à ces minéraux, au cours de leur cristallisation. Ils ont un ratio initial élevé en U-Pb (>1000) variant avec l'âge. Les diffusivités faibles en U (10^{-20} cm^2s^{-1}) et Pb (10^{-20} à 10^{-16} cm^2s^{-1}; Cherniak et Watson, 2003) avec une température de fermeture élevée (~ 900°C) pour le zircon permettent d'enregistrer un âge de cristallisation magmatique qui sera conservé même après un événement métamorphique. Bien que les baddeleyites se forment généralement dans des magmas sous-saturés en silice et que les zircons se forment dans des magmas sursaturés en silice, il est possible de trouver des zircons dans des roches mafiques. Ceci pourrait être dû à de la contamination crustale changeant la

composition magmatique, à une cristallisation très fractionnée ou à un mélange des deux (Davies et al., 2021). Le zircon est le minéral le plus utilisé car il peut survivre aux processus d'altération physico-chimique, de transport et métamorphiques de haut-grade. S'il n'est pas formé in situ dans le magma il peut donc être hérité.

Les baddeleyites et zircons présentent souvent des domaines ayant été endommagés par des radiations résultant du recul alpha et de l'accumulation de traces de fission (Reiners et al., 2017). Ceux-ci produisent des données discordantes telle que la perte en Pb, compliquant souvent l'interprétation correct de l'âge de l'échantillon. Ainsi, les baddeleyites étaient auparavant considérées comme un minéral idéal pour la datation U-Pb car il est moins affecté par la perte en Pb que les zircons (Heaman et LeCheminant, 1993). Cependant, la précision des âges des baddeleyites a été revue (Schaltegger et Davies, 2017) car ils sont plus jeunes que les âges des zircons chimiquement érodés et bien que la pétrologie montre que la baddeleyite est la phase cristallisée la plus précoce (Davies et al. 2017; Gaynor et al., 2020; Pohlner et al. 2020). La technique abrasion chemique permet ainsi de retirer les zones radiation endommagées des zircons ayant été possiblement affectées par la perte en Pb avant analyse (Widmann et al. 2019), menant à des âges U-Pb de zircons nettement plus précis que ceux des baddeleyites (Schaltegger et Davies, 2017). La technique d'abrasion chimique n'apparaît pas fonctionner pour la baddeleyite (Rioux et al. 2010) et pour laquelle aucune méthode n'existe pour enlever les effets de la perte en Pb (Pohlner et al. 2020).

Statistique Bayésienne

Dans le but d'améliorer la précision des âges obtenus, il est possible d'utiliser des méthodes statistiques telle que la méthode Bayésienne (Johnstone et al., 2019). Appliqué à la géologie, celle-ci implique d'avoir au préalable un ordre chronologique clairement établi entre les successions géologiques, qu'elles soient sédimentaires (loi de superposition stratigraphique) ou d'unités recoupant d'autres formations (Halverson et al., 2022). Lorsque cela est vérifié, on emploi la méthode de Monte-Carlo pour améliorer les incertitudes absolues sur l'âge d'emplacement en éliminant les combinaisons d'échantillons ne répondant pas à la relation de recoupement.

Géochimie isotopique Sm-Nd

Le système Samarium-Néodyme (Sm-Nd) est quant à lui seulement basé sur la désintégration radioactive du ^{147}Sm en ^{143}Nd. Ce sont deux éléments intermédiaires des terres rares, le Nd étant plus incompatible que le Sm. La très longue durée de demi-vie du ^{147}Sm ($t_{1/2}$ = 106 Ga) fait qu'il produit des petites variations

isotopiques en Nd. Connaissant que le ratio $^{147}Sm/^{144}Nd$ de la Terre est similaire à la valeur chondritique (CHUR) et le ratio $^{143}Nd/^{144}Nd$ initial, on peut déterminer l'évolution du $^{143}Nd/^{144}Nd$ au cours du temps. Les variations étant petites de l'ordre de 10 000 on utilise la notation ε (epsilon) avec la valeur ε_{Nd} définie comme suit :

$$\varepsilon_{Nd} = 10^4 * \left(\frac{\frac{^{143}Nd}{^{144}Nd}échantillon}{\frac{^{143}Nd}{^{144}Nd}CHUR} - 1 \right).$$

Les ratios Sm/Nd tendent à être plus élevés dans les roches mafiques et ultramafiques, et plus faibles dans les roches felsiques. Cela a donc fait évoluer différemment le ratio $^{143}Nd/^{144}Nd$ de la croûte continentale et du manteau (White, 2005) avec les variations en $\varepsilon_{Nd} < 0$ reflétant l'évolution de la croûte et celles en $\varepsilon_{Nd} > 0$ représentant l'évolution du manteau. Le Sm-Nd est un système isotopique assez robuste du fait qu'il est résistant à l'altération et au métamorphisme de faible grade. Ce couple isotopique peut etre compare à des proxys d'éléments en trace afin de pouvoir discerner l'origine des sources des roches.

Objectifs et hypothèses de recherche

D'autre part, la géochimie permet aussi de corréler l'histoire magmatique des roches qui varie selon la composition du manteau et le contexte tectonique. C'est le cas pour la période de Mackenzie, où les âges U-Pb disponibles ne sont actuellement pas assez précis pour déterminer s'il existe des différences en termes d'âge entre les roches (LeCheminant et Heaman, 1989 ; Heaman et LeCheminant, 1993). Les roches de Franklin présentent aussi une diversité géochimique importante.

Bien que la large province ignée de Franklin ait fait l'objet de datations, les âges manquent aujourd'hui de précision et la géochronologie est ainsi importante pour contraindre la tectonique, la paléogéographie et les grands événements climatiques à ces époques. Ainsi, les âges U-Pb baddeleyites de de Franklin compris entre 725 et 712 Ma ne permettent pas de contraindre suffisamment la durée de l'épisode de Franklin (Heaman et al., 1992; Pehrsson et Buchan, 1999; Denyszyn et al., 2009a, b; Macdonald et al., 2010). Par ailleurs, il est difficile d'établir un lien précis entre le volcanisme de Franklin et la glaciation du Sturtien Snowball Earth qui s'est déroulée entre 717 et 659 Ma (Hoffman et al., 1998 ; Macdonald et Wordsworth, 2017).

Questions scientifiques

L'étude approfondie de la géochimie de ces LPIs nous permet de comprendre en détail la formation, l'histoire de ces provinces ignées et la tectonique régionale. Observe-t-on alors quelconque variations géographiques et temporelles dans les LPIs de Mackenzie et Franklin ? Quels sont les processus magmatiques et les compositions des sources impliquées dans la formation et l'évolution de ces deux provinces ignées ? Quels sont les implications tectoniques et lithosphériques associées avec ces LPIs ? Il faut donc utiliser la géochimie de l'ensemble de Mackenzie pour comprendre davantage le mise en place de la plume, de ses roches et de leurs relations par rapport à la tectonique à cette époque (Objectif 1, voir ci-dessous), qui est supposée être synchrone à la formation des bassins de Bylot (Fahrig et al., 1981). Il est aussi nécessaire d'étudier en détail la géochimie de Franklin pour caractériser la lithosphère aux échelles régionales (Objectif 3).

Par ailleurs, il est important d'établir une corrélation entre le volcanisme et les événements environnementaux majeurs. Ainsi, nous cherchons à comprendre si l'épisode de Franklin event a été impliqué dans l'initiation of the Sturtian Snowball Earth event ? Nous nous intéressons donc à contraindre davantage la durée de la LPI de Franklin avec une géochronologie de haute-précision afin de comprendre l'impact de Franklin sur le climat global de la Terre à ca. 720 Ma (Objectif 2).

Objectif 1 :

Le premier chapitre de cette thèse consiste à mieux comprendre, à travers la géochimie, la mise en place du magmatisme de Mackenzie ainsi que du contexte géodynamique du continent Laurentien. Pour cela, nous avons compilé la géochimie totale et des isotopes de Nd de basaltes, filons-couche et filons de Mackenzie, complétée avec de nouvelles données des bassins de Fury et Hecla (nord-ouest de l'île de Baffin) et de l'essaim de filons (nord central du Canada).

Objectif 2 :

Le deuxième chapitre porte sur essentiellement sur la présentation de nouveaux âges U-Pb de zircons des roches de Franklin afin de déterminer la chronologie exacte de l'épisode de Franklin par rapport à la Terre boule de neige. Pour ce faire, des zircons provenant de deux filons et deux filons-couche des zones de Fury et Hecla et de Thulé (nord-ouest du Groenland) ont été analysés. Une compilation d'isotopes de $\delta^{13}C$, $^{87}Sr/^{86}Sr$ et $^{187}Os/^{188}Os$ est également utilisée pour observer les variations biogéochimiques à cette période.

Objectif 3 :

Le troisième chapitre traite de l'étude de la géochimie de Franklin et cherche comprendre la mise en place du magmatisme en lien avec la tectonique du continent Laurentien. Ce chapitre compile l'ensemble des données géochimiques de roche totale et des isotopes de Nd disponibles sur l'événement magmatique, et est complété par de nouvelles données issues des filons et filons-couche des zones de Fury et Hecla et de Thulé.

Ces trois objectifs ont fait l'objet de trois articles scientifiques rédigés en anglais, dont un soumis et les deux autres en voie de soumission.

Chapitre I. New whole-rock geochemistry and Nd isotopes highlight the early and late phases of the Mackenzie LIP. À soumettre au journal *Canadian Journal of Earth Sciences*.

Chapitre II. New U-Pb CA-ID TIMS zircon ages implicate the Franklin LIP as the proximal trigger for the Sturtian Snowball Earth event. A été soumis au journal *Earth and Planetary Science Letters*.

Chapitre III. Major and trace element and Nd isotope compositions reveal low-, and high-Ti provinces in the Franklin LIP implicating changes in lithosphere thickness and Arctic Laurentia tectonics. À soumettre au journal *Precambrian Research*.

CHAPITRE 1

NEW WHOLE-ROCK GEOCHEMISTRY AND ND ISOTOPES HIGHLIGHT THE EARLY AND LATE EMPLACEMENT PHASES OF THE MACKENZIE LIP

Frédéric Dufour[1], Thomas Skulski[2], Ross Stevenson[1]

[1]Département des Sciences de la Terre et de l'Atmosphère, Université du Québec à Montréal, Montréal, Québec, H3C 3P8, CANADA

[2]Geological Survey of Canada, Natural Resources Canada, Ottawa, Ontario K1A 0E8, Canada

Abstract

The Mackenzie large igneous province (ca. 1270 Ma) includes the continental flood basalts of the Coppermine River Group, the Muskox Layered Intrusion, a giant radiating dyke swarm in north-central Canada, and numerous distal lavas and sills across Canada and Greenland. We present new whole-rock geochemistry and Nd isotope data for Mackenzie dykes and distal eastern basalts of the Fury and Hecla Basin and compare them to previously studied Mackenzie igneous rocks, and examine if the geochemical variations in the Mackenzie dykes, sills and basalts, are recorded in the geochemical stratigraphy of the Coppermine River Group. We also investigate the petrogenesis of the Mackenzie LIP and its tectonic setting.

Our new and compiled data show that the radiating dyke swarm and distal volcanic members display a chemical-spatial pattern that can be related to the temporal chemical evolution of the volcanic rocks in the proximal, focal region. The Mackenzie rocks form two distinct geochemical groups based on major and trace element data. The first group represented by an early magmatic phase was focused on the northern margin and resulted in the emplacement of low-TiO_2 (< 2%) and crustally contaminated ($-7 < \varepsilon_{Nd}^{1270} < 0$) magmas including the Bear River dykes, the Tweed Lake volcanics, and basalts and sills of the Bylot basins. The lower September Creek member of the Coppermine River basalts, is cut by Mackenzie dykes which also feed the upper members, is similarly contaminated, but has a ra,nge of values TiO_2 contents. These features are aligned in a northeasterly direction across the Canadian Arctic, and are interpreted to be emplaced during a crustal stretching episode related to an early phase of the Mackenzie magmatism. The focus of the Mackenzie plume coincides with thermal lithospheric erosion, and wide-scale marine to continental sedimentation following the Mackenzie LIP, reflect lithospheric extension along Laurentia's northern margin (present coordinates). The second, more southerly group is defined as a late magmatic phase consisting of high TiO_2 (> 2%) and relatively uncontaminated rocks ($0 < \varepsilon_{Nd}^{1270} < +4.5$) that includes the majority of the Mackenzie dyke swarm and the upper Coppermine River Group, was less contaminated, reflecting derivation from a progressively depleted mantle source.

1.1 Introduction

Continental large igneous provinces (LIPs) events are largely characterized by mafic rocks covering large areas of the crust, and are commonly associated with continental break up and rifting (Coffin and Eldholm, 1994; Courtillot et al., 1999; Ernst, 2014). Continental LIPs extrude large volumes of magma, emplace continental flood basalts, sills, mafic-ultramafic layered intrusions, and dyke swarms in a short-time period of ~1–5 Ma (Bryan and Ernst, 2008; Kasbohm et al., 2021). The large volume of magma produced over a short period is inferred to reflect mantle plume-induced melting as the cause of LIP magmatism (Campbell and Griffiths, 1979; Bryan and Ernst, 2008; Ernst et al., 2021) but many other origins have been proposed (see summary in Ernst et al., 2005).

The large extent, radiating, synchronous emplacement of LIP dyke swarms make them an important tool in paleogeographic reconstructions (Halls, 1987). Giant dyke swarms associated with LIPs show radiating or linear patterns, extending over long distances (>2000 km) from the swarm focus, such as seen in the Mackenzie, Franklin, and Paraná-Etendenka dyke swarms (LeCheminant and Heaman, 1989; Heaman et al., 1992; Simões et al., 2019). Dyke swarms can have a vertical flow direction within the focal region, and a lateral direction outside the focal region as seen in the Mackenzie dyke swarm (Ernst and Baragar, 1992; Hastie et al., 2014). The direction of the flow is thought to reflect the paleostress field of the continental blocks, commonly parallel to the contemporaneous regional horizontal maximum compressive stress direction and perpendicular to the extension direction. The radiating dyke swarms are commonly emplaced in association with mantle plume or volcanic edifices, parallel dykes generally forming within pre-existing fractures, and circumferential dyke swarms circumscribing the plume source tangentially (Pollard, 1987; Smith, 1987; LeCheminant and Heaman, 1989; Hou et al., 2010; Ju et al., 2013; Ernst et al., 2019; Buchan and Ernst, 2021).

The short duration and large volume of these mafic magmatic events have been interpreted in terms of derivation from a central, plume head and outward migration of magmas through a radial dyke swarm (Ernst et al., 1995; Kiselev et al., 2012; Li et al., 2015). This would imply a relationship between lava composition and the feeder dykes. In particular, the temporal evolution in magmatism due to changes in mantle source(s), melting regime, fractionation, and interaction with continental crust, may be recorded in volcanic stratigraphy. Inferred spatial chemical variations in dyke composition may reflect the lateral extent of the melting regime, source region heterogeneity, temporal changes in dyke geometry (Ernst and Buchan, 2001), or the material assimilated.

The Mackenzie event is a very large LIP in Earth's history that emplaced about 2.90 Mkm^2 of volcanic mafic lavas, sills, the Muskox layered intrusion, and a large dyke swarm radiating in a few million years across the Canadian Arctic and over half of the Canadian Shield (Ernst et al., 1995; LeCheminant and

Heaman, 1989). The Mackenzie LIP is a natural laboratory for examining the temporal and spatial evolution of the magmatism because of four important characteristics. (1) The Mackenzie LIP includes a giant radiating dyke swarm fanning over 2500 km; (2) with magnetic anisotropy data showing that the Mackenzie dykes have a vertical paleo-magma flow within 500 km of the focal region, and a lateral flow at distances greater than 500–2100 km (Ernst and Baragar, 1992); (3) a thick succession of flood basalts of the Coppermine River Group (~4 km) which lies within 500 km of the focus, and are locally fed by dykes; and (4) U-Pb ages on dykes and sills across the Mackenzie LIP yield ages of ca. 1270 Ma. Previous authors have studied the geochemical evolution of the magmas of the Coppermine River Group, the Muskox Intrusion, and the radiating dyke swarm. These authors found that magmas range towards more evolved compositions, both upward in the Coppermine lava sequence and outward along the swarm, and that the lower Copper Creek member correlates with the Muskox Intrusion (Gibson et al., 1987; Baragar et al., 1996; Day et al., 2013).

The goal of this paper is to demonstrate that geochemical variations in the Mackenzie dykes, sills and basalts, are recorded in the geochemical stratigraphy of the Coppermine River Group, and to determine if these variations produce spatial and temporal geochemical patterns? We also examine these geochemical variations in term of the petrogenesis of the Mackenzie LIP and its tectonic setting.

1.2 Geological Settings

The Mackenzie LIP comprises a giant radiating dyke swarm, the Coppermine River flood basalts, and the Muskox layered intrusion in north-central Canada (Fig. 1.1; LeCheminant and Heaman, 1989; Baragar et al., 1996). Distal volcanic rocks and sills along the length of the dyke swarm and in the Arctic Archipelago such as the Tweed Lake volcanics, the Fortress Gabbro, and rocks in the Bylot basins also correlate stratigraphically and have identical ages with the Mackenzie event (Hoffman, 1988; Sevigny et al., 1991; Fahrig et al., 1981). The magmatism emplaced about 2.90 Mkm^2 of mafic rock between 1272–1265 Ma (Table 1; LeCheminant and Heaman, 1989; Ernst et al., 2021). This large volume of magma emplaced over a short period, together with evidence of uplift in the Coppermine homocline and Elu basin, and the radiating dyke swarm converging towards a focal point on Victoria Island have led researchers to suggest that the Mackenzie LIP was a product of mantle plume melting (LeCheminant and Heaman, 1989; Baragar et al., 1996). The domal uplift, centered on Victoria Island, has a diameter of >1000 km and is believed to have caused graben collapse and outward-extending radial fractures leading to the Mackenzie dyke swarm (Baragar et al., 1996; Blanchard et al., 2017). Dykes related to the Mackenzie dyke swarm may also be present in southern Siberia (Ernst et al., 2016)

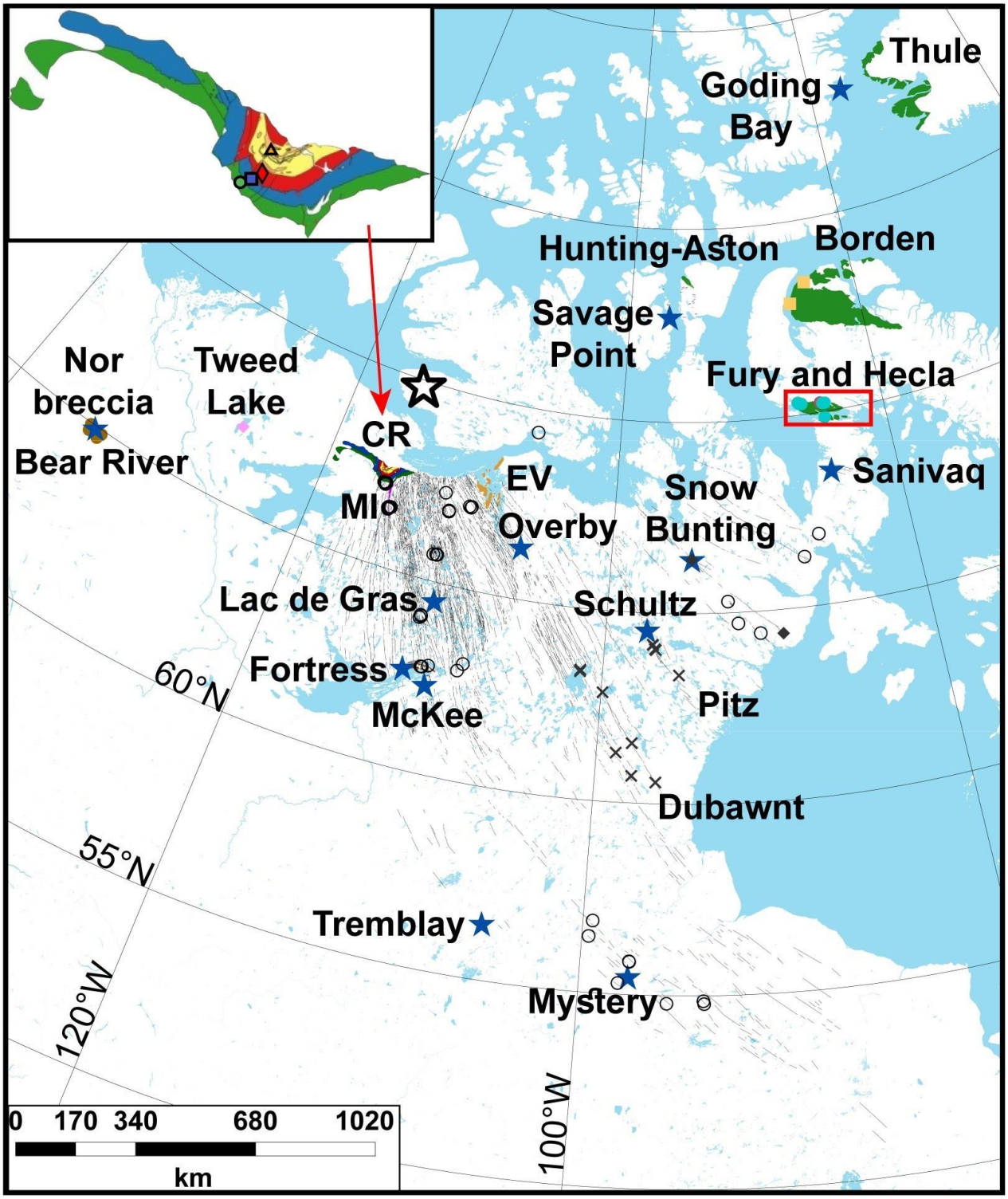

Figure 1.1: Map of the Mackenzie igneous suites. Colored fields are from Buchan et al. (2010); light brown field is the Coppermine River Group; purple field is the Muskox Intrusion; orange field is the Ekalulia volcanics; the red brown field is the Fortress Gabbros; the dark lines are the Mackenzie dyke swarm. Green fields are the Bylot basins. Red box indicates location of Fig. 1.2. Inset map is the Coppermine River Group modified from Skulski et al. (2018) with lower divisions of the Copper Creek Formation (green field, September Creek member; blue field, Stony Creek member; red field, Burnt Creek member) and the Husky Creek Formation (orange field). Black open star is the proposed Mackenzie

plume (Baragar et al., 1996). Blue stars are the U-Pb ages from Table 1.1. CR, Coppermine River; MI; Muskox Intrusion; EV, Ekalulia volcanics.

1.2.1 Coppermine River Group

The Coppermine River Group, located near the plume center, extends laterally over ~300 km (Fig. 1.1) and comprises ~4.9 km (vertical extent) of Mesoproterozoic subaerial volcanic flows of the Copper Creek Formation overlain by clastic red-beds and interbedded basaltic lava flows of the Husky Creek Formation (Baragar and Donaldson, 1973; Skulski et al., 2018). The Coppermine River Group along with the Hornby Bay and Dismal Lake groups form the gently northward-dipping Coppermine homocline, but the Coppermine River Group is separated from the sedimentary groups by a major unconformity (Kerans et al., 1981; Hahn et al., 2013).

The Copper Creek Formation is a ~3000 m thick subaerial tholeiitic sequence composed of ~ 150 flows (averaging 10–30 m thick; Baragar, 1969; Baragar and Donaldson, 1973; Dostal et al., 1983) that was subdivided by Skulski et al. (2018) into the following three stratigraphic members: the September Creek (at the base and locally pillowed), the Stony Creek and Burnt Creek. The Husky Creek Formation overlies the Copper Creek Formation and is composed of ~1900 m of reddish lithic sandstone, with interbedded basalt flows, locally pillowed (Baragar and Donaldson, 1973; Skulski et al., 2018; Meek et al., 2019). Mineralogy of the Coppermine River basalts generally consists of a fine-grained to aphanitic texture, containing microphenocrysts of plagioclase and clinopyroxene in an intergranular groundmass of plagioclase, clinopyroxene, Fe-Ti oxides, native copper, and quartz (Baragar, 1969; Skulski et al., 2018). The September Creek member includes olivine-phyric picrite, orthopyroxene-phyric high MgO basalt, and glassy high Cr andesite (Day et al. 2013; Skulski et al., 2018).

The Coppermine River Group is correlated to the Mackenzie LIP with a Re-Os age of 1263 +16/-20 Ma and comparable paleopoles to those of other Mackenzie igneous rocks (Robertson, 1969; Baragar and Robertson, 1973; Day et al., 2013). Field relationships show that Mackenzie dykes cut the September Creek member and appear to be feeder dykes for the Stony Creek and Burnt Creek members (Baragar et al., 1996).

1.2.2 Mackenzie dyke swarm and distal correlatives rocks

1.2.2.1 Size of the swarm, distribution of dykes and sills and existing age constraints

The Mackenzie giant radiating dyke swarm is the largest known dyke swarm on Earth, fanning over 2500 km across the Canadian Shield with an arc of 100° (Fig. 1.1; Ernst et al., 1995). Beyond ~1000 km from the plume focus, the dykes generally trend in a southeast direction. Dykes up to 2000 km in length have been recorded, with dyke widths ranging from 1–150 m, with an average width of ~30 m (Fahrig, 1987). The rocks are gabbro bodies, with medium- to coarse-grained textures in their centers and a well-defined chilled

margin. The mineralogy typically comprises plagioclase, pyroxene, Fe-Ti oxides in most of the dykes, while the Pitz-Dubawnt and Snow Bunting dykes contain a larger proportion of K-feldspar suggesting an alkaline nature that was loosely interpreted as originating from a deeper source (LeCheminant and Heaman, 1989; Baragar et al., 1996). The number of dykes decreases with increasing distance from the plume center (Ernst and Buchan, 2001). The dykes distinctly cut the Muskox Intrusion (Irvine, 1978), and the September Creek member of the Coppermine Group, but are believed to feed the upper volcanic sequence (Baragar et al., 1996).

The Muskox Intrusion was emplaced early during the Mackenzie magmatism, is situated 400 km south of the plume center, and outcrops over a distance >125 km (Fig. 1.1; Mackie et al., 2009). The mafic–ultramafic layered intrusion is a funnel-shaped body that intruded sedimentary strata and crystalline basement rocks beneath the Coppermine River Group, primarily fed by the keel dyke, and is composed of gabbroic and peridotitic cumulates (Irvine, 1970). The Muskox Intrusion has a parental magma composition consistent with both the Coppermine River basalts and Mackenzie dykes (Francis, 1994).

Volcanic sequences stratigraphically correlated with the Coppermine strata and sills are found along strike of the dyke swarm (Fig. 1.1). The Tweed Lake volcanics (9 m thick) exposed ~500 km west of the swarm focal point and the Ekalulia volcanics (500 m thick) are found in the Elu basin (Campbell, 1979; Sevigny et al., 1991) and are believed to be stratigraphically coeval with the Coppermine River Group. Other intrusions dated at ca. 1268 Ma (Table 1) include the Fortress intrusions that are ~1000 km south of the focal point and north of the Great Slave Lake, and includes the East Arm and Christie Bay sills (Hoffman, 1988). The Tremblay sills outcrop ~1800 km south from the focal point in the Athabasca region (Hulbert et al., 1993).

Dykes with contrasting orientations are also found. The ENE McKee dyke is orthogonal to the swarm and located south of the Great Bear Lake, yields a Mackenzie age (1267 ±3 Ma; Fig. 1.1; Pehrsson et al., 1993). Northern Yukon hosts the N to NW-trending Bear River dykes (~1000 km from the focal point) striking 50° off to the plume focus, with similar ages and geochemistry to the Mackenzie event (Schwab et al., 2004). The identification of a rotation of the Yukon block relative to Laurentia during the Early Cambrian or Neoproterozoic indicates that their original orientation is consistent with that of the Mackenzie swarm (Eyster et al., 2017). The emplacement of the Bear River dykes is suspected to have caused the formation of the NOR breccia in northern Yukon (Parrish and Bell, 1987) by hydrothermal fluids resulting from crustal heating induced by the magmatism (Thorkelson et al., 2001). The intrusion of mafic sills in the Lac de Gras area (Fig. 1.1; Davis, 1997) provoked hydrothermal circulation and the formation of diagenetic xenotime in the Lady Nye Formation (Davis et al., 2008).

Distal northeastern basalts and gabbro sills are exposed in the four Mesoproterozoic Bylot basins were related to the Mackenzie igneous event based on coeval ages and paleomagnetic poles (Fig. 1.1; Fahrig et

al., 1981). In the Hunting-Aston basin, the Savage Point sill (120–300 m thick) intrudes the Aston formation on Prince of Wales Island (Mayr et al., 2004). The Nyeboe basalts (member of the Nyeboe formation) and the Hansen sill (up to 30 m thick) occur in the lower reaches of the Fury and Hecla basin on northwestern Baffin Island (Fig. 1.2; Dufour et al., 2020). The Nyeboe basalts comprise two or possibly three red-oxidized flows (up to 4 m thick) that are locally pillowed (Patzke et al., 2021). The Borden basin on northern Baffin Island includes seven flows within the Nauyat Formation (up to 200 m thick), locally pillowed (Dostal et al., 1989; Long and Turner, 2012). Lastly, the Thule basin in eastern Ellesmere Island and northwestern Greenland (Dawes, 1997) contains volcaniclastic deposits, basalts (twelve flows with occurrences of pillow structure), and sills (1–140 m thick) with the prominent Goding Bay sill (140 m thick) in the Nares Strait Group.

Tableau 1.1 : Published Mackenzie ages

Name and rock type	**Age**	**+/-**	**Methodology**	**Mineral**	**Reference**
T43 dyke	1267	3	$^{207}Pb/^{206}Pb$	baddeleyite	Pehrsson et al. (1993)
Fortress sill	1268	-	$^{207}Pb/^{206}Pb$	baddeleyite	Heaman and LeCheminant (1993)
Mystery dyke	1268	-	$^{207}Pb/^{206}Pb$	baddeleyite	Heaman and LeCheminant (1993)
Savage Point sill	1268	-	$^{207}Pb/^{206}Pb$	baddeleyite	Heaman and LeCheminant (1993)
Goding Bay sill	1268	-	$^{207}Pb/^{206}Pb$	baddeleyite	Heaman and LeCheminant (1993)
Sanivaq dyke	1272	2	upper intercept age	baddeleyite	Heaman and LeCheminant (1993)
Tremblay sill	1267	2	upper intercept age	baddeleyite	Heaman and LeCheminant (1993)
Schultz dyke	1267	2	upper intercept age	baddeleyite	LeCheminant and Heaman (1989)
Overby dyke	1267	2	upper intercept age	baddeleyite	LeCheminant and Heaman (1989)
Snow Bunting dyke	1267	2	upper intercept age	baddeleyite	LeCheminant and Heaman (1989)
Dyke 1 and 2	1268.5	1.5	upper intercept age	baddeleyite	Schwab et al. (2004)
Dyke 3	1264.6	1.2	upper intercept age	zircon	Schwab et al. (2004)
Muskox Intrusion	1270	4	upper intercept age	baddeleyite	LeCheminant and Heaman (1989)
Muskox Intrusion	1269	-	$^{207}Pb/^{206}Pb$	baddeleyite	Mackie et al. (2009)
Muskox Intrusion	1269.4	1.1	$^{207}Pb/^{206}Pb$	baddeleyite/zircon	French et al. (2002)
NOR breccia	1264.7	1.2	$^{207}Pb/^{206}Pb$	monazite	Parish and Bell (1987)

Xenolith	1280	-	-	zircon	Davis (1987)
Lady Nye Formation	1284	11	U-Pb	xenotime	Davis (2008)
Coppermine River basalts	1263	+20/-16	$^{187}Re/^{187}Os$	-	Day et al. (2013)

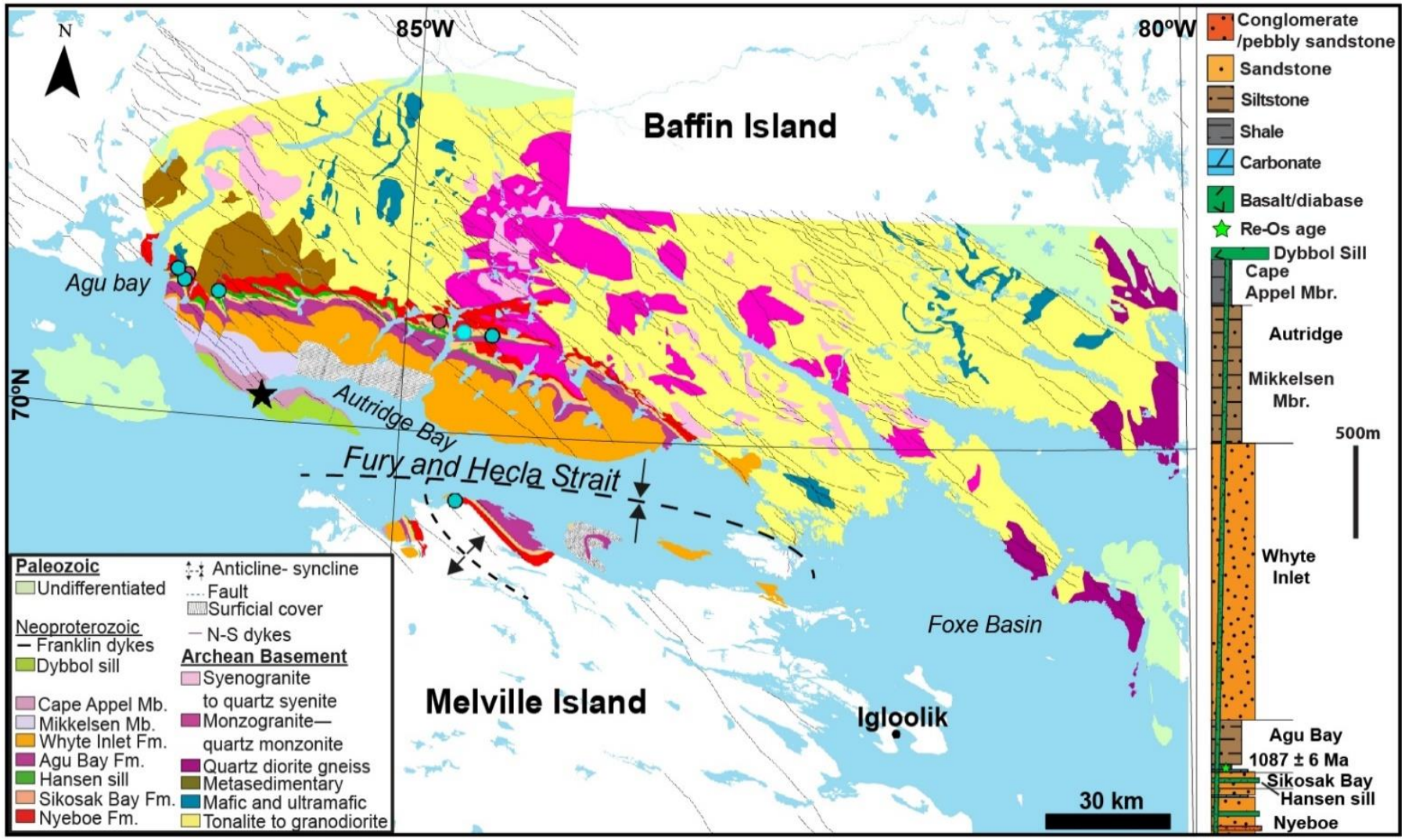

Figure 1.2: Geological map of Fury and Hecla Basin and the Archean basement modified from Dufour et al. (submitted). The Paleozoic rocks and the Fury and Hecla Basin are adapted from Chandler (1988), Long and Turner (2012), and Greenman et al. (2020). The Neoproterozoic Franklin intrusions and the Archean basement are adapted from Steenkamp et al. (2018) and Dufour et al. (2020). Dark star indicates location of the U-Pb ages of the Fury and Hecla dyke and Dybbol sill determined in Dufour et al. (submitted). Inset figure is the stratigraphy of the Fury and Hecla Basin after Chandler (1988) and Greenman et al. (2021).

1.2.2.2 Previous work on the chemistry of dykes

Gibson et al. (1987) and Baragar et al. (1996) demonstrated the existence of geochemical variations along the strike of the Mackenzie swarm. Within 600 km of the focal point of the plume, both volcanic and intrusive rocks exhibit a larger range of differentiation in major and trace elements whereas magmas found more than 600 km from the focal point were found to show a more limited range of differentiation. They also observed that the Pitz-Dubawnt subswarm (Fig. 1.1) has a higher proportion of alkalic compositions, incompatible and compatible elements, has high Ce/Yb ratios, suggesting that these compositions originated from a deeper source (Fig. 24 in Baragar et al., 1996) than the mainstream magmas of the Mackenzie swarm (Baragar et al., 1996). Trace-element compositions of the Mackenzie dykes match those of the Coppermine River Group, both upward in the lava sequence and outward along with the swarm (Baragar et al., 1996). A limited Nd isotope study of the interior of the dykes showed that magmas have εNd values that are indicative of derivation from a depleted mantle source with some crustal contamination (-2.8 to 4.9; Dudás and Peterson, 1992). The most negative values occur near to the dyke margins which was thought to be the result of contamination by the host rocks. Schwab et al. (2004) noted that the Bear River dykes have mantle-normalized trace element profiles similar to those of the Mackenzie dykes between 400–500 km from the focus and to those of the Copper Creek Formation.

Existing geochemical data from the Bylot basins indicate low TiO_2 (<1.25 wt. %) compositions and a continental tholeiitic affinity (Dostal et al., 1989; Dufour et al., 2021). The geochemistry of these rocks is further investigated in this paper.

1.2.2.3 Paleomagnetic data, common paleopole

LIPs and associated dyke swarms are excellent markers for paleo-reconstructions as they are spatially distributed in a short-time period (Halls, 1982), and comprise generally mafic rocks which are faithful recorders of the paleomagnetic pole at the time of their emplacement. In the case of the Mackenzie event, both U-Pb ages and paleomagnetic data are remarkably consistent over distances >1000 km. Primary paleomagnetic pole positions all yield a normal polarity (Fahrig and Jones, 1969) with a grand-mean pole of 4°N, 190°E (14 sites; Buchan and Halls, 1990) that is confirmed by field tests (Irving et al., 1972; Buchan et al., 2009). The Muskox Intrusion, the Savage Point sill, and the East Arm sills all share similar U-Pb ages and paleomagnetic data (Robertson, 1969; Jones and Fahrig, 1978; Heaman and LeCheminant, 1993; Mackie et al., 2009). Chronostratigraphic correlations from paleopoles are used to link distal strata given the Mackenzie Magnetostratigraphic Interval (Fahrig et al., 1971). This technique was employed to correlate the lower Hunting-Aston basin to the Borden basin, with 12 paleopoles from the Aston Formation and

Savage Point sill, and 12 poles from the Nauyat volcanics and Adams Sound formation (Jones and Fahrig, 1978; Fahrig et al., 1981).

1.3 Methodology

Both new and compiled data representing the bulk of the Mackenzie igneous event are used to investigate the magmatic evolution of rocks with respect to relative age and tectonic activity.

Mapping and sampling of the basalt and gabbro rocks were done in conjunction with the Fury and Hecla Geoscience Project during the summers of 2018 and 2019. Well preserved outcrops of the Nyeboe formation are limited and only two fine-grained samples from this unit could be sampled. Samples of the Coppermine River Group are from Thomas Skulski and Mackenzie dykes are from the Tony Peterson, W.R.A. Baragar collection, and from Natasha Wodicka and Anthony LeCheminant of the Geological Survey of Canada. The samples were cut with a rock saw to remove weathered surfaces, crushed using a hydraulic press, and reduced to powder form in a SPEX 8500 Shatterbox using an alumina ceramic bowl.

1.3.1 Whole-rock geochemistry

Whole rock geochemical analyses were obtained from Activation Laboratories Ltd. (Ancaster, Ontario). Major elements were analyzed on a Thermo Jarrell-Ash Enviro II inductively coupled plasma–emission spectrometer (ICP-ES) or a Varian Vista 735 ICP-ES and trace elements were analyzed on a Perkin Elmer Sciex Elan 6000/6100/9000-type inductively coupled plasma–mass spectrometer. Whole-rock geochemistry is reported in Tables A1.1 and A1.2

1.3.2 Sm-Nd analyses

The Sm and Nd concentrations in Tables A1.3 and A1.4 and the Nd isotope data were determined by isotope dilution. Approximately ~0.08 g of rock powder was spiked with a $^{150}Nd/^{149}Sm$ enriched tracer and dissolved using a HF-HNO_3 acid mixture in Teflon beakers. The resulting solutions were evaporated, and concentrated HNO_3 was added to facilitate conversion of fluoride salts to nitrates. The solutions were again evaporated and dissolved in 6N HCl acid to obtain chloride salts. Three different ion-exchange columns were used to obtain Nd and Sm concentrates. In the first column, Fe is removed using an anion exchange resin (AG1-X8). The second column eliminates most of the sample matrix while extracting a REE concentrate using the Eichrom TRU Resin. The final column uses the Eichrom LN Resin to separate Sm and Nd fractions (Pin and Zalduegui, 1997). The $^{147}Sm/^{144}Nd$ and $^{143}Nd/^{144}Nd$ isotopes were measured using a ThermoFisher Nu Plasma II Multi-Collector ICP-MS at the GEOTOP laboratory at Université du Québec à Montréal. At the time of the measurements, the $^{143}Nd/^{144}Nd$ JNDi-1 standard yielded an average of 0.512087 ±6 [(n = 26) compared to the accepted mean of $^{143}Nd/^{144}Nd$ is 0.512115 ±7 (Tanaka et al., 2000)]. The USGS BHVO-1

reference had a value of 0.513006 ±6 [(n = 2) compared to the accepted mean of $^{143}Nd/^{144}Nd$ of 0.512986 ±9 (Weis et al., 2006)]. Isotopic measurements were normalized to a $^{146}Nd/^{144}Nd$ value of 0.7219. The Nd compositions for the Mackenzie samples were age-corrected to 1268 Ma (LeCheminant and Heaman, 1989).

1.4 Results

The compilation presented for the Mackenzie magmatic event includes new geochemical data for 127 whole rock samples (Tables A1.1, A1.2) and 45 Nd isotope samples (Table A1.3). This includes new data for the Nyeboe basalts and the Hansen sill from the Fury and Hecla Basin, the Savage Point (SP) sill of the Hunting-Aston Basin, new analyses for dykes from the Mackenzie dyke swarm in north-central Canada, and new data for the Coppermine River (CR) basalts. These data are compared to 92 whole-rock geochemical and isotopic data for basalts and related intrusive rocks from the Borden Basin (Nauyat basalts; Dostal et al., 1989), lavas and sills in the Cape Combermere Formation (Dawes, 2006), the Tweed Lake volcanics (Sevigny et al., 1991), the Bear River dykes (Schwab et al., 2004), Mackenzie dykes (Gibson et al., 1987; Ernst and Buchan, 2010), and Nd isotope compilation of the Coppermine River Group (Griselin et al, 1997; Day et al., 2013).

1.4.1 Coppermine River Group

Variations of the major elements of the Coppermine stratigraphy are shown in Fig. 1.3. The Coppermine samples range from 45 to 58% SiO_2, slightly decreasing from the September Creek member towards the top of the sequence (Fig. 1.3A). The MgO concentrations in the lavas span from 4–13% (Fig. 1.3B), decreasing in the September Creek and the Stony Creek members, but reverse in the Burnt Creek and Husky Creek members. The September Creek samples contain variable TiO_2 concentrations of 1.2% to almost 4% (Fig. 1.3C). However, TiO_2 concentrations in the Stony Creek member show a progressive increase from just under 2% to over 4% followed by a decreasing trend to 1.6% TiO_2 in the Burnt Creek member. The TiO_2 concentrations remain low (<2 wt. %) in the Husky Creek member. Fe_2O_3 concentrations vary similarly to the TiO_2 with values increasing from around 11% to over 16% (Fig. 1.3D) from the September Creek to the Stony Creek members and subsequently decreasing in the Burnt Creek and Husky Creek members.

Trace element ratios and Nd isotopic compositions are presented in Figs. 1.4. The Ce/Yb ratio is indicative of different degrees of partial melting or change in the composition of the melting, whereas the Th/Nb ratio is suggestive of the enrichment of incompatible elements (Pearce, 2008). Ce/Yb ratios show an overall decrease towards the top of the sequence with small reversals in the Stony Creek and Burnt Creek (Fig. 1.4A). A similar distinct decline occurs from the September Creek to the Husky Creek in the Th/Nb ratios (Fig. 1.4B). Lastly, the ε_{Nd}^{1270} values increase from -6 at the base of September Creek to +2 at the 960 m level and as high as +4.5 in the upper Coppermine members (Fig. 1.4C).

The variations in the abundances of the rare earth elements (REE), high field strength elements (HFS: Zr, Hf, Nb, Y), and large ion lithophile elements (LILE: Ba, Eu, Th, U) of the Coppermine samples are presented in Figs. 1.5A and 5B. The plotted lines depict the maximum and minimum profiles from a given area.

There is a high degree of overlap among the REE profiles of the three lower members of the Coppermine Group. The profiles range from moderately to highly enriched in light REE (26─150 x chondrite with La/Yb ratios of 2.6─4.4). The profiles of the Husky Creek member overlap only the moderately enriched profiles of the other three members (Fig. 1.5A). Some profiles are comparable to the ocean island basalt (OIB) profile. Among the Coppermine members, only the Burnt Creek member displays a small Eu depletion indicating plagioclase fractionation.

Primitive mantle (PM) normalized trace element profiles (Fig. 1.5B) for the Coppermine basalts are generally enriched in incompatible elements such as Th, U (but less enriched than OIB) with variable depletions in Nb, Ta. The September Creek tends to have the strongest Ta and Nb depletions of the Coppermine River. In contrast, Th and U are depleted in the Husky Creek profile and Ta and Nb show little to no depletion.

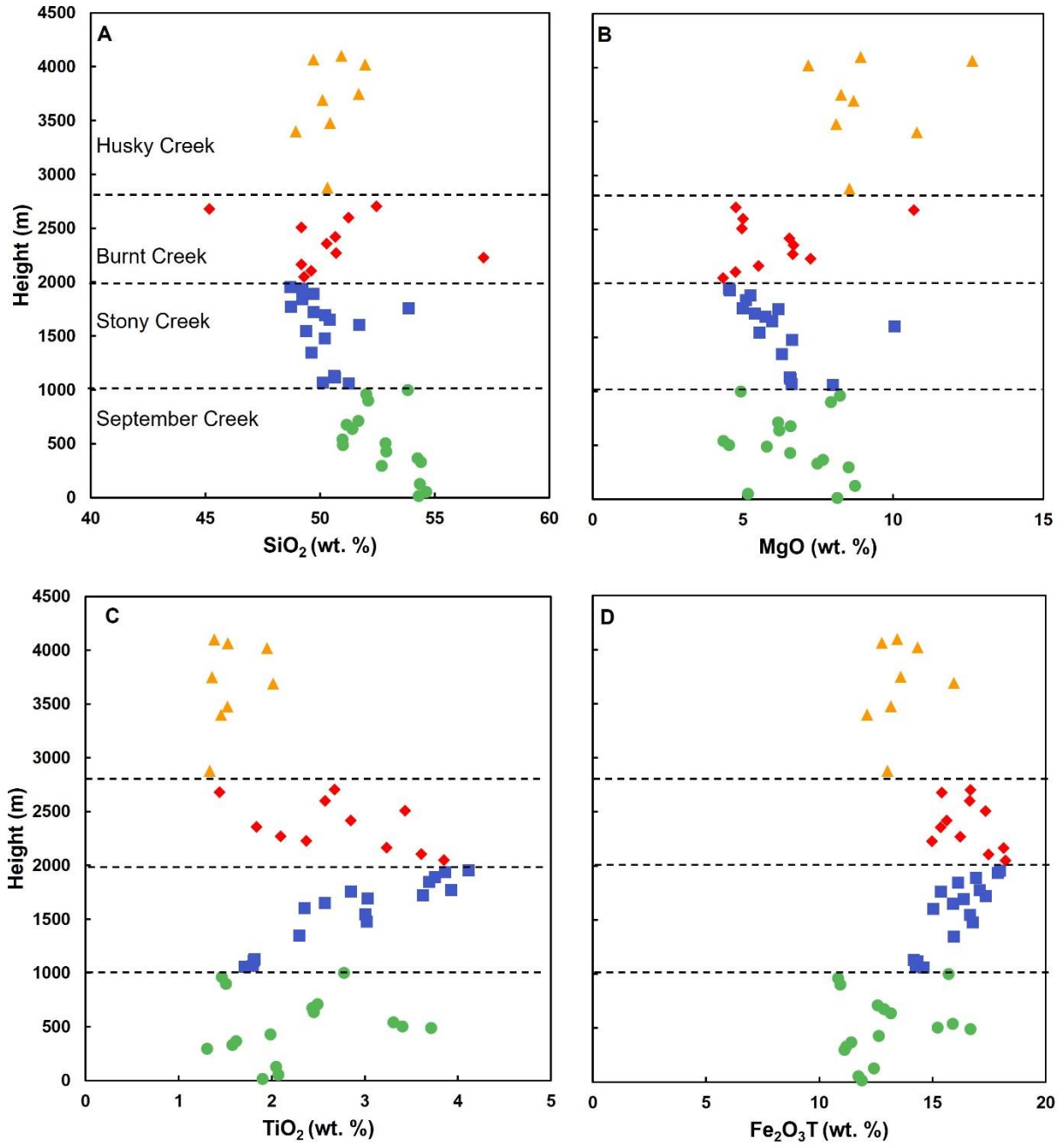

Figure 1.3: SiO_2, MgO, TiO_2 and Fe_2O_3 variations with stratigraphic height in the Coppermine River Group. Data is normalized to 100%.

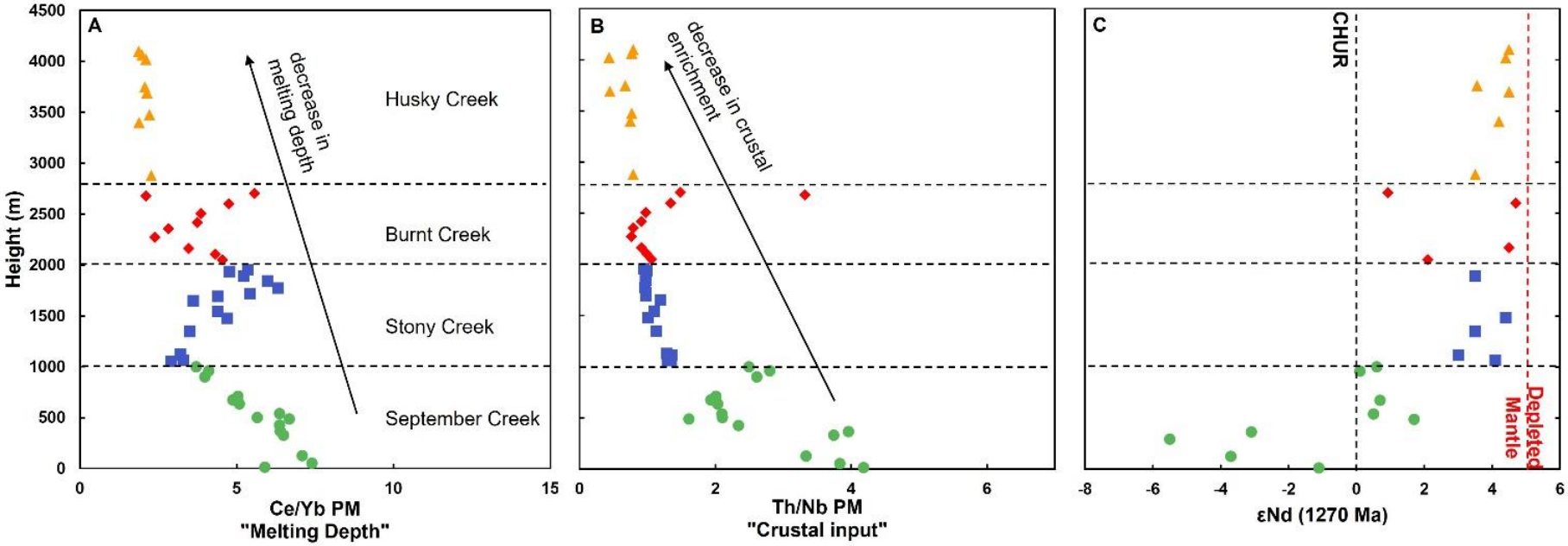

Figure 1.4: Ce/Yb, Th/Nb and εNd variations with stratigraphic height in the Coppermine River Group. Depleted Mantle is from DePaolo (1981). εNd data is compiled from Griselin et al. (1997) and Day et al. (2013).

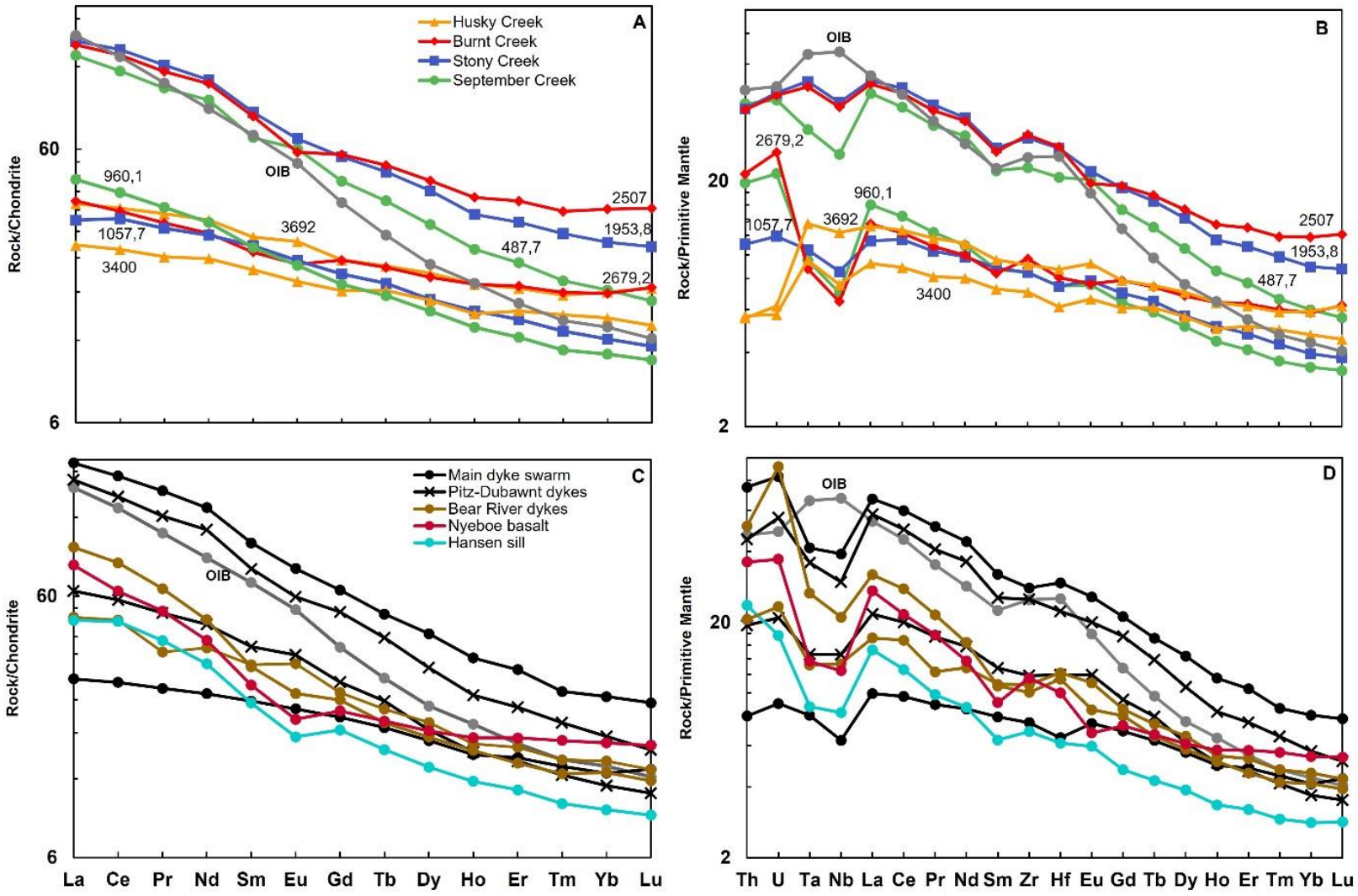

Figure 1.5: Chondrite and Primitive Mantle normalized diagrams with selected Mackenzie data. Normalized values are from McDonough and Sun (1995). A and B are the diagrams of the Coppermine River Group with numbers corresponding to the stratigraphic heights. C and D are the diagrams of the Mackenzie dyke swarm and basalts, sills across Canada and Greenland.

1.4.2 Mackenzie dyke swarm, distal lavas, and intrusive rocks

Figure 6 shows plots of SiO_2, TiO_2 and Fe_2O_{3T} with respect to the MgO contents of the Mackenzie dyke swarm, distal basalts, and sills. The diagrams highlight a group of high SiO_2 (>51 wt. %), low TiO_2 (<2 wt. %), and Fe_2O_{3T} (<13 wt. %) including the Nyeboe and Nauyat basalts, the Hansen and Savage Point sills, the Cape Combermere volcanics, and sills, the Bear River dykes, a few Mackenzie dykes and possibly the Tweed Lake volcanics. Another group of low SiO_2 (<51 wt. %), high TiO_2 (>2 wt. %) and Fe_2O_{3T} (>13 wt. %) includes dykes from the main swarm, the Pitz-Dubawnt dykes, and the Snow Bunting dykes, but these latter two dyke groups appear to be compositionally different from most of the dykes of the main swarm. The rocks largely plot between 1.4–11.5% MgO with the high TiO_2 group yielding slightly lower MgO compositions compared to those of the low TiO_2 group. The low TiO_2 group has a similar range of SiO_2, MgO, and TiO_2 compositions with the September Creek member, whereas the high TiO_2 group has trace element abundances and ratios similar to those of the upper Coppermine members.

The distinction between the high and low Ti rocks is also evident in Fig. 1.7A in which the low and high TiO_2 rocks mostly have similar Ce/Yb ratios, with the exception of the Pitz-Dubawnt and Snow Bunting dykes that tend towards higher Ce/Yb ratios. A similar relationship is observed in a plot of Th/Nb and Ce/Yb ratios in which most of the high TiO_2 dykes have low Th/Nb ratios, with the Pitz-Dubawnt and Snow Bunting dykes trending towards higher Ce/Yb ratios (Fig. 1.7B), and have comparable Ce/Yb ratios to that the Stony, Burnt and Husky Creek members. The Bear River dykes, one sample of the Tweed Lake volcanics, a few dykes, lavas, and sills have higher Th/Nb ratios, comparable to those of the September Creek member. The Nd isotope compositions for dykes from this study are reported in Table A1.2 and shown in Fig. 1.7C along with Nd data from previous studies. The Nyeboe basalts, the Hansen and Savage Point sills, the Bear River dykes and a few Mackenzie dykes have enriched ε_{Nd}^{1270} values (-6 to -1.9), overlapping some samples of the September Creek member (blue field) but lower than most of the Mackenzie dykes (0 to +4.8) and those of the upper Coppermine Group. The Pitz-Dubawnt and Snow Bunting dykes have slightly distinct εNd values from the main dyke swarm. The Muskox Intrusion (green field) displays low ε_{Nd}^{1270} values that overlap with samples of the Hansen sill.

The range of the REE profiles for the Mackenzie dykes, distal lavas, and sills is represented by a few selected profiles to reduce cluster and bracketed by the upper and lower REE profiles for a given group in Fig. 1.5C, as well as representative patterns for the Nyeboe basalts and Hansen sill. They all present enriched profiles with La contents ranging from 30─200 x chondrite and La/Yb ratios of 3.75─8.7. The main dyke swarm and the Pitz-Dubawnt dykes have comparable slopes to those of the Stony, Burnt, and Husky Creek members. The REE-rich profiles from these dyke swarms are comparable to a typical OIB profile. However, the Bear River dykes, the Nyeboe basalts, the Hansen sill, and the Savage Point sill (not shown) have a

different slope marked by a small Eu depletion suggestive of plagioclase fractionation, and have similar REE abundances to those of the September Creek member.

The trace element profiles (Fig. 1.5D) are enriched in most incompatible elements and the most enriched profiles overlap the OIB profile. Samples from the Bear River dykes, the Nyeboe basalts, the Hansen sill, and the Savage Point sill (not shown) tend to have the strongest depletions in HFS elements (Nb, Ta), comparable to the September Creek profile. However, the main dyke swarm and Pitz-Dubawnt dykes have patterns comparable to those of the upper members of the Coppermine River Group.

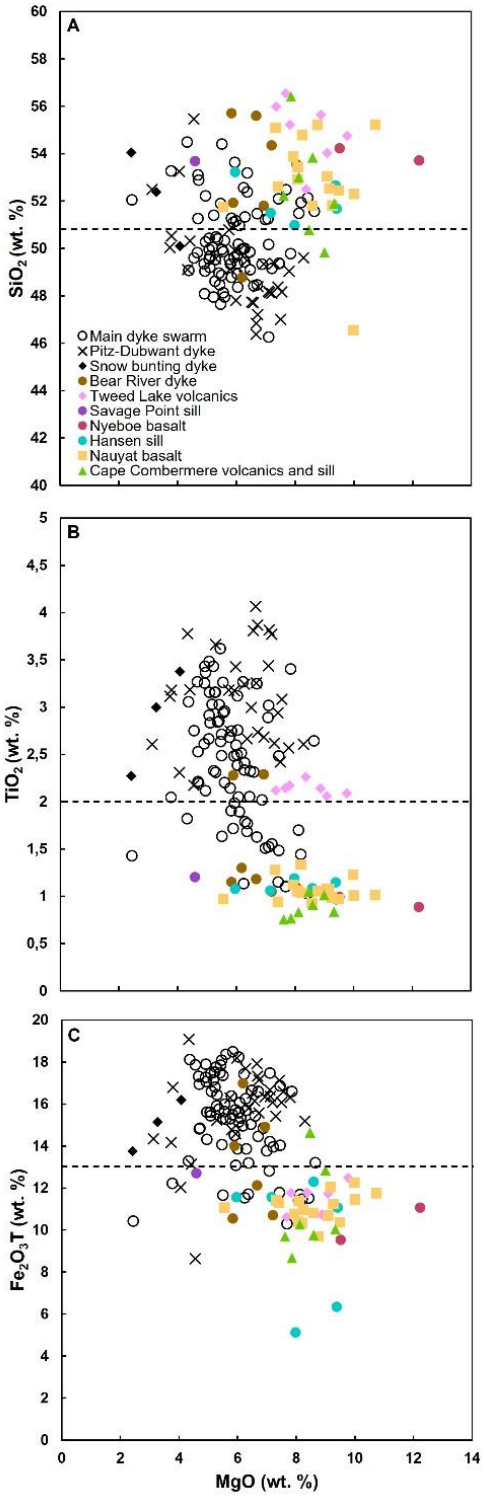

Figure 1.6: SiO_2, TiO_2 and Fe_2O_3 variations vs MgO of the Mackenzie dyke swarm and basalts, sills across Canada and Greenland. Data is normalized to 100%. The Nyeboe basalts, Hansen and Savage Point sills data are from this study; the Tweed Lake volcanics are from Sevigny et al. (1991); the Nauyat basalts from Dostal et al. (1989); the basalts and sills of the Cape Combermere Formation from Dawes (2006); the Bear River dykes from Schwab et al. (2004); the Mackenzie dykes are from this study, Gibson et al. (1987) and Ernst and Buchan (2010).

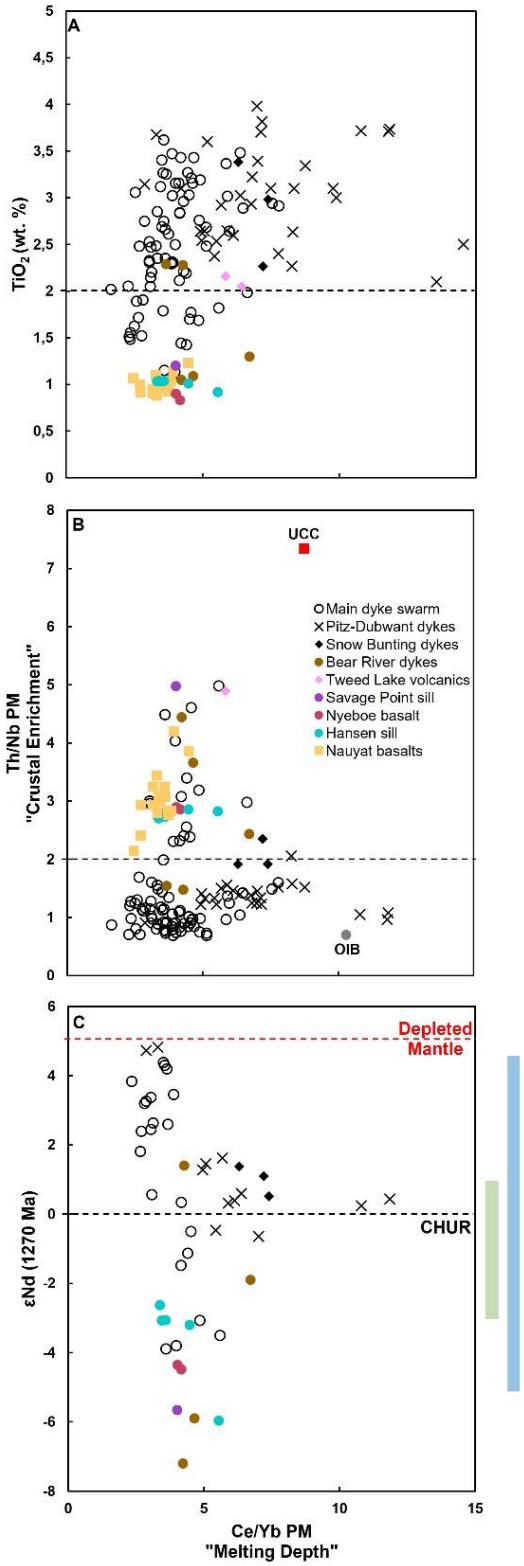

Figure 1.7: TiO_2, Th/Nb and εNd variations vs Ce/Yb of the Mackenzie dyke swarm and basalts, sills across Canada and Greenland. Data points according to Fig. 1.5. Green bar is the εNd data range of the Coppermine River Group and blue bar is the εNd range of the Muskox Intrusion from Mackie et al. (2009). Depleted Mantle is from DePaolo (1981).

1.5 Discussion

Previous studies of the Mackenzie dykes focused specifically on differences between the dyke sub-swarms (Gibson et al., 1987; Baragar et al., 1996). The new data presented in this paper allow this comparison to be extended to include a geochemical comparison between the different Mackenzie dyke suites and lavas of the Coppermine River Group, the Tweed Lake volcanics, and the Bylot basins.

We examine how Ti-rich or Ti-poor mafic magmas may reflect the timing of emplacement (early vs late) and distance from the plume center. Because Mackenzie magmatism is largely preserved within extensional basins, the tectonic implications and stratigraphic correlations are also discussed with regards to the emplacement of the Mackenzie LIP.

1.5.1 Early Mackenzie magmatism

1.5.1.1 Geochemical similarities and contamination in early Mackenzie rocks

The September Creek basalts, the lavas and sills in the Bylot basins, the Tweed Lake volcanics, the Bear River dykes, and a number of other Mackenzie dykes share geochemical similarities (Figs. 1.3, 1.6). This group is generally characterized by low TiO_2 concentrations, although the September Creek member has variable TiO_2 contents, the least contaminated sections with lowest SiO_2 and highest MgO near the top of the member are low TiO_2 that allow it to be included among the low TiO_2 suites. Low TiO_2 may reflect crustal contamination, but can also result from higher degrees of partial melting of the upper mantle or melting at shallower depths (Arndt et al., 1993; Gibson et al., 1995; Jourdan et al., 2007; Lai et al., 2012). The modelling of Day et al. (2013) indicated low degrees of partial melting for the September Creek basalts. However, the low εNd values of the September Creek rocks indicate significant crustal contamination. Potential contaminant compositions such as the upper and lower continental crust (Rudnick and Gao, 2003) along with more local contaminants such as the Wopmay paragneiss (Day et al., 2008) were modeled with the results shown in Fig. 1.8. The modelling indicates that the Wopmay paragneisses provide the best fit for the data and that the September Creek member assimilated between 15 to 30% of the Wopmay paragneiss (Day et al., 2008). Thus, it is likely that the low TiO_2 compositions resulted from crustal contamination as indicated by the generally negative ε_{Nd}^{1270} values associated with these magmas (Fig 1.4C, 1.6C, 1.8; Dostal et al., 1983; Dostal et al., 1989; Sevigny et al., 1991; Dupuy et al., 1992; Griselin et al., 1997; Schwab et al., 2004; Day et al., 2013). Examples of low Ti series magmas with large crustal contamination are observed in many LIPs (Jourdan et al., 2007; Hou et al., 2011; Marzoli et al., 2018; Simões et al., 2019). Crustal contamination may also be responsible for rocks with higher SiO_2 contents in this suite (Figs. 1.3A, 1.6A). A few September Creek rocks described as andesitic rocks with high Cr compositions (Day et al., 2013) indicate up to 50% contamination due to assimilation of quartz-rich xenoliths (Skulski et al., 2018).

Nevertheless, the MgO (Figs. 1.3A–C, 1.6A–C) and Fe_2O_{3T} (Figs. 1.3D, 1.6C) contents of these lavas and sills are consistent with a low degree of crystal fractionation and may indicate that these lavas were erupted early from a magma chamber.

Depletion in HFS elements and light REE enrichment due to crustal contamination leads to high Th/Nb and Ce/Yb ratios (Sevigny et al., 1991; Dupuy et al., 1992; Griselin et al., 1997). This suggest that high Th/Nb and Ce/Yb ratios in the basal September Creek member of the Coppermine River group are an artefact of a greater degree of crustal contamination compared to the overlying lavas (Fig. 1.4B, 1.7B). This difference in contamination was also observed by Day et al. (2013) who suggested that the September Creek lavas essentially insulated the succeeding sequences from crustal contamination. Crustal contamination of the September Creek lavas is also evident from the enriched ε_{Nd}^{1270} values (-5.5 to +1.7) seen in Fig. 1.4C.

The September Creek member is a distinct member of the Coppermine River Group due to the greater degree of crustal contamination as indicated by the geochemical data and by the occurrence of quartz-rich xenoliths (Skulski et al., 2018) and patchy K-feldspar-rich mesostasis in the groundmass of lower flows (Baragar et al., 1996). Previous studies of the concentrations of Ni, Cr, siderophile elements/isotopes, degrees of partial melting, and negative εNd values of the September Creek, suggest that this member may share an origin with the Muskox Intrusion (Francis, 1994; Mackie et al. 2009; Day et al., 2008; Day et al., 2013).

The geochemistry of the September Creek member also shows strong similarities with the Bear River dykes, the Tweed Lake volcanics, and the lavas and sills in the Bylot basins, suggesting that the rocks belong to a geochemical group distinct from those of the upper Coppermine basalts and the majority of the Mackenzie dykes. This group is characterized by higher SiO_2, lower Fe_2O_3, lower TiO_2 and pervasive crustal contamination that is also found in the first 500 m of the September Creek member of the Coppermine River basalts. The comparable low TiO_2 and degree of contamination amongst these rocks over a large distance supported by a lateral magma flow from the focus plume (Ernst and Baragar, 1992), and the fact that the September Creek member and the Muskox Intrusion are cross-cut by the Mackenzie dykes and interpreted to be feeders of the upper Coppermine members (Baragar et al., 1996), suggest these suites are representative of the early magmatic phase of the Mackenzie LIP.

Magnetic anisotropy indicates that magma flow was vertical within 400–600 km of the Mackenzie plume focal point (Ernst and Baragar, 1992) after-which magma is believed to have flown laterally outwards to form the Savage Point and Goding Bay sills (Ernst et al., 1995). Given the geochemical similarities of the more distal eastern and western suites, we suggest that lateral flow continued as far east as the Fury and Hecla, Borden and Thule Basins and as far west as the Bear River Dykes.

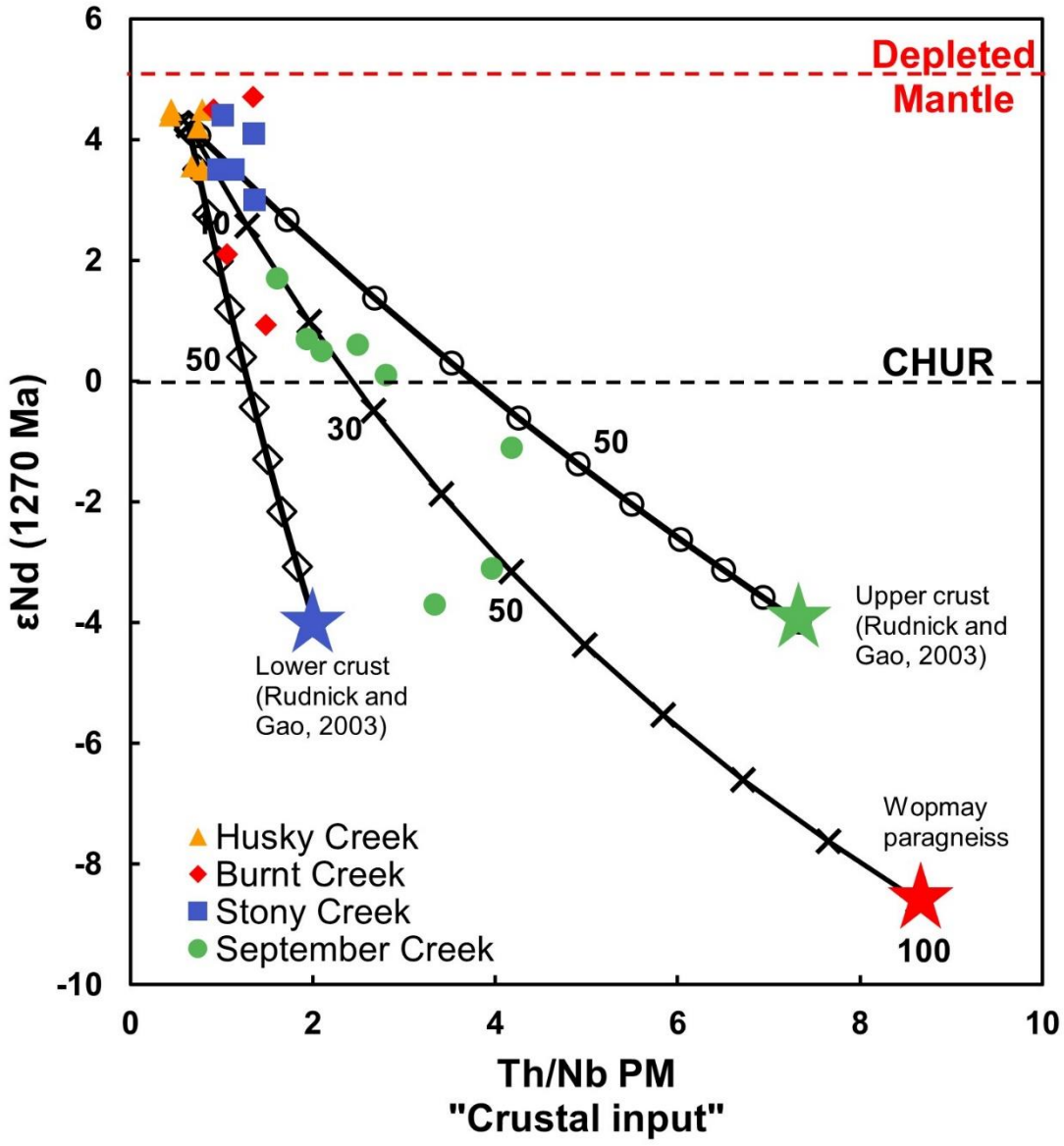

Figure 1.8: Initial εNd isotopic compositions vs. Th/Nb ratios. Mixing line is calculated using trace elements and isotopic composition of the Wopmay paragneiss (Day et al., 2008), and a basalt from the Husky Creek Formation. Primitive-mantle values are normalized are from Sun and McDonough (1989). The curves are marked at 10% intervals.

1.5.1.2 Western extensional tectonic features

A glance at Fig. 1.1 reveals that the Mackenzie LIP-related Bear River dykes, Tweed Lake volcanics, and the Bylot basins align in a northeasterly direction over a distance of ~2000 km from west to east. We further investigate the extensional events that are coeval with the Mackenzie plume along this NE direction.

The Bear River dykes are the only known Mackenzie dykes to occur west of the Mackenzie focal point with a 50° offset from the main Mackenzie dyke swarm (Fig. 1.1; Schwab et al., 2004 Eyster et al., 2017). The intrusion of Mackenzie magmas this far west may have been facilitated by local extension and crustal thinning associated with the formation of the Proterozoic Wernecke basin (Schwab et al., 2004). The location of the Tweed Lake volcanics within a basin (the lower sequences of the basin are stratigraphically correlated to the Hornby Bay and Dismal Lake groups) with a long-lived and active tectonic history (Sevigny et al., 1991) could explain the presence of Mackenzie magmatism in this area.

The ~5 km thick basalts of the Coppermine River Group (Skulski et al., 2018) strongly contrasts with the relatively thin basalt flows observed in the Bylot basins and Tweed Lake volcanics. The volume of magma associated with the Coppermine River Group likely reflects proximity to the Mackenzie plume focal point and to a lesser degree a greater degree of crustal stretching associated with the Coppermine homocline.

1.5.1.3 Northeastern crustal stretching and implications on the history of the lower Bylot Supergroup

Previous studies suggested that sedimentation in the Bylot basins was a product of ca. 1268 Ma rifting related to the Mackenzie igneous event constrained by U-Pb ages and paleomagnetic poles (Fahrig et al., 1981; Jackson and Ianelli, 1981; Heaman and LeCheminant, 1993). However, recent Re-Os ages of 1048 ± 12 Ma and 1046 ± 16 Ma from the Arctic Bay Formation (Gibson et al., 2018), and 1087 ± 6 Ma from the Agu Bay Formation (Greenman et al., 2021), indicate that the majority of the Borden and Fury and Hecla stratigraphy postdates Mackenzie magmatism by >200 Ma, implying the presence of a major unconformity within the Bylot Supergroup.

The lower stratigraphy of the Fury and Hecla, Borden, and Thule basins are broadly similar, transitioning from terrestrial (basal conglomerate) to nearshore-marine (sandstone) facies, and basaltic volcanism near the base of the stratigraphy (Dawes, 1997; Long and Turner, 2012; Patzke et al., 2021). The Hunting-Aston basin differs in that it is characterized by a nearshore-marine sandstone facies rather than terrestrial facies (Mayr et al., 2004). The Fury and Hecla basin has been interpreted as a half-graben, due to modest crustal stretching (Patzke et al., 2021), whereas the Borden basin is believed to be a sag basin (Turner and Kamber, 2012), and the Hunting-Aston basin was interpreted to reflect crustal flexure in response to uplift (Mayr et al., 2004). The Thule basin comprises a faulted basin delimiting an early central depression believed to represent an early rift (Dawes, 1997).

The differences in the tectonic settings of the Bylot basins make it difficult to reconcile a common history. Previous studies have used the basal mafic rocks to suggest that the lower Bylot Supergroup is a result of the Mackenzie igneous event. The Savage Point and Goding Bay sills (Fig. 1.1) have been dated by high-precision U-Pb geochronology at 1268 Ma (Heaman and LeCheminant, 1993) and paleomagnetic poles constrain the Hunting-Aston and Thule basins to a minimum age of 1268 Ma, synchronous with Mackenzie magmatism (Fahrig et al., 1981; Heaman and LeCheminant, 1993). The Nauyat basalts (Borden basin) also yield a Mackenzie pole (Fahrig et al., 1981), but the Nyeboe and Nauyat basalts, and the Hansen sill still lack high-precision geochronology, hampering the correlation of the Fury and Hecla and Borden basins to that same period.

Despite a lack of geochronology and tectonic information, geochemistry can help correlate the igneous rocks of the Bylot basins to more western rocks of the September Creek member, the Tweed Lake volcanics, and the Bear River dykes. These rocks are aligned in a northeasterly direction over a distance of ~2000 km, suggesting that NE-SW crustal stretching associated with the plume may have occurred along this trend. This is supported by the dislocation of the Supercontinent Nuna at 1.3 Ga with Australia separating from Laurentia (Kirscher et al., 2020) favoring extension along the northern margin of Laurentia. The Mackenzie plume is believed to have thermally eroded the lithosphere provoking stretching (Jackson and Ianelli, 1981; LeCheminant and Heaman, 1989; stade 2 in Baragar et al., 1996; Liu et al., 2021), leading to deposition of the lower Bylot Supergroup (Patzke et al., 2021) in the Eastern Arctic. NE-SW extension in Bear River, Tweed Lake, Coppermine areas and in the Bylot basins is supported by the eruption of magma from NE-trending fissures (Baragar and Robertson, 1973; Jackson and Ianelli, 1981; Sevigny et al., 1991; NE-trending vent fed basalt flows, Fig. 61 in Dawes, 1997; Schwab et al., 2004; basalt flows pinching out to the east, Patzke et al., 2021). Patzke et al. (2021) suggested that the amount of magma extruded in the Bylot basins varies relative to the degree of crustal stretching. In our scenario, the stretching would be larger than previously thought, propagating northeasterly into intracratonic areas from the northern Yukon to northwestern Greenland, resulting in contrasting degrees of crustal stretching and different amounts of extruded magma.

1.5.2 Late Mackenzie magmatism

1.5.2.1 Geochemical differentiation

The increasing TiO_2 and Fe_2O_{3T} and decrease in MgO (Figs. 1.3B–3D) in the Stony Creek member of the Coppermine River basalts is indicative of an iron enrichment trend during magma differentiation. Opposing major element trends in the Burnt Creek member reflect differentiation and new injections of juvenile magma. The Husky Creek member is relatively unfractionated compared to the preceding basalt members. The Mackenzie dykes are compositionally similar to those of the Stony Creek and Burnt Creek, showing

comparable iron enrichment trends leading to higher TiO_2, Fe_2O_{3T}, and SiO_2, and a decrease in MgO (Figs. 5). These variations suggest that the middle Coppermine basalts and Mackenzie dykes share similar degrees of differentiation and do not represent primary magma compositions (Dostal et al., 1983; Dupuy et al., 1992; Griselin et al., 1997; Day et al., 2013). Similarly, the Ti, Fe and Ce/Yb ratios from the Stony Creek and Burnt Creek members increase with decreasing MgO reflecting differentiation, and decrease with increasing MgO representing injections of new batches of magma. Day et al. (2013) estimated that the Stony Creek and Burnt Creek magmas were generated by 8 and 18% partial melting of an enriched mantle source. The higher Ce/Yb ratios (Figs. 1.6A–6B) of the Pitz-Dubawnt and Snow Bunting dykes may indicate a lower degree of melting relative to the main dyke swarm (Gibson et al., 1987; Baragar et al., 1996).

The upper Coppermine members are relatively uncontaminated. This is supported by lower SiO_2 contents, lower Ce/Yb and Th/Nb ratios, and high ε_{Nd}^{1270} compositions (Figs. 1.4A–C; Griselin et al., 1997). A decrease in LREE enrichment and smaller depletions in Ta and Nb in the Stony Creek, Burnt Creek, and Husky Creek members (Figs. 1.5A–5B) also suggest a reduction in contamination in these upper Coppermine lava members and may indicate increasing degrees of melting towards the top of the Coppermine succession (Griselin et al., 1997; Day et al., 2013). The Mackenzie dykes display similar trace element patterns to those of the Stony and Burnt Creek and high ε_{Nd}^{1270} values indicating limited crustal contamination among the dykes (Figs. 1.5C–5D; Baragar et al., 1996; Schwab et al., 2004). The Husky Creek member is the least contaminated and the least differentiated unit, and incongruent partial melting models indicate that these magmas were produced by ~12% melting of an enriched mantle (Fig. 1.9).

Previous trace element studies indicated that lavas of the lower September Creek member were the product of melting within the garnet stability field of the mantle, whereas lavas of the upper Husky Creek member were the product of melting in the shallower spinel stability field (Dupuy et al., 1992; Griselin et al., 1997; Schwab et al., 2004; Day et al., 2013). The Ce/Yb ratios from this study (Fig. 1.4A) are consistent with a transition from deep (garnet stability field) melting for the September Creek member to shallow (spinel field) mantle melting for the Husky Creek member. The transition towards shallower melting in the upper Coppermine River lavas suggests a progressive thinning of the lithosphere and ascent of the plume (Griselin et al., 1997; Day et al., 2013).

We propose that the deeper melting associated with the lower Copper Creek formation and its coeval timing with the Muskox intrusion (Mackie et al., 2009; Day et al., 2013) constituted an early magmatic phase of the Mackenzie LIP. This early phase was followed by a later magmatic pulse derived from a shallower mantle in which the Mackenzie dykes acted as feeder dykes to the Stony and Burnt Creek members (Kerans, 1983; Baragar et al., 1996). This late magmatic phase produced both the upper Coppermine River units and the principal radiating dyke swarm of the Mackenzie LIP.

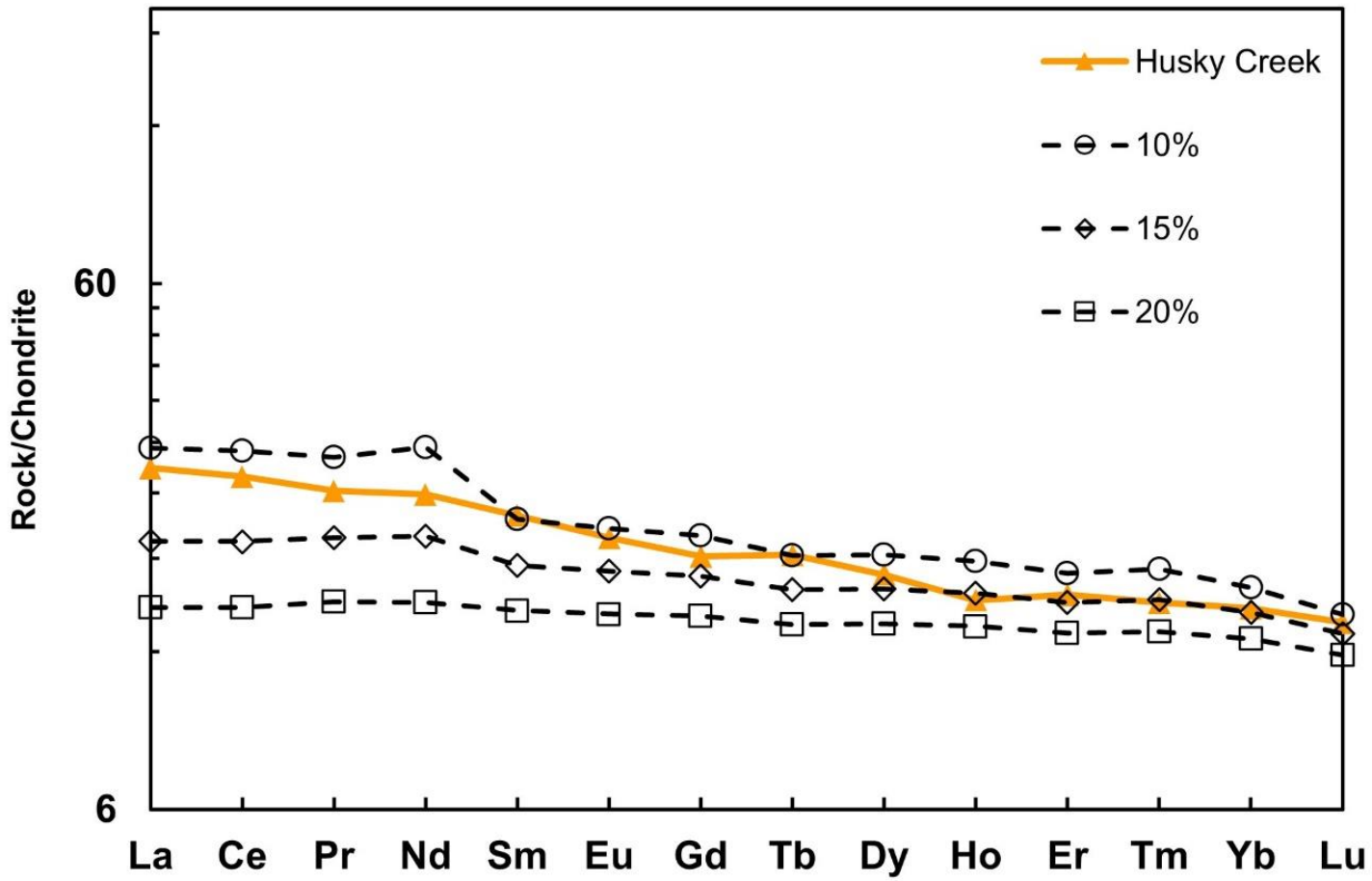

Figure 1.9: Trace-element modeling results for incongruent dynamic mantle melting for tholeiitic lava from the Husky Creek Formation. The melting model is from Zou and Reid (2001). Melt reaction coefficients of spinel lherzolite are from Kinzler and Grove (1992), and partition coefficients are from Salters and Stracke (2004), and Shaw (2000). An enriched mantle (Sun and McDonough, 1989) spinel lherzolite with source mineralogy of 0.3cpx:0.15opx:0.52ol:0.03sp was the best fit to model the partial melting.

1.5.2.2 Emplacement of the late Mackenzie dyke swarm and upper Coppermine sequence

Despite a general consensus for a mantle plume origin for the Mackenzie LIP, the character of the magmatic plumbing system is not completely understood. The plume is believed to have induced domal uplift, followed by a central graben collapse. Graben collapse provoked the formation of radial and circular faults and the development of underlying primary large magma chamber within the core of the uplift and subsidiary magma chambers around the focus area feeding the Mackenzie lavas, sills and dyke swarm (LeCheminant and Heaman, 1989; Baragar et al., 1996; Blanchard et al., 2017). Deep and shallow melting, and the fractional crystallization in these different magma chambers have facilitated different degrees of magmatic differentiation, producing the large geochemical compositional range observed throughout the Mackenzie rocks.

Baragar et al. (1996) suggested that older dykes were shorter while the later dykes were emplaced out to the end of the swarm, observing a change in the average composition of the dykes with distance. Although this observation appears to hold true for increasing differentiation along the strike of the radial dyke swarm, it does not appear to correspond to the lavas, dykes, and sills forming the NE-SW trend along the northern continental margin that have a relatively constant geochemistry over thousands of kilometers, and which are believed to have formed from a common source at the focus of the magmatism.

Magmatism of the Mackenzie LIP began with domal uplift due to the rising mantle plume beneath the northern Laurentian crust that provoked NE-SW extension across the northern Laurentian margin (LeCheminant and Heaman, 1989; Baragar et al., 1996). This early phase of Mackenzie magmatism emplaced the Bear River Dykes, Tweed Lake volcanics, the lower most Coppermine River lavas and the basalts and gabbros of the Bylot basins over a distance of 2000 km. This early suite is also characterized by significant crustal contamination (Griselin et al., 1997; Day et al., 2013). This early extension was followed by a later magmatic phase of the Mackenzie LIP which rapidly injected large quantities of magma, characterized by higher TiO_2 magmas, to form the radial dyke swarm and the lavas of the upper Coppermine River basalts. The radiating portion of the Mackenzie swarm (controlled by domal uplift above the plume head) transitions outward into a linear trend controlled by a regional stress field (Baragar et al., 1996; Hou et al., 2010; Buchan and Ernst, 2021).

1.6 Conclusion

This new whole-rock geochemical and Nd compilation reveals that the Mackenzie igneous event has a more complex history than previously thought, likely producing an early and relatively low Ti, contaminated series, and a late and high Ti, uncontaminated series.

The early magmatic phase includes the Bear River dykes, the Tweed Lake volcanics, the September Creek member and the igneous rocks in the Bylot basins comprising magmas of limited differentiation with low TiO_2 compositions, and high LREE, high Th/Nb and Ce/Yb ratios, and strongly enriched ε_{Nd}^{1270} (< 0) values consistent with crustal contamination. The earlier age of this suite is supported by observation that the Muskox Intrusion and the September Creek member are both cut by the Mackenzie dykes, and by geochemical affinities between the September Creek member and the Muskox Intrusion. Magmatic suites belonging to this early phase are aligned along a NE-SW trend interpreted to result from northeastern crustal stretching induced by the Mackenzie plume as part of the initiation of the magmatism.

The late phase of the Mackenzie LIP includes the dyke swarm and the upper Coppermine sequence (Stony Creek, Burnt Creek and Husky Creek) and is characterized by variable fractionation, producing a larger compositional range of TiO_2 and MgO. They also show less crustal contamination with low LREE, low Th/Nb, and Ce/Yb ratios, small Ta, Nb depletions, and depleted ε_{Nd}^{1270} (> 0) values. The dykes and the upper Coppermine basalts may have been emplaced from multiple magma chambers around the focal area of the plume, facilitating a rapid extrusion of magma.

1.7 Acknowledgments

The authors would like to thank the Canada-Nunavut Geoscience Office and the Natural Resources Canada's Polar Continental Shelf Program for the logistical support. We thank Natasha Wodicka and Anthony LeCheminant for providing samples. This work is part of the PhD program of the lead author, and was supported by a Strategic Partnership Grant from the Natural Sciences and Engineering Research Council of Canada.

1.8 References

Arndt, N. T., Czamanske, G. K., Wooden, J. L. et Fedorenko, V. A. (1993). Mantle and crustal contributions to continental flood volcanism. Tectonophysics, 223(1-2), 39–52.

Baragar, W. R. A. et Donaldson J. A. (1973). Coppermine and Dismal lakes map-areas. (report and maps 1337a and 1338a.

Baragar, W. R. A., Ernst, R. E., Hulbert, L. et Peterson, T. (1996). Longitudinal petrochemical variation in the Mackenzie dyke swarm, northwestern Canadian Shield. Journal of Petrology, 37(2), 317–359.

Baragar, W. R. A. et Robertson, W. A. (1973). Fault rotation of paleomagnetic directions in Coppermine River Lavas and their revised pole. Canadian Journal of Earth Sciences, 10(10), 1519–1532.

Blanchard, J. A., Ernst, R. E. et Samson, C. (2017). Gravity and magnetic modelling of layered mafic–ultramafic intrusions in large igneous province plume centre regions: case studies from the 1.27 Ga Mackenzie, 1.38 Ga Kunene–Kibaran, 0.06 Ga Deccan and 0.13–0.08 Ga High Arctic events. Canadian Journal of Earth Sciences, 54(3), 290–310.

Bryan, S. E. et Ernst, R. E. (2008). Revised definition of large igneous provinces (LIPs). Earth-Science Reviews, 86(1-4), 175–202.

Buchan, K. L. et Halls, H. C. (1990). Paleomagnetism of Proterozoic mafic dyke swarms of the Canadian Shield. In International dyke conference. In: Parker, A.J., Rickwood, P.C., Tucker, D.H. (Eds.), Mafic Dykes and Emplacement Mechanisms. Balkema, Rotterdam, 209–230.

Buchan, K. L. et Ernst, R. E. (2021). Plumbing systems of large igneous provinces (LIPs) on Earth and Venus: Investigating the role of giant circumferential and radiating dyke swarms, coronae and novae and mid-crustal intrusive complexes. Gondwana Research, 100, 25–43.

Buchan, K. L., LeCheminant, A. N. et van Breemen, O. (2009). Paleomagnetism and U–Pb geochronology of the Lac de Gras diabase dyke swarm, Slave Province, Canada: implications for relative drift of Slave and Superior provinces in the Paleoproterozoic. Canadian Journal of Earth Sciences, 46(5), 361–379.

Buchan, K. L., Ernst, R. E., Bleeker, W., Davies, W., Villeneuve, M., Van Breemen, O., Hamilton, M. A. et Söderlund, U. (2010). Proterozoic magmatic events of the Slave craton, Wopmay orogen and environs. Geological Survey of Canada, Open File 5985.

Campbell, F. H. A. (1979). Stratigraphy and sedimentation in the Helikian Elu Basin and Hiukitak Platform, Bathurst Inlet-Melville Sound, Northwest Territories. Energy, Mines and Resources Canada.

Campbell, I. H. et Griffiths, R. W. (1990). Implications of mantle plume structure for the evolution of flood basalts. Earth and Planetary Science Letters, 99(1-2), 79–93.

Chandler, F.W. (1988). Geology of the late Precambrian Fury and Hecla Group, northwest Baffin Island, District of Franklin. Geological Survey of Canada, Bulletin 370, 30 p., https://doi.org/10.4095/126938.

Coffin, M. F. et Eldholm, O. (1994). Large igneous provinces: crustal structure, dimensions and external consequences. Reviews of Geophysics, 32(1), 1–36.

Courtillot, V., Jaupart, C., Manighetti, I., Tapponnier, P. et Besse, J. (1999). On causal links between flood basalts and continental breakup. Earth and Planetary Science Letters, 166(3-4), 177–195.

Davis, W. J. (1997). U-Pb zircon and rutile ages from granulite xenoliths in the Slave province: Evidence for mafic magmatism in the lower crust coincident with Proterozoic dike swarms. Geology, 25(4), 343–346.

Davis, W. J., Rainbird, R. H., Gall, Q. et Jefferson, C. J. (2008). In situ U-Pb dating of diagenetic apatite and xenotime: Paleofluid flow history within the Thelon, Athabasca and Hornby Bay basins. Geochimica et Cosmochimica Acta Supplement, 72(12), A203.

Dawes, P. R. (1997). The Proterozoic Thule supergroup, Greenland and Canada: history, lithostratigraphy and development. Geology of Greenland Survey Bulletin, 174, 1–150.

Dawes, P. R. (2006). Explanatory notes to the Geological map of Greenland, 1: 500 000, Thule, Sheet 5. Geological Survey of Denmark and Greenland Map Series, 2, 1–100.

Day, J. M., Pearson, D. G. et Hulbert, L. J. (2008). Rhenium–osmium isotope and platinum-group element constraints on the origin and evolution of the 1.27 Ga Muskox layered intrusion. Journal of Petrology, 49(7), 1255–1295.

Day, J. M., Pearson, D. G. et Hulbert, L. J. (2013). Highly siderophile element behaviour during flood basalt genesis and evidence for melts from intrusive chromitite formation in the Mackenzie large igneous province. Lithos, 182, 242–258.

DePaolo, D. J. (1981). Trace element and isotopic effects of combined wallrock assimilation and fractional crystallization. Earth and planetary science letters, 53(2), 189–202.

Dostal, J., Baragar, W. R. A. et Dupuy, C. (1983). Geochemistry and petrogenesis of basaltic rocks from Coppermine River area, Northwest Territories. Canadian Journal of Earth Sciences, 20(5), 684–698.

Dostal, J., Jackson, G. D. et Galley, A. (1989). Geochemistry of Neohelikian Nauyat plateau basalts, Borden rift basin, northwestern Baffin Island, Canada. Canadian Journal of Earth Sciences, 26(11), 2214–2223.

Dudas, F. O. et Peterson, T. D. (1992). Nd isotopic composition of Mackenzie dikes, Northwest Territories, Canada. In EOS, Transactions of the American Geophysical Union, Spring Meeting Supplement, p. 339.

Dufour, F., Stevenson, R. et Halverson, G.P. (2020). Timing of emplacement of mafic rocks of the Fury and Hecla Group and younger mafic intrusions, northwestern Baffin Island, Nunavut; in Summary of Activities 2019, Canada-Nunavut Geoscience Office, 27–36.

Dufour, F., Stevenson, R. et Skulski, T. (2021). Geochemical comparison of Mackenzie and Franklin igneous mafic rocks in Nunavut, Northwest Territories and northwestern Greenland; in Summary of Activities 2020.

Dupuy, C., Michard, A., Dostal, J., Dautel, D. et Baragar, W. R. A. (1992). Proterozoic flood basalts from the Coppermine River area, Northwest Territories: isotope and trace element geochemistry. Canadian Journal of Earth Sciences, 29(9), 1937–1943.

Ernst, R. E. (2014). Large igneous provinces. Cambridge University Press.

Ernst, R. E. et Baragar, W. R. A. (1992). Evidence from magnetic fabric for the flow pattern of magma in the Mackenzie giant radiating dyke swarm. Nature, 356(6369), 511–513.

Ernst, R. E. et Buchan, K. L. (2001). Large mafic magmatic events through time and links to mantle-plume heads. In: Ernst, R.E., Buchan, K.L. Mantle Plumes: Their Identification Through Time. Geological Society of America Special Paper 352, 483–575.

Ernst, R.E. et Buchan, K.L., 2010. Geochemical Database of Proterozoic Intraplate Mafic Magmatism in Canada. Geological Survey of Canada Open File 6016, 1 CD-ROM.

Ernst, R. E., Head, J. W., Parfitt, E., Grosfils, E. et Wilson, L. (1995). Giant radiating dyke swarms on Earth and Venus. Earth-Science Reviews, 39(1-2), 1–58.

Ernst, R. E., Buchan, K. L. et Campbell, I. H. (2005). Frontiers in large igneous province research. Lithos, 79(3-4), 271–297.

Ernst, R. E., Hamilton, M. A., Söderlund, U., Hanes, J. A., Gladkochub, D. P., Okrugin, A. V., Kolotilina, T., Mekhonoshin, A. S., Bleeker, W., LeCheminant, A. N., Buchan, K. L., Chamberlain, K. R. et Didenko, A. N. (2016). Long-lived connection between southern Siberia and northern Laurentia in the Proterozoic. Nature Geoscience, 9(6), 464–469.

Ernst, R. E., Liikane, D. A., Jowitt, S. M., Buchan, K. L. et Blanchard, J. A. (2019). A new plumbing system framework for mantle plume-related continental Large Igneous Provinces and their mafic-ultramafic intrusions. Journal of Volcanology and Geothermal Research, 384, 75–84.

Ernst, R. E., Bond, D. P., Zhang, S. H., Buchan, K. L., Grasby, S. E., Youbi, N., et Doucet, L. S. (2021). Large igneous province record through time and implications for secular environmental changes and geological time-scale boundaries. Large igneous provinces: A driver of global environmental and biotic changes, 1–26.

Eyster, A. E., Fu, R. R., Strauss, J. V., Weiss, B. P., Roots, C. F., Halverson, G. P., et Macdonald, F. A. (2017). Paleomagnetic evidence for a large rotation of the Yukon block relative to Laurentia: Implications for a low-latitude Sturtian glaciation and the breakup of Rodinia. Bulletin, 129(1-2), 38–58.

Fahrig, W. F. et Jones, D. L. (1969). Paleomagnetic evidence for the extent of Mackenzie igneous events. Canadian Journal of Earth Sciences, 6(4), 679–688.

Fahrig, W. F., Irving, E. et Jackson, G. D. (1971). Paleomagnetism of the Franklin diabases. Canadian Journal of Earth Sciences, 8(4), 455–467.

Fahrig, W. F., Christie, K. W., Jones, D. L. et Campbell, F. H. A. (1981). Paleomagnetism of the Bylot basins: evidence for Mackenzie continental tensional tectonics. Proterozoic basins of Canada. Edited by FHA Campbell. Geological Survey of Canada, Paper, 81(10), 303–312.

Fahrig, W.F. (1987). The tectonic setting of continental mafic dyke swarms: failed arm and early passive margin. In: Halls, H.C. and Fahrig, W.F. (eds.) Mafic Dyke Swarms. Geological Association of Canada Special Paper 34, 331–348.

Francis, D. (1994). Chemical interaction between picritic magmas and upper crust along the margins of the Muskox intrusion, Northwest Territories. Geological Association of Canada, Special Paper 92-12, 98 p.

French, J. E., Heaman, L. M. et Chacko, T. (2002). Feasibility of chemical U–Th–total Pb baddeleyite dating by electron microprobe. Chemical geology, 188(1-2), 85–104.

Gibson, I. L., Sinha, M. N. et Fahrig, W. F. (1987). The geochemistry of the Mackenzie dyke swarm, Canada. In Mafic dyke swarms. Geological Association of Canada, Special Paper 34, 109–121.

Gibson, S. A., Thompson, R. N., Dickin, A. P. et Leonardos, O. H. (1995). High-Ti and low-Ti mafic potassic magmas: Key to plume-lithosphere interactions and continental flood-basalt genesis. Earth and Planetary Science Letters, 136(3–4), 149–165.

Gibson, T. M., Shih, P. M., Cumming, V. M., Fischer, W. W., Crockford, P. W., Hodgskiss, M. S. W., Wörndle, S., Creaser, R. A., Rainbird, R. H., Skulski, T. M. et Halverson, G. P. (2018). Precise age of Bangiomorpha pubescens dates the origin of eukaryotic photosynthesis. Geology, 46(2), 135–138.

Greenman, J.W., Patzke, M., Halverson, G.P. et Ielpi, A. (2020) Updated stratigraphy of the Fury and Hecla Group of Melville Peninsula and northwestern Baffin Island, Nunavut, in Summary of Activities 2019: Iqaluit, Canada-Nunavut Geoscience Office, 37–50.

Greenman, J. W., Rooney, A. D., Patzke, M., Ielpi, A. et Halverson, G. P. (2021). Re-Os geochronology highlights widespread latest Mesoproterozoic (ca. 1090–1050 Ma) cratonic basin development on northern Laurentia. Geology, 49(7), 779–783.

Griselin, M., Arndt, N. T. et Baragar, W. R. A. (1997). Plume–lithosphere interaction and crustal contamination during formation of Coppermine River basalts, Northwest Territories, Canada. Canadian Journal of Earth Sciences, 34(7), 958–975.

Heaman, L. M. et LeCheminant, A. N. (1993). Paragenesis and U-Pb systematics of baddeleyite (ZrO2). Chemical Geology, 110(1-3), 95–126.

Hahn, K., Rainbird, R. et Cousens, B. (2013). Sequence stratigraphy, provenance, C and O isotopic composition and correlation of the late Paleoproterozoic–early Mesoproterozoic upper Hornby Bay and lower Dismal Lakes groups, NWT and Nunavut. Precambrian Research, 232, 209–225.

Halls, H. C. (1982). The importance and potential of mafic dyke swarms in studies of geodynamic processes. Geoscience Canada, 9, 145–154.

Halls H. C. (1987) Dyke swarms and continental rifting: some concluding remarks. In: Halls HC, Fahrig WF (eds.) Mafic dyke swarms. Geological Association of Canada, Special Paper 34, 483–492.

Hastie, W. W., Watkeys, M. K. et Aubourg, C. (2014). Magma flow in dyke swarms of the Karoo LIP: Implications for the mantle plume hypothesis. Gondwana Research, 25(2), 736–755.

Hoffman, P. F. (1988). United plates of America, the birth of a craton: Early Proterozoic assembly and growth of Laurentia. Annual Review of Earth and Planetary Sciences, 16(1), 543–603.

Hou, G., Kusky, T. M., Wang, C. et Wang, Y. (2010). Mechanics of the giant radiating Mackenzie dyke swarm: a paleostress field modeling. Journal of Geophysical Research: Solid Earth, 115(B2).

Hou, T., Zhang, Z., Kusky, T., Du, Y., Liu, J. et Zhao, Z. (2011). A reappraisal of the high-Ti and low-Ti classification of basalts and petrogenetic linkage between basalts and mafic–ultramafic intrusions in the Emeishan Large Igneous Province, SW China. Ore Geology Reviews, 41(1), 133–143.

Hulbert, L., Williamson, B. et Thériault, R. (1993). Geology of Middle Proterozoic Mackenzie diabase suites from Saskatchewan: An overview and their potential to host Noril'sk-type Ni-Cu-PGE mineralization. Summary of investigations, Saskatchewan Geological Survey, Sask. Energy Mines, 93–4.

Irvine, T. N. (1978). Infiltration metasomatism, adcumulus growth and secondary differentiation in the Muskox intrusion. Carnegie Inst. Washington, Yearb., 77, 743–50.

Irving, E., Park, J. K. et McGlynn, J. C. (1972). Paleomagnetism of the Et-then Group and Mackenzie diabase in the Great Slave Lake area. Canadian Journal of Earth Sciences, 9(6), 744–755.

Jackson, G. D. et Iannelli, T. R. (1981). Rift-related cyclic sedimentation in the Neohelikian Borden Basin, northern Baffin Island. Geological Association of Canada, Special Paper 81(10), 269–302.

Jones, D. L. et Fahrig, W. F. (1978). Paleomagnetism and age of the Aston dykes and Savage Point sills of the Boothia Uplift, Canada. Canadian Journal of Earth Sciences, 15(10), 1605–1612.

Jourdan, F., Bertrand, H., Schärer, U., Blichert-Toft, J., Féraud, G. et Kampunzu, A. B. (2007). Major and trace element and Sr, Nd, Hf et Pb isotope compositions of the Karoo large igneous province, Botswana–Zimbabwe: lithosphere vs mantle plume contribution. Journal of Petrology, 48(6), 1043–1077.

Ju, W., Hou, G. et Hari, K. R. (2013). Mechanics of mafic dyke swarms in the Deccan Large Igneous Province: Palaeostress field modelling. Journal of Geodynamics, 66, 79–91.

Kasbohm, J., Schoene, B. and Burgess, S. (2021). Radiometric constraints on the timing, tempo and effects of large igneous province emplacement. Large Igneous Provinces: A Driver of Global Environmental and Biotic Changes, 27–82.

Kerans, C. (1983). Timing of emplacement of the Muskox intrusion: constraints from Coppermine homocline cover strata. Canadian Journal of Earth Sciences, 20(5), 673–683.

Kerans, C., Ross, G. M., Donaldson, J. A., Geldsetzer, H. J. et Campbell, F. H. A. (1981). Tectonism and depositional history of the Helikian Hornby Bay and Dismal Lakes groups, District of Mackenzie. Proterozoic basins of Canada. Edited by FHA Campbell. Geological Association of Canada, Special Paper 81-10.

Kinzler, R. J. (1997). Melting of mantle peridotite at pressures approaching the spinel to garnet transition: Application to mid‐ocean ridge basalt petrogenesis. Journal of Geophysical Research: Solid Earth, 102(B1), 853–874.

Kirscher, U., Mitchell, R. N., Liu, Y., Nordsvan, A. R., Cox, G. M., Pisarevsky, S. A., Wang, C., Wu, L., Murphy, J. B. et Li, Z. X. (2021). Paleomagnetic constraints on the duration of the Australia-Laurentia connection in the core of the Nuna supercontinent. Geology, 49(2), 174–179.

Kiselev, A. I., Ernst, R. E., Yarmolyuk, V. V. et Egorov, K. N. (2012). Radiating rifts and dyke swarms of the middle Paleozoic Yakutsk plume of eastern Siberian craton. Journal of Asian Earth Sciences, 45, 1–16.

Lai, S., Qin, J., Li, Y., Li, S. et Santosh, M. (2012). Permian high Ti/Y basalts from the eastern part of the Emeishan Large Igneous Province, southwestern China: Petrogenesis and tectonic implications. Journal of Asian Earth Sciences, 47, 216–230.

LeCheminant, A. N. et Heaman, L. M. (1989). Mackenzie igneous events, Canada: Middle Proterozoic hotspot magmatism associated with ocean opening. Earth and Planetary Science Letters, 96(1–2), 38–48.

Li, H., Zhang, Z., Ernst, R., Lü, L., Santosh, M., Zhang, D., & Cheng, Z. (2015). Giant radiating mafic dyke swarm of the Emeishan Large Igneous Province: Identifying the mantle plume centre. Terra Nova, 27(4), 247–257.

Liu, J., Pearson, D. G., Wang, L. H., Mather, K. A., Kjarsgaard, B. A., Schaeffer, A. J., Irvine G. J., Kopylova, M. G. et Armstrong, J. P. (2021). Plume-driven recratonization of deep continental lithospheric mantle. Nature, 592(7856), 732–736.

Long, D. G. et Turner, E. C. (2012). Tectonic, sedimentary and metallogenic re-evaluation of basal strata in the Mesoproterozoic Bylot basins, Nunavut, Canada: Are unconformity-type uranium concentrations a realistic expectation?. Precambrian Research, 214, 192–209.

McDonough, W. F. et Sun, S. S. (1995). The composition of the Earth. Chemical Geology, 120(3–4), 223–253.

Mackie, R. A., Scoates, J. S. et Weis, D. (2009). Age and Nd–Hf isotopic constraints on the origin of marginal rocks from the Muskox layered intrusion (Nunavut, Canada) and implications for the evolution of the 1.27 Ga Mackenzie large igneous province. Precambrian Research, 172(1–2), 46–66.

Marzoli, A., Callegaro, S., Dal Corso, J., Davies, J. H., Chiaradia, M., Youbi, N., Bertrand H., Reisberg, L., Merle, R. et Jourdan, F. (2018). The Central Atlantic Magmatic Province (CAMP): A review. The Late Triassic World, 91–125.

Mayr, U., Brent, T.A., de Freitas, T., Frisch, T., Nowlan, G.S. et Okulitch, A.V. 2004: Geology of eastern Prince of Wales Island and adjacent smaller islands, Nunavut; Geological Survey of Canada, Bulletin 547, 88 p.

Meek, R. (2019). Sedimentology and Stratigraphy of the Mesoproterozoic Husky Creek Formation, Lower Coppermine River Region, Nunavut. Geological Survey of Canada, Open File 8559, 2019, 28 p.

Parrish, R. R. et Bell, R. T. (1987). Age of the NOR breccia pipe, Wernecke Supergroup, Yukon Territory. Radiogenic age and isotopic studies, Report 1, 87-2.

Patzke, M., Greenman, J. W., Halverson, G. P. et Ielpi, A. (2021). The initiation of the Mesoproterozoic Bylot basins (Nunavut, Arctic Canada) as recorded in the Nyeboe Formation, Fury and Hecla Group. Journal of Sedimentary Research, 91(11), 1166–1187.

Pearce, J. A. (2008). Geochemical fingerprinting of oceanic basalts with applications to ophiolite classification and the search for Archean oceanic crust. Lithos, 100(1-4), 14–48.

Pehrsson, S. J., Van Breemen, O. et Hanmer, S. (1993). Ages of diabase dyke intrusions, Great Slave Lake shear zone, Northwest Territories. Papers-Geological Survey of Canada, 23-23.

Pin, C. and Zalduegui, J. S. (1997). Sequential separation of light rare-earth elements, thorium and uranium by miniaturized extraction chromatography: application to isotopic analyses of silicate rocks. Analytica Chimica Acta, 339(1-2), 79-89.

Pollard, D. D. (1987). Elementary fracture mechanics applied to the structural interpretation of dykes. In Mafic dyke swarms. Edited by H.C. Halls and W.F. Fahrig. Geological Association of Canada, Special Paper 34, 5–24.

Rainbird, R. H., Rooney, A. D., Creaser, R. A. et Skulski, T. (2020). Shale and pyrite Re-Os ages from the Hornby Bay and Amundsen basins provide new chronological markers for Mesoproterozoic stratigraphic successions of northern Canada. Earth and Planetary Science Letters, 548, 116492.

Robertson, W. A. (1969). Magnetization directions in the Muskox Intrusion and associated dykes and lavas. Geological Survey of Canada, Bulletin 167, 1969, 51 p.

Rudnick, R. L. et Gao, S., (2003). Composition of the continental crust. In: Holland, H.D., Turekian, K.K. (Eds.), Treatise on Geochemistry, Elsevier, Amsterdam, Netherlands, 3, 1–64.

Salters, V. J. et Stracke, A. (2004). Composition of the depleted mantle. Geochemistry, Geophysics, Geosystems, 5(5).

Schwab, D. L., Thorkelson, D. J., Mortensen, J. K., Creaser, R. A. et Abbott, J. G. (2004). The Bear River dykes (1265–1269 Ma): westward continuation of the Mackenzie dyke swarm into Yukon, Canada. Precambrian Research, 133(3–4), 175–186.

Sevigny, J. H., Cook, F. A. et Clark, E. A. (1991). Geochemical signature and seismic stratigraphic setting of Coppermine basalts drilled beneath the Anderson Plains in northwest Canada. Canadian Journal of Earth Sciences, 28(2), 184–194.

Shaw, D. M. (2000). Continuous (dynamic) melting theory revisited. The Canadian Mineralogist, 38(5), 1041–1063.

Simões, M. S., Lima, E. F., Rossetti, L. M. et Sommer, C. A. (2019). The low-Ti high-temperature dacitic volcanism of the southern Paraná-Etendeka LIP: geochemistry, implications for trans-Atlantic correlations and comparison with other Phanerozoic LIPs. Lithos, 342, 187–205.

Skulski, T., Rainbird, R. H., Turner, E. C., Meek, R., Ielpi, A., Halverson, G. P., Davis, W. J., Mercadier, J., Girard, E. et Loron, C. C. (2018). Bedrock Geology of the Dismal Lakes-lower Coppermine River Area, Nunavut and Northwest Territories: GEM-2 Coppermine River Transect, Report of Activities 2017-2018. Geological Survey of Canada, Open File 8522, 2018, 37 p.

Smith, R. P. (1987). Dyke emplacement at Spanish Peaks, Colorado. In: H.C. Halls and W.F. Fahrig (Editors), Mafic Dyke Swarms. Geological Association of Canada, Special Paper 34, 47–54.

Steenkamp, H. M., Bovingdon, P. J., Dufour, F., Généreux, C. A., Greenman, J. W., Halverson, G. P., Ielpi, A., Patzke M. et Tinkham, D. K. (2018). New regional mapping of Precambrian rocks north of Fury and Hecla Strait, northwestern Baffin Island, Nunavut. Summary of Activities, 47–62.

Tanaka, T. and 19 co-authors. (2000). JNdi-1: a neodymium isotopic reference in consistency with LaJolla neodymium. Chemical Geology, 168(3–4), 279–281.

Thorkelson, D. J., Abbott, J. G., Mortensen, J. K., Creaser, R. A., Villeneuve, M. E., McNicoll, V. J. et Layer, P. W. (2005). Early and middle Proterozoic evolution of Yukon, Canada. Canadian Journal of Earth Sciences, 42(6), 1045–1071.

Turner, E. C. et Kamber, B. S. (2012). Arctic Bay Formation, Borden Basin, Nunavut (Canada): Basin evolution, black shale and dissolved metal systematics in the Mesoproterozoic ocean. Precambrian Research, 208, 1–18.

Wang, C. Y., Zhou, M. F. et Qi, L. (2007). Permian flood basalts and mafic intrusions in the Jinping (SW China)–Song Da (northern Vietnam) district: mantle sources, crustal contamination and sulfide segregation. Chemical Geology, 3(243), 317–343.

Weis, D., Kieffer, B., Maerschalk, C., Barling, J., De Jong, J., Williams, G. A., Hanano, D., Pretorius, W., Mattielli, N., Scoates, J. S., Goolaerts, A., Friedman, R. M. et Mahoney, J. B. (2006). High-precision isotopic characterization of USGS reference materials by TIMS and MC-ICP-MS. Geochemistry, Geophysics, Geosystems, 7(8).

Xu, Y., Chung, S. L., Jahn, B. M. et Wu, G. (2001). Petrologic and geochemical constraints on the petrogenesis of Permian–Triassic Emeishan flood basalts in southwestern China. Lithos, 58(3-4), 145–168.

CHAPITRE 2

NEW U-PB CA-ID TIMS ZIRCON AGES IMPLICATE THE FRANKLIN LIP AS THE PROXIMAL TRIGGER FOR THE STURTIAN SNOWBALL EARTH EVENT

Frédéric Dufour[1], Joshua H. F. L. Davies[1], J. Wilder Greenman[2], Thomas Skulski[3], Galen P. Halverson[2], Ross Stevenson[1]

[1]Département des sciences de la Terre et de l'atmosphère/Geotop, Université du Québec à Montréal, Montréal, Québec H2X 3Y7, Canada
[2]Department of Earth and Planetary Sciences/Geotop, McGill University, Montréal, Québec H3A 0E8, Canada
[3]Geological Survey of Canada, Natural Resources Canada, Ottawa, Ontario K1A 0E8, Canada

L'article a été soumis à la revue *Earth and Planetary Science Letters* en Septembre 2022

Abstract

The Franklin igneous event (ca. 720 Ma) emplaced basalts and mafic intrusions across Arctic Laurentia just prior to the onset of the ca. 717–661 Ma Sturtian Snowball Earth event. Given the close association in time between these two events, it has been widely argued that the Franklin event contributed to the initiation of global glaciation. However, a lack of accurate high-precision geochronology has hampered establishing the timeframe of Franklin magmatism and discerning its precise temporal and possible causative relationship to glaciation. Here we present the first Franklin high-precision U-Pb CA-ID TIMS zircon ages for two dykes and two sills from Baffin Island, Canada, and Avannaata, northwest Greenland. Combined with field relationships showing that the dykes cross-cut the sills, these four dates indicate magmatic activity over 0.53 ± 0.58 Ma at ca 718 Ma, immediately prior to Sturtian glaciation, which we estimate to have initiated at 717.19 +0.26/-0.33 Ma.

2.1 Introduction

The Franklin large igneous province (LIP) was the largest of a series of LIPs emplaced during the Tonian Period (1000–720 Ma) and has been linked to the break-up of the Rodinian supercontinent (Ernst et al., 2013). It produced basalts, mafic sills, and a large radiating dyke swarm, which together span a distance of 2500 km from Alaska, across northern Canada, to northwestern Greenland (Fig. 2.1; Heaman et al., 1992; Denyszyn et al., 2009a; Cox et al., 2015; Macdonald and Wordsworth, 2017). The LIP is centered on Melville Island (Fig. 2.1), and from there a dyke swarm fans from NE-striking in the west, to W-SW-striking on Ellesmere Island and Greenland. Remnants of the Natkusiak flood basalts cap the Stenian (1200–1000 Ma) to Tonian Shaler Supergroup on Victoria Island, at the inferred center of the Franklin LIP (Heaman et al., 1992).

Previously published high-precision geochronology of the Franklin LIP, based on $^{207}Pb/^{206}Pb$ or upper intercept baddeleyite ages, suggests that magmatic activity spanned from ca. 723 to 712 Ma (millions of years ago; Heaman et al., 1992; Pehrsson and Buchan, 1999; Macdonald et al., 2010; Denyszyn et al., 2009a, b). A magmatic episode of ca. 10 Ma for the Franklin LIP is unlike typical Phanerozoic LIPs, which were emplaced within ca. 1 Myr (millions of years in duration; Kasbohm et al., 2021), suggesting either that some of the dated rocks may not belong to the Franklin, some of the ages are inaccurate, or that the Franklin was not a typical Phanerozoic style LIP

The emplacement of Phanerozoic LIPs has been linked to global environmental perturbations, including both warming and cooling events, negative carbon isotope anomalies, and mass extinctions (Ernst et al., 2021a). Similarly, it has been argued that the Franklin LIP perturbed global climate and biogeochemical cycles (Cox et al., 2016; Macdonald and Wordsworth, 2017). The first Cryogenian global glaciation, i.e. the Sturtian Snowball event, was initiated at ca. 717 Ma (Macdonald et al., 2010, 2018; MacLennan et al., 2018), shortly after or during the Franklin event. Several studies have suggested that weathering of the Franklin LIP, potentially along with other Neoproterozoic LIPs emplaced in tropical Rodinia (Denyszyn et al., 2009a; Lu et al., 2022), led to a dramatic drawdown of CO_2 and catastrophic planetary cooling that triggered the Sturtian glaciation (Goddéris et al., 2003; Cox et al., 2016). However, the long duration of Franklin magmatism, as indicated by the currently available dates, prevents establishing a clear temporal, and hence causal link, if any, between LIP emplacement and the onset of a Snowball glaciation.

Here, we present four new chemical abrasion, isotope dilution, thermal ionization mass spectrometry (CA-ID-TIMS) U-Pb zircon ages from mafic intrusions crosscutting the Fury and Hecla and Thule basins in northeastern Canada and northwestern Greenland (Fig. 2.1). These are the first high-precision U-Pb zircon

ages reported on the Franklin event and together indicate a pair of Franklin magmatic pulses over 0.53 ± 0.58 Ma at ca. 718 Ma, coincident with a negative carbon isotope excursion recorded in marine carbonates ($\delta^{13}C_{carb}$), which shows a sharp decline just prior to the onset of Sturtian glaciation (Fairchild et al., 2018; MacLennan et al., 2018). Using available age constraints bracketing the onset of Sturtian glaciation (Macdonald et al., 2010, 2018) and a simple Bayesian model, we estimate glacial initiation at 717.19 +0.26/-0.33 Ma. This new calibration of global events across the Tonian–Cryogenian boundary demonstrates a close temporal link between the Franklin LIP, perturbation to the global carbon cycle, and the onset of Neoproterozoic glaciation. The Franklin LIP is believed to have contributed to the initiation of the Sturtian Snowball Earth event, preceding the glaciation by ca. 1 Myr.

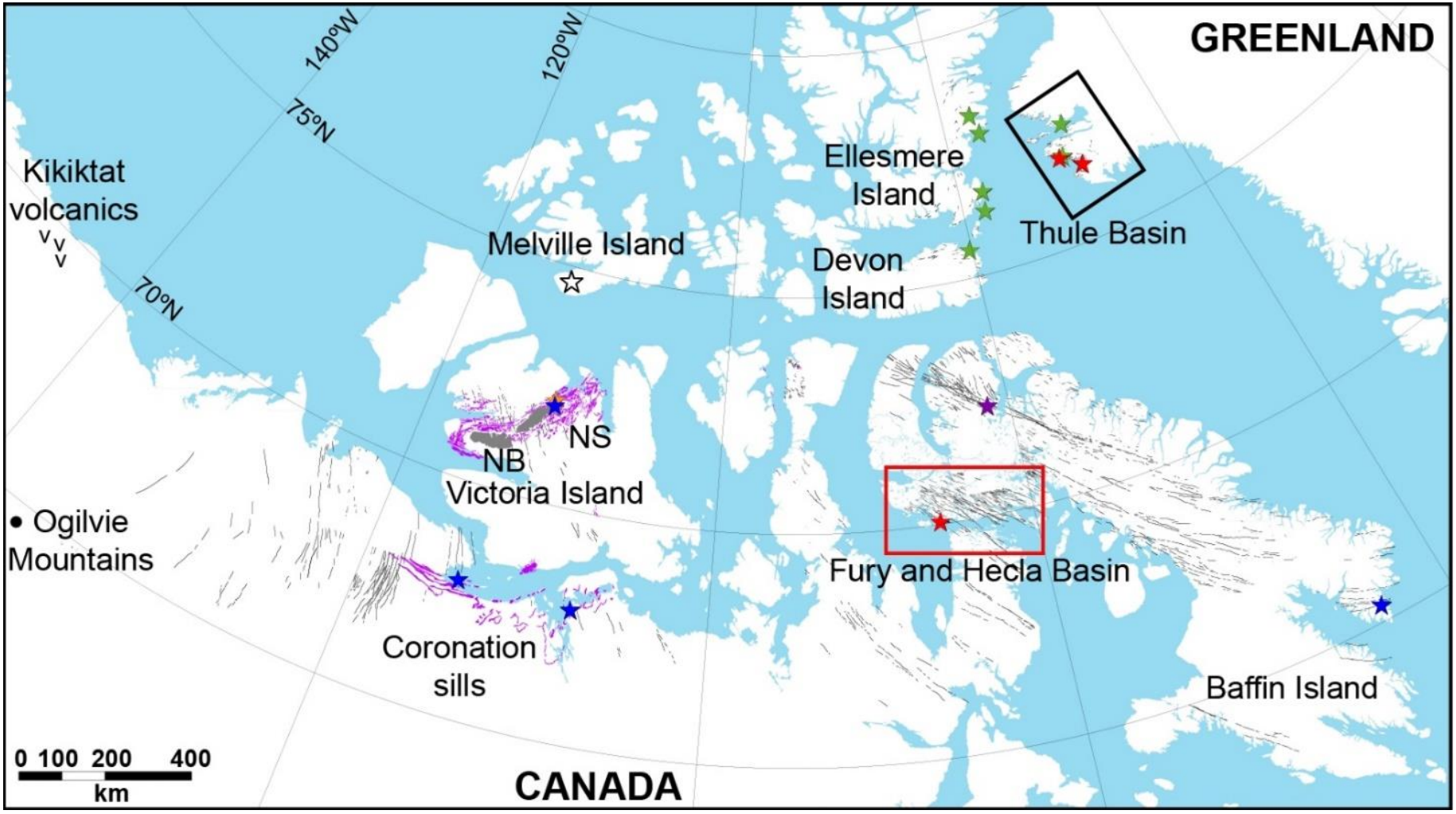

Figure 2.1: Map of the Franklin igneous suites. Red box indicates location of Fig. A2.2, and black box is location of Fig. A2.3. Black lines are the mafic dyke swarm. Black open star is the proposed plume location (Denyszyn et al., 2009a). Filled stars denote U-Pb ages; blue stars are from Heaman et al. (1992); green stars from Denyszyn et al. (2009a, b); purple star is from Macdonald et al. (2010); orange star is from Pehrsson and Buchan (1999); red stars are from this study. NB, Natkusiak basalts; NS, Natkusiak sills.

2.2 Materials and Methods

2.2.1 U-Pb geochronology

U-Pb geochronology samples were prepared at the GEOTOP laboratory at the Université du Québec à Montréal using conventional mineral-separation techniques. Rock samples were crushed to a powder in a jaw crusher and a disk mill and then passed over a Wilfley table. Dried mineral concentrates from the Wilfley table were then processed with a hand magnet and a Frantz magnetic separator at susceptibilities of 0.25, 0.75, and 1.0 A to isolate the non-magnetic minerals. The least magnetic fraction was further processed using heavy liquids (diiodomethane). Zircons were hand-picked under a binocular microscope with tweezers from the dense non-magnetic mineral fraction.

Picked zircons were annealed and chemically abraded in order to remove areas of the grains that had been affected by Pb loss (Mattinson, 2005; Widmann et al., 2019). Zircon crystals were annealed in a muffle furnace at 950 °C for 48 h, then placed in a solution of 29N HF at 180 °C for 12 h to 18 h for chemical abrasion (see section Zircon treatment in Table A1). The remaining zircon fragments were then ultra-sonically cleaned four times in 3N HNO_3 and loaded into Savillex microcapsules with 3 drops of 29N HF and trace HNO_3, then spiked with the $^{205}Pb+^{233}U+^{235}U$ EARTHTIME tracer ET535 (Condon et al., 2015; McLean et al., 2015). The microcapsules were placed in a Parr digestion vessel which was placed into an oven 210 °C for 48 h for dissolution. After dissolution, samples were evaporated on a hot plate at 80 °C. Three drops of 6N HCl were added to the Savillex microcapsules, and the beakers were placed back in the Parr vessel and back in the oven for 18 h at 180 °C to convert the fluoride salts to chlorides. After drying again on the hot plate, the sample solutions were loaded into pre-cleaned columns filled with AG1X8 anion exchange resin. U and Pb fractions were separated following a modified version of the procedure of Krogh (1973). The purified U and Pb fractions were collected in pre-cleaned 7 ml Savillex beakers and dried with one drop of 0.04N H_3PO_4.

U-Pb measurements were performed on a Thermo TRITON thermal ionization mass spectrometer (TIMS) at the GEOTOP laboratory at the Université du Québec à Montréal. Each sample was loaded onto an outgassed Re-filament with one drop of silicate gel emitter (modified from the Gerstenberger and Haase, 1997 recipe). Pb isotopes were measured in dynamic mode on a MasCom secondary electron multiplier. U isotopes were analyzed as UO_2 in static mode on Faraday cups with 10^{13} ohm resistors with a $^{18}O/^{16}O$ ratio of 0.00205. The mass fractionation for Pb was corrected using the fractionation determined from repeat measurements of SRM981 at the same running conditions as the samples. For U the in-run fractionation was corrected using a $^{233}U/^{235}U$ of 0.99506, and the uranium isotopic composition of the analyzed zircon was assumed to be $^{238}U/^{235}U$ of 137.818 ± 0.045 (2σ; Hiess et al., 2012). U-Pb data were reduced and

uncertainties were propagated using the Tripoli and U-Pb Redux software (Bowring et al., 2011) which uses the algorithms of McLean et al. (2011). $^{206}Pb/^{238}U$ dates are reported with [X]/[Y]/[Z] 2σ uncertainties (Schoene et al., 2006), where X is the internal uncertainty, Y is tracer calibration error and Z includes both tracer calibration and decay constant uncertainties and are Th-corrected for initial Th/U disequilibrium using a partition coefficient relationship between the Th/U of the zircon and the Th/U ratio of magma from which zircon crystallized (the same as Davies et al. 2017). All common Pb was assumed to be procedural blank and was corrected according to the following long-term lab blank isotopic composition: $^{206}Pb/^{204}Pb = 18.102 \pm 0.23$, $^{207}Pb/^{204}Pb = 15.35 \pm 0.14$, $^{208}Pb/^{204}Pb = 38.01 \pm 0.55$ (all 1σ absolute errors). The weighted mean and Concordia figures of $^{206}Pb/^{238}U$ and $^{207}Pb/^{206}Pb$ were plotted in IsoplotR (Vermeesch, 2018). Analytical results are given in Table A1. Zircons used in the calculation of each sample weighted mean are respectively: z3, 5 and 6 for the Fury and Hecla dyke; z3, 5, 7, 8, 10, 11 and 12 for the Dybbol sill; z4, 9, 12 and 13 for the Steensby Land sill complex; and z3 for the Thule dyke.

2.2.2 Isotopic compilations

The late Tonian marine carbonate $\delta^{13}C$, $^{87}Sr/^{86}Sr$ and $^{187}Os/^{188}Os$ records, as shown in Figure 4 and 5, are compiled from previously published data. The $\delta^{13}C$ record (Fig. 2.5A) is based on age-calibrated data from Svalbard (ca. 820–720 Ma; Halverson et al., 2022), with the addition of data from the ca. 745–717 Ma Ugab Subgroup in Namibia (Lamothe et al., 2019), calibrated based on ages from Svalbard (Millikin et al., 2022) and Ethiopia (Park et al., 2020, 2021). Within the framework of recent geochronological constraints, it is now clear that two distinct negative carbon isotope anomalies punctuate the Tonian Period. The older Russøya anomaly occurs ca. 740 Ma (Millikin et al., 2022; Halverson et al., 2022), and the younger Garvellach anomaly is a sharp downturn in $\delta^{13}C$ that leads into the onset of Sturtian glaciation (Fairchild et al., 2018).

The strontium isotope ($^{87}Sr/^{86}Sr$) record is based on well preserved marine limestones and is modified from Cox et al. (2016) using the age models developed for $\delta^{13}C$. The Tonian Os isotope record (Fig. 2.5B) has been modified from Millikin et al. (2022) to include available earlier Tonian data. It includes both chemostratigraphic $^{187}Os/^{188}Os$ ratios (Rooney et al., 2014) and initial Os isotope ratios (Os_i) from Tonian Re-Os isochrons generated from organic-rich sediments. The striking feature in this compilation is the downturn from values near 0.6 at ca. 760 to mantle-like values of 0.1–0.2 in the latest Tonian, which is consistent with a coeval but less resolved downturn in marine $^{87}Sr/^{86}Sr$ in the late Tonian (Cox et al., 2016; Zhou et al., 2020).

2.3 Results

2.3.1 Sample selection for geochronology

Dykes and sills chosen for U-Pb geochronology cross-cut the stratigraphy of the Stenian to Tonian Fury and Hecla (FH), and Thule basins (one dyke and one sill from each basin; Fig. 2.1) with dykes displaying a NW orientation (Chandler, 1988; Dawes, 2006). Samples from the FH dykes and Dybbol sill were collected from the Autridge Peninsula on northwestern Baffin Island (Fig. A2.1). Although at the sample site the dyke and the sill are not in contact (Figs. A2.2A–B), Chandler (1988) inferred on the basis of aerial photographic data that the dykes cross-cut the sill within the basin. Previous K-Ar ages for the Dybbol sill (DS) and dykes in the Fury and Hecla basin range from 746–631 Ma (Chandler and Stevens, 1981) suggesting a Franklin affinity, which is supported by their geochemistry (Dufour et al., 2021; Fig. A2.2).

In the Thule basin, the dykes and sills cut the basinal sediments which overlie the Archean basement. Intrusive field relationships in the Steensby Land area indicate that the dykes clearly crosscut the sills (Dawes, 2006; Fig. A2.3). Previously reported U-Pb baddeleyite ages from the Steensby Land sill complex (SLSC) and dykes of the Thule basin (Denyszyn et al., 2009a) of 712 ± 2 Ma and 721 ± 2 Ma, respectively, are broadly consistent with the Franklin magmatic event. Samples of a Thule dyke (TD) were collected west of Granville Fjord, where it cross-cuts a SLSC sill (Fig. A2.4A), while samples of the SLSC are from near Thule Air Base (Fig. A2.3).

2.3.2 U-Pb geochronology

The CA-ID-TIMS U-Pb isotopic data are presented in Table A1 and the Concordia diagrams in Fig. 2.2. The analytical details are provided in the Materials and Methods section. The reported ages are weighted mean $^{206}Pb/^{238}U$ ages with uncertainties calculated following the method of Schoene et al. (2006; see Materials and Methods).

Three chemically abraded zircons from the FH dyke yield a weighted mean $^{206}Pb/^{238}U$ age of 717.73 ± 0.72/0.77/1.1 Ma with an MSWD of 0.54. Four grains were omitted in the weighted mean calculation as this younger population of grains is discordant and likely records Pb loss. Seven zircons from the DS yield a weighted mean $^{206}Pb/^{238}U$ age of 718.33 ± 0.19/0.35/0.85 Ma with an MSWD of 1.9, which is identical, within uncertainty, to the age on the FH dyke. Four grains were excluded in the weighted mean calculation due to suspected Pb loss.

Only one zircon from the TD is thought to record the crystallization age of the dyke whereas the rest scatter to younger and more discordant ages, the oldest concordant grain yielded a $^{206}Pb/^{238}U$ age of 718.12 ± 0.94/0.98/1.2 Ma. Four zircons from the SLSC yield a weighted mean $^{206}Pb/^{238}U$ age of 718.60 ± 0.31/0.43/0.88 Ma with an MSWD of 0.47. Three grains yielding younger ages have likely experienced Pb

loss and are omitted in the calculation, as well as one older grain that is much older than the main cluster and is suspected to have a xenocryst core (e.g. Davies et al. 2021). All of the dyke and sill U-Pb ages generated here are identical within uncertainty, though the dykes are known to be younger than the sills as the dykes cut the sills.

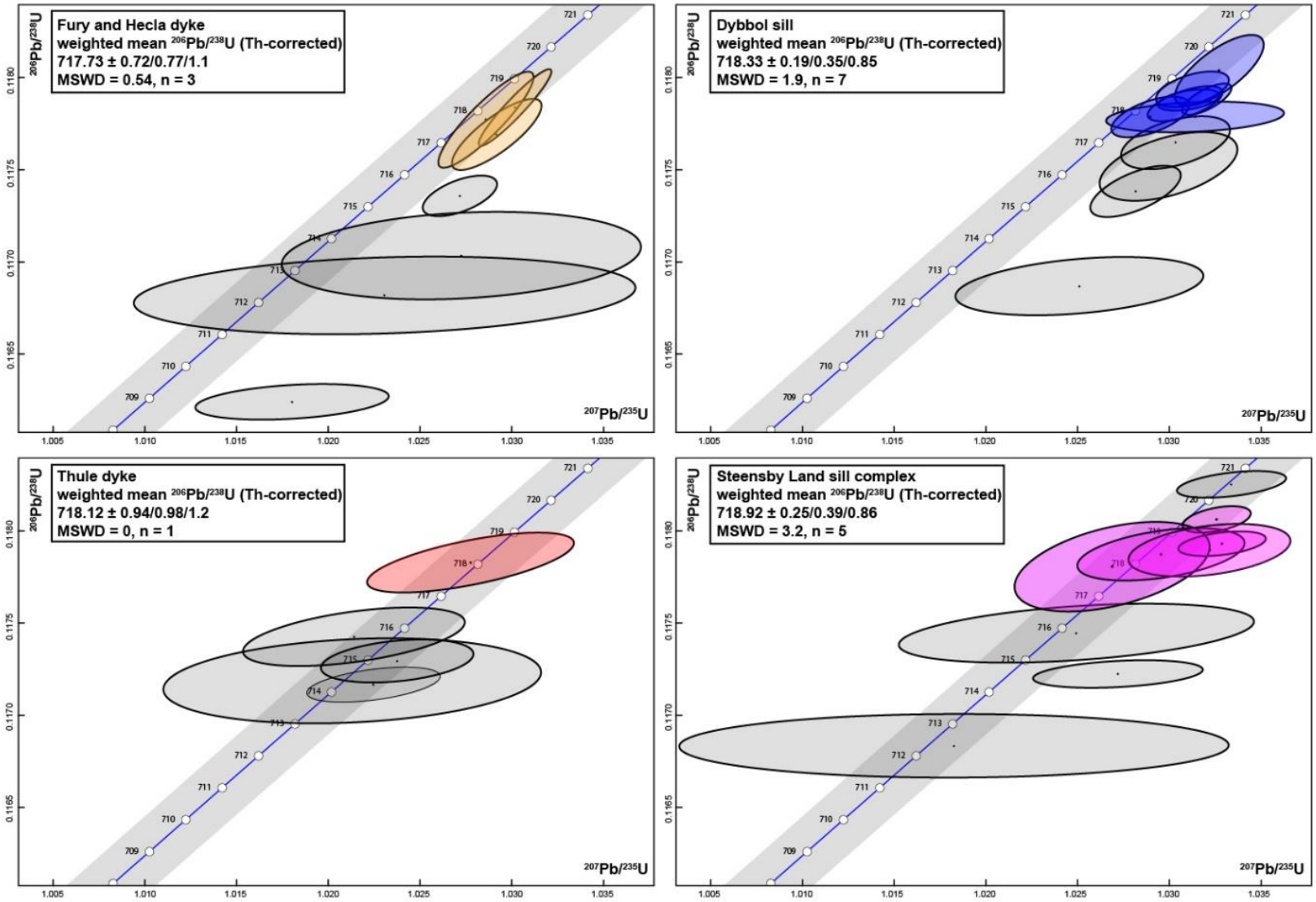

Figure 2.2 : Concordia diagrams showing the results of U-Pb zircon CA-ID-TIMS geochronology of Fury and Hecla dyke, Dybbol sill, Thule dyke, Steensby Land sill complex (2σ error ellipses). Reported ages are Th-corrected $^{206}Pb/^{238}U$ weighted mean ages.

2.4 Discussion

2.4.1 Bayesian updated ages and combined weighted mean ages

The observation that the dykes cross-cut the sills in both the Fury and Hecla and Thule basins, allows us to improve the absolute uncertainties on the emplacement ages by incorporating this prior geological information (Fig. A2.5). We applied a simple Bayesian model (Johnstone et al., 2019), requiring a clear established stratigraphic superposition or chronological order (e.g. cross-cutting relationship), and that incorporates our geological constraint that the sills must be older than the dykes. This model yields updated ages of 718.33 ± 0.18 Ma and 717.71 +0.55/-0.69 Ma for the Dybbol sill (DS) and Fury and Hecla dyke (FH), respectively (Fig. 2.3A). The same approach applied to the Thule sill (SLSC) and dyke (TD) yields updated ages of 718.02 +0.59/-0.83 Ma and 718.61 ± 0.30 Ma respectively (Fig. 2.3A).

Given that the FH and TD dykes closely overlap in age, share the same orientation, and cross-cut the sills in their respective regions, we suggest that they represent the same magmatic pulse. Similarly, it is reasonable to presume that the DS and SLSC sills represent a single, earlier magmatic pulse. Based on these assumptions, we can pool the individual zircon ages for both dykes and both sills to generate combined weighted mean emplacement ages for the sills and for the dykes. The combined ages of 718.40 ± 0.16 Ma for the sills and 717.87 ± 0.56 Ma for the dykes suggest that they were emplaced within 0.53 +0.58/-0.53 Ma of each other (Fig. 2.3B), which means that they may have been emplaced either close to exactly the same time, or up to around 1 Ma apart.

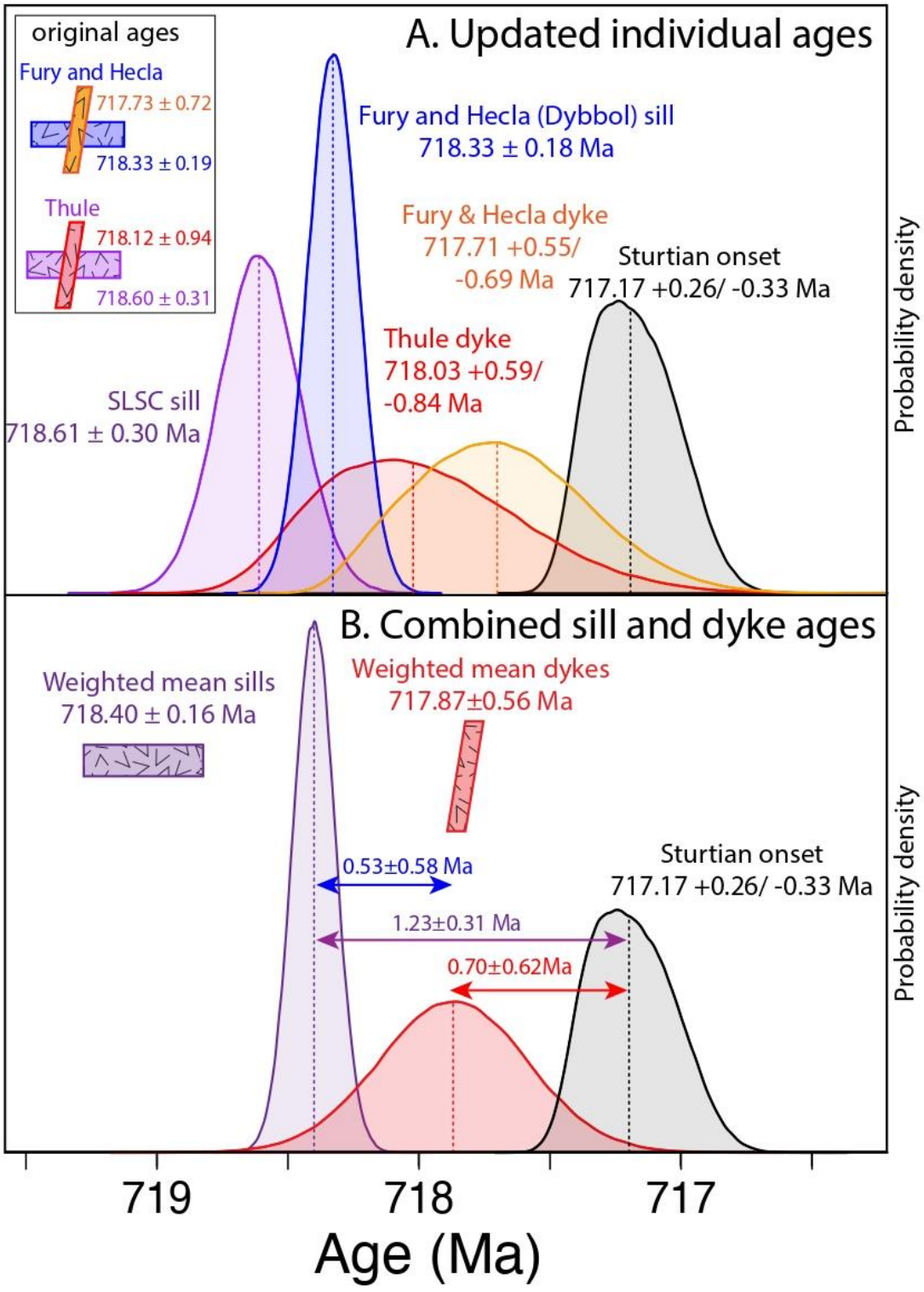

Figure 2.3 : Probability density plots for the ages of the Fury and Hecla and Thule intrusions and onset of the Sturtian glaciation. (A) Updated ages for the dykes and sills based on the observation of cross-cutting relationships, compared with a Monte Carlo estimate for the age for the onset of Sturtian glaciation. (B) Combined weighted mean ages of the sills and the dykes based on the assumption that dykes and sills were the product of two separate pulses of Franklin magmatism. The difference between emplacement ages and onset of Sturtian glaciation is shown by arrows.

2.4.2 Timing of the Franklin event

Our new ages provide significantly more precise constraints for Franklin intrusive rocks cutting strata of the Fury and Hecla and Thule basins compared to previous U-Pb baddeleyite ages (Denyszyn et al., 2009a). Our ages also provide a minimum age for deposition within the Fury and Hecla and Thule basins of ca. 718 Ma and indicate that Franklin magmatism occurred in coevally across the eastern Arctic.

All previous U-Pb ages for the Franklin LIP have come from baddeleyite and discordant zircon analysis (Heaman et al., 1992; Denyszyn et al., 2009a, b; Pehrsson and Buchan, 1999; Macdonald et al., 2010). Baddeleyite was previously considered an ideal mineral for U-Pb geochronology because it suffers less Pb loss than zircon (Heaman and LeCheminant, 1993). However, the accuracy of baddeleyite U-Pb ages has recently been called into question (Schaltegger and Davies, 2017). Mafic samples that contain both baddeleyite and zircon have been dated using both minerals, producing baddeleyite ages that are consistently younger than chemically abraded zircon (about > 2 Ma), despite petrologic evidence showing that baddeleyite was the earlier crystalizing phase (Davies et al. 2017; Gaynor et al., 2020; Pohlner et al. 2020). The chemical abrasion technique removes areas of radiation damaged zircon that are susceptible to Pb loss prior to analysis (Widmann et al. 2019), yielding zircon U-Pb ages that are significantly more accurate than baddeleyite U-Pb ages (Schaltegger and Davies, 2017). The chemical abrasion technique does not appear to work for baddeleyite (Rioux et al. 2010), and there is no current method to remove the effects of Pb loss (Pohlner et al. 2020). Therefore, zircons are preferable to baddeleyites when dating mafic rocks, and if baddeleyites are used, they should be interpreted with caution.

The CA-ID-TIMS zircon ages presented here are the first such dates reported on the Franklin LIP. These new ages are compared with recalculated to previous published Franklin ages in Fig. 2.4A, clearly demonstrating the excess dispersion of the baddeleyite U-Pb ages, displayed by larger uncertainties, in comparison to the zircon ages. We recalculated all the published baddeleyite ages from other regions (Heaman et al., 1992; Pehrsson and Buchan, 1999; Denyszyn et al., 2009a, b) as $^{206}Pb/^{238}U$ ages, eliminating fractions that likely suffered Pb loss. Thus, $^{207}Pb/^{206}Pb$ ages presented in earlier studies to avoid discordant data, now show inaccurate ages compared to the $^{206}Pb/^{238}U$ ages. For example, the NE upper sill and the middle sill $^{207}Pb/^{206}Pb$ ages in Victoria Island were respectively interpreted at 717 Ma and 716 Ma (Heaman et al., 1992), whereas recalculated $^{206}Pb/^{238}U$ ages of the same sills are 719.39 ± 1.1 Ma and 717.89 ± 1.84 Ma. The Coronation sill yielded an $^{207}Pb/^{206}Pb$ age of 723 Ma (Heaman et al., 1992), but is now 713.27 ± 5.2 Ma when recalculated to a $^{206}Pb/^{238}U$ age. Using $^{207}Pb/^{206}Pb$ ages will result in a systematic error in the U decay constant ratio at this time (Schoene et al., 2006; Vermeesch, 2021), thus this new compilation of $^{206}Pb/^{238}U$ ages is certainly more precise and accurate than $^{207}Pb/^{206}Pb$ ages in the studying of the Franklin LIP. Although we do not have comparably precise and accurate zircon ages for other regions of the Franklin

LIP, including associated flood basalts, our new data suggests that Franklin magmatism was likely much shorter-lived than previously indicated by baddeleyite and more consistent with age duration estimates of < 1 Myr from Phanerozoic LIPs (Kasbohm et al. 2021).

2.4.3 The Franklin LIP as a trigger for Snowball Earth

Large igneous provinces are frequently associated with supercontinent break-up and global environmental crises, including climate change and mass extinctions (Ernst et al., 2021b; Kasbohm et al. 2021). Magmatic release of SO_2 can drive cooling over the time scale of eruptions (Geux et al., 2016), whereas longer-term warming ($<10^5$ years) results from the release of massive amounts of CO_2 (e.g. Schaller et al., 2012), and subsequent cooling ($>10^5$ years) can be caused by accelerated silicate weathering of fresh continental flood basalts (Dessert et al., 2001). The release of massive amounts of CO_2 is predicted to trigger a negative $\delta^{13}C$ anomaly that corresponds with the initial phase of global warming, while subsequent drawdown of CO_2 due to weathering of the juvenile basalt may be detected by declines in marine $^{87}Sr/^{86}Sr$ and $^{187}Os/^{188}Os$ (Cox et al., 2016).

Franklin magmatism emplaced about 2.64 Mkm^2 of mafic rocks across northern Laurentia and possibly southern Siberia (Ernst et al., 2021a), and over 99% of these rocks erupted within ~15° of the equator (Buchan et al., 2000; Denyszyn et al., 2009a; Park et al., 2021). In terms of both areal extent and paleogeography, the Franklin LIP is analogous to the Central Atlantic Magmatic Province (CAMP), which was emplaced at the onset of Pangea break-up and is associated with a negative carbon isotope anomaly and initial global warming, followed by longer-term cooling (Schaller et al., 2012; Lindström et al., 2021).

Two recent hypotheses have linked Franklin magmatism with the onset of Sturtian glaciation. Macdonald and Wordsworth (2017) proposed that the release of SO_2 during Franklin emplacement, enhanced by the intrusion of Franklin dykes and sills into evaporite-bearing sediments of the late Stenian–Tonian Shaler Supergroup on Victoria Island (Fig. 2.1), could have initiated rapid global cooling leading into Cryogenian Snowball glaciation. This hypothesis predicts that the onset of Sturtian glaciation was coeval with LIP emplacement. Alternatively, building on earlier hypotheses linking low-latitude break-up of Rodinia and mafic magmatism to the onset of Cryogenian glaciation (Goddéris et al., 2003; Donnadieu et al., 2004), Cox et al. (2016) argued that weathering of the Franklin LIP initiated Sturtian Snowball Earth by driving CO_2 below the critical threshold at which runaway glaciation occurs. This hypothesis predicts that Franklin LIP emplacement should have occurred $>10^5$ years prior to the onset of glaciation. A recent estimate for the onset of the Sturtian glaciation of 717.1 +0.7/-0.9 Ma based on a maximum age constraint on the basal Sturtian contact in Ethiopia (MacLennan et al., 2018) is consistent with a link between Franklin magmatism and glacial onset but is insufficiently precise to discriminate between these two hypotheses.

2.4.4 New estimate for the timing of onset of Sturtian glaciation

U-Pb zircon ages have been previously obtained on presumed pre-glacial lava flows of the Mount Harper volcanic complex and from tuffs intercalated with overlying, syn-glacial diamictites in the Ogilvie Mountains of Yukon (Macdonald et al., 2010, 2018). These include three ages of successive rhyolitic flows (F837A–C) in the Mount Harper Group interpreted to be pre-glacial, and two ages (F917-1 and F840A) from tuffs in the overlying, glaciogenic Eagle Creek Formation (Rapitan Group; Table 1), all of which were obtained using the EARTHTIME ET535 tracer (Condon et al., 2015). We selected these ages as input in a similar Bayesian model employed for the dykes and sills to update the ages based on the prior constraints of superposition. We then used the updated age distributions from the youngest pre-glacial age (717.43 ± 0.13 Ma) and the oldest post-glacial age (716.94 ± 0.23 Ma), to estimate the age of the boundary probabilistically through a simple Monte Carlo simulation where only age combinations from those distributions that obey stratigraphic superposition were considered. The result is an estimate for the age of onset of the Sturtian glaciation of 717.17 +0.26/-0.33 Ma (Figs. 2.3, A2.6). This estimate is similar to but more precise than the estimate based on the pre-glacial age from Ethiopia (MacLennan et al., 2018). It indicates onset of Sturtian glaciation occurred 0.7 ± 0.6 Myr after dyke emplacement and 1.2 ± 0.3 Myr after sill emplacement in the FH and Thule basins (Fig. 2.3B). It is possible that these ages reflect the earliest intrusive phases of the Franklin LIP and that the eruptive phase followed ~2 x 10^5 years after the intrusions had cooled and densified the crust (Tian and Buck, 2022). However, even allowing for such a time lag, our new ages imply that the bulk of Franklin LIP emplacement preceded the onset of Sturtian glaciation by >10^5 years, which is inconsistent with the sulfur degassing hypothesis for Snowball initiation.

Tableau 2.1 : U-Pb zircon $^{206}Pb/^{238}U$ weighted mean ages from the Mount Harper region in the Ogilvie Mountains used to generate an age estimate for the onset of Sturtian glaciation (Macdonald et al., 2010, 2018).

Stratigraphic Rank	Sample ID	Age mean	Updated age
1	F837A	717.85 ± 0.24	717.88 + 0.22/ -0.21
2	F837C	717.68 ± 0.31	717.66 ± 0.21
3	F837B	717.43 ± 0.14	717.43 ± 0.13
4	F917-1	716.94 ± 0.23	716.94 + 0.23
5	F840A	716.47 ± 0.23	716.47 ± 0.22

Samples are ranked from stratigraphically lowest (1) to highest (5). Age uncertainty is at the 95% level (recalculated from the original data using IsoplotR; Vermeesch, 2021). Bayesian updated ages are also included, generating a median age and the plus and minus uncertainties using quantiles, with 95% uncertainty bounds allowing for non-Gaussian distributions. The code is provided in A2.7.

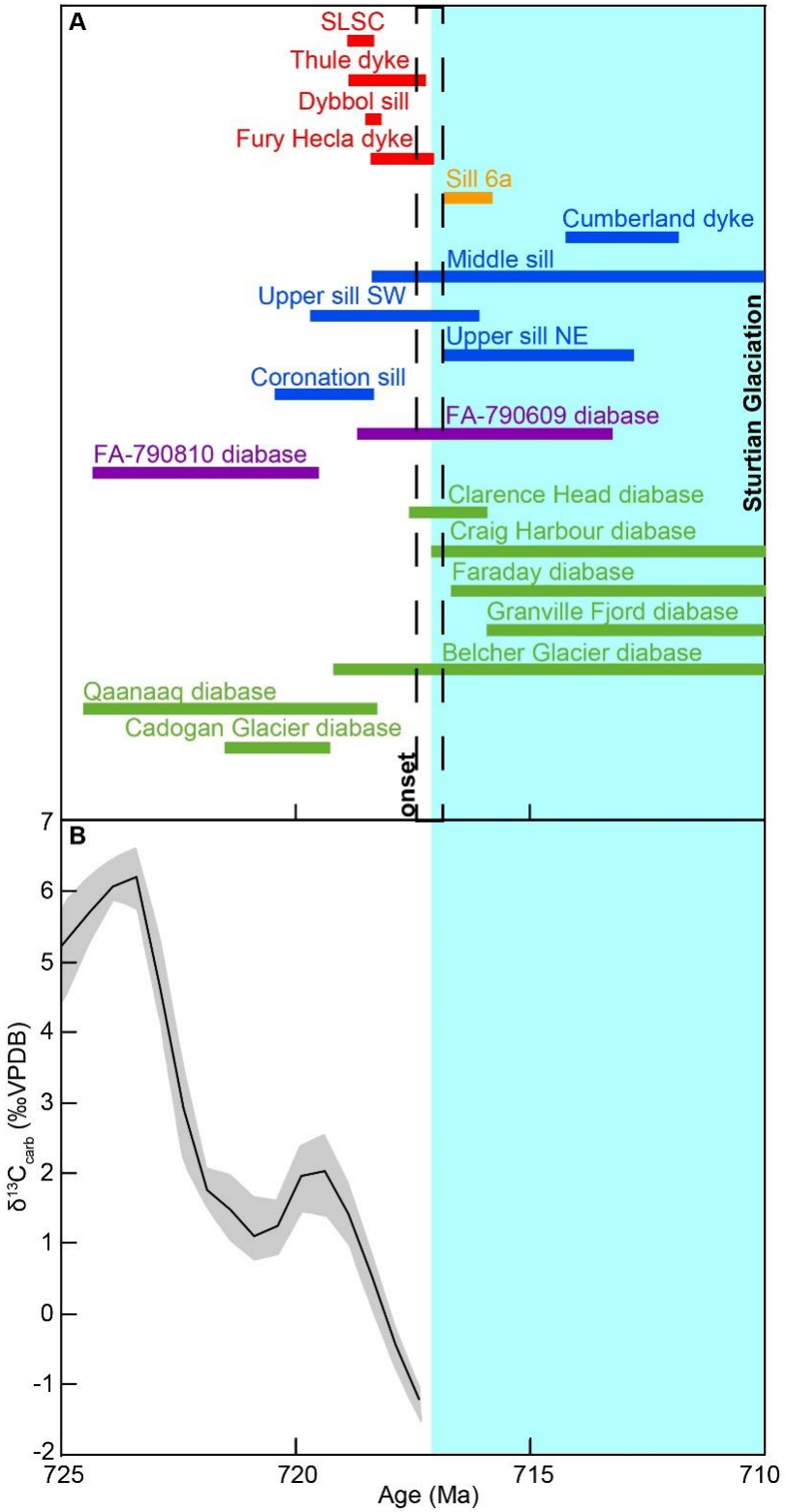

Figure 2.4 : Timing constraints for the Franklin LIP and the onset of the Sturtian glaciation. (A) $^{206}Pb/^{238}U$ zircon ages (red) and baddeleyite ages (all others) of the Franklin event. Ages are color-coded as in Fig. 2.1. The onset of the Sturtian glaciation is based on our estimated age 717.17 +0.26/-0.33 Ma. SLSC, Steensby Land sill complex. All ages are given with 95% uncertainty. (B) Summary of $\delta^{13}C$ for marine carbonates 725–718 Ma. Grey shading and black lines indicate the 95% uncertainty and mean values from a LOESS smoothing fit.

2.4.5 The role of basalt weathering in the onset of Sturtian glaciation

We cannot rule out the possibility that a younger phase of Franklin magmatism not represented by the Fury and Hecla and Thule dykes and sills occurred closer to the onset of Sturtian glaciation and contributed to cooling via release of sulfate aerosols (Macdonald and Wordsworth, 2017). However, our new ages and chronology allow us to assert confidently that Franklin magmatism occurred 0.1–1.5 m.y. prior to glaciation. This timeframe is consistent with tropical basalt weathering (Li et al., 2016) as a contributing mechanism for global cooling, following an initial increase in CO_2 related to the earliest phase of LIP emplacement (Goddéris et al., 2003; Cox et al., 2016; Tian and Buck, 2022). A time lag between LIP emplacement and the onset of Sturtian glaciation is further supported by the $\delta^{13}C$ record, which shows declining $\delta^{13}C$ values ahead of glaciation (Fig. 2.4B). We note that the temporal resolution of the $\delta^{13}C$ record is poor compared to our estimate for the age of Franklin magmatism and that we cannot link it directly with our Franklin ages. However, a large drop in $\delta^{13}C$ values in marine carbonates leading up to the onset of Sturtian glaciation (Fig. 2.4B) is recorded in three separate successions where sub-Sturtian glacial erosional truncation is inferred to be nonexistent to minimal: the Mariam Bohkahko Formation in Ethiopia (MacLennan et al., 2018; Park et al., 2020), the Garbh Eileach Formation in Scotland (Fairchild et al., 2018), and the Ugab Subgroup in northern Namibia (Lamothe et al., 2019). Therefore, to the extent that this negative $\delta^{13}C$ excursion records CO_2 released during Franklin magmatism, this outgassing must have preceded the onset of glaciation.

The ability of mafic LIPs to provoke sufficient global cooling through silicate weathering to trigger glaciation has recently been called into question. Park et al. (2021) argued that insofar as continental flood basalts, the crowning feature of mafic LIPs, tend to accumulate in low relief regions, their subdued topography might counteract the influence of tropical temperatures and heavy rainfall on weathering rates. However, in the case of the Franklin suite, stratigraphic data from the Natkusiak volcanic sequence indicate valley-filling flows and pyroclastic rocks in the lower 100 m (Jefferson et al., 1985), overlain by at least 1000 m of generally thin (15–20 m), regionally extensive sheet flows that would have formed a broad, regionally extensive high plateau.

Park et al. (2021) further noted a poor correlation between tropical LIP area and ice extent throughout the Phanerozoic, which they attributed in part to a soil shielding effect, which limits the weatherability of LIPs (Goddéris et al., 2017). However, Neoproterozoic LIPs predate the emergence of vascular plants, and the absence of vegetative cover would have had far-reaching impact on soil formation, erosion, and the carbon cycle. Vascular plants promote silicate weathering, the formation of thick tropical soils, reduced soil erosion, and the formation of carbon sinks in terrestrial environments (Goddéris et al., 2017; Ibarra et al., 2019). Furthermore, in the presence of vegetative cover, soils tend to retain and recycle bio-limiting phosphorus, whereas in the absence of vegetation, phosphorus in the soil is easily leached and transported in surface

waters (Dzombak and Sheldon, 2020) to ultimately promote organic productivity and carbon burial in a marine environment (Cox et al., 2016). Given a constant rate of volcanic degassing, the burial of carbon in terrestrial vegetated environments following the emergence of land plants, requires that the overall rate of chemical weathering has to be slower, compared to the pre-vegetated Earth to maintain stability in the carbon cycle (D'Antonio et al., 2020). In tropical environments, the absence of vegetation in the Neoproterozoic, would have led to thinner soil cover as a result of reduced rates of biologically-induced weathering (Ibarra et al., 2019) and enhanced soil erosion (Ielpi et al., 2022). The higher overall rates of chemical weathering predicted by D'Antonio et al. (2020) could have been sustained in the Neoproterozoic tropics by reduced soil-shielding in a warm, humid environment where inorganic silicate weathering prevailed. The extensive alteration and thin soil profiles on the tops of individual Natkusiak basalt flows (Jefferson et al., 1985) that were erupted at low latitudes and on the windward coastal side of eastern Laurentia (at ca. 717 Ma; Cox et al., 2016), seem to support this model. The successive eruption of numerous, relatively thin basalt flows over ca. 1 Ma in the Franklin LIP, would have provided a steady supply of fresh glass and silicate mineral substrate, that would be highly reactive to surface weathering in the relatively warm and humid climate of tropical Laurentia (Cox et al., 2016).

Other studies have suggested processes that entail active uplift of mafic lithologies in the tropics playing a much more significant role in regulating long-term global silicate weathering rates than LIPs. Specifically, ophiolite obduction and arc-continent collisions in the tropics could episodically dominate global silicate weathering (Swanson-Hysell and Macdonald, 2017; Macdonald et al., 2019; Park et al., 2021). The isotopic record provides some insight on the question of the role of long-term mafic weathering on Tonian climate. It was previously noted that following ca. 100 Myr of nearly monotonic increase in the early Tonian, marine $^{87}Sr/^{86}Sr$ reached a peak near 0.7070 ca. 770 Ma and subsequently decreased to 0.7063 by the late Tonian (Cox et al., 2016; Zhou et al., 2020; Park et al., 2021). Cox et al. (2016) argued that this pattern in the marine $^{87}Sr/^{86}Sr$ record was the manifestation of weathering of multiple Neoproterozoic LIPs in the core of Rodinia as the supercontinent began to break up. While a coupled climate-biogeochemical model demonstrated this scenario to be viable (Goddéris et al., 2017), it is also likely that arc accretion and ophiolite obduction, particularly on the tropical proto-Arabian–Nubian shield (Johnson et al., 2003; Johnson, 2014), contributed to the late Tonian decline in marine $^{87}Sr/^{86}Sr$ (Park et al., 2020, 2021).

Further geochemical evidence for prolonged, late Tonian dominance of basalt weathering is found in the $^{187}Os/^{188}Os$ record, which shows a dramatic decline from values near 0.6 ca. 760 Ma to values of 0.1–0.2 between 740–720 Ma (Rooney et al., 2014; Millikin et al., 2022). Marine Os isotope ratios are much more sensitive to change than Sr isotope ratios due to a residence time that is two orders of magnitude lower (Peucker-Ehrenbrink and Ravizza, 2000), and the Tonian Os isotope record is strongly biased by data from

northwestern Canada (49). Nevertheless, a low initial $^{187}Os/^{186}Os$ ratio of 0.26 ± 0.03 from a Re-Os isochron on the 737.5 ± 9.5 Ma Russøya Member in Svalbard, which was far from any known LIPs or accreted arcs at the time (Cox et al., 2016), attests to a global ocean strongly influenced by weathering of juvenile basalts tens of millions of years in advance of Sturtian glaciation. (Millikin et al., 2022). Therefore, we propose that late Tonian climate was already strongly influenced by chemical weathering of mafic lithologies prior to Franklin LIP emplacement.

Independent evidence that the late Tonian suffered global cooling prior to the onset of the Sturtian snowball glaciation is found in the occurrence of ca. 751 Ma tropical, glaciolacustrine sediments in southwestern Virginia (MacLennan et al., 2020). Insofar as Earth had already cooled sufficiently by 751 Ma to initiate alpine glaciers in the tropics, then intense mafic weathering sustained over another 30 Myr would have rendered latest Tonian global climate highly unstable. Even if emplacement of the Franklin LIP on its own was not sufficient to trigger global glaciation, the rapid resurfacing of a massive region of tropical Rodinia by highly weatherable continental flood basalt at a time when global climate was already vulnerable might have nudged Earth beyond the Snowball tipping point.

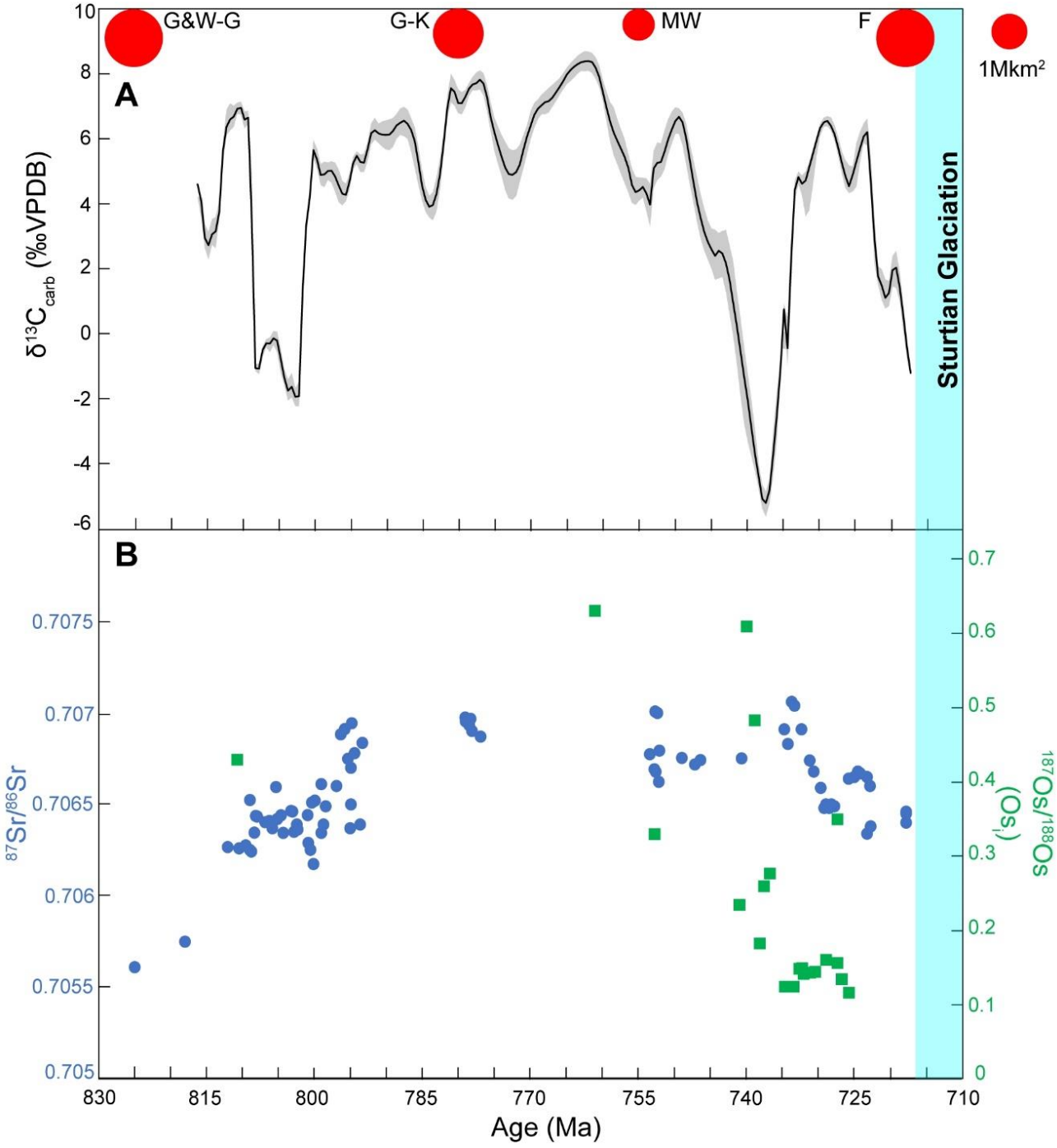

Figure 2.5 : Late Tonian isotopic compilations (830–710 Ma). (A) Summary of $\delta^{13}C$ for marine carbonates. Grey shading and black lines indicate the 95% uncertainty and mean values from a LOESS smoothing fit. Red circles are scaled to estimated erupted LIPs area (Ernst et al., 2021a). G&W-G, Guibei, Willouran and Gairdner; G-K, Gunbarrel and Kangding; MW, Mundine Well; F, Franklin. (B) Summary of the $^{87}Sr/^{86}Sr$ and $^{187}Os/^{188}Os$ records. Green squares are $^{187}Os/^{188}Os$ data, and blue circles are $^{87}Sr/^{86}Sr$ data.

2.5 Conclusion

Zircon U-Pb CA-ID TIMS ages of intrusions in the Fury and Hecla and Thule basins combined with field constraints indicate that Franklin magmatic activity took place over 0.53 ± 0.58 Ma at ca. 718 Ma and 0.1–1.6 Ma before the 717.19 +0.26/-0.33 Ma onset of Sturtian glaciation. This chronology implies that Franklin magmatism was relatively short-lived, similar to most other major LIPs (Kasbohm et al., 2021), rather than drawn out over as much as 10 Ma as implied by previous, less precise and potentially inaccurate ages on the Franklin event (Figure 4). The temporal offset between the Franklin magmatism and Sturtian onset, as well as the global $\delta^{13}C$ record, suggest that like the Central Atlantic Magmatic Province, Franklin emplacement released large amounts of CO_2 into the atmosphere, but the subsequent weathering of the flood basalts subsequently drew CO_2 down and triggered global cooling. Occurring at a time when global paleogeography already favored a cool climate, this cooling was evidently sufficient to trigger Snowball glaciation (Lu et al., 2022).

2.6 Acknowledgments

We thank Angelo dos Santos, and Tianran Zhang for their assistance in Greenland. The Canada-Nunavut Geoscience Office, Blue Jay Mining PLC, and Thule Air Force Base are thanked for logistical support in the field.

2.7 References

Bowring, J. F., McLean, N. M. et Bowring, S. A. (2011). Engineering cyber infrastructure for U-Pb geochronology: Tripoli and U-Pb_Redux. Geochemistry, Geophysics, Geosystems, 12(6).

Chandler, F. W. (1988). Geology of the late Precambrian Fury and Hecla Group, northwest Baffin Island, District of Franklin: Geological Survey of Canada, Bulletin 370, 30 p., https://doi.org/10.4095/126938.

Chandler, F. W. et Stevens, R. D. (1981). Potassium-argon age of the late Proterozoic Fury and Hecla Formation, northwest Baffin Island, District of Franklin: Geological Survey of Canada, Paper 81-1A, 37–40, https://doi.org/10.4095/109521.

Condon, D. J., Schoene, B., McLean, N. M., Bowring, S. A. et Parrish, R. R. (2015). Metrology and traceability of U–Pb isotope dilution geochronology (EARTHTIME Tracer Calibration Part I). Geochimica et Cosmochimica Acta, 164, 464–480.

Cox, G. M., Halverson, G. P., Stevenson, R. K., Vokaty, M., Poirier, A., Kunzmann, M., Li, Z.-X., Denyszyn, S. W., Strauss, J. V. et Macdonald, F. A. (2016). Continental flood basalt weathering as a trigger for Neoproterozoic Snowball Earth. Earth and Planetary Science Letters, 446, 89–99.

Cox, G. M., Strauss, J. V., Halverson, G. P., Schmitz, M. D., McClelland, W. C., Stevenson, R. S. et Macdonald, F. A. (2015). Kikiktat volcanics of Arctic Alaska—Melting of harzburgitic mantle associated with the Franklin large igneous province. Lithosphere, 7(3), 275–295.

D'Antonio, M. P., Ibarra, D. E. et Boyce, C. K. (2020). Land plant evolution decreased, rather than increased, weathering rates. Geology, 48(1), 29–33.

Davies, J. H. F. L., Marzoli, A., Bertrand, H., Youbi, N., Ernesto, M. et Schaltegger, U. (2017). End-Triassic mass extinction started by intrusive CAMP activity. Nature communications, 8(1), 1–8.

Dawes, P. R. (2006). Explanatory notes to the Geological map of Greenland, 1: 500 000, Thule, Sheet 5. Geological Survey of Denmark and Greenland Map Series, 2, 1–100.

Denyszyn, S. W., Halls, H. C., Davis, D. W. et Evans, D. A. (2009). Paleomagnetism and U–Pb geochronology of Franklin dykes in High Arctic Canada and Greenland: a revised age and paleomagnetic pole constraining block rotations in the Nares Strait region. Canadian Journal of Earth Sciences, 46(9), 689–705.

Denyszyn, S. W., Davis, D. W. et Halls, H. C. (2009). Paleomagnetism and U–Pb geochronology of the Clarence Head dykes, Arctic Canada: orthogonal emplacement of mafic dykes in a large igneous province. Canadian Journal of Earth Sciences, 46(3), 155–167.

Dessert, C., Dupré, B., François, L. M., Schott, J., Gaillardet, J., Chakrapani, G. et Bajpai, S. (2001). Erosion of Deccan Traps determined by river geochemistry: impact on the global climate and the 87Sr/86Sr ratio of seawater. Earth and Planetary Science Letters, 188(3-4), 459–474.

Donnadieu, Y., Goddéris, Y., Ramstein, G., Nédélec, A. et Meert, J. (2004). A 'snowball Earth'climate triggered by continental break-up through changes in runoff. Nature, 428(6980), 303–306.

Dufour, F., Stevenson, R. et Skulski, T. (2021). Geochemical comparison of Mackenzie and Franklin igneous mafic rocks in Nunavut, Northwest Territories and northwestern Greenland, in Summary of Activities 2020: Iqaluit, Canada-Nunavut Geoscience Office, 33–46.

Dzombak, R. M. et Sheldon, N. D. (2020). Weathering intensity and presence of vegetation are key controls on soil phosphorus concentrations: Implications for past and future terrestrial ecosystems. Soil Systems, 4(4), 73.

Ernst, R. E., Bleeker, W., Söderlund, U. et Kerr, A. C. (2013). Large Igneous Provinces and supercontinents: Toward completing the plate tectonic revolution. Lithos, 174, 1–14.

Ernst, R.E., Bond, D.P.G., Zhang, S.H., Buchan, K.L., Grasby, S.E., Youbi, N., El Bilali, H., Bekker, A. et Doucet, L.S. (2021a). Large Igneous Province Record Through Time and Implications for Secular Environmental Changes and Geological Time-Scale Boundaries. In: R.E. Ernst, A.J. Dickson, A. Bekker (eds) Large Igneous Provinces: A Driver of Global Environmental and Biotic Changes, American Geophysical Union Geophysical Monograph 255, 3–26.

Ernst, R. E., Dickson, A. et Bekker, A. (Eds.). (2021b). Large igneous provinces: A driver of global environmental and biotic changes (Vol. 255). John Wiley & Sons.

Fairchild, I. J., Spencer, A. M., Ali, D. O., Anderson, R. P., Anderton, R., Boomer, I., Dove, D., Evans, J. D., Hambrey, M. J., Howe, J., Sawaki, Y., Shields, G. A., Skelton, A., Tucker, M. E., Wang, Z. et Zhou, Y. (2018). Tonian-Cryogenian boundary sections of Argyll, Scotland. Precambrian Research, 319, 37–64.

Gaynor, S. P., Svensen, H. H., Polteau, S. et Schaltegger, U. (2022). Local melt contamination and global climate impact: Dating the emplacement of Karoo LIP sills into organic-rich shale. Earth and Planetary Science Letters, 579, 117371.

Gerstenberger, H. et Haase, G. (1997). A highly effective emitter substance for mass spectrometric Pb isotope ratio determinations. Chemical Geology, 136(3–4), 309–312.

Goddéris, Y., Donnadieu, Y., Carretier, S., Aretz, M., Dera, G., Macouin, M. et Regard, V. (2017). Onset and ending of the late Palaeozoic ice age triggered by tectonically paced rock weathering. Nature Geoscience, 10(5), 382–386.

Goddéris, Y., Donnadieu, Y., Nédélec, A., Dupré, B., Dessert, C., Grard, A., Ramstein, G., et Francois, L. (2003). The Sturtian 'snowball'glaciation: fire and ice. Earth and Planetary Science Letters, 211(1–2), 1–12.

Guex, J., Pilet, S., Müntener, O., Bartolini, A., Spangenberg, J., Schoene, B., Sell, B. et Schaltegger, U. (2016). Thermal erosion of cratonic lithosphere as a potential trigger for mass-extinction. Scientific reports, 6(1), 1–9.

Halverson, G. P., Shen, C., Davies, J. H. F. L. et Wu, L. (2022). A Bayesian Approach to Inferring Depositional Ages Applied to a Late Tonian Reference Section in Svalbard. Front. Earth Sci, 10, 798739.

Heaman, L. M. et LeCheminant, A. N. (1993). Paragenesis and U-Pb systematics of baddeleyite (ZrO2). Chemical Geology, 110(1-3), 95–126.

Heaman, L. M., LeCheminant, A. N. et Rainbird, R. H. (1992). Nature and timing of Franklin igneous events, Canada: implications for a Late Proterozoic mantle plume and the break-up of Laurentia. Earth and Planetary Science Letters, 109(1–2), 117–131.

Hiess, J., Condon, D. J., McLean, N. et Noble, S. R. (2012). 238U/235U systematics in terrestrial uranium-bearing minerals. Science, 335(6076), 1610–1614.

Ibarra, D. E., Rugenstein, J. K. C., Bachan, A., Baresch, A., Lau, K. V., Thomas, D. L., Lee, J., Boyce, C. K., et Chamberlain, C. P. (2019). Modeling the consequences of land plant evolution on silicate weathering. American Journal of Science, 319(1), 1–43.

Ielpi, A., Lapôtre, M. G., Gibling, M. R. et Boyce, C. K. (2022). The impact of vegetation on meandering rivers. Nature Reviews Earth & Environment, 3(3), 165–178.

Jefferson, C. W., Nelson, W. E., Kirkham, R. V., Reedman, J. H. et Scoates, R. F. J. (1985). Geology and copper occurrences of the Natkusiak basalts, Victoria Island, District of Franklin. Geological Survey of Canada, Current Research, Part A, 203-214.

Johnson, P. R. (2014). An expanding Arabian-Nubian Shield geochronologic and isotopic dataset: defining limits and confirming the tectonic setting of a Neoproterozoic accretionary orogen. The Open Geology Journal, 8(1).

Johnson, P. R., Abdelsalam, M. G. et Stern, R. J. (2003). The Bi'r Umq-Nakasib suture zone in the Arabian-Nubian shield: a key to understanding crustal growth in the East African orogen. Gondwana Research, 6(3), 523–530.

Johnstone, S. A., Schwartz, T. M. et Holm-Denoma, C. S. (2019). A stratigraphic approach to inferring depositional ages from detrital geochronology data. Frontiers in Earth Science, 7, 57 p.

Kasbohm, J., Schoene, B. et Burgess, S. (2021). Radiometric constraints on the timing, tempo, and effects of large igneous province emplacement. In: R.E. Ernst, A.J. Dickson, A. Bekker (eds) Large Igneous Provinces: A Driver of Global Environmental and Biotic Changes, American Geophysical Union Geophysical Monograph 255, 27–82.

Krogh, T. E. (1973). A low-contamination method for hydrothermal decomposition of zircon and extraction of U and Pb for isotopic age determinations. Geochimica et Cosmochimica Acta, 37(3), 485–494.

Lamothe, K. G., Hoffman, P. F., Greenman, J. W. et Halverson, G. P. (2019). Stratigraphy and isotope geochemistry of the pre-Sturtian Ugab Subgroup, Otavi/Swakop Group, northwestern Namibia. Precambrian Research, 332, 105387.

Li, G., Hartmann, J., Derry, L. A., West, A. J., You, C. F., Long, X., Zhan, T., Li, L., Li, G., Qiu, W., Li, T., Liu, L., Chen, Y., Ji, J. et Chen, J. (2016). Temperature dependence of basalt weathering. Earth and Planetary Science Letters, 443, 59–69.

Lindström, S., Callegaro, S., Davies, J., Tegner, C., van De Schootbrugge, B., Pedersen, G. K., Youbi, N., Sanei, H. et Marzoli, A. (2021). Tracing volcanic emissions from the Central Atlantic Magmatic Province in the sedimentary record. Earth-Science Reviews, 212, 103444.

Lu, K., Mitchell, R. N., Yang, C., Zhou, J. L., Wu, L. G., Wang, X. C. et Li, X. H. (2022). Widespread magmatic provinces at the onset of the Sturtian snowball Earth. Earth and Planetary Science Letters, 594, 117736.

Macdonald, F. A., Schmitz, M. D., Crowley, J. L., Roots, C. F., Jones, D. S., Maloof, A. C., Strauss, J. V., Cohen, P. A., Johnston, D. T. et Schrag, D. P. (2010). Calibrating the cryogenian. Science, 327(5970), 1241–1243.

Macdonald, F. A. et Wordsworth, R. (2017). Initiation of Snowball Earth with volcanic sulfur aerosol emissions. Geophysical Research Letters, 44(4), 1938–1946.

Macdonald, F. A., Schmitz, M. D., Strauss, J. V., Halverson, G. P., Gibson, T. M., Eyster, A., Cox, G., Mamrol, P. et Crowley, J. L. (2018). Cryogenian of Yukon. Precambrian Research, 319, 114–143.

Macdonald, F. A., Swanson-Hysell, N. L., Park, Y., Lisiecki, L. et Jagoutz, O. (2019). Arc-continent collisions in the tropics set Earth's climate state. Science, 364(6436), 181–184.

MacLennan, S. A., Eddy, M. P., Merschat, A. J., Mehra, A. K., Crockford, P. W., Maloof, A. C., Southworth, C. S. et Schoene, B. (2020). Geologic evidence for an icehouse Earth before the Sturtian global glaciation. Science Advances, 6(24), eaay6647.

MacLennan, S., Park, Y., Swanson-Hysell, N., Maloof, A., Schoene, B., Gebreslassie, M., Antilla, E., Tesema, T., Alene, M., et Haileab, B. (2018). The arc of the Snowball: U-Pb dates constrain the Islay anomaly and the initiation of the Sturtian glaciation. Geology, 46(6), 539–542.

Mattinson, J. M. (2005). Zircon U–Pb chemical abrasion ("CA-TIMS") method: combined annealing and multi-step partial dissolution analysis for improved precision and accuracy of zircon ages. Chemical Geology, 220(1–2), 47–66.

McLean, N. M., Bowring, J. F. et Bowring, S. A. (2011). An algorithm for U‐Pb isotope dilution data reduction and uncertainty propagation. Geochemistry, Geophysics, Geosystems, 12(6).

McLean, N. M., Condon, D. J., Schoene, B. et Bowring, S. A. (2015). Evaluating uncertainties in the calibration of isotopic reference materials and multi-element isotopic tracers (EARTHTIME Tracer Calibration Part II). Geochimica et Cosmochimica Acta, 164, 481–501.

Millikin, A. E., Strauss, J. V., Halverson, G. P., Bergmann, K. D., Tosca, N. J. et Rooney, A. D. (2022). Calibrating the Russøya excursion in Svalbard, Norway, and implications for Neoproterozoic chronology. Geology, 50(4), 506–510.

Park, Y., Swanson-Hysell, N. L., MacLennan, S. A., Maloof, A. C., Gebreslassie, M., Tremblay, M. M., Schoene, B., Alene, M., Anttila, E. S. C., Tesema, T. et Haileab, B. (2020). The lead-up to the Sturtian Snowball Earth: Neoproterozoic chemostratigraphy time-calibrated by the Tambien Group of Ethiopia. GSA Bulletin, 132(5–6), 1119–1149.

Park, Y., Swanson-Hysell, N. L., Lisiecki, L. E. et Macdonald, F. A. (2021). Evaluating the relationship between the area and latitude of large igneous provinces and Earth's long‐term climate state. In: R.E. Ernst, A.J. Dickson, A. Bekker (eds) Large Igneous Provinces: A Driver of Global Environmental and Biotic Changes, American Geophysical Union Geophysical Monograph 255, 153–168.

Pehrsson, S. J. et Buchan, K. L. (1999). Borden dykes of Baffin Island, Northwest Territories: a Franklin U-Pb baddeleyite age and a paleomagnetic reinterpretation. Canadian Journal of Earth Sciences, 36(1), 65–73.

Peucker-Ehrenbrink, B. et Ravizza, G. (2000). The marine osmium isotope record. Terra Nova, 12(5), 205–219.

Pohlner, J. E., Schmitt, A. K., Chamberlain, K. R., Davies, J. H., Hildenbrand, A. et Austermann, G. (2020). Multimethod U–Pb baddeleyite dating: insights from the Spread Eagle Intrusive Complex and Cape St. Mary's sills, Newfoundland, Canada. Geochronology, 2(2), 187–208.

Rioux, M., Bowring, S., Dudás, F. et Hanson, R. (2010). Characterizing the U–Pb systematics of baddeleyite through chemical abrasion: application of multi-step digestion methods to baddeleyite geochronology. Contributions to Mineralogy and Petrology, 160(5), 777–801.

Rooney, A. D., Macdonald, F. A., Strauss, J. V., Dudás, F. Ö., Hallmann, C. et Selby, D. (2014). Re-Os geochronology and coupled Os-Sr isotope constraints on the Sturtian snowball Earth. Proceedings of the National Academy of Sciences, 111(1), 51–56.

Schaller, M. F., Wright, J. D., Kent, D. V. et Olsen, P. E. (2012). Rapid emplacement of the Central Atlantic Magmatic Province as a net sink for CO2. Earth and Planetary Science Letters, 323, 27–39.

Schaltegger, U. et Davies, J. H. (2017). Petrochronology of zircon and baddeleyite in igneous rocks: Reconstructing magmatic processes at high temporal resolution. Reviews in Mineralogy and Geochemistry, 83(1), 297–328.

Schoene, B., Crowley, J. L., Condon, D. J., Schmitz, M. D. et Bowring, S. A. (2006). Reassessing the uranium decay constants for geochronology using ID-TIMS U–Pb data. Geochimica et Cosmochimica Acta, 70(2), 426–445.

Swanson-Hysell, N. L. et Macdonald, F. A. (2017). Tropical weathering of the Taconic orogeny as a driver for Ordovician cooling. Geology, 45(8), 719–722.

Vermeesch, P. (2018). IsoplotR: A free and open toolbox for geochronology. Geoscience Frontiers, 9(5), 1479–1493.

Widmann, P., Davies, J. H. F. L. et Schaltegger, U. (2019). Calibrating chemical abrasion: Its effects on zircon crystal structure, chemical composition and UPb age. Chemical Geology, 511, 1–10.

Zhou, Y., von Strandmann, P. A. P., Zhu, M., Ling, H., Manning, C., Li, D., He, T. et Shields, G. A. (2020). Reconstructing Tonian seawater 87Sr/86Sr using calcite microspar. Geology, 48(5), 462–467.

CHAPITRE 3

MAJOR AND TRACE ELEMENT AND ND ISOTOPE COMPOSITIONS REVEAL LOW-, AND HIGH-TI PROVINCES IN THE FRANKLIN LIP INDICATING CHANGES IN LITHOSPHERE THICKNESS AND ARCTIC LAURENTIA TECTONICS

Frédéric Dufour[1], Thomas Skulski[2], Ross Stevenson[1]

[1]Département des Sciences de la Terre et de l'Atmosphère, Université du Québec à Montréal, Montréal, Québec, H3C 3P8, CANADA

[2]Geological Survey of Canada, Natural Resources Canada, Ottawa, Ontario K1A 0E8, Canada

Abstract

The Franklin large igneous province (ca. 720 Ma) is the one of the largest of a series of LIPs emplaced during the Neoproterozoic (1000–540 Ma) and has been linked to the break-up of the Rodinian supercontinent. It produced mafic rocks of basalts, sills, and a large radiating dyke swarm fanning over a distance of 2500 km from Alaska, across northern Canada, to northwestern Greenland. Precedent studies on the Franklin event have shown that the rocks have comparable geochemistry across this LIP (e.g. TiO_2 compositions below <2%), suggesting that the magmatic source is overall similar.

Here we investigate in this paper if the Franklin LIP presents any large-scale spatial geochemical variations, and if they imply specific magmatic processes and sources. The causes of the petrogenesis of the rocks are compared with the tectonics and lithospheric structure. We present new whole-rock geochemistry and Nd isotope data for Franklin dykes and sills in northwestern Baffin Island and Greenland, and compare them to previously studied Franklin igneous rocks. This study reveals the presence of geochemical provinces within the Franklin LIP based on the abundance of TiO_2, with rocks from northwestern Laurentia having low-(<2%) TiO_2 compositions, whereas rocks from northeastern Laurentia yield higher (2–6%) TiO_2 contents. The low-Ti rocks exhibit flat to slightly light-REE enriched and incompatible element profiles that are consistent with high degrees of partial melting of a spinel lherzolitic mantle source. The high-Ti rocks are enriched in LREE and incompatible elements, and can be modelled with lower degrees of partial melting of a garnet lherzolitic mantle source. Nd isotope analyses indicate that crustal contamination among these suites range from negligible to as high as 50% in more differentiated samples. The REE modelling of the least contaminated rocks from these suites indicates that they likely originated from the same Franklin plume material, but that they experienced different conditions of partial melting related to the thickness of the lithosphere across the Arctic Laurentia. The break-up of Rodinia at 775–720 Ma in northwestern Laurentia would have favored extensive thinning of the lithosphere and shallower melting of the mantle, while the lithosphere thickness would have been unchanged in northeastern Laurentia, leading to deeper mantle melting within the garnet stability field.

3.1 Introduction

Large igneous provinces (LIP) emplace large volumes of mostly mafic magma (> 0.1 Mkm^3), over a period of a few million years (Ernst et al., 2021; Kasbohm et al. 2021). They occur either in continental or oceanic settings (Bryan and Ernst, 2008), and may be associated with mantle plumes (Coffin and Eldholm, 1994). The geochemistry of the LIPs can be studied using the Ti and incompatible element contents of the mafic magmas to correlate different magmatic units (Ernst et al., 2008) and have led to the identification of low-Ti and high-Ti magma suites in LIPs such as the Emeishan, the Central Atlantic magmatic province, Karoo and Deccan LIPs (Xu et al., 2001; Melluso et al., 2006; Jourdan et al., 2007; Marzoli et al., 2018).

Studies of the Emeishan, Karoo, Deccan LIPs have shown that the geochemistry of high-Ti magmas, represented by enriched trace elements and trace element ratios reflecting a garnet source, can be explained by low degrees of melting of a deep mantle source (Arndt et al., 1993; Xu et al. 2001; Jourdan et al., 2007; Wang et al., 2007; Prasanth et al., 2019). Conversely, low-Ti concentrations in LIP magmas have been largely interpreted as a product either of contamination from the sub-continental lithospheric mantle (SCLM) and/or continental crust material (Hergt et al., 1991; Jourdan et al., 2007; Xiao et al., 2004; Day et al., 2013; Sibik et al., 2015; Marzoli et al., 2018), or the product of high degrees of partial melting from a shallow-level mantle source (Arndt et al., 1993; Xu et al. 2004; Zhang et al., 2019).

Both magma suites are characterized by a relative enrichment in rare earth elements, but the high-Ti magmas have a greater enrichment in REE compared to the low-Ti magmas, highlighting the possibility of a common source related by different pressures and degrees of partial melting producing variations in Ti contents (Xu et al., 2001; Jourdan et al., 2007; Zhang et al., 2019). Because HREE are compatible in a garnet-lherzolite mantle, melting of the mantle in the garnet-stability field will yield magmas enriched in Ti and light REE, whereas melting in the shallower spinel stability field will yield less enrichment in both Ti and light-REE. This suggests that the various tectonic settings in which the LIPs occur, such as plate boundaries and/or intraplate settings (Bryan and Ernst, 2008), may explain the geochemical heterogeneities observed in the LIPs.

The Franklin LIP provides a classic example for investigating the origins of low-, and high-Ti magmas. The Franklin igneous province has the largest extent of any Neoproterozoic LIP and its emplacement has been correlated with the break-up of the supercontinent Rodinia with the separation of Laurentia from Siberia at ca. 720 Ma (Ernst et al., 2013; Ernst et al., 2016; Ernst et al., 2021; Swanson-Hysell, 2021). The Franklin LIP resulted in extensive flood basalts (Beard et al., 2017), sills, and a large dyke swarm that radiated across Alaska, northern Canada, and northwestern Greenland (Heaman et al., 1992; Denyszyn et al., 2009a, b; Cox et al., 2015). Both low-Ti basalts (~1% TiO_2; Kikiktat volcanics, Natkusiak basalts) and high-Ti basalts (<2%

TiO_2; Natkusiak basalts) have been documented in the western Canadian Arctic (Cox et al., 2015; Beard et al., 2017).

We examine in this study if there are any large-scale spatial geochemical variations in the Franklin LIP, the magmatic processes and sources implicated in the petrogenesis, and their implications in terms of tectonics and lithospheric structure. We present a review of published Franklin geochemical data (major and trace elements, Nd isotopes) with the addition of 35 new analyses from Franklin dykes and sills sampled in the Eastern Canadian Arctic and Western Greenland. The data highlights the presence of very high Ti magmas from the Eastern arctic.

3.2 Geological settings

The Franklin LIP emplaced about ~2.64 Mkm^2 of mafic rock across northern North America (Ernst et al., 2021) over a relative short period of time (718 Ma, cross correlate with chapter two; Dufour et al., submitted). Examples of Franklin magmatism include the Natkusiak basalt Formation and sills on Victoria Island (Heaman et al., 1992; Bédard et al., 2016; Beard et al., 2017), the Kikiktat volcanics in northeastern Alaska (Cox et al., 2015), and a radiating dyke swarm and distal sills that spread-out across northern Canada to northwestern Greenland (Heaman et al., 1992; Shellnutt et al., 2004; Denyszyn et al., 2009a, b). The Irkutsk LIP in southern Siberia is also believed be a continuation of the Franklin LIP (Ernst et al., 2016).

3.2.1 Natkusiak Formation basalts and sills

The Natkusiak Formation basalts and Natkusiak sills outcrop on northwestern Victoria Island in the Canadian Arctic Archipelago. The Natkusiak basalts cap the Tonian sedimentary rocks of the Shaler Supergroup, composed of shallow water clastic rocks, carbonates and sulfate evaporites, and the Natkusiak sills intrude the same sedimentary sequence (Heaman et al., 1992; Rainbird, 1993). Numerous NW-trending mafic dykes, and the Natkusiak sills cut the Shaler Supergroup (Baragar, 1976; Dostal et al., 1986; Heaman et al., 1992; Bédard et al., 2012; Hayes et al., 2015; Williamson et al., 2016). The most precise age of the Natkusiak igneous rocks is derived from sill 6a which yielded a $^{206}Pb/^{238}U$ baddeleyite age of 716.33 ± 0.53 Ma (Macdonald et al., 2010).

The Natkusiak basalts are preserved in two erosional remnants; a northern (~1100 m thick) and a southern (~200 m thick) lobe that record a volcanic sequence of ~51 flows. The volcanic sequence includes a basal lava sequence of hyaloclastite, rubbly and pillowed flows (V_0, 30–100 m thick), a volcaniclastic unit (C_1 and C_2, <100 m thick), and basalt units (V_1 and V_2 cycles, up to ~1100; Baragar, 1976; Jefferson et al., 1985; Dostal et al., 1986; Williamson et al., 2016; Beard et al., 2017). The Natkusiak basalts are aphanitic to subophitic, and consist of clinopyroxene, plagioclase, titanomagnetite and olivine (Jefferson et al., 1985; Dostal et al., 1986; Williamson et al., 2016; Beard et al., 2017).

Thirteen diabase gabbro sills can be laterally traced over tens of km, range from 20 to 60 m thick, with many of them forming composite intrusions (Baragar, 1976; Jefferson, 1985; Bédard et al., 2012; Hayes et al., 2015). Two generations of sills are recognized; early sills that mostly occur in the lower part of the Shaler Group, that are cross-cut by late sills that are disseminated in the Shaler Supergroup (Beard et al., 2017). Some of the NW-trending dykes and sills represent feeders to the lavas whereas other are suspected to feed the sills (Baragar, 1973; Dostal et al., 1986; Bédard et al., 2012; Hayes et al., 2015; Williamson et al., 2016). The sills are mostly composed of plagioclase, clinopyroxene, olivine, titanomagnetite, and are divided into two magma types in Natkusiak following Hayes et al. (2015) and Bedard et al. (2016) such as the Type 1 sills characterized by olivine cumulate zones (high MgO) near their base, cut by the Type 2 sills which present intergranular to subophitic textures.

Geochemical studies have highlighted that the Type 1 and 2 Natkusiak sills are correlated to the volcanic sequence of the Natkusiak Formation (Hayes et al., 2015; Bédard et al., 2016; Beard et al., 2017). Type 1 is a low-TiO_2 (1.0–1.2 wt. %) magma which includes the basal basalts (V_0; Fig. 3.5; Bédard et al., 2016) of the Natkusiak Formation (8–10.3 wt. % MgO) and oldest Type 1 sills (6.5–13 wt. % MgO in chilled margins). The type 2 (1.2–1.8 wt. % MgO) suite comprises the sheet flow basalts (V_1, V_2; Fig. 3.5; Bédard et al., 2016) of the Natkusiak Formation and youngest Type 2 sills.

3.2.2 Distal Franklin basalts, sills and dyke swarm

The Franklin radiating dyke swarm is one of the largest dyke swarms on Earth, fanning out over a distance of 2500 km (Ernst and Buchan, 1997; Denyszyn et al., 2009a; b). Centered on Melville Island (Fig. 3.1), the dyke swarm spans from NE-striking in the west, to NW-striking in Arctic Archipelago and Baffin Island, and W- to SW-striking on Ellesmere Island and Greenland, with the dykes striking towards an inferred plume center on Melville Island (Heaman et al., 1992; Denyszyn et al., 2009a). However, some subswarms have an N-S trend and are possibly part of a giant circumferential dyke swarm including the Clarence Head dykes, the Strathcona Sound dykes, and the Lasard River dykes (Fig. 3.1; Denyszyn et al., 2009b; Buchan and Ernst, 2021). The highest density of subswarms occur west of the Coronation sills, and in the east, across Baffin, Ellesmere, and Devon islands, and in the Thule area. The dykes are on average ~30 m wide, can reach lengths of ~100 km, and are mafic gabbro bodies with a fine-grained texture in chilled margins, medium- to coarse-grained texture in the interiors of the dykes with subophitic to ophitic textures (Heaman et al., 1992; Pehrsson and Buchan, 1999; Denyszyn et al., 2009a, b). The mineralogy is mainly composed of plagioclase, clinopyroxene, oxides, with occasional olivine or quartz.

Franklin sills and dykes intrude the late Mesoproterozoic basins in northeastern Canada and northwestern Greenland, collectively referred to as the Bylot basins (Fahrig et al., 1981) comprising the Fury and Hecla, Hunting-Aston, Borden, and Thule basins. The intrusions in northwestern Baffin Island include NW-

trending mafic dykes cutting both the Archean basement and the Fury and Hecla Group (Fig. 3.2), and the Dybbol sill which is a gentle southerly-dipping mafic intrusion forming a cliff on the Autridge peninsula and capping the Fury and Hecla Basin (Chandler, 1988). The dykes can be traced over tens of km, range from 10 to 500 m thick, and the Dybbol sill reaches a maximum thickness of 80 m with the development of columnar-jointed structures (Dufour et al., 2020). The dykes are inferred to cross-cut the sill (Chandler, 1988). These mafic intrusions are gabbroic rocks, have medium- to coarse-grained (fine-grained in dyke chilled margins), homogeneous, equigranular and ophitic textures, and are essentially composed of plagioclase, clinopyroxene, and minor olivine in the sill (Dufour et al., 2020; Dufour et al., submitted). The rocks have similar geochemical compositions to other Franklin dykes and sills and range from 1–2.75% TiO_2 (Dufour et al., 2021). High-precision $^{206}Pb/^{238}U$ zircon dating indicates that the emplacement of the sills with a composite age of 718.33 ± 0.18 Ma preceded the intrusion of the dykes with an age of 717.71 +0.55/-0.69 Ma (cross reference to Chapter two; Dufour et al., submitted).

Similar dykes and sills occur in northwestern Greenland, referred to as the Thule dyke (TD) swarm and the Steensby Land sill complex (SLSC), and cut both the Archean–Paleoproterozoic basement and Thule Basin (Fig. 3.3). The SLSC sills are located between Moriusaq and Pituffik (Thule Air Base) intruding the Mesoproterozoic sandstone and carbonate of the Dundas Group, range from a few meters to 100 m thick, show columnar-jointing, and are consistently cut by the faults of the Thule half-graben system (Dawes, 2006). The dykes trend WNW–ESE, cut the SLSC, and are parallel to and/or exploit the faults of the Thule half-graben system (Dawes, 2006; Dufour et al., submitted). The dykes are 1–200 m thick, form prominent ridges, and display dyke bifurcation, and locally, cross-cutting relationships. The dykes and the sills are fine- to coarse-grained gabbros and melanogabbro, have homogeneous to porphyritic, ophitic textures, and are composed of plagioclase, clinopyroxene, with local occurrences of small granophyric pockets of K-feldspar and interstitial quartz (Dawes, 2006; Dufour et al., submitted). The trace element geochemistry is relatively comparable to other Franklin rocks (further discussed below), but the Thule dykes and sills display the highest TiO_2 composition of the Franklin igneous suite, possibly indicating a greater degree of differentiation and/or differences in the magma sources (Dufour et al., 2021). The dykes are observed to crosscut the SLSC sills in the Steensby Land area. The emplacement of the dykes after the sills is supported by new $^{206}Pb/^{238}U$ zircon ages indicating that the Thule dykes (718.03 +0.59/-0.84 Ma) are younger than the SLSC sills (718.61 ± 0.30 Ma), and are correlated with the Franklin LIP (Denyszyn et al., 2009a; Dufour et al., submitted).

The Kikiktat volcanics are found on the North Slope subterrane in northeastern Alaska (Cox et al., 2015) and consist of basalt flows with a total thickness of 80–500 m showing abundant pillow lava, columnar-jointed structures, and a few meters of sills and volcaniclastic rocks. The basalts contain abundant

plagioclase laths, subophitic interstitial clinopyroxene, and a variable proportion of olivine that reflects the high or low Mg content in the samples. The Kikiktat volcanics are characterized by low TiO_2 concentrations (0.9–1.8 wt. %) and are correlated to the Franklin magmatism by a $^{206}Pb/^{238}U$ detrital zircon age of 719.47 ± 0.29 Ma from the overlying volcaniclastic rock (Cox et al., 2015).

The Coronation sills are exposed for over ~500 km (Fig. 3.1), and are stratigraphically correlated with the Natkusiak sills (Heaman et al., 1992; Rainbird et al., 1996; Shellnutt et al., 2004). The Coronation sills range from 20–100 m thick, are composed of plagioclase, clinopyroxene, and minor amounts of olivine and comparable in isotopic, trace element variations and aspect to the Natkusiak basalts and sills (Shellnutt et al., 2004; Beard et al., 2017).

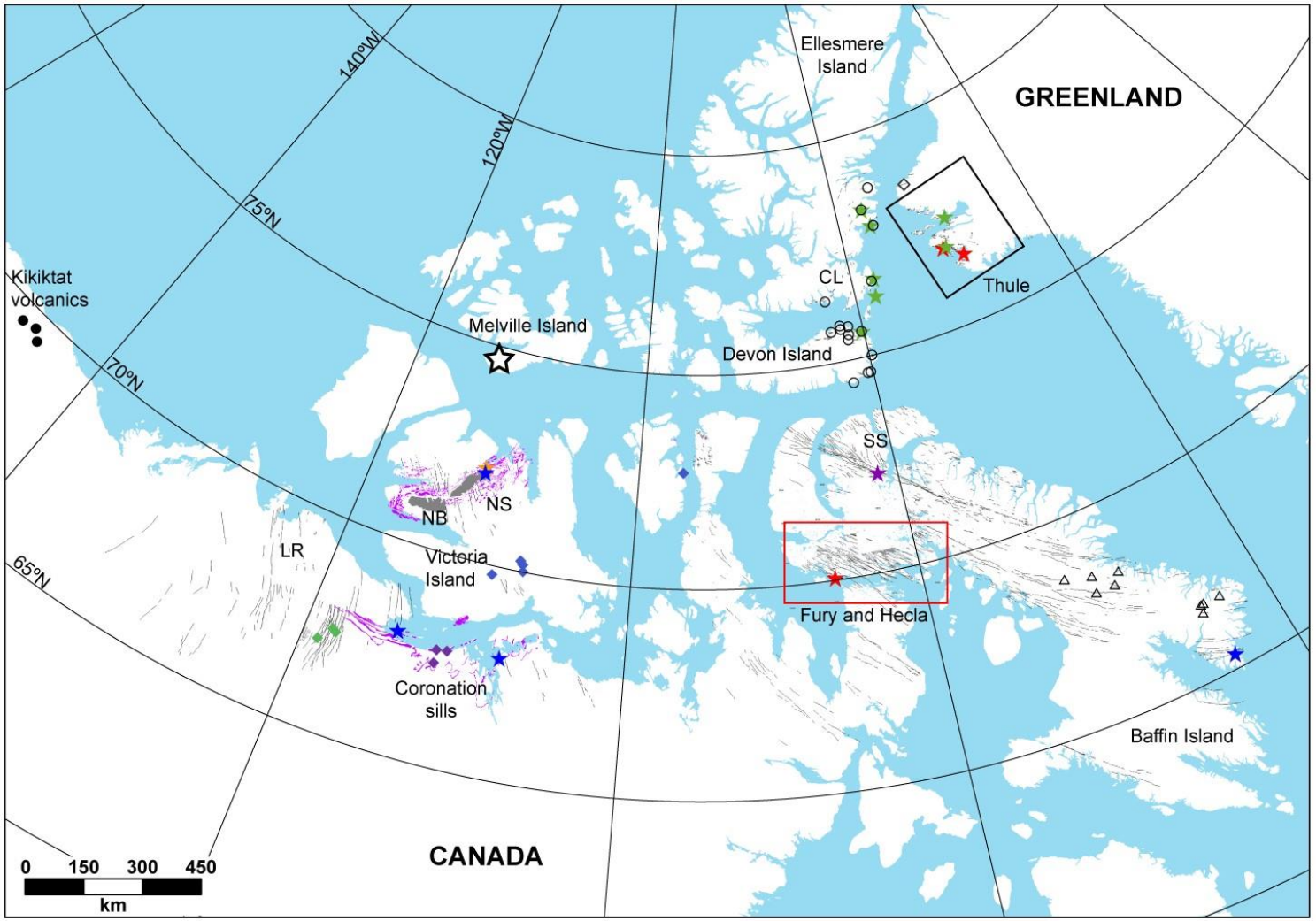

Figure 3.1: Map of the Franklin igneous suites modified from Dufour et al. (submitted). Red box indicates location of Fig. 3.2, and black box is location of Fig. 3.3. Black lines are the mafic dyke swarm. Black open star is the proposed plume location (Denyszyn et al., 2009a). Filled stars denote U-Pb ages; blue stars are from Heaman et al. (1992); green stars from Denyszyn et al. (2009a, b); purple star is from Macdonald et al. (2010); orange star is from Pehrsson and Buchan (1999); red stars are from Dufour et al. (submitted). NB, Natkusiak basalts; NS, Natkusiak sills; CL, Clarence Head dykes; LR; Lasard River dykes; SS, Strathcona Sound dykes. Samples locations are color-coded as in the geochemistry plots.

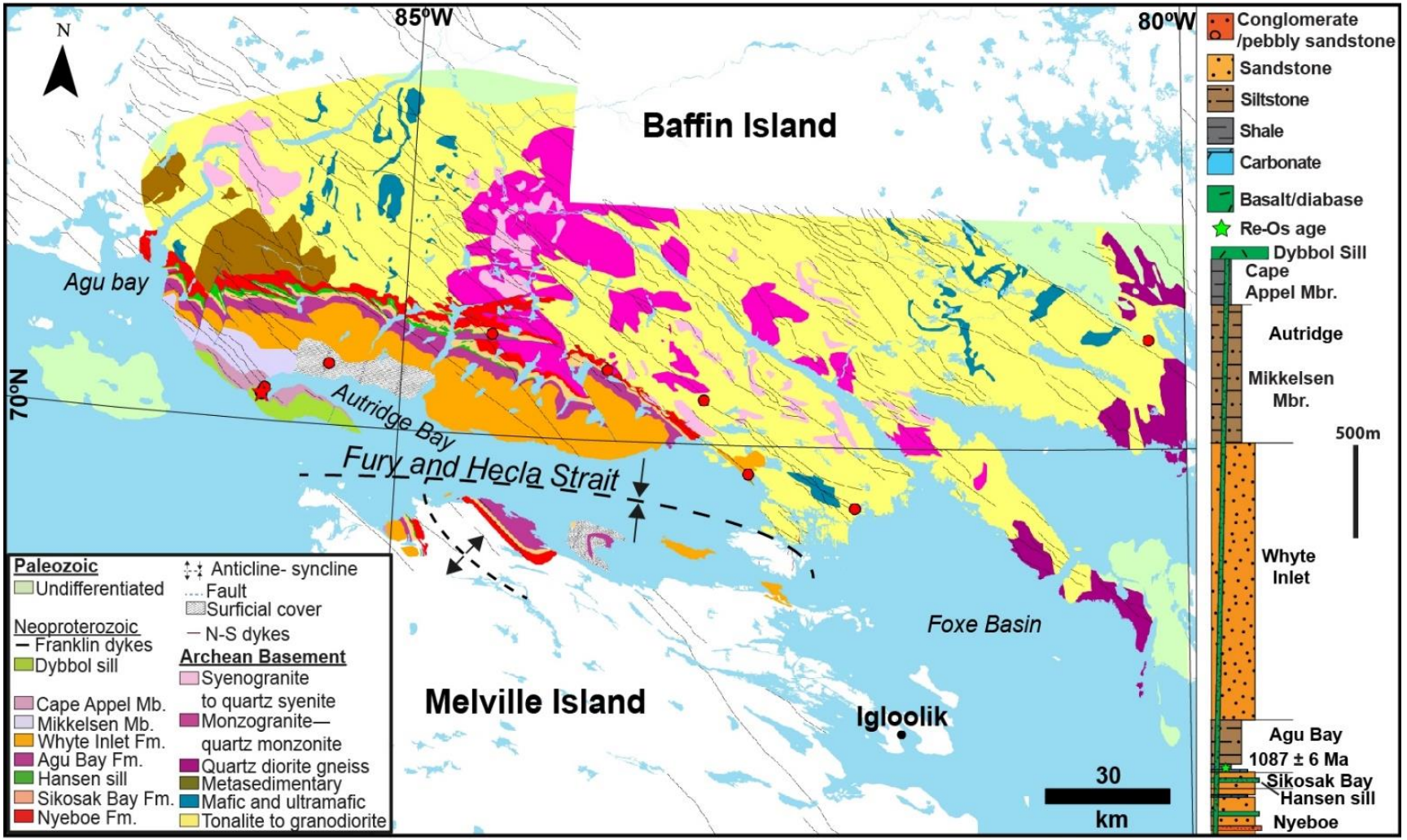

Figure 3.2: Geological map of Fury and Hecla Basin and the Archean basement modified from Dufour et al. (submitted). The Paleozoic rocks and the Fury and Hecla Basin are adapted from Chandler (1988), Long and Turner (2012), and Greenman et al. (2020). The Neoproterozoic Franklin intrusions and the Archean basement are adapted from Steenkamp et al. (2018) and Dufour et al. (2021). Red star indicates location of the U-Pb ages of the Fury and Hecla dyke and Dybbol sill. Inset figure is the stratigraphy of the Fury and Hecla Basin after Chandler (1988) and Greenman et al. (2021). Red circles are sample locations of the Franklin dykes.

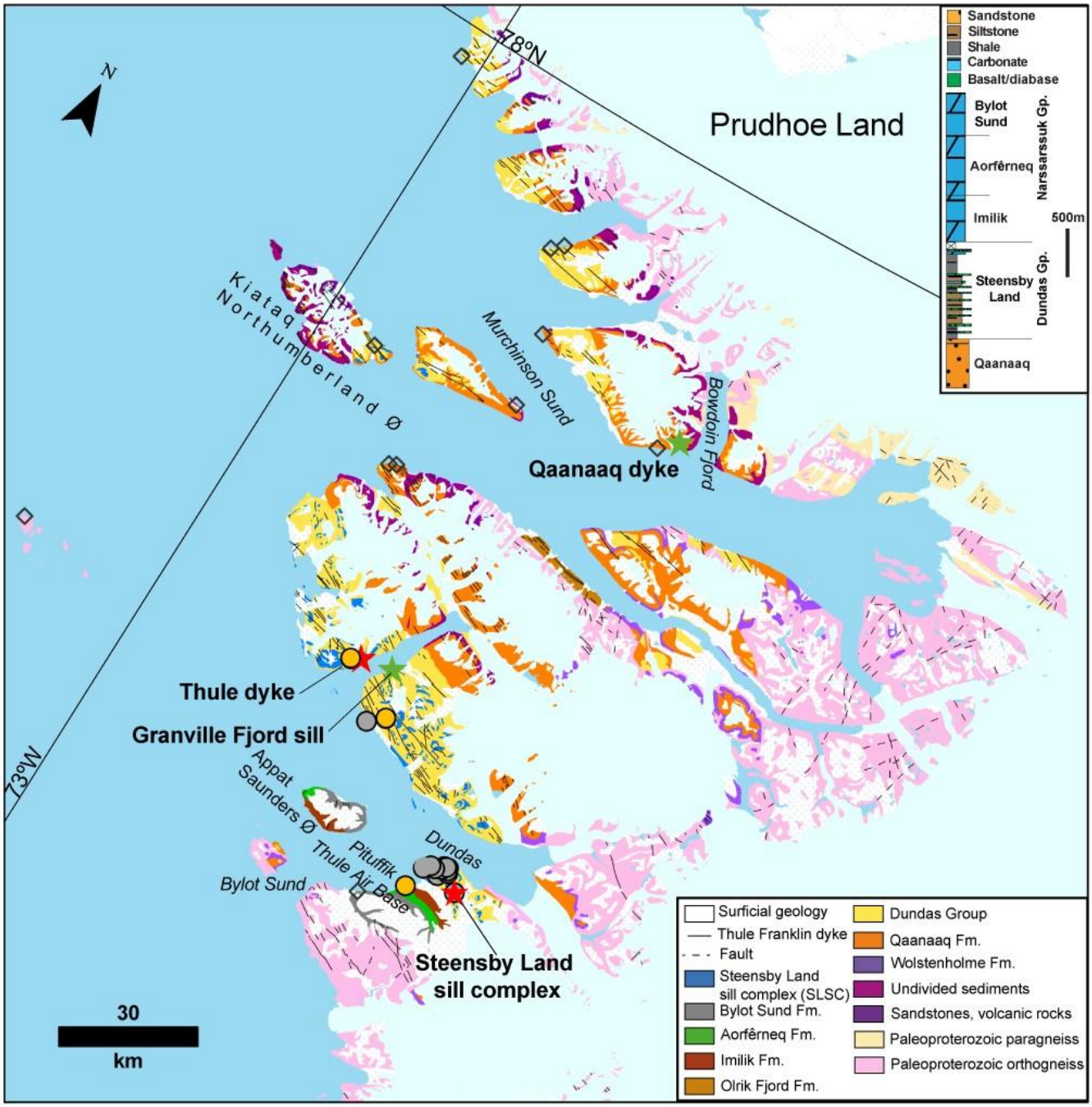

Figure 3.3: Geological map of the Thule area is modified from Dufour et al. (submitted) and the Geological Survey of Denmark and Greenland. Inset figure is the stratigraphy of the Thule Basin after Dawes (1997). Samples locations colors are used in the geochemistry plots.

3.3 Methodology

Thirty-five samples of dykes and sills centers and margins were collected from the Fury and Hecla (northwestern Baffin Island) and Thule (northwestern Greenland) basins during the summers of 2018 and 2019. Six different dykes were sampled including margins and centers of the dykes to determine if any geochemical variation and contamination exist across the Fury and Hecla dykes. A similar sampling method was used in Thule area where samples of sixteen outcrops were collected. Samples were cut with a rock saw to remove weathered surfaces, crushed under a hydraulic press, and crushed into powder form in a SPEX 8500 Shatterbox using an alumina ceramic bowl.

3.3.1 Whole-rock geochemistry

Whole-rock geochemistry was performed at Activation Laboratories Ltd. (Ancaster, Ontario). Major elements were analyzed on a Thermo Jarrell-Ash Enviro II inductively coupled plasma–emission spectrometer (ICP-ES) or a Varian Vista 735 ICP-ES, while trace elements were analyzed on a Perkin Elmer Sciex Elan 6000/6100/9000-type inductively coupled plasma–mass spectrometer (Actlabs, 2019; https://actlabs.com/geochemistry/lithogeochemistry-and-whole-rock-analysis/lithogeochemistry). Whole-rock geochemistry is reported in Table A3.1.

3.3.2 Sm-Nd analyses

The Sm and Nd concentrations and the Nd isotope data (Table A3.2) were determined by isotope dilution. About ~ 0.08 g of each sample was spiked with a $^{150}Nd/^{149}Sm$ enriched tracer and dissolved using a HF-HNO_3 acid mixture in Teflon beakers. The solutions were then evaporated and the salts were dissolved with concentrated HNO_3 to facilitate the conversion of fluoride salts to nitrates. The sample was again evaporated and dissolved in 6N HCl acid to obtain chloride salts. Nd and Sm concentrates were obtained using three different ion-exchange columns. The first column removed Fe with an anion exchange resin (AG1-X8), following a second column that eliminated most of the sample matrix while extracting a REE concentrate using the Eichrom TRU Resin. The REE concentrate was then loaded onto columns with Eichrom LN Resin to separate Sm and Nd fractions (Pin and Zalduegui, 1997). $^{147}Sm/^{144}Nd$ and $^{143}Nd/^{144}Nd$ isotopes were measured using a ThermoFisher Nu Plasma II Multi-Collector ICP-MS at the GEOTOP laboratory at Université du Québec à Montréal. At the time of the measurements, the $^{143}Nd/^{144}Nd$ JNDi1 standard yielded a value of 0.512105 ± 6 [(n = 16); the accepted mean of $^{143}Nd/^{144}Nd$ is 0.512115 ± 7 (Tanaka et al., 2000)]. Isotopic measurements were normalized to a $^{146}Nd/^{144}Nd$ value of 0.7219. The Nd compositions for the Franklin samples were age-corrected to 718 Ma (Dufour et al., submitted).

3.4 Results

New major and trace element data of 35 whole-rock samples (Table A3.1) and 20 Nd isotope analyses (Table 3.2) are presented for mafic dykes and sills in Fury and Hecla (northwestern Baffin Island) and Thule (northwestern Greenland) basins. These new samples are compared to a compilation of Franklin-related rocks such as the Kikiktat volcanics in northeastern Alaska (Cox et al., 2015), sills and dykes of northern mainland Canada, Victoria Island, and eastern Baffin Island (Ernst and Buchan, 2010), the Coronation sills (Shellnutt et al., 2004), dykes in Ellesmere and Devon islands and northwestern Greenland (Denyszyn, 2008), and to a compilation of the Natkusiak basalts and sills from Victoria Island (Bédard et al., 2016; Beard et al., 2017).

Whole-rock major-element chemistry for the Franklin basalts, sills and dykes reveals that the vast majority of samples are sub-alkaline, fall within the basalt/gabbro field in the Total Alkali-Silica diagram (LeBas et al., 1986) and overlap the Franklin Natkusiak compositions between 48–51% SiO_2 and 2–5% $Na_2O + K_2O$ (Fig. 3.4). Fig. 3.5 shows the geochemical variation within the Natkusiak Formation (from Bédard et al., 2016) as a function of stratigraphic height and indicates that most of the geochemical variations occur within the first 40 m of the stratigraphy corresponding to the V_0 unit. MgO decreases from 7.5 to 10% and TiO_2 increases from 1–1.8% within the V_0 unit, whereas the overlaying V_1 and V_2 units have constant MgO and TiO_2. Differentiation among the Franklin igneous suites is indicated by a trend of increasing TiO_2 with decreasing MgO (8.2 to 3.1%; Fig. 3.6A; $30 < Mg\# < 70$). The Fury and Hecla dykes, the Dybbol sill, the Coronation sills, the Kikiktat volcanics, a few dykes in Eastern Baffin Island, dykes and sills in northern mainland Canada and the Natkusiak basalts and sills in Victoria Island mostly yield low TiO_2 (0.8–2%) concentrations, whereas the Ellesmere and Devon islands dykes, northwestern Greenland dyke and sills have higher TiO_2 values (2–6%). Within the low-Ti igneous suite, the Kikiktat volcanics are the least differentiated samples (5.5–12% MgO; Fig. 3.6A), while the Fury and Hecla dykes are the most differentiated (3.1–8.2% MgO). TiO_2 concentrations appear to gradually increase from northeastern Alaska to northeastern Canada and northwestern Greenland.

A plot of Ni vs Zr (Fig. 3.6B) highlights the crystal fractionation and partial melting trends of the rocks as a consequence of the compatible behavior of Ni and the incompatible behavior of Zr during magmatic differentiation (after Cocherie, 1986). The diagram indicates that the high- and low-Ti suites follow different partial melting trends with the low-Ti suites plotting between 40–130 ppm Ni and 60–130 ppm Zr, but that the Ellesmere, Devon, Thule dykes and sills and a few Eastern Baffin dykes are more enriched in Zr (130–590 ppm).

Partial melting and fractionation vs crustal input are investigated with a plot of Zr/Y vs Th/Nb (Fig. 3.6C). The Zr/Y ratio is suggestive of a deep mantle source because Zr and Y are strongly fractionated during

partial melting in the presence of garnet (Fitton et al., 1997), whereas the Th/Nb ratio indicates the enrichment of incompatible elements (Pearce, 2008). Thus, low Zr/Y ratios are related to higher degrees of partial melting in the absence of garnet, and high Th/Nb ratios are indicative of crustal enrichment. The low-Ti Franklin rocks correspond to low Zr/Y (<1.85) ratios associated with normal and enriched mid-ocean-ridge basalts (N-, and E-MORB), suggesting high degrees of partial melting and low fractionation, in contrast to the high-Ti rocks that range values higher Zr/Y (>1.85) ratios implying a lower degree of partial melting and higher fractionation. Th/Nb ratios are the highest in the Kikiktat and the lowest in northeastern Canada and northwestern Greenland. A similar trend is evident in Fig. 3.6D (adapted from Pearce and Norry, 1979), where low-Ti rocks are distinct from the high-Ti group and appear to be characterized by a less incompatible enriched magma to those of the high-Ti group. A plot of the samples in an AFM diagram (Fig. 3.7) indicates that the Franklin rocks follow an iron enrichment trend produced by the fractionation of Mg-rich olivine and pyroxenes.

Mantle sources and degree of partial melting can be investigated using the Pearce (2008) diagram in Fig. 8A which confirms that the Franklin rocks are defined by two compositional types. The low-Ti group essentially plots within the shallow melting, while the high-Ti group fall within a deeper melting field. This is further illustrated by the Dy/Yb vs Ce/Yb plot (Fig. 3.8B; Haase and Dewey, 1996), where high Dy/Yb and Ce/Yb are indicative of an enriched source with a low degree of partial melting from a garnet lherzolitic mantle, whereas low Dy/Yb and Ce/Yb ratios are related to an enriched mantle source with high degrees of partial melting from a spinel lherzolitic mantle. The Fury and Hecla dykes and Dybbol sill plot with most of the Franklin rocks, with low Dy/Yb and Ce/Yb ratios, indicating a ~5–15% (incongruent dynamic melting model) degree of partial melting of a primitive mantle source in spinel facies field. Data from the Natkusiak basalts and sills that extend to higher Dy/Yb ratios (at almost constant Ce/Yb ratios) are suggestive of partial melting of an enriched source ranging from the spinel to garnet fields. In contrast, the intrusions from Ellesmere and Devon islands and Greenland have high Dy/Yb and Ce/Yb ratios, consistent with a lower (4–15%; incongruent dynamic melting model) degree of partial melting of an enriched source in the garnet stability zone. The Kikiktat volcanics and a few dykes of Eastern Baffin Island form a distinct group with slightly higher Ce/Yb ratios. Fig. 3.8C demonstrates that the Kikiktat volcanics are the most crustally contaminated rocks of the Franklin suite ($-12.2 < \varepsilon Nd_{718\ Ma} < 0.7$) that could lead to higher Ce/Yb ratios, whereas all other rocks have relatively higher initial εNd values ($0 < \varepsilon Nd_{718\ Ma} < 6$) that are consistent with a lower degree of crustal contamination.

Trace-element concentrations normalized to Chondrites and Primitive Mantle (PM; Sun and McDonough, 1989; McDonough and Sun, 1995) are presented in Fig. 3.9. The range of the REE profiles for the Franklin dykes, lavas, and sills is depicted using selected profiles to avoid cluttering and bracketed by the upper and

lower REE profiles for a given group. The low-Ti group has La contents ranging from 19─46 x chondrite and La/Yb ratios of 2.3–2.7, are light (LREE) enriched, and displays relatively sub-parallel REE profiles comparable to those of the Natkusiak basalts and sills profiles (Figs. 9A and 9C). Contrastingly, the high-Ti group shows predominantly steep REE profiles, with LREE and middle (MREE) enrichments similar to OIB, but with higher HREE, and distinct from other Franklin rocks with La contents ranging from 79─170 x chondrite and La/Yb (4.5–9.6) ratios. The low-Ti group is characterized by trace element patterns (Figs. 9B and 9D) that are characterized by a moderate enrichment in incompatible elements (Th, U) and strong depletions (Nb, Ta), whereas the high-Ti group show strongly enriched profiles with little Nb depletion.

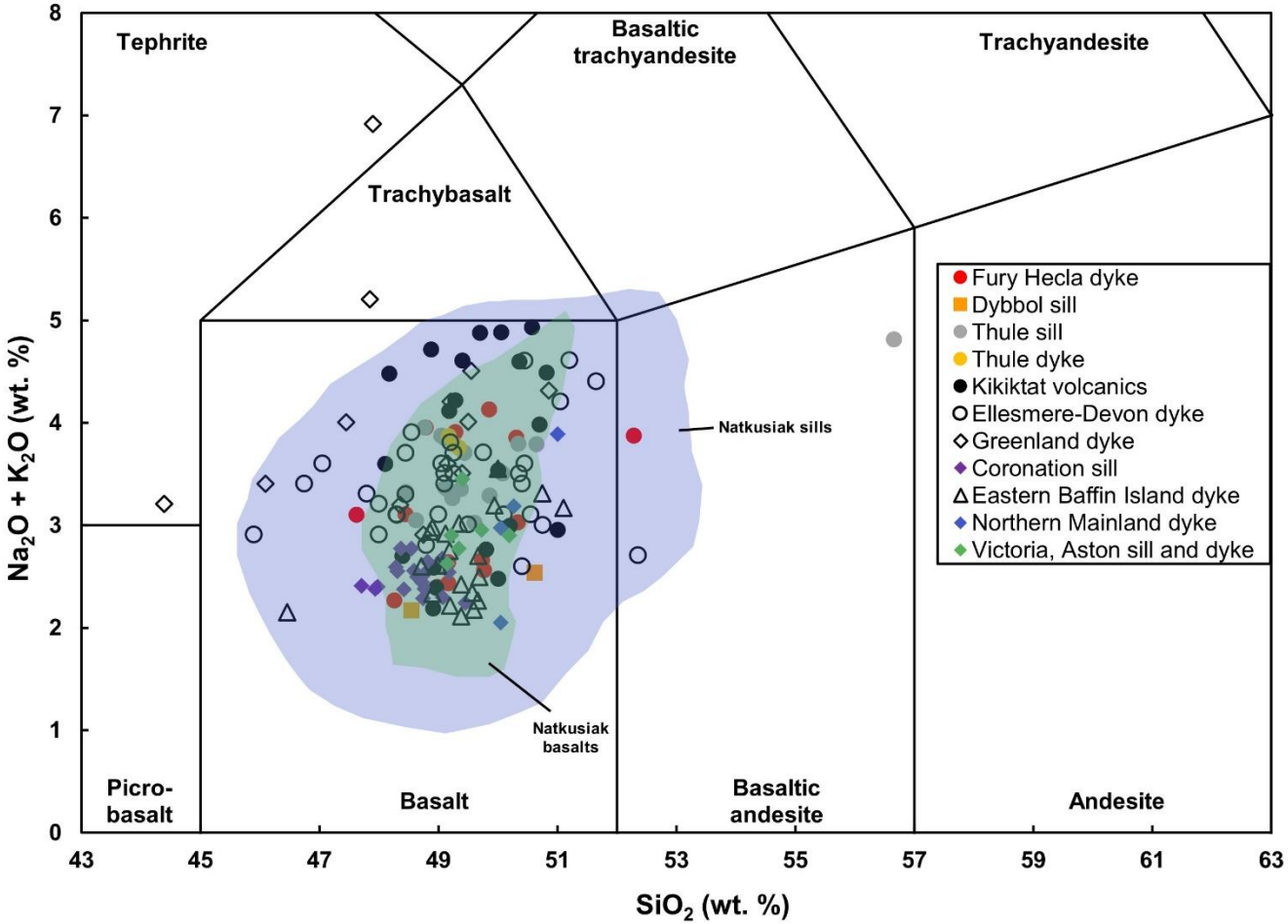

Figure 3.4: Total-alkali silica diagram from LeBas et al. (1986). The Fury and Hecla dykes, the Dybbol sills, and the Thule sills and dykes are from this study. The Kikiktat volcanics are from Cox et al. (2015). The Ellesmere-Devon dykes and the Greenland dykes are from Denyszyn (2008). The Coronation sills are from Shellnutt et al. (2004). The Eastern Baffin Island dykes, the northern mainland dykes, the Victoria dykes, and the Aston sill are from Ernst and Buchan (2010). The Natkusiak basalts and sills are from Bédard et al. (2016).

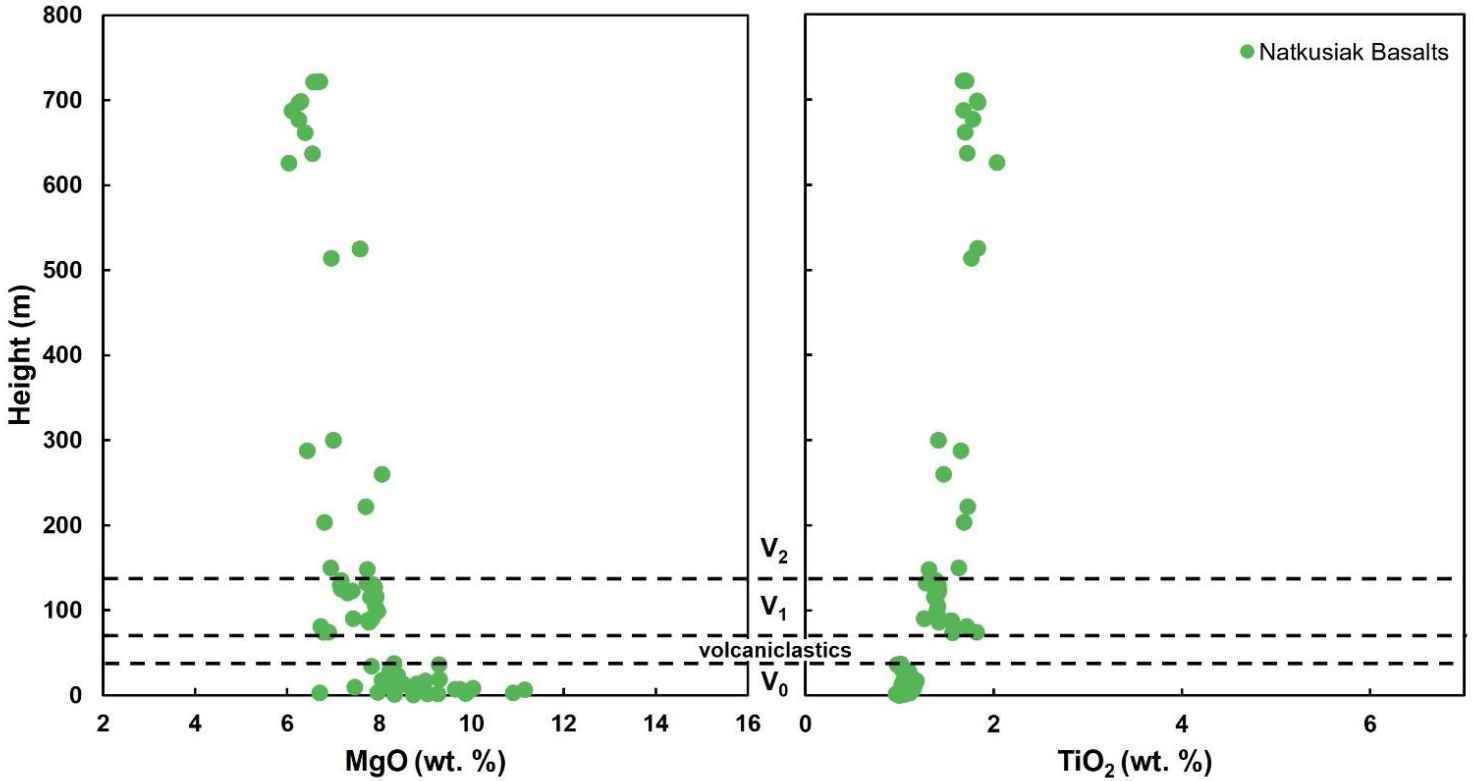

Figure 3.5: MgO and TiO_2 variations with stratigraphic height in the Natkusiak Formation (data from Bédard et al., 2016).

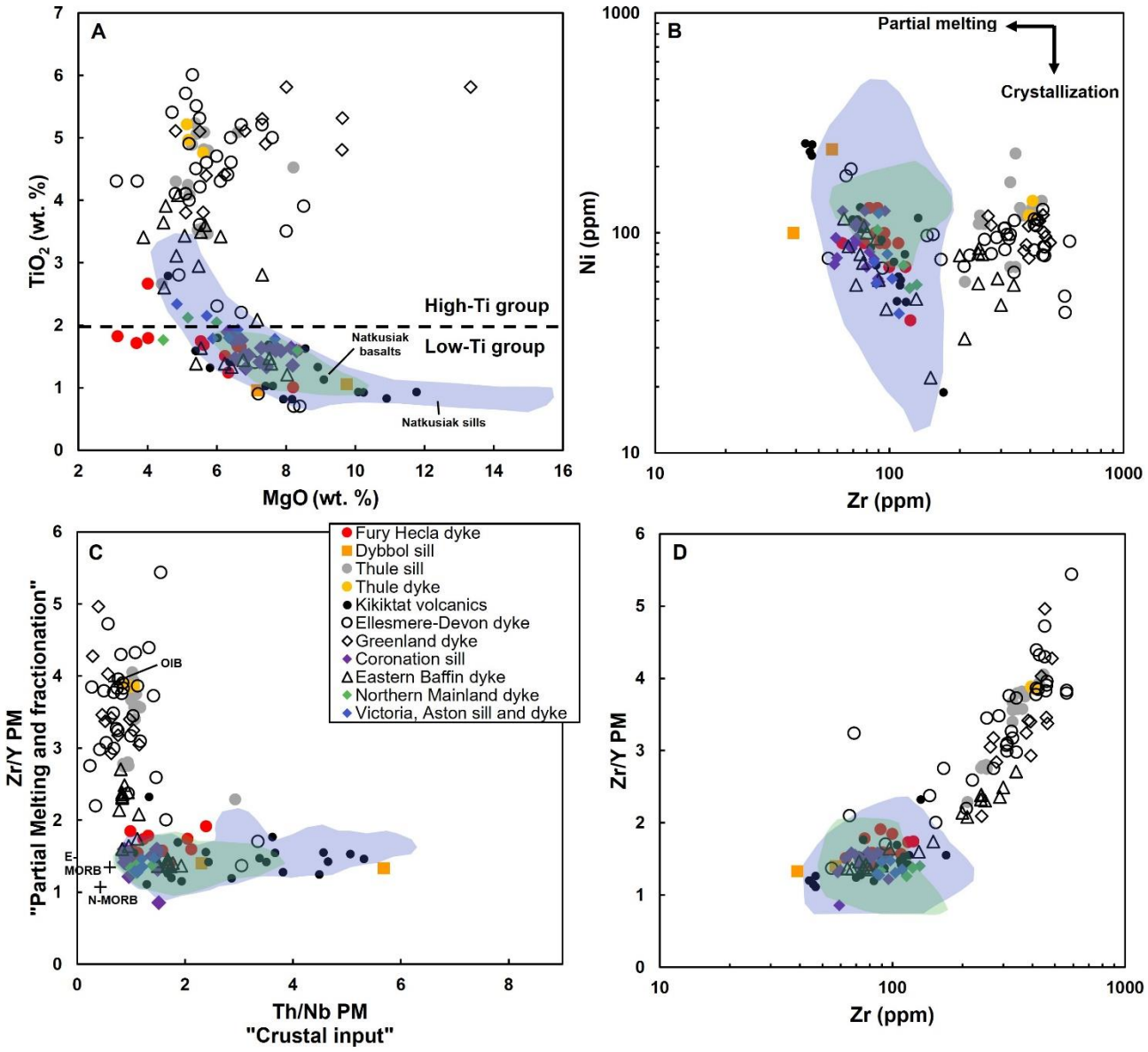

Figure 3.6: Major and trace elements variations diagrams of the Franklin igneous suites. A is the TiO_2/MgO plot. B shows variations of Ni vs Zr after Cocherie (1986). C indicates variations of Zr/Y (partial melting and fractionation) vs Th/Nb (crustal input). D is the classification diagram modified after Pearce and Norry (1979) with variations of Zr/Y vs Zr. OIB, E-, N-MORB, and primitive-mantle (PM) values are from Sun and McDonough (1989).

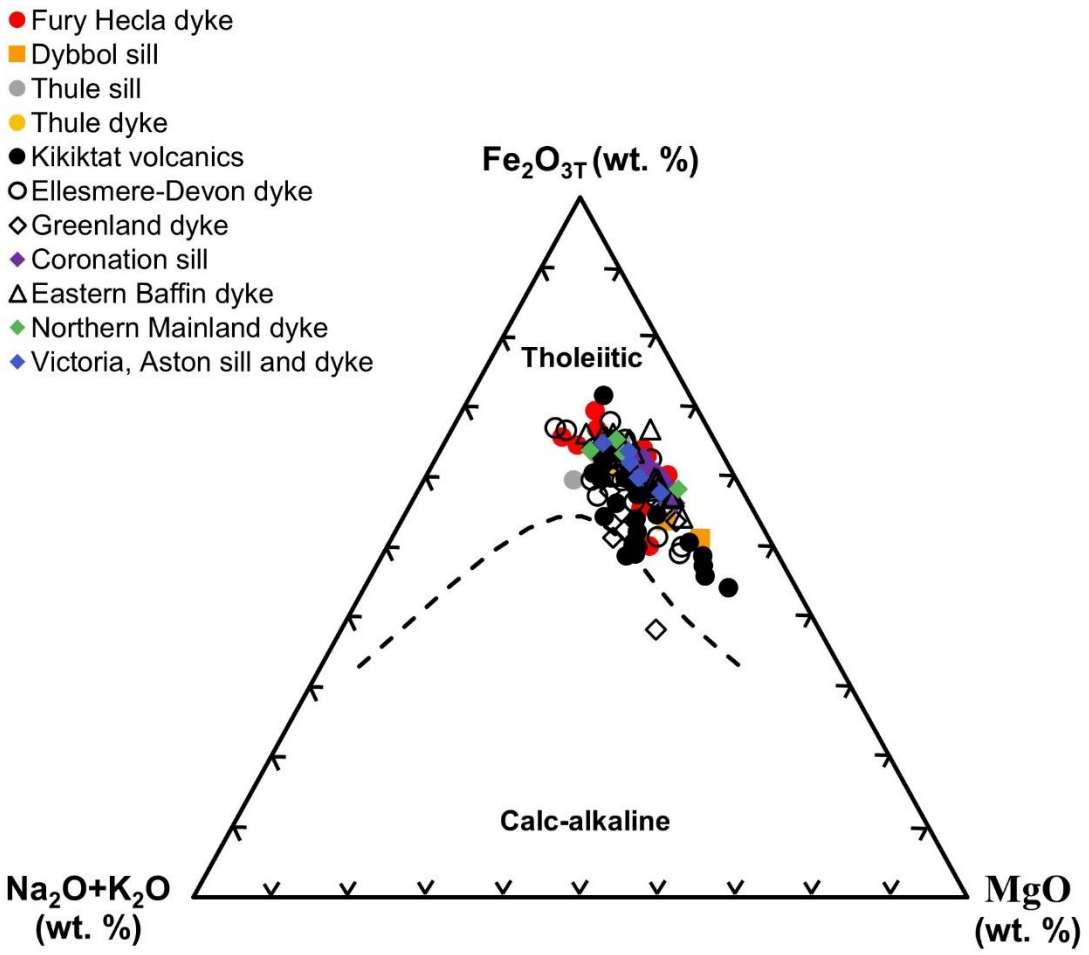

Figure 3.7: Alkali ($Na_2O + K_2O$), Fe_2O_{3T}, MgO (AFM) diagram. Dashed line represents the separation between the tholeiitic and calc-alkaline sub-fields (after Irvine and Baragar, 1971).

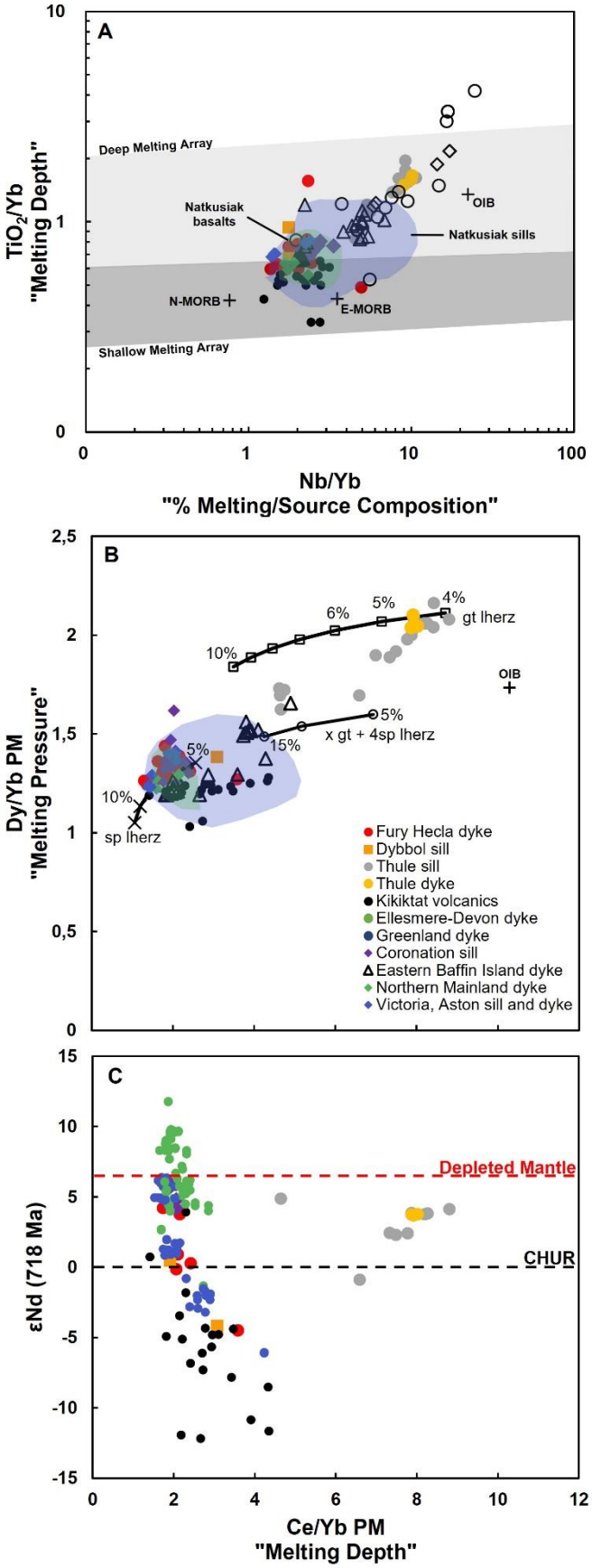
A
Deep Melting Array
Natkusiak basalts
Natkusiak sills
OIB
N-MORB
E-MORB
Shallow Melting Array
TiO2/Yb "Melting Depth"
Nb/Yb "% Melting/Source Composition"
B
4%
5%
6%
10%
gt lherz
OIB
5%
x gt + 4sp lherz
15%
5%
10%
sp lherz
Fury Hecla dyke
Dybbol sill
Thule sill
Thule dyke
Kikiktat volcanics
Ellesmere-Devon dyke
Greenland dyke
Coronation sill
Eastern Baffin Island dyke
Northern Mainland dyke
Victoria, Aston sill and dyke
Dy/Yb PM "Melting Pressure"
C
Depleted Mantle
CHUR
εNd (718 Ma)
Ce/Yb PM "Melting Depth"

Figure 3.8: Major, trace element ratios and Nd diagrams. A is the geochemical proxy diagram for melting depth (TiO_2/Yb) and source composition (Nb/Yb) after Pearce (2008). B and C represent the variations of Dy/Yb and $\varepsilon Nd_{718\ Ma}$ vs Ce/Yb. Black lines in B indicate the incongruent dynamic melting model (Zou and Reid, 2001) of garnet lherzolite (gt lherz), spinel lherzolite (sp lherz) and a mixture of 1x garnet and 4x spinel lherzolite (1x gt + 4x sp lherz; Greene et al., 2009). Melt reaction coefficients of spinel lherzolite and garnet lherzolite are from Kinzler and Grove (1992), and Walter (1998). Partition coefficients (Table A3.3) are from Salters and Stracke (2004), and Shaw (2000). Source mineralogy (PM is from Sun and McDonough, 1989) for spinel lherzolite (0.18cpx:0.27opx:0.52ol:0.03sp) is from Kinzler (1997), and for garnet lherzolite (0.34cpx:0.08opx:0.53ol:0.05gt) is from Salters and Stracke (2004). Data are similar to previous figures and are supplemented with those of Beard et al. (2017). OIB, E-, N-MORB, and Primitive Mantle (PM) values are from Sun and McDonough (1989). Depleted Mantle line is from DePaolo (1981).

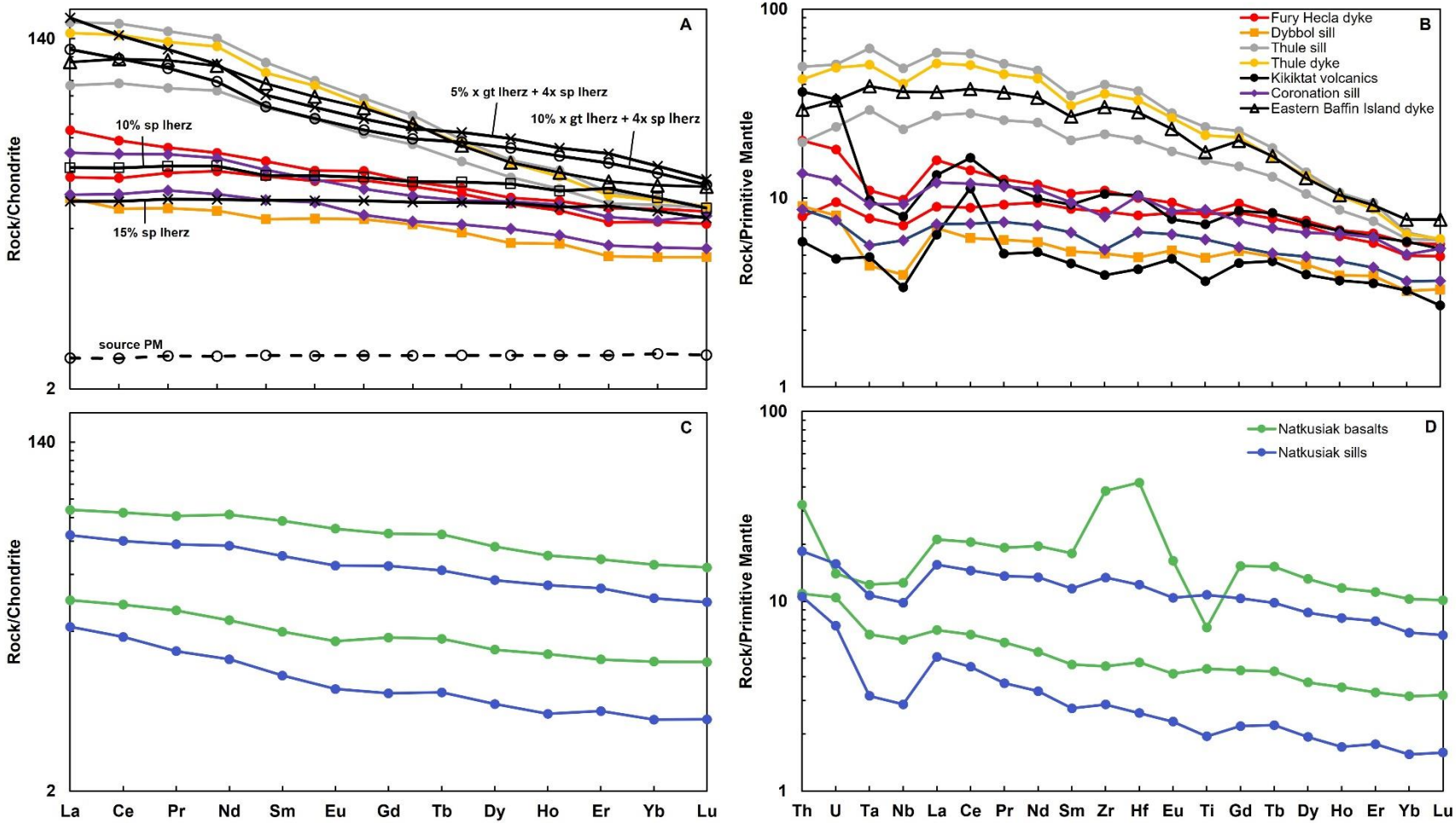

Figure 3.9: Chondrite and Primitive Mantle normalized diagrams of selected Franklin data. Chondrite normalized values are from McDonough and Sun (1995), and Primitive Mantle values are from Sun and McDonough (1989). A and B are the diagrams of the Franklin igneous suites in Alaska, Canada, and Greenland. C and D are the diagrams of the Natkusiak basalts and sills in Victoria Island. The Franklin data are from Beard et al. (2017). The profiles plotted depict the maximum and minimum profiles from a given area. The melting model used in 9A is similar to Fig. 3.8B. Primitive-mantle source is from Sun and McDonough (1989).

3.5 Discussion

3.5.1 Evidence for low-, and high Ti provinces associated with the Franklin LIP

The addition of Franklin-related suites from the eastern Arctic reveals that the Franklin large igneous province is defined by a larger TiO_2 range (0.8–6 wt. %) than the 0.8–2% documented in the western Arctic (Dostal et al., 1986; Shellnutt et al., 2004; Cox et al., 2015; Beard et al., 2017). The TiO_2 contents of the Franklin igneous suites increase from low values in the Kikiktat volcanics in the west, to intermediate contents in dykes in north-central Canada, the Natkusiak basalts and sills, dykes and sills in Baffin Island, and reach their highest TiO_2 compositions in dykes and sills in Ellesmere, Devon, eastern Baffin islands and northwestern Greenland.

Low-, and high-Ti provinces are also observed in other LIPs. The Franklin igneous event yields higher TiO_2 compositions than those of the Emeishan, Deccan, Karoo and CAMP LIPs, which generally yield low-Ti suites with compositions between 0.5–2% and high-Ti suites ranging from 2–4.5% (Xu et al., 2001; Melluso et al., 2006; Jourdan et al., 2007; Marzoli et al., 2018).

3.5.2 Fractional crystallization

Although the TiO_2 content of the Eastern Arctic rocks is higher to those of the Western Arctic rocks, the Franklin suites do not present relevant correlations between the TiO_2 and MgO (Fig. 3.6A), indicating that fractional crystallization probably does not explain the distinction between these two geochemical suites. The Franklin suites show they have a similar composition in Fe_2O_{3T} (Fig. 3.7) interpreted as a tholeiitic fractionation, but the Fury and Hecla, Baffin Island dykes and Ellesmere, Devon and Greenland intrusions record an increase in TiO_2 which is not resulting from fractionation. The fractionation appears to have not play a sufficient role in the differentiation of the Franklin rocks (Figs. 3.6B–C) to explain the degree of enrichment in TiO_2 and incompatible elements, increasing with distance from the inferred source towards the northeast.

3.5.3 Contamination

Low-Ti Franklin rocks have trace element profiles (Figs. 3.9B and 9D) with intermediate enrichment in Th, and little Nb and Ta depletions, the most prominent being those of the Kikiktat volcanics and Dybbol sill. High Th/Nb ratios are indicative of crustal assimilation (Fig. 3.10; Taylor and McLennan, 1995) and are supported by lower εNd_i values reflecting a slight enrichment such as seen in the Kikiktat volcanics (Cox et al., 2015) that are the most contaminated of the Franklin suites. The high-Ti suites have absence of depletions in Nb and Ta (Figs. 9B and 9D), which is consistent with higher εNd values that indicate a lower degree of crustal contamination. Additional εNd data (Cox et al., 2016) from the Cadogan Glacier dyke on

Ellesmere Island ($\varepsilon Nd_{718\ Ma}$ = +4.2), the Eastern Glacier dyke on Devon Island ($\varepsilon Nd_{718\ Ma}$ = +7.8), the Kap Powlett ($\varepsilon Nd_{718\ Ma}$ = +3.2) and Qaanaaq ($\varepsilon Nd_{718\ Ma}$ = -1.1) dykes in Greenland are similar to our εNd data in Greenland. The degree of contamination appears to be higher in the west as observed in the Kikiktat volcanic in Alaska and decreases towards the east. Cox et al. (2015) estimated that the degree of crustal assimilation in the Kikiktat volcanics is ~26% (explained as involving possible different types of contaminants), whereas Beard et al. (2017) inferred that the Natkusiak Type 1 sills incorporated up to 10% of Slave Province granodiorite basement rocks and 10% of the Shaler Supergroup metasedimentary rocks, and that the Type 2 sills assimilated up to 5% of the same granitoid rocks. We estimate that most of the Fury and Hecla dykes have digested between 20–30% of the Fury and Hecla basement mix. The basement mix represents an average derived from the compositions of meta-tonalite, meta-monzogranite and meta-sedimentary semi-pelite rocks representing that dominate the Fury and Hecla basement; Table A3.4), whereas the Thule dykes and sills would have assimilated 5–10% of basement rocks (Fig. 3.10). Crustal contamination drives TiO_2 and εNd_i to lower values, but even the least contaminated Natkusiak basalts exhibit Ti contents lower than those of Ellesmere/Thule samples, suggesting that this process is likely not responsible for low and high TiO_2 compositions observed across the Franklin LIP.

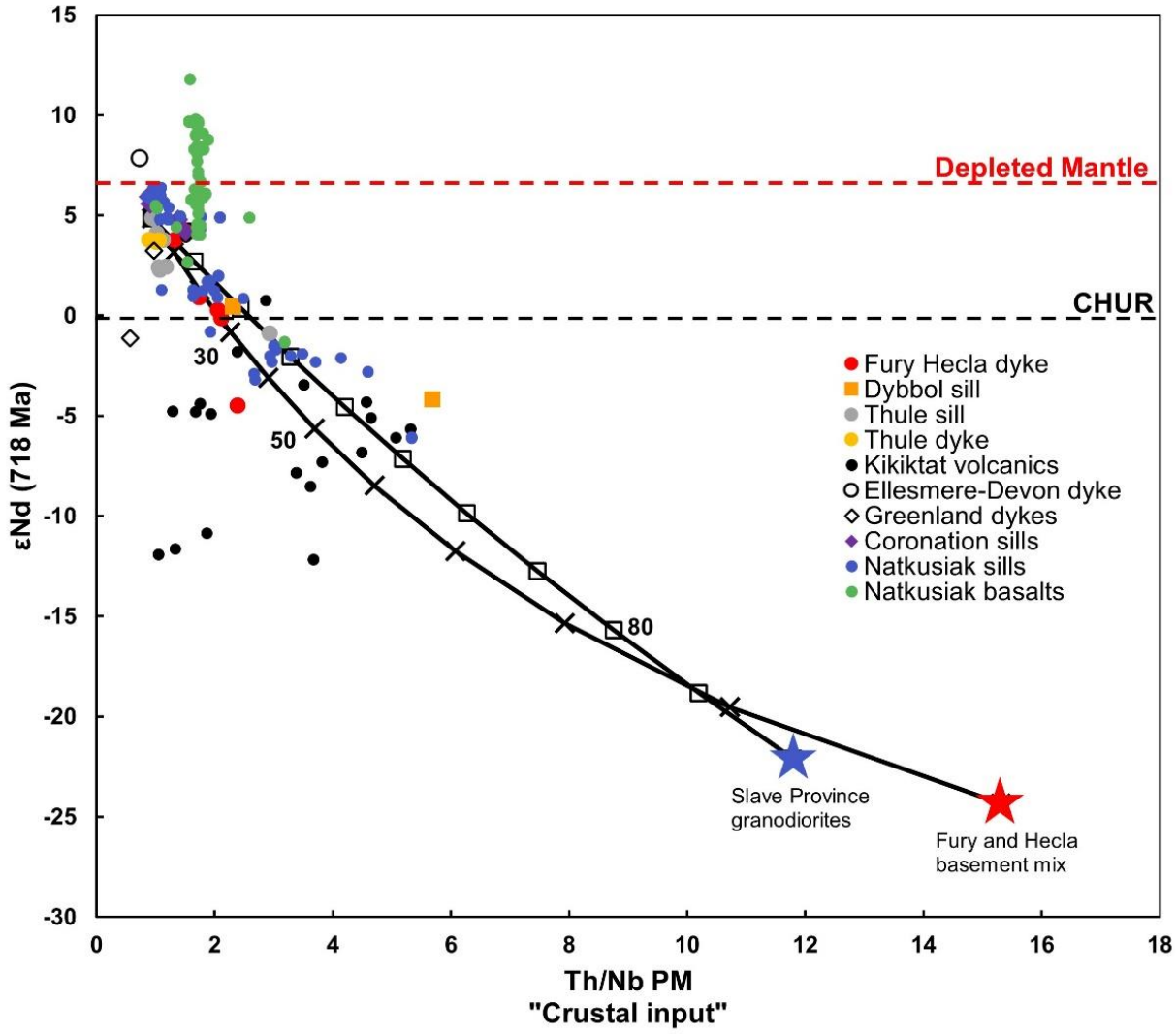

Figure 3.10: Modelling of crustal contamination in the Franklin rocks with initial εNd isotopic compositions vs. Th/Nb ratios. Mixing line with diamond marks is calculated using a mix of trace elements and isotopic composition of Slave Province granodiorites (Yamashita et al., 1999), and a Thule sill. Mixing line with x marks uses a mean of trace elements and isotopic composition of the representative Fury and Hecla basement rocks (this study, M152, C074, P043 and P110 geochemical compositions are provided in Table A3.4). The curves are marked at 10% intervals. Primitive-mantle values are normalized are from Sun and McDonough (1989).

3.5.4 Partial melting and mantle sources of the Franklin LIP

The degree of enrichment in light-REE and incompatible elements that is observed across the Franklin rocks cannot be explained by the limited degree of crystal fractionation of olivine and pyroxene that led to the Fe and Ti enrichment trend. Thus, neither assimilation nor fractional crystallization are responsible for the overall low and high TiO_2 contents of the Franklin LIP. Alternatively, as Ti is more incompatible in the garnet lherzolitic mantle and that garnet is the stable phase in the mantle at ~100 km depth, it is probable that low-Ti rocks were produced from partial melting of a shallow spinel-bearing lherzolitic mantle, and that high-Ti rocks were produced from more a deeper garnet lherzolitic mantle source (Arndt et al., 1993; Xu et al. 2001; Jourdan et al., 2007; Wang et al., 2007; Prasanth et al., 2019). Given the similar ranges of Nd isotope composition observed in the Ellesmere, Devon and Greenland dykes and sills we can assume that rocks have a similar depleted mantle source as the Natkusiak, Coronation area. The clear difference in Zr concentrations (Fig. 3.6B) also supports that enrichment in incompatible elements occurs between the low-, and high-Ti groups.

Chondrite-normalized light REE-enriched REE profiles (Fig. 3.9), and high TiO_2/Yb, Dy/Yb, and Ce/Yb ratios (Figs. 3.8A and 8B) for the high-Ti group are consistent with magmas derived from a low degree of melting as illustrated by a 5% degree of melting of a garnet and spinel lherzolite (incongruent dynamic melting model). This suggests that the high-Ti rocks originate from a deeper mantle source. Thus, the enrichment in incompatible elements (e.g. Ti) and depletion in compatible elements (e.g. Yb) can be explained by an onset of partial melting in the garnet stability field in the mantle. Contrastingly, the low-Ti rocks have flatter REE, unfractionated HREE patterns (Figs. 9) with low TiO_2/Yb, Dy/Yb, Ce/Yb ratios (Figs. 8A and 8B) consistent with higher degrees of melting (10–15%) of spinel lherzolite, indicating that the low-Ti group formed under conditions of shallow melting and high degrees of partial melting characteristic of the plume head (Beard et al., 2017). The low Ti, Ca, and Fe abundances in the Kikiktat volcanics were also modeled as products of melting of a shallow harzburgitic mantle involving a subcontinental lithospheric mantle (~1.6 kbar or ~5 km depth) as a result of significant crustal thinning (Cox et al., 2015). One Fury and Hecla dyke appears to be consistent with a partial melting of a mix garnet and spinel lherzolitic source (associated with the Thule samples), whereas others are rather consistent with a partial melting from a spinel lherzolitic source (associated with the Natkusiak samples). Thus, melting of a shallow spinel lherzolitic mantle produced low-Ti rocks proximal to the plume focal area (Natkusiak) and eastwards to the Fury and Hecla basin, whereas melting of a deeper garnet lherzolitic mantle formed the more distal high-Ti rocks in northeastern Laurentia (Ellesmere, Devon and Thule).

Previous studies suggested that higher degrees of partial melting in the Natkusiak area can be explained by its proximity to the plume focal point on Melville Island (Denyszyn et al., 2009a), producing the so-called

high Ti magmas (1.2–2%) in Natkusiak, whereas the low-Ti magmas of the Kikiktat would be a product of melting at a greater distance from the Franklin plume head (Cox et al., 2015; Beard et al., 2017). Although high degrees of partial melting are consistent with proximity to the plume head (Campbell and Griffiths, 1990; White and McKenzie, 1995; Sobolev et al., 2011), the relationship between distance and low-Ti magma does not seem tenable given that distal higher Ti compositions are found in northeastern Laurentia. The present-day distance between the plume focus and Natkusiak is ~330 km, while the distance to eastern Ellesmere and the Thule basin is 900–1200 km, and 1700–1900 km to eastern Baffin Island. However, the hot and primitive mantle suggested by Cox et al. (2015) would be plausible for producing magmas in proximity to the plume.

3.5.5 Relationships between the Arctic Laurentia tectonics and geochemical Ti provinciality

The association between low-Ti provinces derived from shallow spinel lherzolite with high degrees of partial melting and high-Ti provinces characterized by low degrees of melting and a deep-seated garnet lherzolite source have been interpreted to reflect the presence of thin and thick lithospheres, respectively (Arndt et al., 1993; Gibson et al., 1995; Jourdan et al., 2007; Niu et al., 2011; Lai et al., 2012; Srivastava and Samal, 2019). The thickness of the lithosphere affects the depth and degree of partial melting of the mantle (McKenzie and Bickle, 1988; Ellam, 1992; Saunder et al., 1992), and the geochemistry of LIP magmatism. For example, LIP magmas with low-Ti magmas is found mostly in areas underlain by post-Archaean crus, whereas the high-Ti magmas have been associated with cratonic regions (Sweeney and Watkeys, 1990; Marzoli et al., 2018). The large geographical extent of the Franklin LIP from northeastern Alaska to northwestern Greenland provides a unique opportunity to observe the influence of lithosphere thickness on the geochemistry of the Franklin magmas. In the following section, we discuss how the mantle/crust tectonic setting in Arctic Laurentia can explain the wide range of Ti compositions.

There is a general lack of geophysical studies indicating lithospheric thickness across the North American Arctic. However, the studies that do exist indicate that the lithospheric thickness in the western portion that encompasses the Kikiktat–Coronation Gulf and Victoria Island regions is thinner than the eastern Bylot basins region. O'Driscoll and Miller (2015) found that lithospheric thickness in the North Slope region of Alaska is thin (80–90 km), reflecting a thinning of the lithosphere associated with the formation of the Cordilleran Orogen, and that this thin lithosphere persists eastwards through the Yukon Territory. Lithosphere thickness increases rapidly east of the Rocky Mountain front towards the Coronation Gulf and Victoria Island regions (Schaeffera and Lebedeva, 2014). Lithosphere thickness is greater east of the Coronation Gulf region, but appears to stabilize from just east of the Coronation Gulf to Greenland (Darbyshire, 2003; Schaeffera and Lebedeva, 2014). Although these thicknesses undoubtedly bring robust

information on the lithospheric architecture at present time, the tectonic settings existing at 720 Ma should be taken into consideration as lithosphere thickness may have changed over time.

The northwestern Laurentian lithosphere has a more active tectonic history than the northeastern Laurentian lithosphere. During the disaggregation of Rodinia, the northwestern margin of Laurentia separated from Australia/Mawsonland and North China at ca. 775 Ma due to extension related to the Gunbarrel LIP (Harlan et al., 2003; Li et al., 2008; Swanson-Hysell, 2021), and subsequently drifted away from the Siberia due to extension related to the Franklin LIP at ca. 720 Ma (Heaman et al., 1992; Rainbird et al., 1998; Macdonald et al., 2012; Swanson-Hysell, 2021). These rifting/extension episodes produced a thinner lithosphere, provoking mantle melting at a shallower depth that resulted in the production of low-Ti magmas. The absence of rifting in the eastern Arctic likely preserved a thicker lithosphere that led to deeper melting, resulting in magmas that formed a high-Ti province. A representation of the low-, and high-Ti provinces within the paleoreconstruction of Rodinia at 720 Ma is proposed in Fig. 3.11. Magmas of the two provinces are believed to have formed contemporaneously given the ages of the rocks are comparable in both geographic areas (Heaman et al., 1992; Macdonald et al., 2010; c.f.; chapter two; Dufour et al., submitted).

It should be noted that the exact position of the North Slope subterrane (Kikiktat volcanics) during the rifting of Rodinia is the subject of debate. Studies have placed the North Slope terrane in the vicinity of Victoria Island in the early Mesozoic (Gottlieb et al., 2014). However, inconsistencies in stratigraphic correlations with the Shaler Supergroup led Macdonald et al., (2009) to infer that the North Slope subterrane was displaced by sinistral movement along the Canadian Arctic margin. The petrogenetic differences between the Kikiktat and the Natkusiak basalts led Cox et al. (2015) and Strauss et al. (2019) to suggest that at 720 Ma, the North Slope subterrane was in fact closer to Ellesmere Island. Our interpretation of the Kikiktat volcanics as part of the low Ti province is consistent with the position of the North Slope terrane in western Laurentia adjacent to Victoria Island rather than in eastern Laurentia.

Thus, tectonic activity (ca. 720 Ma) in western Laurentia would have favored the thinning of the lithosphere facilitating melting conditions within a spinel lherzolitic mantle below northwestern Laurentia and the North Slope subterrane. The lack of tectonic activity in eastern Laurentia preserved a thicker lithosphere in eastern Baffin Island, Ellesmere, Devon islands and northwestern Greenland, provoking deeper melting conditions in a garnet lherzolitic mantle.

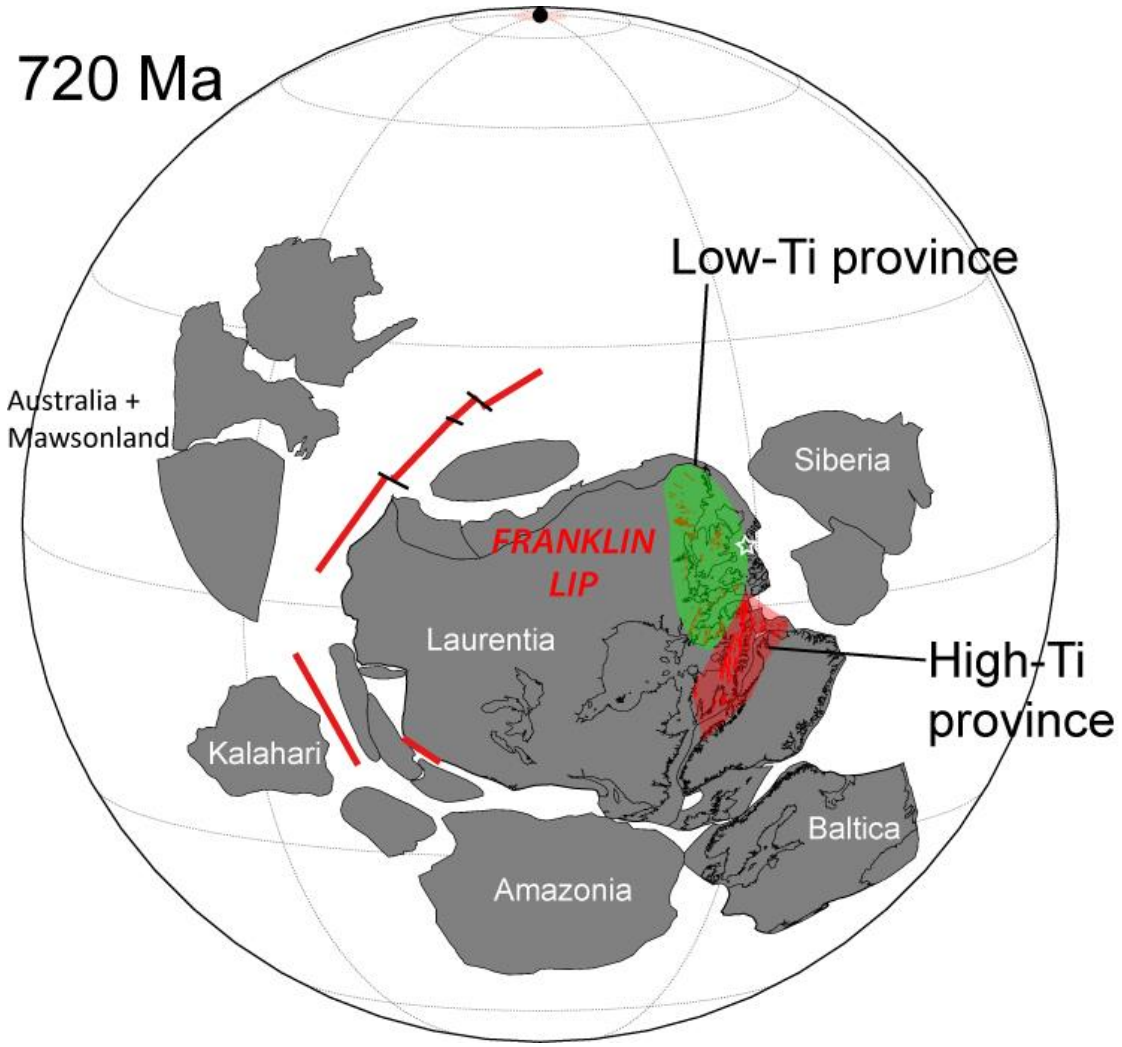

Figure 3.11: Paleogeographic reconstruction of Rodinia at 720 Ma is modified after Swanson-Hysell (2021) integrating the low-, and high-Ti provinces of the Franklin LIP. Open white star is the proposed plume location (Denyszyn et al., 2009a).

3.6 Conclusion

A new geochemical compilation is presented indicating that the Franklin rocks of Kikiktat, Natkusiak, north-central Canada and Fury and Hecla are characterized by low- (<2%) TiO_2 compositions while dykes and sills from Ellesmere, Devon, eastern Baffin islands and northwestern Greenland are defined by high (2–6%) TiO_2. The low-Ti group is depleted in LREE and incompatible elements, reflecting high degrees of partial melting of a spinel lherzolitic mantle source, whereas the high-Ti group is enriched in LREE and incompatible elements, implying low degrees of partial melting of a garnet lherzolitic mantle source. Similar Nd isotopic data shows that the rocks largely escaped crustal contamination, and that they essentially derived from a depleted mantle. Break-up of the Rodinian supercontinent might have facilitated the thinning of the northwestern Laurentia lithosphere creating conditions of high degrees of partial melting, in contrast to an unaffected thicker cratonic lithosphere in northeastern Laurentia, favoring low degrees of partial melting.

3.7 Acknowledgments

The Canada-Nunavut Geoscience Office, Blue Jay Mining PLC, and Thule Air Force Base are thanked for logistical support in the field. We thank the Fury and Hecla team, Wilder Greenman, Angelo dos Santos, and Tianran Zhang for their assistance in Greenland. This work is part of the PhD program of the lead author, which is supported by a Strategic Partnership Grant to Galen Halverson and Ross Stevenson from the Natural Sciences and Engineering Research Council of Canada.

3.8 References

Arndt, N. T., Czamanske, G. K., Wooden, J. L. et Fedorenko, V. A. (1993). Mantle and crustal contributions to continental flood volcanism. Tectonophysics, 223(1-2), 39–52.

Bas, M. L., Maitre, R. L., Streckeisen, A., Zanettin, B. et IUGS Subcommission on the Systematics of Igneous Rocks. (1986). A chemical classification of volcanic rocks based on the total alkali-silica diagram. Journal of petrology, 27(3), 745–750.

Baragar, W. R. A. (1976). The Natkusiak Basalts, Victoria Island, District of Franklin, in Report of Activities: Geological Survey of Canada Paper 76–1A, 347–352.

Beard, C. D., Scoates, J.S., Weis, D., Bédard, J.H. et Dell'Oro, T.A. (2017). Geochemistry and origin of the Neoproterozoic Natkusiak flood basalts and related Franklin sills, Victoria Island, Arctic Canada; Journal of Petrology, v. 58, issue 11, 2191–2220.

Bédard, J. H., Naslund, H. R., Nabelek, P., Winpenny, A., Hryciuk, M., Macdonald, W., Hayes, B., Steigerwaldt, K., Hadlar, T., Rainbird, R., Dewing, K. et Girard, É. (2012). Fault-mediated melt ascent in a Neoproterozoic continental flood basalt province, the Franklin sills, Victoria Island, Canada. Bulletin, 124(5-6), 723–736.

Bédard, J. H., Hayes, B., Hryciuk, M., Beard, C., Williamson, N., Dell'Oro, T.A., Rainbird, R. H., Prince, J., Baragar, W. R. A., Nabelek, P., Weis, D., Wing, B., Scoates, J. S., Naslund, H.R., Cousens, B., Williamson, M.-C., Hulbert, L.J., Montjoie, R., Girard, E., Ernst, R. et Lissenberg, C.J. (2016). Geochemical database of Franklin sills, Natkusiak basalts and Shaler Supergroup rocks, Victoria Island, Northwest Territories, and correlatives from Nunavut and the mainland; Geological Survey of Canada, Open File Report 8009, 11 p., URL <https://doi: 10.4095/297842>.

Bryan, S. E. et Ernst, R. E. (2008). Revised definition of large igneous provinces (LIPs). Earth-Science Reviews, 86(1-4), 175–202.

Buchan, K. L. et Ernst, R. E. (2021). Plumbing systems of large igneous provinces (LIPs) on Earth and Venus: Investigating the role of giant circumferential and radiating dyke swarms, coronae and novae and mid-crustal intrusive complexes. Gondwana Research, 100, 25–43.

Campbell, I. H. et Griffiths, R. W. (1990). Implications of mantle plume structure for the evolution of flood basalts. Earth and Planetary Science Letters, 99(1–2), 79–93.

Chandler, F. W. (1988). Geology of the late Precambrian Fury and Hecla Group, northwest Baffin Island, District of Franklin; Geological Survey of Canada, Bulletin 370, 30 p.

Cocherie, A. (1986). Systematic use of trace element distribution patterns in log-log diagrams for plutonic suites. Geochimica et Cosmochimica Acta, 50(11), 2517–2522.

Coffin, M. F. et Eldholm, O. (1994). Large igneous provinces: crustal structure, dimensions, and external consequences. Reviews of Geophysics, 32(1), 1–36.

Cox, G. M., Strauss, J. V., Halverson, G. P., Schmitz, M. D., McClelland, W. C., Stevenson, R. S. et Macdonald, F. A. (2015). Kikiktat volcanics of Arctic Alaska—Melting of harzburgitic mantle associated with the Franklin large igneous province. Lithosphere, 7(3), 275–295.

Cox, G. M., Halverson, G. P., Stevenson, R. K., Vokaty, M., Poirier, A., Kunzmann, M., Li, Z.-X., Denyszyn, S. W., Strauss, J. V. et Macdonald, F. A. (2016). Continental flood basalt weathering as a trigger for Neoproterozoic Snowball Earth. Earth and Planetary Science Letters, 446, 89–99.

Day, J. M. (2013). Hotspot volcanism and highly siderophile elements; Chemical Geology, v. 341, 50–74.

Darbyshire, F. A. (2003). Crustal structure across the Canadian High Arctic region from teleseismic receiver function analysis. Geophysical Journal International, 152(2), 372–391.

Dawes, P. R. (1997). The Proterozoic Thule supergroup, Greenland and Canada: history, lithostratigraphy and development. Geology of Greenland Survey Bulletin, 174, 1–150.

Dawes, P. R. (2006). Explanatory notes to the geological map of Greenland, 1:500 000, Thule, Sheet 5; Geological Survey of Denmark and Greenland, Map Series 2, 97 p.

Denyszyn, S. W. (2008). Paleomagnetism, geochemistry, and U–Pb geochronology of Proterozoic mafic intrusions in the High Arctic: Relevance to the Nares Strait problem (Doctoral dissertation, PhD thesis, University of Toronto, Toronto, Ont).

Denyszyn, S. W., Halls, H. C., Davis, D. W. et Evans, D. A. (2009a). Paleomagnetism and U–Pb geochronology of Franklin dykes in High Arctic Canada and Greenland: a revised age and paleomagnetic pole constraining block rotations in the Nares Strait region; Canadian Journal of Earth Sciences, 46(9), 689–705.

Denyszyn, S. W., Davis, D. W. et Halls, H. C. (2009b). Paleomagnetism and U-Pb geochronology of the Clarence Head dykes, Arctic Canada: orthogonal emplacement of mafic dykes in a large igneous province; Canadian Journal of Earth Sciences, 46(3), 155–167.

DePaolo, D. J. (1981). Neodymium isotopes in the Colorado Front Range and crust–mantle evolution in the Proterozoic. Nature, 291(5812), 193–196.

Dostal, J., Baragar, W. R. A. et Dupuy, C. (1986). Petrogenesis of the Natkusiak continental basalts, Victoria Island, Northwest Territories, Canada; Canadian Journal of Earth Sciences, v. 23, no. 5, 622–632.

Dufour, F., Stevenson, R. et Skulski, T. (2021). Geochemical comparison of Mackenzie and Franklin igneous mafic rocks in Nunavut, Northwest Territories and northwestern Greenland; *in* Summary of Activities 2020: Iqaluit, Canada-Nunavut Geoscience Office, 33–46.

Dufour, F., Davies, J. H. F. L., Greenman, W., Skulski, T., Halverson, G. P., Stevenson., R. (2022). New U-Pb CA-ID TIMS zircon ages implicate the Franklin LIP as the proximal trigger for the Sturtian Snowball Earth event. Manuscript submitted for publication.

Ellam, R. M. (1992). Lithospheric thickness as a control on basalt geochemistry. Geology, 20(2), 153–156.

Ernst, R. E. et Buchan, K. L. (1997). Giant radiating dyke swarms: their use in identifying pre-Mesozoic large igneous provinces and mantle plumes. Geophysical Monograph-American Geophysical Union, 100, 297–334.

Ernst, R. et Buchan, K.L. (2010). Geochemical database of Proterozoic intraplate mafic magmatism in Canada; Geological Survey of Canada, Open File 6016, 1 CD-ROM, URL <https://doi.org/10.4095/261831>.

Ernst, R. E., Bleeker, W., Söderlund, U. et Kerr, A. C. (2013). Large Igneous Provinces and supercontinents: Toward completing the plate tectonic revolution. Lithos, 174, 1–14.

Ernst, R. E., Hamilton, M. A., Söderlund, U., Hanes, J. A., Gladkochub, D. P., Okrugin, A. V., Kolotilina, T., Mekhonoshin, A. S., Bleeker, W., LeCheminant, A. N., Buchan, K. L., Chamberlain, K. R. et Didenko, A. N. (2016). Long-lived connection between southern Siberia and northern Laurentia in the Proterozoic. Nature Geoscience, 9(6), 464–469.

Ernst, R.E., Bond, D.P.G., Zhang, S.H., Buchan, K.L., Grasby, S.E., Youbi, N., El Bilali, H., Bekker, A. et Doucet, L.S. (2021). Large Igneous Province Record Through Time and Implications for Secular Environmental Changes and Geological Time-Scale Boundaries. In: R.E. Ernst, A.J. Dickson, A. Bekker (eds) Large Igneous Provinces: A Driver of Global Environmental and Biotic Changes, American Geophysical Union Geophysical Monograph 255, 3–26.

Fahrig, W. F., Christie, K. W. et Jones, D. L. (1981). Paleomagnetism of the Bylot basins: evidence for Mackenzie continental tensional tectonics; in Proterozoic basins of Canada, F.H.A. Campbell (ed.), Geological Survey of Canada, Paper 81-10, 303–312.

Fitton, J. G., Saunders, A. D., Norry, M. J., Hardarson, B. S. et Taylor, R. N. (1997). Thermal and chemical structure of the Iceland plume. Earth and Planetary Science Letters, 153(3–4), 197–208.

Gottlieb, E. S., Meisling, K. E., Miller, E. L. et Mull, C. G. G. (2014). Closing the Canada Basin: Detrital zircon geochronology relationships between the North Slope of Arctic Alaska and the Franklinian mobile belt of Arctic Canada. Geosphere, 10(6), 1366–1384.

Gibson, S. A., Thompson, R. N., Dickin, A. P. et Leonardos, O. H. (1995). High-Ti and low-Ti mafic potassic magmas: Key to plume-lithosphere interactions and continental flood-basalt genesis. Earth and Planetary Science Letters, 136(3–4), 149–165.

Greene, A. R., Scoates, J. S., Weis, D., Nixon, G. T. et Kieffer, B. (2009). Melting history and magmatic evolution of basalts and picrites from the accreted Wrangellia oceanic plateau, Vancouver Island, Canada. Journal of Petrology, 50(3), 467–505.

Greenman, J. W., Patzke, M., Halverson, G. P. et Ielpi, A. (2019). Updated stratigraphy of the Fury and Hecla Group of Melville Peninsula and northwestern Baffin Island, Nunavut, in Summary of Activities 2019: Iqaluit, Canada-Nunavut Geoscience Office, 37–50.

Greenman, J. W., Rooney, A. D., Patzke, M., Ielpi, A. et Halverson, G. P. (2021). Re-Os geochronology highlights widespread latest Mesoproterozoic (ca. 1090–1050 Ma) cratonic basin development on northern Laurentia. Geology, 49(7), 779–783.

Haase, K. M. et Devey, C. W. (1996). Geochemistry of lavas from the Ahu and Tupa volcanic fields, Easter Hotspot, southeast Pacific: Implications for intraplate magma genesis near a spreading axis. Earth and Planetary Science Letters, 137(1-4), 129–143.

Harlan, S. S., Heaman, L., LeCheminant, A. N. et Premo, W. R. (2003). Gunbarrel mafic magmatic event: A key 780 Ma time marker for Rodinia plate reconstructions. Geology, 31(12), 1053–1056.

Hayes, B., Lissenberg, C. J., Bédard, J. H. et Beard, C. (2015). The geochemical effects of olivine slurry replenishment and dolostone assimilation in the plumbing system of the Franklin Large Igneous Province, Victoria Island, Arctic Canada. Contributions to Mineralogy and Petrology, 169(2), 1–18.

Heaman, L. M., LeCheminant, A. N. et Rainbird, R. H. (1992). Nature and timing of Franklin igneous events, Canada: implications for a Late Proterozoic mantle plume and the breakup of Laurentia; Earth and Planetary Science Letters, v. 109, 117–131.

Hergt, J. M., Peate, D. W. et Hawkesworth, C. J. (1991). The petrogenesis of Mesozoic Gondwana low-Ti flood basalts. Earth and Planetary Science Letters, 105(1-3), 134–148.

Irvine, T. N. et Baragar, W. R. A. (1971). A guide to the chemical classification of the common volcanic rocks. Canadian Journal of Earth Sciences, 8(5), 523–548.

Jefferson, C. W. (1985). Uppermost Shaler Group and its contact with the Natkusiak basalts, Victoria Island District of Franklin. Geological Survey of Canada Current Research, 85, 103–110.

Jefferson, C. W., Nelson, W. E., Kirkham, R. V., Reedman, J. H. et Scoates, R. F. J. (1985). Geology and copper occurrences of the Natkusiak basalts, Victoria Island, District of Franklin. Geological Survey of Canada, Current Research, Part A, 203–214.

Jourdan, F., Bertrand, H., Schärer, U., Blichert-Toft, J., Féraud, G. et Kampunzu, A. B. (2007). Major and trace element and Sr, Nd, Hf, and Pb isotope compositions of the Karoo large igneous province, Botswana–Zimbabwe: lithosphere vs mantle plume contribution. Journal of Petrology, 48(6), 1043–1077.

Kinzler, R. J. (1997). Melting of mantle peridotite at pressures approaching the spinel to garnet transition: Application to mid‐ocean ridge basalt petrogenesis. Journal of Geophysical Research: Solid Earth, 102(B1), 853–874.

Kinzler, R. J. et Grove, T. L. (1992). Primary magmas of mid‐ocean ridge basalts 1. Experiments and methods. Journal of Geophysical Research: Solid Earth, 97(B5), 6885–6906.

Li, Z. X., Bogdanova, S., Collins, A. S., Davidson, A., De Waele, B., Ernst, R. E., Fitzsimons, I. C. W., Fuck, R. A., Gladkochub, D. P., Jacobs, J., Karlstrom, K. E., Lu, S., Natapov, L. M., Pease, V., Pisarevsky, S. A., Thrane, K. et Vernikovsky, V. (2008). Assembly, configuration, and break-up history of Rodinia: a synthesis. Precambrian research, 160(1–2), 179–210.

Macdonald, F. A., McClelland, W. C., Schrag, D. P. et Macdonald, W. P. (2009). Neoproterozoic glaciation on a carbonate platform margin in Arctic Alaska and the origin of the North Slope subterrane. Geological Society of America Bulletin, 121(3–4), 448–473.

Macdonald, F. A., Schmitz, M. D., Crowley, J. L., Roots, C. F., Jones, D. S., Maloof, A. C., Strauss, J. V., Cohen, P. A., Johnston, D. T. et Schrag, D. P. (2010). Calibrating the Cryogenian. Science, 327(5970), 1241–1243.

Macdonald, F., Halverson, G., Strauss, J., Smith, E., Cox, G., Sperling, E. et Roots, C. (2012). Early Neoproterozoic Basin Formation in Yukon, Canada: Implications for the make-up and break-up of Rodinia. Geoscience Canada, 39(2), 77–100.

McDonough, W. F. et Sun, S. S. (1995). The composition of the Earth. Chemical Geology, 120(3–4), 223–253.

McKenzie, D. A. N. et Bickle, M. J. (1988). The volume and composition of melt generated by extension of the lithosphere. Journal of Petrology, 29(3), 625–679.

Melluso, L., Mahoney, J. J. et Dallai, L. (2006). Mantle sources and crustal input as recorded in high-Mg Deccan Traps basalts of Gujarat (India). Lithos, 89(3–4), 259–274.

Kasbohm, J., Schoene, B. et Burgess, S. (2021). Radiometric constraints on the timing, tempo, and effects of large igneous province emplacement. In: R.E. Ernst, A.J. Dickson, A. Bekker (eds) Large Igneous Provinces: A Driver of Global Environmental and Biotic Changes, American Geophysical Union Geophysical Monograph 255, 27–82.

Marzoli, A., Callegaro, S., Dal Corso, J., Davies, J. H., Chiaradia, M., Youbi, N., Bertrand, H., Reisberg, L., Merle, R. et Jourdan, F. (2018). The Central Atlantic magmatic province (CAMP): A review. The Late Triassic World, 91–125.

O'Driscoll, L. J. et Miller, M. S. (2015). Lithospheric discontinuity structure in Alaska, thickness variations determined by Sp receiver functions. Tectonics, 34(4), 694–714.

Pearce, J. A. et Norry, M. J. (1979). Petrogenetic implications of Ti, Zr, Y, and Nb variations in volcanic rocks. Contributions to Mineralogy and Petrology, 69(1), 33–47.

Pearce, J. A. (2008). Geochemical fingerprinting of oceanic basalts with applications to ophiolite classification and the search for Archean oceanic crust. Lithos, 100(1–4), 14–48.

Pehrsson, S. J. et Buchan, K. L. (1999). Borden dykes of Baffin Island, Northwest Territories: a Franklin U-Pb baddeleyite age and a paleomagnetic reinterpretation; Canadian Journal of Earth Sciences, 36, 65–73.

Pin, C. et Zalduegui, J. S. (1997). Sequential separation of light rare-earth elements, thorium and uranium by miniaturized extraction chromatography: application to isotopic analyses of silicate rocks. Analytica Chimica Acta, 339(1–2), 79–89.

Prasanth, M. P., Hari, K. R. et Santosh, M. (2019). Tholeiitic basalts of Deccan large igneous province, India: An overview. Geological Journal, 54(5), 2980–2993.

Rainbird, R. H. (1993). The sedimentary record of mantle plume uplift preceding eruption of the Neoproterozoic Natkusiak flood basalt. The Journal of Geology, 101(3), 305–318.

Rainbird, R. H., Jefferson, C. W. et Young, G. M. (1996). The early Neoproterozoic sedimentary Succession B of northwestern Laurentia: Correlations and paleogeographic significance. Geological Society of America Bulletin, 108(4), 454–470.

Rainbird, R. H., Stern, R. A., Khudoley, A. K., Kropachev, A. P., Heaman, L. M. et Sukhorukov, V. I. (1998). U–Pb geochronology of Riphean sandstone and gabbro from southeast Siberia and

its bearing on the Laurentia–Siberia connection. Earth and Planetary Science Letters, 164(3–4), 409–420.

Saunders, A. D., Storey, M., Kent, R. W. et Norry, M. J. (1992). Consequences of plume-lithosphere interactions. Geological Society, London, Special Publications, 68(1), 41–60.

Salters, V. J. et Stracke, A. (2004). Composition of the depleted mantle. Geochemistry, Geophysics, Geosystems, 5(5).

Schaeffer, A. J. et Lebedev, S. (2014). Imaging the North American continent using waveform inversion of global and USArray data. Earth and Planetary Science Letters, 402, 26–41.

Shaw, D. M. (2000). Continuous (dynamic) melting theory revisited. The Canadian Mineralogist, 38(5), 1041–1063.

Shellnutt, J. G., Dostal, J. et Keppie, J. D. (2004). Petrogenesis of the 723 Ma Coronation sills, Amundsen basin, Arctic Canada: implications for the break-up of Rodinia. Precambrian Research, 129(3-4), 309–324.

Sibik, S., Edmonds, M., Maclennan, J. et Svensen, H. (2015). Magmas erupted during the main pulse of Siberian Traps volcanism were volatile-poor. Journal of Petrology, 56(11), 2089–2116.

Sobolev, S. V., Sobolev, A. V., Kuzmin, D. V., Krivolutskaya, N. A., Petrunin, A. G., Arndt, N. T., Radko, V. A. et Vasiliev, Y. R. (2011). Linking mantle plumes, large igneous provinces and environmental catastrophes. Nature, 477(7364), 312–316.

Srivastava, R. K. et Samal, A. K. (2019). Geochemical characterization, petrogenesis, and emplacement tectonics of Paleoproterozoic high‐Ti and low‐Ti mafic intrusive rocks from the western Arunachal Himalaya, northeastern India and their possible relation to the~ 1.9 Ga LIP event of the Indian shield. Geological Journal, 54(1), 245–265.

Sun, S. S. et McDonough, W. F. (1989). Chemical and isotopic systematics of oceanic basalts: implications for mantle composition and processes. Geological Society, London, Special Publications, 42(1), 313–345.

Swanson-Hysell, N. L. (2021). The Precambrian paleogeography of Laurentia. In Ancient Supercontinents and the Paleogeography of Earth. Elsevier, 109–153.

Tanaka, T., Togashi, S., Kamioka, H., Amakawa, H., Kagami, H., Hamamoto, T., Yuhara, M., Orihashi, Y., Yoneda, S., Shimizu, H., Kunimaru, T., Takahashi, K., Yanagi, T., Nakano T., Fujimaki, H., Shinjo, R., Asahara, Y., Tanimizu, M., Dragusanu, C. (2000). Jndi-1: a neodymium isotopic reference in consistency with LaJolla neodymium. Chemical Geology, 168(3–4), 279–281.

Taylor, S. R. et McLennan, S. M. (1995). The geochemical evolution of the continental crust. Reviews of Geophysics, 33(2), 241–265.

Walter, M. J. (1998). Melting of garnet peridotite and the origin of komatiite and depleted lithosphere. Journal of Petrology, 39(1), 29–60.

Wang, C. Y., Zhou, M. F. et Qi, L. (2007). Permian flood basalts and mafic intrusions in the Jinping (SW China)–Song Da (northern Vietnam) district: mantle sources, crustal contamination and sulfide segregation. Chemical Geology, 3(243), 317–343.

Williamson, N., Ootes, L., Rainbird, R. H., Bédard, J. H. et Cousens, B. (2016). Initiation and early evolution of the Franklin magmatic event preserved in the 720 Ma Natkusiak Formation, Victoria Island, Canadian Arctic. Bulletin of Volcanology, 78(3), 1–19.

White, R. S. et McKenzie, D. (1995). Mantle plumes and flood basalts. Journal of Geophysical Research: Solid Earth, 100(B9), 17543–17585.

Xiao, L., Xu, Y. G., Mei, H. J., Zheng, Y. F., He, B. et Pirajno, F. (2004). Distinct mantle sources of low-Ti and high-Ti basalts from the western Emeishan large igneous province, SW China: implications for plume–lithosphere interaction. Earth and Planetary Science Letters, 228(3–4), 525–546.

Xu, Y., Chung, S. L., Jahn, B. M. et Wu, G. (2001). Petrologic and geochemical constraints on the petrogenesis of Permian–Triassic Emeishan flood basalts in southwestern China. Lithos, 58(3-4), 145–168.

Xu, Y. G., He, B., Chung, S. L., Menzies, M. A. et Frey, F. A. (2004). Geologic, geochemical, and geophysical consequences of plume involvement in the Emeishan flood-basalt province. Geology, 32(10), 917–920.

Yamashita, K., Creaser, R. A., Stemler, J. U. et Zimaro, T. W. (1999). Geochemical and Nd-Pb isotopic systematics of late Archean granitoids, southwestern Slave Province, Canada: constraints for granitoid origin and crustal isotopic structure. Canadian Journal of Earth Sciences, 36(7), 1131–1147.

Zhang, L., Ren, Z. Y., Handler, M. R., Wu, Y. D., Zhang, L., Qian, S. P., Xia, X.-P., Yang, Q. et Xu, Y. G. (2019). The origins of high-Ti and low-Ti magmas in large igneous provinces, insights from melt inclusion trace elements and Sr-Pb isotopes in the Emeishan large Igneous Province. Lithos, 344, 122–133.

CONCLUSION

Les larges provinces ignées sont des événements magmatiques qui mettent en place rapidement des grandes quantités de roches sur des grandes distances et qui perturbent fortement l'environnement global de la Terre. Cette thèse avait pour objectif de contraindre la chronologie et la géochimie des événements magmatiques de Mackenzie (ca. 1270 Ma) et de Franklin (ca. 720 Ma). Une des avancées majeures de cette étude est qu'elle a permis de montrer que l'épisode de Franklin se déroule juste avant la glaciation du Sturtien et qu'elle doit avoir participé dans son initiation. De plus, l'autre importance de ce travail est que l'on a également comprendre comment l'architecture et la structure de la croûte contrôle les mécanismes d'emplacement des LPIs.

Ainsi le premier chapitre révèle que la LPI de Mackenzie montre des variations géochimiques reflétant une phase précoce au nord ou les magmas primitifs ont interagit intensément avec la croute continentale, et une phase tardive au sud dérivant progressivement d'un manteau appauvri. Ces interprétations ont permis d'apporter une nouvelle perspective sur le magmatisme de Mackenzie qui était précédemment vu comme une LPI mettant en place toutes les roches au cours d'une seule injection magmatique, mais améliore aussi les connaissances sur le magmatisme des LPIs. De même, ce chapitre supporte que l'événement de Mackenzie ait largement contribué à l'évolution tectonique au nord du Canada et nord-ouest du Groenland au Mésoprotérozoïque, initiant probablement l'ouverture des bassins de Bylot et d'Amundsen.

Le deuxième chapitre de la thèse a permis sur la base de nouveaux âges U-Pb des roches de Franklin, de contraindre précisément le magmatisme à 718 Ma. Les ages démontrent que le magmatisme précède la glaciation du Sturtien de 0.1–1.6 Ma, et corrélé avec une anomalie négative de $\delta^{13}C_{carb}$ (-1.5‰) supportent fortement que l'altération chimique et tropicale des basaltes a déclenché la glaciation du Sturtien. Cet article a donc une portée majeure car il permet de mieux comprendre l'évolution tectonique de l'Amérique du Nord au Néoprotérozoïque, le climat global et les conséquences des LPIs sur les perturbations environnementales globales.

Enfin, le troisième chapitre a permis de mettre en évidence que les roches de Franklin présentent d'importantes variations géochimiques à travers l'Arctic reflétant des différences dans les épaisseurs de la lithosphère et dans la fusion partielle. En effet, elles sont caractérisées par un groupe avec une faible teneur en Ti et des taux de fusion partiels élevés qui reflètent une lithosphère plus mince dans le nord-ouest de Laurentia alors que les roches du nord-est de Laurentia sont davantage définies par des hautes teneurs en Ti et des taux de fusion partiels plus faibles, suggérant une lithosphère plus épaisse dans cette zone. Ces variations géographiques améliorent les reconstructions paléogéographiques. Ainsi, ce chapitre a montré

comment le magmatisme de Franklin est affecté par la lithosphère et la tectonique globale, apportant également de nouvelles informations sur la formation des LPIs.

Ce doctorat contribue à l'avancement des connaissances sur les larges provinces ignées et sur les changements environnementaux globaux. Les résultats en géochronologie et géochimie pourront servir de base pour des futures recherches sur la pétrologie, la tectonique, la paléogéographie et la stratigraphie.

ANNEXE A

DONNEES DU CHAPITRE I

Table A1.1: Whole-rock compositions of the Coppermine River Group.

Sample	Latitude	Longitude	Stratigraphic Height (m)	Stratigraphy	SiO_2	Al_2O_3	$Fe_2O_3(T)$	MnO	MgO	CaO	Na_2O	K_2O	TiO_2	P_2O_5	LOI	Total
BLS-22-66	67,244	-116,41	13,7	September Creek	51,79	11,11	11,34	0,123	7,77	5,82	0,81	4,65	1,815	0,17	4,11	95,39
BLS-23-66	67,245	-116,407	51,8	September Creek	53,22	12,98	11,44	0,174	5,03	7,6	2,13	2,65	2,018	0,2	2,00	97,43
BLS-24-66	67,246	-116,393	125	September Creek	52,4	11,84	11,97	0,133	8,42	5,55	2,31	1,61	1,974	0,2	3,31	96,41
BLS-25-66	67,246	-116,373	295,7	September Creek	53,2	13		0,15	8,6	8,4	3	1,5	1,32	0,6	2,50	100,98
BLS-26-66	67,249	-116,363	329,2	September Creek	53,52	11,74	11,01	0,142	7,36	8,74	2,48	1,68	1,551	0,15	1,55	98,38
BLS-27-66	67,251	-116,355	365,8	September Creek	53,13	11,75	11,17	0,158	7,51	8,13	2,39	1,95	1,585	0,16	2,14	97,94
BLS-28-66	67,251	-116,348	426,7	September Creek	50,99	12,31	12,19	0,209	6,34	7,13	2,9	2,25	1,916	0,2	2,51	96,43
BLS-29-66	67,253	-116,335	487,7	September Creek	48,85	11,91	15,99	0,124	5,55	5,26	2,22	1,97	3,558	0,38	4,09	95,80
BLS-30-66	67,253	-116,332	502,9	September Creek	50,79	12,98	14,64	0,16	4,36	4,5	4,7	0,38	3,271	0,34	3,03	96,11
BLS-31-66	67,253	-116,33	539,5	September Creek	50	12,87	15,59	0,171	4,27	7,74	2,53	1,37	3,242	0,31	1,60	98,08
BLS-32-66	67,255	-116,311	637	September Creek	50,68	13,6	12,97	0,166	6,12	9,11	2,18	1,1	2,418	0,25	1,30	98,59
BLS-33-66	67,256	-116,303	675,1	September Creek	50,33	13,64	12,66	0,159	6,48	9,41	2,17	0,93	2,396	0,23	1,50	98,40
BLS-8-66	67,26	-116,272	710,2	September Creek	50,84	13,68	12,38	0,158	6,07	9,42	2,2	0,96	2,455	0,25	1,60	98,41
BLS-7-66	67,262	-116,254	899,2	September Creek	51,12	12,77	10,72	0,156	7,78	11,21	1,86	0,9	1,481	0,13	1,49	98,13
BLS-6-66	67,262	-116,257	960,1	September Creek	50,75	12,72	10,56	0,17	8,03	9,04	2,66	2,07	1,428	0,13	2,08	97,56
BLS-5-66	67,263	-116,249	999,7	September Creek	51,83	12,02	15,14	0,166	4,75	4,27	3,74	1,46	2,673	0,27	2,53	96,31
BLS-4-66	67,264	-116,242	1057,7	Stony Creek	48,97	13,05	13,96	0,179	7,64	5,21	4,03	0,75	1,633	0,13	3,69	95,55
BLS-3-66	67,264	-116,242	1066,8	Stony Creek	48,99	13,44	13,95	0,201	6,48	9,93	2,21	0,67	1,754	0,13	2,17	97,75
BLS-2-66	67,264	-116,236	1115,6	Stony Creek	49,32	13,31	13,95	0,213	6,42	8,99	2,29	1	1,76	0,14	2,55	97,39
BLS-16-66	67,267	-116,226	1127,8	Stony Creek	49,53	13,29	13,89	0,201	6,42	9,61	2,29	0,73	1,777	0,14	1,80	97,87
BLS-17-66	67,273	-116,198	1345,7	Stony Creek	48,61	13,03	15,63	0,239	6,17	7,63	3,26	0,95	2,253	0,19	2,64	97,95
BLS-18-66	67,275	-116,188	1478,3	Stony Creek	48,76	12,26	16,31	0,246	6,45	5,1	2,91	1,85	2,933	0,32	2,87	97,13

Sample	Latitude	Longitude	Stratigraphic Height (m)	Stratigraphy	SiO_2	Al_2O_3	Fe_2O_3(T)	MnO	MgO	CaO	Na_2O	K_2O	TiO_2	P_2O_5	LOI	Total
BLS-19-66	67,277	-116,178	1545,3	Stony Creek	48,19	12,22	16,26	0,235	5,42	9,29	2,1	0,63	2,934	0,28	2,00	97,56
BLS-20-66	67,279	-116,168	1603,2	Stony Creek	49,9	12,6		0,21	9,7	2,1	2	3	2,27	0,22	5,20	96,50
BLS-9-66	67,281	-116,16	1649	Stony Creek	49,43	12,41	15,59	0,276	5,85	8,33	2,22	1,21	2,52	0,22	2,17	98,06
BLS-10-66	67,284	-116,147	1691,6	Stony Creek	49,12	12,08	16,01	0,279	5,62	6,83	3,26	1,38	2,966	0,27	2,27	97,82
BLS-11-66	67,285	-116,144	1722,1	Stony Creek	48,65	11,93	17	0,378	5,28	6,53	2,79	1,43	3,546	0,34	2,40	97,87
BLS-12-66	67,285	-116,142	1758,7	Stony Creek	51,4	9,2		0,23	5,9	6,5	3,2	1,1	2,72	0,52	5,30	95,45
BLS-13-66	67,286	-116,137	1772,4	Stony Creek	47,77	12,18	16,76	0,243	4,9	8,11	2,48	1,37	3,849	0,37	1,90	98,03
BLS-14-66	67,288	-116,127	1844	Stony Creek	48,38	12,33	15,85	0,24	5,02	8,79	2,61	1,09	3,628	0,37	1,90	98,31
BLS-15-66	67,29	-116,118	1889,8	Stony Creek	48,48	11,84	16,52	0,217	5,13	7,62	2,4	1,26	3,66	0,4	2,40	97,52
BLS-40-66	67,292	-116,11	1935,5	Stony Creek	48,59	11,56	17,66	0,235	4,51	8,65	2,28	0,94	3,809	0,45	2,00	98,68
BLS-41-66	67,294	-116,104	1953,8	Stony Creek	48	11,48	17,73	0,197	4,48	8,69	2,31	1,1	4,052	0,53	2,70	98,56
BLS-42-66	67,299	-116,085	2049,8	Burnt Creek	48,42	11,44	17,9	0,225	4,26	8,79	2,15	0,85	3,781	0,42	2,10	98,23
BLS-43-66	67,301	-116,082	2106,2	Burnt Creek	48,93	11,58	17,24	0,261	4,69	8,51	2,29	1,16	3,556	0,42	2,00	98,63
BLS-50-66	67,305	-116,078	2164,1	Burnt Creek	48,01	11,58	17,71	0,237	5,39	8,2	2,23	0,8	3,159	0,31	2,41	97,62
BLS-49-66	67,31	-116,073	2228,1	Burnt Creek	55,9	10,1		0,07	7,1	2,7	4,6	0,2	2,32	0,21	5,20	97,85
BLS-48-66	67,31	-116,072	2270,8	Burnt Creek	49,36	11,84	15,8	0,233	6,48	6,36	3,39	1,66	2,042	0,19	2,14	97,35
BLS-47-66	67,317	-116,065	2356,1	Burnt Creek	48,91	12,61	14,94	0,257	6,5	7,87	2,61	1,61	1,787	0,17	2,20	97,26
BLS-46-66	67,32	-116,057	2418,6	Burnt Creek	49,47	12,13	15,27	0,181	6,39	5,61	3,47	2,03	2,782	0,31	2,57	97,64
BLS-45-66	67,328	-116,052	2507	Burnt Creek	48,36	11,89	17,05	0,258	4,88	8,26	2,2	1,44	3,375	0,61	2,30	98,31
BLS-44-66	67,331	-116,049	2599,9	Burnt Creek	50,48	11,97	16,4	0,205	4,93	8,15	2,38	1,15	2,535	0,32	2,11	98,52
BLS-1-66	67,335	-116,045	2679,2	Burnt Creek	43,04	12,97	14,69	0,218	10,19	11,24	1,26	0,18	1,373	0,13	5,20	95,28
BLS-115-66	67,346	-116,042	2703,6	Burnt Creek	51,22	11,92	16,28	0,239	4,65	5,84	2,91	1,67	2,612	0,32	2,20	97,66
BLS-113-66	67,386	-116,052	2880,4	Husky Creek	49,04	13,32	12,69	0,2	8,33	10,19	1,57	0,66	1,301	0,17	1,95	97,47
BLS-112-66	67,435	-116,065	3400	Husky Creek	45,13	13,88	11,18	0,12	9,95	7,66	1,67	1,18	1,344	0,12	7,12	92,22
BLS-155-66	67,448	-116,065	3477,8	Husky Creek	48,21	13,58	12,58	0,146	7,75	9,45	1,85	0,45	1,457	0,13	4,40	95,60
BLS-156-66	67,462	-116,061	3692	Husky Creek	47,12	12,66	15	0,128	8,17	6,44	1,59	0,87	1,893	0,17	5,35	94,04
BLS-157-66	67,476	-116,047	3749	Husky Creek	50,13	13,13	13,2	0,192	8,02	8,87	1,65	0,35	1,319	0,13	2,31	96,98
BLS-158-66	67,499	-116,045	4022	Husky Creek	50,77	12,85	14,01	0,216	7,01	8,58	1,93	0,26	1,904	0,17	2,37	97,70
BLS-159-66	67,506	-116,066	4065	Husky Creek	45,87	14,15	11,78	0,085	11,66	3,8	1,13	2,28	1,412	0,12	7,33	92,28
BLS-160-66	67,513	-116,063	4100	Husky Creek	49,03	13,4	12,95	0,248	8,59	6	3,61	1	1,333	0,12	3,10	96,28

Sample	Sc	V	Cr	Co	Ni	Cu	Zn	Ga	Ge	Rb	Sr	Y	Zr	Nb	Cs	Ba
BLS-22-66	28	279	350	45	90	120	80	17	1,7	96	134	24,6	146	7,9	0,6	779
BLS-23-66	25	272	150	44	80	40	110	21	1,6	64	279	26,1	170	9,8	0,8	732
BLS-24-66	24	264	530	50	200	40	110	19	1,6	39	218	24,9	162	9,7	0,6	495
BLS-25-66																
BLS-26-66	26	268	430	49	210	40	90	18	1,3	37	262	20,5	125	5,8	0,4	507
BLS-27-66	26	267	420	49	200	20	110	18	1,4	45	264	20,5	124	5,4	0,7	746
BLS-28-66	30	303	220	46	70	30	120	19	1,6	57	390	25,6	146	9,1	0,4	858
BLS-29-66	25	423		49	60	30	120	24	1,6	44	313	39,1	254	18,3	1,1	588
BLS-30-66	22	404	30	49	60	130	160	25	1,8	8	223	35,9	238	15,7		185
BLS-31-66	23	412	50	51	80	60	140	25	1,6	36	355	35,1	228	15,8	0,4	399
BLS-32-66	31	377	200	43	100	120	100	21	1,5	25	289	29,7	171	11,5	0,4	382
BLS-33-66	31	372	210	45	110	120	110	21	1,6	22	277	29,7	170	11,7	0,3	255
BLS-8-66	31	390	220	41	110	80	100	20	1,5	23	279	28,8	169	11	0,4	297
BLS-7-66	35	288	310	42	130	110	80	16	1,4	23	192	20,2	97	5,4	0,3	212
BLS-6-66	34	286	270	41	130	60	90	16	1,6	54	192	19,4	95	5	0,5	463
BLS-5-66	34	494	30	44	60	40	160	20	1,6	27	159	38,4	201	11,1	0,4	721
BLS-4-66	35	373	160	49	80	60	130	17	1,4	11	137	22,8	95	6,1	0,2	221
BLS-3-66	37	366	170	49	90	80	100	19	1,4	16	172	23,1	99	6,2	0,3	201
BLS-2-66	37	364	160	47	90	110	120	18	1,5	25	173	23,5	103	6,4	0,3	203
BLS-16-66	38	381	170	49	90	70	110	19	1,6	21	188	23,6	104	6,6	0,3	163
BLS-17-66	34	450	90	51	70	20	220	21	1,8	29	211	28,7	139	8,9	0,3	320
BLS-18-66	29	410	50	50	60	240	170	21	1,5	30	226	37,1	238	16,2	0,5	537
BLS-19-66	33	498	80	50	70	370	140	22	1,8	13	236	35	194	14	0,2	184
BLS-20-66																
BLS-9-66	36	470	80	47	60	90	160	20	1,6	23	199	32,1	165	11,3	0,4	282
BLS-10-66	33	464	80	48	60	60	210	20	1,7	33	260	34,9	202	15,3	0,3	385
BLS-11-66	32	465	60	48	60	170	270	22	1,5	33	182	39,4	257	20,4	0,3	473
BLS-12-66																
BLS-13-66	31	482	70	48	60	180	150	23	1,7	31	258	38,3	271	23,2	0,4	325
BLS-14-66	31	430	110	45	80	50	160	22	1,5	26	293	37,2	263	22,1	0,4	477

Sample	Sc	V	Cr	Co	Ni	Cu	Zn	Ga	Ge	Rb	Sr	Y	Zr	Nb	Cs	Ba
BLS-15-66	33	423	70	45	50	370	150	22	1,6	26	211	44,5	290	22,5	0,5	458
BLS-40-66	33	465	40	46	40	220	150	22	1,6	23	255	49,8	303	26,2	0,3	309
BLS-41-66	32	436	50	47	50	540	160	23	1,7	27	214	52,5	336	29,8	0,3	274
BLS-42-66	34	485	20	48	40	320	160	23	1,6	21	224	49,3	285	23,9	0,2	243
BLS-43-66	35	491	60	45	60	300	150	23	1,6	29	209	49,1	274	22,9	0,2	296
BLS-50-66	39	548	70	49	50	90	150	21	1,6	20	185	41,3	211	17,1	0,4	287
BLS-49-66																
BLS-48-66	44	462	90	48	60	120	130	17	1,6	44	307	33	128	10,2	1	911
BLS-47-66	44	412	120	49	70	40	120	16	1,6	45	257	28	113	11	1,3	1228
BLS-46-66	37	460	120	44	70	290	180	19	1,5	28	332	38,9	207	18,2	0,4	497
BLS-45-66	36	430	50	46	60	200	160	21	1,5	33	182	61	346	28,6	0,3	382
BLS-44-66	35	427	80	50	60	280	130	21	1,5	26	216	37,4	207	18,3	0,3	358
BLS-1-66	37	295	760	58	280	80	110	17	1,5	3	133	29,3	108	4,6	0,1	29
BLS-115-66	37	438	30	49	50	150	140	20	1,5	36	328	38,1	238	23,5	0,8	559
BLS-113-66	48	311	180	50	100	70	90	15	1,4	9	133	22,2	88	6,9	0,3	131
BLS-112-66	50	352	190	47	90	130	90	16	1,7	11	142	22,6	79	5,4	0,8	194
BLS-155-66	48	361	130	49	70	110	90	16	1,4	5	149	24,7	86	7,2	0,4	122
BLS-156-66	49	456	90	50	70	120	120	17	1,6	5	117	28,6	102	8,8	0,2	195
BLS-157-66	47	343	100	46	60	100	90	15	1,5	3	130	23,8	78	6,7		137
BLS-158-66	48	451	130	47	140	270	120	16	1,6	2	157	30,2	99	8,5		165
BLS-159-66	50	360	190	47	90	100	90	16	1,5	14	87	22,9	81	5,9	0,5	307
BLS-160-66	48	344	170	47	90	90	100	14	1,6	6	534	23,4	78	5,2	0,2	1029

Sample	La	Ce	Pr	Nd	Sm	Eu	Gd	Tb	Dy	Ho	Er	Tm	Yb	Lu	Hf	Ta	Pb	Th	U
BLS-22-66	20,5	46,7	5,83	24,8	5,8	1,8	5,38	0,86	4,95	0,91	2,45	0,343	2,2	0,307	3,6	0,63	9	3,94	1,1
BLS-23-66	25,4	55,2	6,82	28,3	6,45	2,03	5,92	0,93	5,22	0,95	2,57	0,351	2,07	0,309	4,3	0,76	16	4,48	1,05
BLS-24-66	24,2	53,1	6,55	27,9	6,49	1,9	5,48	0,85	4,88	0,94	2,49	0,333	2,08	0,288	4	0,72	10	3,86	0,94
BLS-25-66																			
BLS-26-66	17,9	38,8	4,84	20,6	4,86	1,55	4,44	0,68	4,02	0,77	1,95	0,273	1,66	0,245	2,8	0,41	8	2,59	0,55
BLS-27-66	17,9	38,7	4,8	20,3	4,69	1,52	4,21	0,69	4,01	0,75	2	0,282	1,68	0,241	3	0,36	10	2,55	0,54
BLS-28-66	22,3	49,3	6,2	26,7	5,96	1,97	5,65	0,89	5,04	0,94	2,55	0,344	2,15	0,304	3,6	0,66	13	2,54	0,65
BLS-29-66	31,3	71	9,31	41,4	9,79	3,39	9,12	1,4	7,82	1,41	3,69	0,489	2,95	0,411	6,4	1,33	10	3,51	0,9
BLS-30-66	25,1	58,7	7,83	33,9	8,76	2,79	8,33	1,31	7,21	1,33	3,43	0,46	2,88	0,42	6	1,15	8	3,94	1,02
BLS-31-66	28,1	64,2	8,4	36,2	8,91	2,84	8,32	1,28	7,2	1,32	3,32	0,451	2,8	0,393	5,8	1,13	10	3,95	1,06
BLS-32-66	20,4	46,9	6,11	26,8	6,68	2,07	6,49	1,01	5,81	1,11	2,99	0,414	2,56	0,374	4,6	0,82	5	2,79	0,73
BLS-33-66	19,7	45,9	5,97	26,7	6,44	2,16	6,39	1,02	5,89	1,1	2,98	0,421	2,61	0,37	4,2	0,82	7	2,7	0,73
BLS-8-66	19,7	45,5	5,95	26,2	6,83	2,08	6,41	0,99	5,67	1,03	2,81	0,398	2,51	0,373	4,2	0,78	6	2,63	0,7
BLS-7-66	11,2	26	3,39	15	3,98	1,26	3,9	0,64	3,83	0,75	2,12	0,295	1,81	0,268	2,3	0,41		1,68	0,46
BLS-6-66	11	25,5	3,41	14,8	3,88	1,27	3,82	0,63	3,77	0,73	1,97	0,273	1,72	0,25	2,3	0,39	8	1,67	0,45
BLS-5-66	19,9	46,8	6,19	27,5	7,15	2,14	7,5	1,23	7,39	1,46	4,03	0,565	3,5	0,532	5,1	0,86	12	3,3	0,91
BLS-4-66	7,83	20,5	2,86	13,3	3,93	1,32	4,17	0,7	4,16	0,84	2,29	0,32	1,95	0,281	2,3	0,43	6	0,94	0,25
BLS-3-66	9,96	24,2	3,33	15,9	4,27	1,45	4,51	0,74	4,46	0,84	2,32	0,315	2,04	0,301	2,5	0,44	7	1	0,28
BLS-2-66	10,2	24,5	3,39	15,1	4,28	1,43	4,58	0,76	4,51	0,88	2,4	0,338	2,13	0,314	2,5	0,47	11	1,04	0,27
BLS-16-66	9,83	24,6	3,39	15,6	4,32	1,46	4,52	0,75	4,49	0,88	2,41	0,333	2,12	0,311	2,6	0,49		1,01	0,28
BLS-17-66	12,5	30,7	4,31	20	5,41	1,99	5,52	0,93	5,59	1,04	2,89	0,407	2,43	0,344	3,5	0,61	12	1,2	0,34
BLS-18-66	20,1	51,7	7,12	33,2	8,54	2,7	8,28	1,31	7,46	1,36	3,67	0,51	3,05	0,452	5,7	1,23	9	1,96	0,6
BLS-19-66	19	46,2	6,33	28,6	7,27	2,46	7,22	1,15	6,87	1,29	3,41	0,486	2,92	0,435	4,6	1,07	8	1,83	0,52
BLS-20-66																			
BLS-9-66	16,4	39,2	5,4	24,1	6,24	2,13	6,18	1,04	6,15	1,17	3,31	0,459	3,01	0,455	4	0,84	9	1,61	0,46
BLS-10-66	19,4	47,8	6,67	29,7	7,51	2,45	7,25	1,19	7	1,29	3,57	0,485	3,01	0,441	5	1,11	16	1,79	0,52
BLS-11-66	25,8	63	8,42	37,1	9,4	2,77	8,67	1,36	7,91	1,43	3,8	0,528	3,23	0,48	6	1,49	21	2,38	0,72
BLS-12-66																			

Sample	La	Ce	Pr	Nd	Sm	Eu	Gd	Tb	Dy	Ho	Er	Tm	Yb	Lu	Hf	Ta	Pb	Th	U
BLS-13-66	28,3	68,7	9,06	40,3	9,79	3,02	8,83	1,38	7,71	1,38	3,73	0,502	3,02	0,458	6,5	1,65	12	2,66	0,76
BLS-14-66	28,3	68	8,94	40	9,84	3,08	8,32	1,33	7,55	1,38	3,65	0,496	3,16	0,467	6,5	1,65	23	2,58	0,66
BLS-15-66	29	70,6	9,36	42,1	10,4	3,14	9,54	1,56	9,06	1,66	4,46	0,6	3,75	0,539	6,9	1,66	12	2,6	0,73
BLS-40-66	31,4	75,2	10	43,3	10,8	3,23	10,2	1,67	9,52	1,79	5,04	0,71	4,37	0,652	7,6	1,81	16	3,1	0,9
BLS-41-66	35,3	85	11,3	49,1	12,1	3,69	11,2	1,79	10,4	1,89	5,19	0,728	4,41	0,649	8,4	2,09	10	3,35	0,96
BLS-42-66	28,8	69,4	9,19	41,5	10,3	3,14	10,1	1,58	9,48	1,77	4,94	0,674	4,24	0,649	7,5	1,7	6	3,02	0,86
BLS-43-66	27,8	66,8	8,85	39,4	9,99	3,05	9,55	1,58	9,44	1,77	4,98	0,666	4,3	0,645	7	1,55	8	2,69	0,75
BLS-50-66	20	48,8	6,57	29,5	7,63	2,53	7,84	1,29	7,76	1,48	4,25	0,606	3,91	0,574	5,4	1,18	9	1,86	0,53
BLS-49-66																			
BLS-48-66	11	27,6	3,86	17,5	5,16	1,61	5,46	0,93	5,89	1,21	3,48	0,492	3,21	0,484	3,3	0,67	7	0,93	0,27
BLS-47-66	12,2	28,6	3,78	16,7	4,43	1,49	4,6	0,77	4,89	0,98	2,77	0,429	2,81	0,422	2,9	0,74	9	1,04	0,31
BLS-46-66	21,4	50,2	6,7	29,7	7,43	2,42	7,51	1,22	7,31	1,4	4,07	0,577	3,72	0,535	5,4	1,27	14	1,98	0,55
BLS-45-66	34,2	81	10,7	47,6	11,7	3,29	11,4	1,89	11,3	2,18	6,2	0,877	5,83	0,897	8,5	1,99	18	3,32	0,94
BLS-44-66	26,6	59,6	7,64	32,3	7,66	2,4	7,33	1,18	7,07	1,33	3,74	0,536	3,48	0,497	5	1,25	9	2,93	0,69
BLS-1-66	9,19	21,8	2,99	13,5	3,73	1,28	4,69	0,8	5,02	1,05	3,03	0,443	2,87	0,461	2,5	0,36		1,82	0,55
BLS-115-66	32,6	73	9,15	37,9	8,1	2,47	7,74	1,22	7,35	1,42	3,94	0,564	3,64	0,524	5,6	1,69	10	4,16	0,98
BLS-113-66	7,57	18,3	2,58	12,3	3,34	1,17	3,51	0,61	4,08	0,81	2,3	0,332	2,23	0,344	2	0,47		0,65	0,15
BLS-112-66	6,34	15,8	2,25	10,9	3,22	1,11	3,62	0,66	4,13	0,82	2,46	0,367	2,33	0,335	1,9	0,39		0,48	0,12
BLS-155-66	8,6	20,8	2,94	13,1	3,43	1,26	3,9	0,68	4,39	0,89	2,68	0,398	2,6	0,387	2,2	0,49		0,66	0,18
BLS-156-66	8,98	22,4	3,23	15,1	4,24	1,55	4,7	0,81	5,2	1,05	2,97	0,433	2,9	0,457	2,7	0,55		0,47	0,13
BLS-157-66	7,3	17,9	2,57	11,8	3,09	1,13	3,64	0,67	4,31	0,88	2,6	0,374	2,4	0,375	1,9	0,48		0,54	0,16
BLS-158-66	8,76	22,2	3,32	15,5	4,39	1,6	4,89	0,88	5,47	1,06	3,11	0,459	2,93	0,442	2,6	0,59		0,44	0,12
BLS-159-66	7,06	16,9	2,37	10,8	3,39	1,17	3,52	0,67	4,2	0,86	2,54	0,364	2,37	0,357	2,1	0,4		0,54	0,15
BLS-160-66	6,77	16,6	2,33	11,1	3,23	1,12	3,68	0,64	4,21	0,9	2,63	0,375	2,45	0,349	1,9	0,36		0,49	0,13

Table A1.2: Whole-rock compositions of the Mackenzie dyke swarm, and distal basalts and sills.

Sample	Rock type	Latitude	Longitude	SiO_2	Al_2O_3	$Fe_2O_3(T)$	MnO	MgO	CaO	Na_2O	K_2O	TiO_2	P_2O_5	LOI	Total
87PHA-CL-3	Mackenzie dyke	66,88	-111,10	49,44	13,54	14,05	0,21	7,47	11,35	2,00	0,50	1,49	0,13	0,65	100,8
87PHA-Cl-4	Mackenzie dyke	66,88	-111,10	49,23	13,78	13,97	0,20	7,23	11,54	2,10	0,44	1,56	0,13	0,59	100,8
87PHA-CL-11	Mackenzie dyke	66,91	-111,12	51,41	12,37	15,52	0,21	5,85	10,30	2,18	0,35	1,91	0,18	0,25	100,5
88PHA-1	Mackenzie dyke	-	-	49,69	13,51	15,37	0,17	5,00	6,41	2,85	2,10	2,87	0,57	2,01	100,6
88PHA-7	Mackenzie dyke	-	-	50,33	12,33	12,88	0,63	8,45	6,40	3,37	0,41	2,58	0,24	2,90	100,5
88PHA-9	Mackenzie dyke	-	-	50,27	12,67	12,56	0,31	6,95	8,49	2,72	1,05	2,83	0,25	2,64	100,7
88PHA-10	Mackenzie dyke	-	-	46,02	13,21	17,37	0,18	7,07	9,02	2,40	1,02	3,00	0,21	0,95	100,5
88PHA-12	Mackenzie dyke	-	-	48,88	13,29	15,67	0,17	5,45	6,98	2,72	1,65	2,88	0,36	1,56	99,6
88PHA-38A	Mackenzie dyke	64,05	-96,97	46,10	13,63	15,76	0,20	7,36	7,74	1,77	2,96	2,37	0,19	2,37	100,4
88PHA-38B	Mackenzie dyke	64,05	-96,97	52,31	15,10	11,81	0,11	3,99	6,37	3,13	2,64	2,27	0,50	2,16	100,4
88PHA-39E	Mackenzie dyke	64,05	-96,97	48,60	11,95	16,10	0,18	6,83	7,80	1,69	2,44	2,64	0,27	2,03	100,5
88PHA-39F	Mackenzie dyke	64,05	-96,97	47,25	12,93	16,27	0,17	7,41	6,90	2,43	1,45	3,02	0,26	2,30	100,4
88PHA-39G	Mackenzie dyke	64,05	-96,97	46,74	13,75	16,16	0,20	6,38	7,39	2,52	1,56	2,93	0,28	2,11	100,0
88PHA-39I	Mackenzie dyke	64,05	-96,97	47,12	14,63	14,17	0,13	5,56	6,52	3,50	1,32	2,63	0,34	2,46	98,4
88PHA-39J	Mackenzie dyke	64,05	-96,97	46,69	12,69	17,76	0,16	5,84	6,24	2,95	1,45	3,35	0,54	2,19	99,9
88PHA-39K	Mackenzie dyke	64,05	-96,97	45,40	12,56	17,53	0,20	6,52	7,55	2,43	1,44	3,98	0,27	2,14	100,0
88PHA-39L	Mackenzie dyke	64,05	-96,97	46,64	12,95	16,93	0,16	6,64	7,36	2,60	1,38	3,82	0,30	1,75	100,5
88PHA-39M	Mackenzie dyke	64,05	-96,97	47,29	12,87	15,80	0,15	7,08	6,30	2,72	2,05	3,70	0,32	2,27	100,6
88PHA-39N	Mackenzie dyke	64,05	-96,97	46,35	13,41	17,15	0,20	6,61	7,59	2,47	1,68	3,22	0,29	1,55	100,5
88PHA-44A	Mackenzie dyke	64,03	-96,92	48,05	12,02	17,01	0,20	7,37	8,15	2,24	1,12	2,92	0,25	1,29	100,6
88PHA-46A	Mackenzie dyke	64,03	-96,92	47,56	12,95	16,44	0,15	7,00	6,04	2,69	2,15	3,39	0,31	1,82	100,5
88PHA-47C	Mackenzie dyke	64,17	-97,11	46,86	13,46	15,08	0,17	6,52	7,55	2,12	2,21	2,65	0,24	1,73	98,6
88PHA-48A	Mackenzie dyke	64,16	-97,10	48,38	12,15	14,81	0,15	8,09	6,64	2,92	1,61	2,54	0,25	2,37	99,9
88PHA-49B	Mackenzie dyke	64,16	-97,10	48,94	13,40	15,28	0,13	7,24	7,47	2,41	1,41	2,60	0,26	1,47	100,6
88PHA-50A	Mackenzie dyke	64,16	-97,10	48,39	12,29	16,09	0,26	7,69	7,20	2,60	1,38	2,54	0,24	1,94	100,6
88PHA-50C	Mackenzie dyke	64,16	-97,10	49,12	12,77	15,67	0,20	6,32	8,77	2,70	0,81	2,65	0,25	1,14	100,4
88PHA-99	Mackenzie dyke	66,50	-115,03	47,96	12,20	17,84	0,24	4,91	9,91	2,07	0,88	3,24	0,48	1,04	100,8
88PHA-100	Mackenzie dyke	66,50	-115,03	52,92	13,86	12,90	0,19	4,20	6,22	2,31	2,59	1,77	0,18	1,57	98,7
88PHA-101A	Mackenzie dyke	66,55	-115,05	51,61	13,98	11,53	0,16	6,28	9,92	2,21	1,02	1,66	0,17	-0,17	98,4

Sample	Rock type	Latitude	Longitude	SiO_2	Al_2O_3	Fe_2O_3(T)	MnO	MgO	CaO	Na_2O	K_2O	TiO_2	P_2O_5	LOI	Total
88PHA-102C	Mackenzie dyke	66,54	-115,06	50,63	12,60	15,22	0,21	6,07	9,83	2,15	0,60	1,88	0,16	0,39	99,7
88PHA-102D	Mackenzie dyke	66,54	-115,06	51,34	12,55	14,41	0,21	6,69	10,14	2,07	0,58	1,62	0,15	0,44	100,2
88PHA-104F	Mackenzie dyke	66,54	-115,06	51,19	13,76	14,52	0,20	5,91	9,85	2,36	0,51	1,72	0,16	0,34	100,5
88PHA-104G	Mackenzie dyke	66,54	-115,06	51,42	13,09	13,82	0,20	7,02	10,70	2,18	0,34	1,51	0,13	0,15	100,6
88PHA-106C	Mackenzie dyke	66,56	-115,02	52,88	12,45	14,75	0,21	4,68	8,75	2,43	1,02	2,20	0,22	0,18	99,8
88PHA-107C	Mackenzie dyke	66,52	-115,00	53,06	12,85	14,89	0,19	4,74	8,48	2,57	1,17	2,20	0,20	0,30	100,7
88PHA-115A	Mackenzie dyke	67,10	-115,70	50,74	12,25	16,76	0,22	4,65	7,87	2,14	1,55	2,50	0,31	1,16	100,2
88PHA-115D	Mackenzie dyke	67,10	-115,70	51,04	12,07	16,67	0,18	5,20	6,36	2,47	2,74	2,31	0,27	1,06	100,4
88PHA-116D	Mackenzie dyke	67,10	-115,70	50,02	13,23	15,16	0,22	5,57	8,88	2,33	1,59	2,19	0,20	0,77	100,2
88PHA-207C	Mackenzie dyke	63,35	-101,31	47,12	12,73	16,01	0,56	6,97	5,15	4,19	0,86	3,73	0,58	2,83	100,7
88PHA-511	Mackenzie dyke	63,39	-101,30	46,56	12,74	15,76	0,43	6,42	6,31	3,43	1,67	3,72	0,57	2,46	100,1
88LAAT-218-5A	Mackenzie dyke	63,37	-95,52	47,82	11,40	18,57	0,25	4,23	8,06	2,12	0,71	3,68	0,55	0,96	98,3
88LAAT-218-6A	Mackenzie dyke	63,37	-95,52	49,94	12,84	16,59	0,23	3,75	7,64	3,08	1,19	3,14	0,44	1,29	100,1
86LAAT-319-2	Mackenzie dyke	66,41	-94,73	53,92	14,61	13,72	0,17	2,41	6,75	3,18	2,24	2,27	0,50	0,93	100,7
86LAAT-319-1B	Mackenzie dyke	66,41	-94,73	50,21	13,43	16,23	0,19	4,08	8,25	2,71	1,46	3,38	0,28	0,18	100,4
BL88-9	Mackenzie dyke	66,55	-115,05	51,52	13,98	11,70	0,19	8,14	9,13	1,97	1,62	1,70	0,15	0,62	100,7
BL88-10	Mackenzie dyke	66,54	-115,07	50,69	12,76	16,50	0,22	5,33	9,31	2,35	0,73	2,32	0,22	0,28	100,7
BL88-17	Mackenzie dyke	66,56	-114,94	49,45	12,00	17,18	0,26	4,64	8,57	2,40	1,05	3,24	0,49	1,02	100,3
BL88-18	Mackenzie dyke	66,57	-114,93	49,42	12,12	16,93	0,24	5,12	8,51	2,37	0,79	2,99	0,29	1,04	99,8
BL88-21	Mackenzie dyke	66,57	-114,90	48,68	12,90	15,63	0,23	5,20	9,09	2,49	0,65	3,10	0,32	0,73	99,0
BL88-25	Mackenzie dyke	66,57	-114,88	49,34	13,23	15,42	0,24	5,26	7,78	2,91	0,73	2,78	0,21	2,73	100,6
BL88-27	Mackenzie dyke	66,57	-114,88	51,37	13,52	12,73	0,22	6,16	6,54	1,46	2,74	1,71	0,14	2,25	98,9
BL88-29	Mackenzie dyke	66,57	-114,88	48,53	12,37	17,24	0,28	5,47	9,91	2,32	0,55	2,47	0,20	0,49	99,8
BL88-30	Mackenzie dyke	66,57	-114,88	49,82	12,96	15,56	0,24	5,06	10,24	2,42	0,55	2,66	0,24	0,82	100,6
BL88-38	Mackenzie dyke	66,57	-115,01	51,40	13,29	14,09	0,18	4,88	8,60	2,65	1,08	2,08	0,19	1,09	99,5
BL88-41	Mackenzie dyke	66,57	-115,02	51,53	13,15	11,38	0,19	8,14	10,32	1,96	0,96	1,43	0,15	1,41	100,6
BL88-59	Mackenzie dyke	67,14	-115,84	48,35	12,40	15,40	0,23	6,59	10,63	2,23	1,49	2,31	0,23	0,75	100,6
BL88-57	Mackenzie dyke	67,14	-115,80	49,33	12,58	17,50	0,23	5,11	8,57	2,23	1,14	3,17	0,44	0,39	100,7
BL88-54	Mackenzie dyke	67,14	-115,79	48,46	12,24	16,15	0,13	7,65	6,47	1,64	0,86	3,31	0,46	3,00	100,4
BL88-63	Mackenzie dyke	67,12	-115,73	47,88	12,19	18,14	0,21	5,73	7,89	1,83	1,24	2,70	0,36	1,52	99,7
BL88-61	Mackenzie dyke	67,12	-115,73	49,30	11,27	18,09	0,30	5,99	7,03	1,35	2,43	3,09	0,34	1,42	100,6

Sample	Rock type	Latitude	Longitude	SiO_2	Al_2O_3	Fe_2O_3(T)	MnO	MgO	CaO	Na_2O	K_2O	TiO_2	P_2O_5	LOI	Total
BL88-75	Mackenzie dyke	67,14	-115,66	48,06	12,54	16,40	0,23	7,26	6,56	1,92	1,63	2,41	0,32	2,89	100,2
BL88-84	Mackenzie dyke	67,13	-115,66	49,65	12,37	15,89	0,24	6,01	8,50	1,61	2,44	2,03	0,22	1,09	100,0
15WGA-W002	Mackenzie dyke	64,42	-90,57	51,20	13,86	11,58	0,18	7,31	10,48	1,76	0,71	1,13	0,10	1,41	99,7
15WGA-L226	Mackenzie dyke	64,37	-89,19	52,14	13,92	15,08	0,17	3,25	6,14	3,00	2,25	2,98	0,61	1,02	100,6
15WGA-W028	Mackenzie dyke	64,71	-91,90	51,87	15,02	11,38	0,18	6,17	10,13	1,91	0,82	1,12	0,11	1,84	100,5
16WGA-S186	Mackenzie dyke	65,30	-92,49	51,86	19,22	10,38	0,13	2,44	9,85	2,89	1,32	1,42	0,13	1,15	100,8
90-LAAT-32-2	Savage Point sill	72,73	-96,52	53,58	14,73	12,68	0,18	4,58	9,13	2,54	1,08	1,20	0,12	0,63	100,4
M012	Nyeboe basalt	70,31	-86,42	50,43	13,19	10,39	0,07	11,48	2,22	0,60	4,56	0,83	0,12	6,30	100,2
F089	Nyeboe basalt	70,25	-84,77	49,20	14,13	8,65	0,08	8,63	4,57	0,57	3,88	0,90	0,12	9,15	99,9
M014	Hansen sill	70,30	-86,44	51,27	13,93	11,14	0,18	5,74	7,99	2,02	2,93	1,04	0,09	2,10	98,4
M085	Hansen sill	70,28	-86,21	48,98	13,91	10,49	0,11	8,92	7,53	1,85	2,02	0,92	0,07	3,84	98,6
F010	Hansen sill	70,32	-86,49	50,26	14,91	11,29	0,13	6,99	10,08	1,76	1,06	1,03	0,08	2,36	100,0
F015	Hansen sill	70,22	-84,43	44,48	14,86	4,47	0,26	6,96	10,77	1,09	3,23	1,04	0,08	12,72	100,0
W008	Hansen sill	70,23	-84,61	49,38	14,16	11,72	0,18	8,19	7,62	2,07	0,88	1,03	0,10	4,71	100,0
1550-5	Hansen sill	69,86	-84,60	46,36	14,67	5,58	0,15	8,26	8,27	1,33	2,32	1,01	0,09	11,85	99,9

Sample	Sc	V	Cr	Co	Ni	Cu	Zn	Ga	Ge	Rb	Sr	Y	Zr	Nb	Cs	Ba
87PHA-CL-3	39	396	260	51	120	240	100	17	1,5	8	188	22	84	4,5	0,5	82
87PHA-Cl-4	39	409	220	50	110	210	90	19	1,6	11	185	24	90	6,1	0,5	78
87PHA-CL-11	38	436	100	51	90	260	120	20	1,3	9	198	27,5	122	7,9	0,6	96
88PHA-1	18	247	120	50	90	50	120	26	1,3	47	567	39,6	286	20,9	1,3	541
88PHA-7	27	402	440	67	320	330	100	24	2,4	34	230	39	167	11,6	1,9	81
88PHA-9	28	446	240	54	160	130	< 30	24	1,3	52	404	31,7	178	11,9	0,8	229
88PHA-10	26	487	280	65	240	280	130	24	1,5	37	480	25,1	150	11,2	1,5	250
88PHA-12	18	302	170	57	160	160	110	25	1,3	55	521	31,6	230	17,2	2	388
88PHA-38A	23	390	300	59	220	290	120	22	1,6	57	575	22,7	133	10,4	1	352
88PHA-38B	12	189	90	29	80	10	30	29	1,3	65	554	41,9	346	21,6	0,5	718
88PHA-39E	26	409	280	57	200	130	90	22	1,3	34	550	26,4	151	10,8	0,8	317
88PHA-39F	23	445	300	70	250	230	170	23	1,3	33	518	25,7	169	12,6	1	263
88PHA-39G	20	388	240	63	250	380	250	24	1,2	32	617	23,4	170	12,9	0,9	378
88PHA-39I	17	282	160	51	140	10	70	26	1,4	31	614	30,5	238	17,1	0,4	389
88PHA-39J	18	322	180	64	160	30	90	26	1,1	32	510	38	281	21,2	1	422
88PHA-39K	25	453	200	69	190	180	240	23	1,3	30	599	24,8	187	14,8	0,8	359
88PHA-39L	23	409	220	64	180	120	130	23	1,3	30	576	26,3	195	16,2	0,9	308
88PHA-39M	23	401	230	66	190	60	50	25	1,5	52	470	28,6	206	16,1	0,5	449
88PHA-39N	21	416	250	64	220	230	220	24	1,2	34	615	27,9	199	15,9	1	459
88PHA-44A	26	417	320	66	250	230	160	23	1,5	27	479	28	173	12,3	1,9	327
88PHA-46A	23	391	240	65	220	170	100	25	1,4	56	590	29,9	219	16,6	1,8	402
88PHA-47C	22	378	270	61	220	230	130	23	1,2	66	559	25,1	150	10,4	1,5	483
88PHA-48A	25	393	340	55	260	20	< 30	23	1,5	32	352	27,8	159	10,5	0,4	490
88PHA-49B	22	362	320	64	270	230	70	24	1,4	45	408	28,4	180	13	1,7	278
88PHA-50A	24	392	310	65	260	180	70	23	1,4	47	320	28	159	11,7	2,5	214
88PHA-50C	25	407	250	59	190	220	90	24	1,4	28	392	29,4	172	11,9	1,8	185
88PHA-99	41	526	< 20	49	50	530	150	21	1,5	26	218	55,2	297	25,9	1,4	296
88PHA-100	28	364	50	41	50	240	180	22	1,4	91	298	27,2	147	9,5	1,8	492
88PHA-101A	31	325	190	42	100	150	90	18	1,2	28	261	22,8	133	7,9	0,6	260
88PHA-102C	41	469	160	54	120	290	120	20	1,4	21	207	29	112	7,3	1,1	103
88PHA-102D	41	397	200	52	130	280	110	18	1,3	21	198	26,2	101	6,4	1,3	87

Sample	Sc	V	Cr	Co	Ni	Cu	Zn	Ga	Ge	Rb	Sr	Y	Zr	Nb	Cs	Ba
88PHA-104F	40	415	180	49	100	260	100	20	1,6	14	234	27,3	110	7,1	0,4	111
88PHA-104G	41	404	250	51	130	210	100	18	1,5	8	193	22,4	87	5,6	0,6	71
88PHA-106C	32	448	40	48	60	230	170	22	1,3	27	281	30,4	167	10,4	1,8	348
88PHA-107C	33	431	40	46	60	270	110	21	1,3	31	294	30,6	171	9,9	0,6	319
88PHA-115A	38	479	30	48	30	90	140	21	1,5	54	143	45,9	201	13,6	2,7	313
88PHA-115D	38	459	40	48	30	90	140	21	1,6	82	262	42,8	183	12,9	2,6	1017
88PHA-116D	33	507	70	46	70	270	110	21	1,6	40	412	26,3	137	9,2	0,2	377
88PHA-207C	26	419	60	40	40	70	400	18	1,3	38	237	20,5	185	24	1	387
88PHA-511	27	424	60	50	50	100	1030	18	1,2	75	497	20,8	182	24,2	1,1	1280
88LAAT-218-5A	39	436	< 20	44	20	780	150	22	1,6	23	188	73,7	344	28,9	0,9	208
88LAAT-218-6A	38	456	< 20	40	30	580	150	22	1,1	36	307	59,1	293	23,3	0,7	214
86LAAT-319-2	16	185	< 20	36	< 20	230	190	29	1,3	62	547	47,9	330	21,9	1,6	542
86LAAT-319-1B	24	499	20	54	70	230	160	25	1,2	38	482	31,2	207	15,3	0,9	358
BL88-9	35	346	350	45	150	160	100	17	1,3	61	281	19,6	107	6,8	0,6	285
BL88-10	41	487	90	52	70	320	170	21	1,4	20	219	35	151	11,5	0,8	154
BL88-17	40	523	< 20	47	30	460	180	21	1,5	45	226	55,8	302	26	1	214
BL88-18	33	524	50	50	50	350	150	22	1,3	25	259	34,3	204	16,5	1,6	192
BL88-21	33	529	60	54	70	320	110	24	1,9	21	289	41,1	217	19,5	1,7	162
BL88-25	39	530	70	46	80	290	80	22	1,9	40	222	33,8	159	11,5	2,5	105
BL88-27	35	388	210	41	110	200	70	18	1,5	148	161	25,5	102	6,1	4	388
BL88-29	38	491	90	51	80	280	110	21	1,4	25	245	29,1	138	10,5	2,3	101
BL88-30	37	513	60	50	70	300	100	21	1,7	23	256	31,7	156	13,1	1,5	97
BL88-38	31	396	40	46	70	210	140	22	1,2	33	269	31	158	10,5	0,6	292
BL88-41	34	299	320	45	160	160	130	17	1,3	24	241	20,6	104	6	0,7	282
BL88-59	33	450	100	52	90	270	130	20	1,5	28	334	27,1	152	9,7	0,8	452
BL88-57	35	429	70	48	90	560	150	21	1,4	25	273	47,2	275	21,3	0,9	321
BL88-54	42	549	70	44	70	350	130	21	1,6	18	196	52,1	282	19,9	2	412
BL88-63	44	537	30	51	70	510	190	20	1,4	27	213	46,8	197	14,9	0,8	309
BL88-61	37	570	< 20	49	60	430	230	22	1,5	47	354	40,7	207	13,7	1,5	379
BL88-75	48	554	100	48	80	400	150	18	1,4	47	162	33,7	142	11,8	1,4	244
BL88-84	42	430	110	49	80	320	120	19	1,4	60	453	31,1	141	11,1	0,9	323

Sample	Sc	V	Cr	Co	Ni	Cu	Zn	Ga	Ge	Rb	Sr	Y	Zr	Nb	Cs	Ba
15WGA-W002	36	313	350	45	130	130	90	17	1,5	24	216	20,6	96	5,2	1,1	178
15WGA-L226	18	232	30	47	50	240	150	30	1,5	62	504	50,2	314	27,9	1,3	623
15WGA-W028	34	293	150	42	80	130	80	18	1,6	30	220	22,3	101	6,8	1,5	218
16WGA-S186	23	295	20	29	30	190	80	23	1,3	56	350	24,6	125	9,2	2,5	220
90-LAAT-32-2	30	340	< 20	48	60	270	90	21	1,3	31	241	19,1	95	4,4	0,5	243
M012	34	230	310	47	120	50	60	15	1,3	81	42	22,2	130	8,3	0,8	882
F089	34	220	240	33	70	30	< 30	16	1	101	53	23,4	130	8,9	1	332
M014	31	303	80	40	70	180	90	19	1,2	74	127	17,6	79	6,7	0,3	217
M085	31	264	270	46	140	20	50	16	1,3	41	110	15,5	67	5,2	0,3	223
F010	32	278	200	46	100	140	50	17	1,4	22	165	15,9	76	6,2	0,4	186
F015	33	279	190	42	110	20	< 30	18	1,2	109	90	16,6	78	6,4	0,9	325
W008	32	273	190	44	110	40	100	18	1,4	22	113	17,7	77	6,4	0,7	193
1550-5	33	306	190	35	100	< 10	< 30	17	0,9	70	102	15,3	77	5,9	0,7	155

Sample	La	Ce	Pr	Nd	Sm	Eu	Gd	Tb	Dy	Ho	Er	Tm	Yb	Lu	Hf	Ta	Th	U
87PHA-CL-3	6,85	17,2	2,47	11,6	3,52	1,25	4,11	0,68	4,13	0,81	2,31	0,33	2,03	0,321	2	0,33	0,68	0,19
87PHA-Cl-4	7,54	18,4	2,53	12,6	3,51	1,29	4,43	0,77	4,36	0,89	2,42	0,335	2,16	0,324	2,6	0,33	0,71	0,2
87PHA-CL-11	10,7	25,8	3,7	17,5	4,94	1,73	5,53	0,89	5,25	1,02	2,85	0,387	2,54	0,363	3,2	0,57	1,04	0,29
88PHA-1	35,8	84,8	11	48,7	11,7	3,63	10,7	1,61	8,44	1,51	3,89	0,501	3,02	0,421	6,9	1,5	3,97	1,05
88PHA-7	22,3	53,9	7,36	33,3	8,76	1,84	9,23	1,37	7,29	1,28	3,22	0,424	2,5	0,365	4,2	0,77	1,72	0,6
88PHA-9	21,5	54,4	7,09	31,2	7,77	2,73	8,12	1,21	6,41	1,16	3,01	0,408	2,33	0,334	4,5	0,87	2,01	1,42
88PHA-10	17,4	40,9	5,38	25	6,28	2,22	6,38	0,96	5,13	0,93	2,47	0,32	1,92	0,279	4,1	0,67	1,82	0,49
88PHA-12	27,4	64,5	8,3	36,8	8,4	2,93	8,09	1,22	6,49	1,14	2,95	0,382	2,37	0,331	5,6	1,16	3,04	0,84
88PHA-38A	14,9	35,6	4,8	21,4	5,69	2,01	5,6	0,86	4,54	0,83	2,24	0,306	1,82	0,26	3,7	0,6	1,65	0,44
88PHA-38B	40,8	92,3	11,6	50,9	11,6	3,45	11,1	1,68	8,73	1,56	4	0,526	3,1	0,463	8,4	1,54	5,29	1,34
88PHA-39E	15,6	37,9	5,16	23,8	6,5	1,98	6,62	1,07	5,59	1,01	2,61	0,358	2,14	0,303	3,8	0,76	1,57	0,46
88PHA-39F	19,6	45,7	6,05	26,8	6,54	2,13	6,64	1	5,3	0,96	2,51	0,336	1,99	0,29	4,3	0,87	2,1	0,56
88PHA-39G	19,2	44,4	5,91	25,9	6,29	2,24	6,21	0,93	5,02	0,91	2,32	0,314	1,82	0,248	4,6	0,87	2,12	0,56
88PHA-39I	28,2	65,8	8,38	34,8	8,14	2,16	8	1,16	6,23	1,09	2,89	0,376	2,2	0,34	6,2	0,97	3,22	0,9
88PHA-39J	39,6	88,3	11,3	49,2	11,3	3,36	10,4	1,5	7,85	1,37	3,61	0,485	2,8	0,381	6,9	1,47	3,83	1,17
88PHA-39K	20,5	48,1	6,11	27,3	6,57	2,39	6,7	0,99	5,2	0,93	2,34	0,306	1,91	0,262	4,7	1,03	2,19	0,59
88PHA-39L	21,8	51,4	6,78	30,1	7,21	2,36	7,11	1,01	5,57	0,98	2,56	0,346	1,99	0,275	5	1,09	2,37	0,62
88PHA-39M	23,2	56,2	7,16	32	7,84	2,41	7,58	1,13	6,02	1,09	2,79	0,374	2,19	0,339	5,1	1,12	2,56	1,1
88PHA-39N	22,3	51,8	7,06	29,5	7,15	2,52	7	1,06	5,65	1,09	2,58	0,348	2,11	0,288	5,3	0,94	2,37	0,73
88PHA-44A	19,7	45,2	6,03	27,4	6,76	2,47	6,93	1,08	5,87	1,01	2,76	0,374	2,21	0,332	4,7	0,86	2,2	0,58
88PHA-46A	24,9	58,1	7,7	33,4	8,19	2,46	7,68	1,19	6,38	1,11	2,94	0,381	2,3	0,331	5,5	1,14	2,87	0,73
88PHA-47C	18,1	41,8	5,59	25	6,04	2,14	6,39	0,98	5,18	0,95	2,43	0,337	1,97	0,288	4	0,75	1,93	0,51
88PHA-48A	16,8	40	5,42	25,1	6,48	2,04	6,91	1,1	5,71	1,03	2,73	0,364	2,24	0,31	4,2	0,75	1,76	1,08
88PHA-49B	20,6	48,1	6,34	28,2	7	2,25	7,05	1,08	5,85	1,05	2,74	0,371	2,18	0,303	4,7	0,9	2,27	0,58
88PHA-50A	16,6	40,4	5,51	24,4	6,37	2,25	6,75	1,04	5,45	1,01	2,71	0,355	2,04	0,312	4,1	0,73	1,71	0,5
88PHA-50C	17,5	42,4	5,78	26,5	7,09	2,34	7,04	1,12	5,98	1,08	2,96	0,39	2,32	0,318	4,6	0,79	1,88	0,54
88PHA-99	29,4	69,6	9,24	40	9,82	2,94	10,6	1,68	10	2,01	5,57	0,782	5,25	0,796	7,6	1,45	2,83	0,79
88PHA-100	23,3	49,6	6,02	25,4	5,83	1,8	5,85	0,9	5,21	1,01	2,8	0,397	2,46	0,383	4,1	0,71	5,64	1,42

Sample	La	Ce	Pr	Nd	Sm	Eu	Gd	Tb	Dy	Ho	Er	Tm	Yb	Lu	Hf	Ta	Th	U
88PHA-101A	16,4	36,4	4,64	19,3	4,61	1,52	4,92	0,76	4,28	0,82	2,32	0,328	2,08	0,317	3,3	0,55	3	0,83
88PHA-102C	10,5	26,1	3,64	17,6	4,53	1,67	5,44	0,93	5,53	1,09	3,06	0,444	2,8	0,426	3,3	0,51	1,13	0,32
88PHA-102D	8,96	22,1	3,1	14,4	4,13	1,46	4,88	0,81	4,75	0,94	2,68	0,391	2,45	0,368	2,7	0,39	0,95	0,28
88PHA-104F	10,7	25,6	3,48	16,8	4,56	1,66	5,19	0,86	5,01	0,99	2,83	0,411	2,67	0,411	3	0,47	1,43	0,41
88PHA-104G	7,49	18,6	2,63	12,5	3,63	1,29	4,12	0,7	4,2	0,81	2,32	0,339	2,23	0,345	2,3	0,36	0,8	0,23
88PHA-106C	17,9	41	5,34	23,7	5,81	2	6,35	1	5,68	1,1	3,01	0,405	2,64	0,415	4,4	0,68	2,98	0,83
88PHA-107C	18,2	41,4	5,38	23,8	5,94	1,92	6,45	1,03	5,78	1,1	3,05	0,423	2,61	0,417	4,3	0,68	3,01	0,82
88PHA-115A	21,7	49,9	6,25	26,8	7,03	2,05	7,93	1,34	8,01	1,58	4,5	0,662	4,53	0,665	5,1	0,95	4,79	1,35
88PHA-115D	20,5	46,7	5,89	25,3	6,64	2,01	7,33	1,29	7,78	1,57	4,52	0,65	4,25	0,657	5	0,91	4,61	1,3
88PHA-116D	11	27,5	3,85	17,9	4,98	1,74	5,58	0,92	5,12	0,99	2,72	0,382	2,43	0,362	3,5	0,61	1,07	0,31
88PHA-207C	29,6	65,7	8,24	35,8	7,39	2,45	6,2	0,85	4,41	0,76	1,99	0,262	1,54	0,243	4,3	1,63	3,08	0,74
88PHA-511	28	63,4	7,9	33,9	6,92	2,55	6	0,81	4,27	0,76	1,96	0,269	1,63	0,241	4,2	1,58	3,03	0,64
88LAAT-218-5A	33,1	79,7	10,6	47,3	12,3	3,65	13,5	2,24	13	2,65	7,41	1,05	6,71	1,06	9,6	1,67	3,15	0,88
88LAAT-218-6A	25,9	61,9	8,32	37,6	9,76	2,92	10,6	1,77	10,7	2,05	6,03	0,876	5,98	0,896	7,3	1,58	2,52	0,75
86LAAT-319-2	41,5	95,3	12,3	53,4	12,3	4,05	11,9	1,84	9,65	1,74	4,42	0,591	3,67	0,541	8,8	1,49	6,14	1,68
86LAAT-319-1B	24,4	56,5	7,35	32,7	7,95	2,61	7,82	1,21	6,5	1,16	3,12	0,425	2,49	0,378	5,5	1,01	3,5	0,96
BL88-9	11,9	27,1	3,58	15,8	3,88	1,38	4,16	0,68	3,9	0,72	1,96	0,268	1,66	0,253	2,7	0,46	1,93	0,52
BL88-10	14,5	35,8	4,89	22,9	6,14	1,95	6,92	1,14	6,43	1,26	3,52	0,498	3,25	0,487	4,1	0,7	1,57	0,44
BL88-17	29	68,1	9,06	41,1	9,93	2,98	10,9	1,74	10,3	2,05	5,68	0,8	5,31	0,812	7,7	1,65	2,84	0,81
BL88-18	18,9	46,7	6,35	29,3	7,55	2,48	7,69	1,18	6,72	1,29	3,43	0,465	2,88	0,438	5,6	1,06	1,99	0,56
BL88-21	24,7	56,3	7,54	33,4	8,42	3,1	9,3	1,39	8,06	1,49	3,92	0,545	3,37	0,515	5,6	1,17	2,26	0,64
BL88-25	18	42,2	5,9	26,2	6,68	3,04	7,07	1,15	6,44	1,26	3,36	0,473	2,81	0,439	4,3	0,86	1,14	0,34
BL88-27	19,1	40,9	5,13	21,2	5,07	1,43	5,16	0,85	4,95	0,94	2,64	0,375	2,48	0,382	2,7	0,51	3,35	0,78
BL88-29	13,8	33	4,58	21,4	5,66	2,01	6,17	0,98	5,75	1,14	3,09	0,434	2,78	0,436	3,7	0,74	1	0,31
BL88-30	14,7	36,3	5,02	23,9	6,4	2,26	6,54	1,11	6,32	1,24	3,38	0,453	2,77	0,419	4,2	0,86	1,13	0,33
BL88-38	17,4	40,3	5,38	23,5	5,58	1,89	6,38	1,02	5,83	1,09	3,09	0,43	2,69	0,427	3,9	0,63	2,9	0,8
BL88-41	12,6	29	3,83	16,3	4,05	1,35	4,37	0,71	4,18	0,78	2,21	0,312	1,91	0,282	2,7	0,47	2,2	0,59
BL88-59	13,6	33,9	4,68	22,2	5,92	2,06	6,22	0,96	5,56	1,07	2,86	0,395	2,42	0,378	4	0,73	1,22	0,35
BL88-57	28,2	67,3	8,83	40,3	9,29	2,89	9,63	1,58	9,03	1,79	4,86	0,71	4,52	0,685	7	1,64	2,77	0,79

Sample	La	Ce	Pr	Nd	Sm	Eu	Gd	Tb	Dy	Ho	Er	Tm	Yb	Lu	Hf	Ta	Th	U
BL88-54	26,4	64,9	8,78	39,3	9,77	2,79	10,4	1,69	10,1	1,97	5,75	0,819	5,13	0,784	7,2	1,58	2,66	0,76
BL88-63	21,2	49,3	6,59	29,3	7,2	2,43	8,46	1,43	8,44	1,76	5,14	0,738	4,75	0,737	5,2	1,13	2,06	0,55
BL88-61	19,4	47,8	6,65	30,1	8,03	2,7	8,63	1,37	8,04	1,53	4,22	0,588	3,83	0,583	5,5	1,05	1,92	0,55
BL88-75	14	33,3	4,62	21	5,55	1,92	5,99	1,04	6,22	1,28	3,73	0,518	3,43	0,544	3,8	0,84	0,99	0,27
BL88-84	16	36,7	4,86	20,8	5,22	1,68	5,96	0,99	5,76	1,16	3,39	0,494	3,3	0,511	3,8	0,73	1,69	0,4
15WGA-W002	12,3	26	3,24	13,5	3,36	0,976	3,4	0,59	3,72	0,76	2,08	0,305	2	0,306	2,2	0,35	2,78	0,64
15WGA-L226	46	106	14,1	59,8	14,2	4,31	12,6	1,85	10,6	1,9	5,02	0,639	3,98	0,576	9,1	1,7	6,38	1,75
15WGA-W028	14,4	29,9	3,7	15,2	3,65	1,05	3,75	0,64	3,92	0,78	2,3	0,326	2,08	0,326	2,3	0,44	3,27	0,75
16WGA-S186	16,6	34,8	4,3	18,1	4,4	1,31	4,31	0,74	4,38	0,85	2,44	0,344	2,19	0,349	2,9	0,48	3,72	0,82
90-LAAT-32-2	12,4	26	3,29	13,7	3,37	1,21	3,7	0,61	3,7	0,69	1,99	0,287	1,8	0,273	2,7	0,31	2,61	0,54
M012	17,8	35,3	4,52	17,4	3,71	1,01	4,37	0,71	4,34	0,86	2,55	0,373	2,35	0,346	3	0,52	2,83	0,77
F089	18,7	38,4	4,88	18,6	4,05	1,14	4,34	0,72	4,5	0,94	2,75	0,415	2,65	0,396	3,1	0,56	3,07	0,78
M014	10,7	22	2,9	11,7	2,94	1,01	3,6	0,58	3,5	0,68	1,94	0,282	1,81	0,273	2	0,41	2,16	0,48
M085	11,5	29,4	3,76	15,1	3,46	0,976	3,67	0,56	3,27	0,64	1,74	0,238	1,47	0,214	1,6	0,35	1,75	0,96
F010	9,77	20,4	2,71	11,4	2,62	0,986	3,19	0,53	3,28	0,63	1,86	0,272	1,7	0,266	1,9	0,39	2,02	0,45
F015	10,7	21,6	2,89	12,1	2,99	1,07	3,61	0,56	3,33	0,66	1,91	0,274	1,67	0,254	2	0,41	2,08	0,47
W008	10,3	21,6	2,87	12	2,98	1,02	3,35	0,6	3,62	0,74	2,04	0,278	1,74	0,254	2	0,44	2,13	0,46
1550-5	10,5	22,4	2,72	11,8	2,81	1	2,82	0,46	2,86	0,55	1,54	0,216	1,39	0,21	1,9	0,36	2,01	0,37

Table A1.3: $^{143}Nd/^{144}Nd$ isotopic composition for the Mackenzie dyke swarm, and distal basalts and sills.

Sample	Rock type	Nd	Sm	$^{147}Sm/^{144}Nd$	$^{143}Nd/^{144}Nd$	2σ	εNd(i)	εNd (1270 Ma)	T_{DM}*
87PHA-CL-3	Mackenzie dyke	13,80	3,82	0,1672	0,512587	5,52E-08	-0,99	3,82	1,85
87PHA-CL-11	Mackenzie dyke	17,51	4,72	0,1628	0,512519	8,88E-08	-2,33	3,19	1,89
88PHA-38A	Mackenzie dyke	23,01	5,71	0,1501	0,512225	1,22E-07	-8,05	-0,47	2,21
88PHA-39F	Mackenzie dyke	27,08	6,57	0,1468	0,512252	7,90E-08	-7,53	0,60	2,04
88PHA-44A	Mackenzie dyke	26,49	6,50	0,1483	0,512317	1,03E-07	-6,25	1,62	1,94
88PHA-46A	Mackenzie dyke	33,05	7,81	0,1428	0,512156	8,29E-08	-9,41	-0,65	2,14
88PHA-47C	Mackenzie dyke	23,80	5,86	0,1490	0,512256	7,98E-08	-7,45	0,32	2,10
88PHA-48A	Mackenzie dyke	24,36	6,25	0,1551	0,512357	9,20E-08	-5,49	1,28	2,06
88PHA-49B	Mackenzie dyke	27,51	6,64	0,1459	0,512234	1,13E-07	-7,88	0,39	2,06
88PHA-50C	Mackenzie dyke	26,52	6,67	0,1520	0,512340	1,30E-07	-5,82	1,46	2,00
88PHA-99	Mackenzie dyke	40,42	9,64	0,1442	0,512333	1,08E-07	-5,95	2,59	1,79
88PHA-100	Mackenzie dyke	25,39	5,68	0,1352	0,511946	1,52E-07	-13,50	-3,51	2,33
88PHA-101A	Mackenzie dyke	20,87	4,87	0,1412	0,512018	8,33E-08	-12,10	-3,07	2,37
88PHA-104F	Mackenzie dyke	16,68	4,42	0,1603	0,512427	9,18E-08	-4,11	1,81	2,06
88PHA-115A	Mackenzie dyke	27,66	6,90	0,1509	0,512381	5,92E-08	-5,02	2,45	1,87
88PHA-115D	Mackenzie dyke	25,69	6,44	0,1516	0,512434	7,27E-08	-3,98	3,37	1,76
88PHA-116D	Mackenzie dyke	18,82	5,01	0,1611	0,512475	7,88E-08	-3,18	2,63	1,95
88PHA-207C	Mackenzie dyke	36,31	7,15	0,1190	0,512012	7,68E-08	-12,21	0,43	1,83
88PHA-511	Mackenzie dyke	35,88	7,08	0,1193	0,512005	8,48E-08	-12,35	0,24	1,85
88LAAT-218-5A	Mackenzie dyke	47,62	11,81	0,1499	0,512494	4,50E-08	-2,81	4,82	1,57
88LAAT-218-6A	Mackenzie dyke	38,80	9,68	0,1508	0,512496	8,94E-08	-2,77	4,72	1,58
86LAAT-319-2	Mackenzie dyke	53,50	11,91	0,1345	0,512176	3,00E-08	-9,02	1,10	1,87
86LAAT-319-1B	Mackenzie dyke	32,26	7,61	0,1426	0,512257	2,91E-08	-7,43	1,37	1,91
BL88-9	Mackenzie dyke	16,30	3,97	0,1472	0,512200	1,02E-07	-8,55	-0,50	2,18
BL88-17	Mackenzie dyke	41,96	9,98	0,1438	0,512416	1,48E-07	-4,34	4,29	1,60
BL88-25	Mackenzie dyke	27,55	6,78	0,1489	0,512256	9,26E-08	-7,45	0,34	2,10
BL88-30	Mackenzie dyke	24,08	6,20	0,1555	0,512509	5,78E-08	-2,52	4,19	1,68
BL88-38	Mackenzie dyke	23,43	5,77	0,1488	0,512163	7,55E-08	-9,27	-1,48	2,31
BL88-59	Mackenzie dyke	21,29	5,53	0,1569	0,512482	6,55E-08	-3,04	3,45	1,79

Sample	Rock type	Nd	Sm	$^{147}Sm/^{144}Nd$	$^{143}Nd/^{144}Nd$	2σ	εNd(i)	εNd (1270 Ma)	T_{DM}*
BL88-54	Mackenzie dyke	39,40	9,41	0,1444	0,512425	8,08E-08	-4,15	4,38	1,59
BL88-63	Mackenzie dyke	29,70	7,37	0,1500	0,512414	7,72E-08	-4,36	3,25	1,76
BL88-75	Mackenzie dyke	20,64	5,21	0,1526	0,512393	1,12E-07	-4,79	2,39	1,89
BL88-84	Mackenzie dyke	21,81	5,37	0,1489	0,512268	6,59E-08	-7,22	0,56	2,07
15WGA-W002C1	Mackenzie dyke	14,41	3,48	0,1460	0,512016	8,16E-08	-12,13	-3,90	2,55
15WGA-L226A	Mackenzie dyke	53,15	11,98	0,1362	0,512160	4,31E-08	-9,33	0,52	1,95
15WGA-W028A1	Mackenzie dyke	15,78	3,73	0,1427	0,511994	1,13E-07	-12,57	-3,80	2,48
16WGA-S186B1	Mackenzie dyke	19,38	4,51	0,1406	0,512112	8,19E-08	-10,25	-1,14	2,16
90-LAAT-32-2	Savage Point sill	13,55	3,32	0,1480	0,511943	5,21E-08	-13,56	-5,66	2,79
M012	Nyeboe basalt	18,04	3,88	0,1301	0,511853	3,19E-08	-15,30	-4,48	2,36
F089	Nyeboe basalt	17,97	3,76	0,1266	0,511831	3,55E-08	-15,74	-4,35	2,30
M014	Hansen sill	12,47	3,09	0,1498	0,512112	7,37E-08	-10,25	-2,63	2,47
M085	Hansen sill	17,13	3,69	0,1302	0,511779	4,43E-08	-16,76	-5,96	2,49
F015	Hansen sill	11,60	2,83	0,1474	0,512070	2,81E-08	-11,08	-3,06	2,47
W008	Hansen sill	11,80	2,93	0,1502	0,512093	2,08E-08	-10,62	-3,07	2,53
1550-5	Hansen sill	12,00	2,87	0,1447	0,512041	3,81E-08	-11,65	-3,20	2,44

*T_{DM} model is from DePaolo (1981)

Table A1.4: εNd isotopic composition for the Coppermine River Group compiled from Griselin et al. (1997) and Day et al. (2013).

Sample	Stratigraphic height	Stratigraphy	εNd (1270 Ma)
BLS-22-66	13,7	September Creek	-1,1
BLS-24-66	125	September Creek	-3,7
BLS-25-66	295,7	September Creek	-5,5
BLS-27-66	365,8	September Creek	-3,1
BLS-29-66	487,7	September Creek	1,7
BLS-31-66	539,5	September Creek	0,5
BLS-33-66	675,1	September Creek	0,7
BLS-6-66	960,1	September Creek	0,1
BLS-5-66	999,7	September Creek	0,6
BLS-3-66	1066,8	Stony Creek	4,1
BLS-2-66	1115,6	Stony Creek	3,0
BLS-17-66	1345,7	Stony Creek	3,5
BLS-18-66	1478,3	Stony Creek	4,4
BLS-15-66	1889,8	Stony Creek	3,5
BLS-42-66	2049,8	Burnt Creek	2,1
BLS-50-66	2164,1	Burnt Creek	4,5
BLS-44-66	2599,9	Burnt Creek	4,7
BLS-115-66	2703,6	Burnt Creek	0,9
BLS-113-66	2880,4	Husky Creek	3,5
BLS-112-66	3400	Husky Creek	4,2
BLS-156-66	3692	Husky Creek	4,5
BLS-157-66	3749	Husky Creek	3,6
BLS-158-66	4022	Husky Creek	4,4
BLS-160-66	4100	Husky Creek	4,5

ANNEXE B

DONNEES DU CHAPITRE II

Table A2.1: U-Pb isotopic data for zircons from dykes and sills in Baffin Island and Greenland from the UQAM/Geotop high-precision TIMS Lab.

Fraction	Zircon treatment	Composition				Dates (Ma)								Isotopic Ratios						
		Th/ U a	Pb* (pg) b	Pbc (pg) c	Pb*/ Pbc d	206Pb/ 238U e	±2σ abs	207Pb/ 235U e	±2σ abs	207Pb/ 206Pb e	±2σ abs	Corr. coef.	%disc f	206Pb/ 204Pb g	206Pb/ 238U h	±2σ%	207Pb/ 235U h	±2σ%	207Pb/ 206Pb h	±2σ%
Fury and Hecla dyke (FHD) (Lat: N 70°03'35.8486", Long: W 85°53'06.2635")																				
FHD_z2	CA* for 12h	1.04	6.59	0.23	29.03	708.89	0.56	712.9	2.7	726	11	0.315	2.31	1545	0.116241	0.083	1.0180	0.52	0.06355	0.5
FHD_z3	CA for 12h	1.31	155	0.32	489.14	718.1	1.2	719.02	0.99	721.9	1.4	0.943	0.52	24280	0.11784	0.18	1.0302	0.19	0.063434	0.055
FHD_z5	CA for 12h	1.44	245	1.07	229.92	717.3	1.1	718.5	1.2	722.4	3	0.807	0.72	11110	0.11769	0.16	1.0292	0.24	0.063451	0.14
FHD_z6	CA for 12h	1.03	58.7	0.30	192.97	717.7	1.5	718.2	1.3	719.8	2.4	0.889	0.29	10177	0.11777	0.22	1.0286	0.25	0.063372	0.11
FHD_z8	CA for 18h	1.08	31.3	0.25	122.60	715.34	0.63	717.5	1	724.3	3.4	0.577	1.24	6401	0.11736	0.094	1.0272	0.2	0.06351	0.16
FHD_z12	CA for 18h	0.89	3.75	0.26	14.48	713.5	1.4	717.6	4.9	730	20	0.200	2.31	806	0.11703	0.2	1.0273	0.95	0.06369	0.93
FHD_z13	CA for 18h	1.17	2.9	0.26	11.26	712.2	1.2	715.5	6.9	726	28	0.198	1.84	594	0.11682	0.18	1.023	1.3	0.06355	1.3
Dybbol sill (DS) (Lat: N 70°03'39.8734",Long: W 85°53'01.8631")																				
DS_z1	CA for 12h	1.08	21.4	0.24	91.16	715.48	0.80	718	1.2	725.9	4	0.630	1.44	4770	0.11738	0.12	1.0282	0.24	0.06355	0.19
DS_z3	CA for 12h	1.09	24.4	0.23	107.33	718.34	0.33	719.45	0.83	722.9	3.1	0.446	0.63	5602	0.117879	0.049	1.0311	0.16	0.063466	0.14
DS_z4	CA for 12h	0.98	10.4	0.22	48.09	716.3	1.1	718.9	1.9	727.2	6.7	0.495	1.5	2584	0.11752	0.16	1.0300	0.36	0.06359	0.32
DS_z5	CA for 12h	1.13	33	0.24	135.23	718.22	0.55	719.4	1	722.9	3.4	0.637	0.64	6983	0.117858	0.081	1.0309	0.2	0.063465	0.16
DS_z6	CA for 12h	1.23	13.5	0.22	61.8	717.01	0.83	719.1	1.5	725.6	5.4	0.478	1.19	3136	0.11765	0.12	1.0303	0.29	0.06355	0.25
DS_z7	CA for 12h	1.16	61.1	0.24	249.55	718.37	0.49	719.95	0.67	724.9	2	0.713	0.9	12797	0.117883	0.072	1.0320	0.13	0.063524	0.088
DS_z8	CA for 18h	1.06	8.95	0.28	31.66	717.81	0.48	719.6	2.4	725.3	9.7	0.249	1.03	1675	0.117787	0.070	1.0314	0.47	0.06354	0.46
DS_z9	CA for 18h	0.83	8.99	0.37	24.5	712.52	0.91	716.5	3.4	729	13	0.352	2.25	1354	0.11687	0.14	1.0251	0.66	0.06364	0.62

DS_z10	CA for 18h	1.25	40.1	0.40	100.33	717.82	0.64	718.4	1.1	720.3	3.6	0.582	0.34	5058	0.11779	0.094	1.0290	0.21	0.06339	0.17
DS_z11	CA for 18h	0.96	24.4	0.26	94.23	718.67	0.56	719.55	0.99	722.3	3.5	0.516	0.5	5062	0.117936	0.082	1.0313	0.19	0.06345	0.16
DS_z12	CA for 18h	1.07	25.5	0.25	100.71	719.3	1.1	720.3	1.2	723.4	3.4	0.725	0.58	5281	0.11804	0.16	1.0327	0.23	0.06348	0.16
Steensby Land sill complex (SLSC) (Lat: N 76°32'48,998", Long: W 68°32'8,921")																				
SLSC_z1	CA for 12h	0.91	10.1	1.10	9.19	712.3	1	713	7.5	715	31	0.019	0.42	516	0.11683	0.15	1.018	1.5	0.06324	1.5
SLSC_z3	CA for 12h	0.78	11.6	0.25	45.41	724.61	0.46	723.8	1.7	721.5	6.7	0.230	-0.44	2556	0.118966	0.067	1.0398	0.33	0.06342	0.32
SLSC_z4	CA for 12h	0.89	18.2	0.27	67.35	718.64	0.39	720.4	1.2	725.7	4.5	0.407	0.98	3683	0.117931	0.057	1.0329	0.23	0.06355	0.21
SLSC_z5	CA for 12h	0.80	7.88	0.23	34.57	714.56	0.43	717.5	2.3	726.8	9.2	0.316	1.68	1937	0.117224	0.064	1.0272	0.45	0.06358	0.43
SLSC_z6	CA for 12h	0.71	23.6	0.24	100.20	719.4	0.41	720.21	0.93	722.7	3.4	0.452	0.46	5705	0.118063	0.061	1.0326	0.18	0.06346	0.16
SLSC_z7	CA for 12h	0.69	14.6	0.24	59.6	720.5	0.42	720.6	1.5	721	5.6	0.460	0.07	3383	0.118253	0.061	1.0334	0.29	0.06341	0.26
SLSC_z9	CA for 12h	0.83	9.55	0.26	36.3	718.31	0.82	718.7	2.3	719.9	8.6	0.431	0.22	1999	0.11787	0.12	1.0295	0.44	0.06338	0.4
SLSC_z11	CA for 12h	0.66	4.01	0.26	15.32	715.84	0.92	716.4	4.9	718	19	0.395	0.31	889	0.11745	0.14	1.0249	0.94	0.06332	0.9
SLSC_z12	CA for 12h	0.75	9.33	0.26	36.38	718.44	0.82	720	2.2	725	8.5	0.356	0.9	2064	0.1179	0.12	1.0322	0.43	0.06353	0.4
SLSC_z13	CA for 12h	0.84	8.64	0.27	31.8	717.9	1.4	717.4	2.7	715.6	9.8	0.449	-0.32	1767	0.11781	0.21	1.0269	0.52	0.06325	0.46
Thule dyke (TD) (Lat: N 76°50'19.839", Long: W 70°15'28.282")																				
TD_z1	CA for 12h	1.53	12.7	0.37	34.13	700.1	1.9	695.7	3.8	681	13	0.620	-2.75	1635	0.11472	0.29	0.9840	0.76	0.06224	0.62
TD_z2	CA for 12h	1.45	12.3	0.29	41.83	714.97	0.67	715.8	2.1	718.4	8.2	0.324	0.48	2032	0.11729	0.099	1.0238	0.41	0.06333	0.38
TD_z3	CA for 12h	1.11	18.8	0.46	40.91	718.05	0.94	717.8	2.8	717	10	0.655	-0.14	2136	0.11783	0.14	1.0278	0.55	0.06329	0.47
TD_z4	CA for 12h	1.20	17.4	0.32	53.56	714.23	0.55	715.2	1.8	718	6.9	0.473	0.53	2734	0.117166	0.081	1.0225	0.36	0.06332	0.32
TD_z5	CA for 12h	1.65	14.8	0.91	16.24	714.4	1.3	714.6	5.2	715	21	0.201	0.13	770	0.11719	0.2	1.021	1	0.06324	0.99
TD_z7	CA for 12h	0.96	6.58	0.25	26.54	715.73	0.92	714.6	3	711	11	0.499	-0.65	1438	0.11743	0.14	1.0214	0.59	0.06311	0.54

a Th contents calculated from radiogenic ^{208}Pb and ^{230}Th-corrected $^{206}Pb/^{238}U$ date of the sample, assuming concordance between U-Pb Th-Pb systems.

b Total mass of radiogenic Pb.

c Total mass of common Pb.

d Ratio of radiogenic Pb (including ^{208}Pb) to common Pb.

e Isotopic dates calculated using λ238 = 1.55125E-10 (Jaffey et al., 1971) and λ235 = 9.8485E-10 (Jaffey et al., 1971).

f % discordance = 100-(100*($^{206}Pb/^{238}U$ date)/($^{207}Pb/^{206}Pb$ date))

g Measured ratio corrected for fractionation and spike contribution only.

h Measured ratios corrected for fractionation, tracer and blank.

*CA: Chemical abrasion

all common Pb was assigned the isotopic composition of the UQAM/Geotop laboratory blank with an isotopic composition of $^{206}Pb/^{204}Pb$= 18.508±0.288, $^{207}Pb/^{204}Pb$ = 15.385±0.224, $^{208}Pb/^{204}Pb$ = 37.626±0.558

Supplementary Text

Fury and Hecla Franklin intrusions

The Fury and Hecla basin in northwestern Baffin Island (Fig. A2.1) is one of four geographically separate but genetically related late Mesoproterozoic basins in northeastern Laurentia, collectively referred to as the Bylot basins (Fahrig et al., 1981). Lower volcanic units in the Bylot basin are believed to be coeval with the ca. 1.27 Ga emplacement of the Mackenzie LIP across northern Canada (LeCheminant and Heaman, 1989), and basin formation continued with the accumulation of clastic and carbonate sequences that yield Re-Os ages of deposition between ca. 1.1–1.0 Ga, and younger undated sedimentary strata. (Gibson et al., 2018; Greenman et al., 2021).

The Fury and Hecla Group comprises 2–6 km of prehnite-pumpellyite facies sedimentary and igneous mafic rocks, overlying a 2.5–3.0 Ga metamorphosed Archean basement (Chandler, 1988; Steenkamp et al., 2018; Fig. A2.1). The basin and surrounding basement are cut by numerous Neoproterozoic, NW-trending (~295°) mafic dykes, and the prominent Dybbol sill intruding the basin. Samples for U-Pb zircon analysis were taken from outcrops of the Dybbol sill and a nearby dyke on the Autridge Peninsula. Outcrops of the dyke and the sill did not show unambiguous cross-cutting relationships (Figs. S2A–B), but Chandler (1988) inferred that the dykes cross-cut the sills.

The dykes are 10 to 500 m thick, and the sill has a maximum thickness of 80 m (Chandler, 1988). The mafic intrusions are relatively unaltered, gabbroic rocks with fine- to coarse-grained, homogeneous, equigranular and ophitic textures, essentially composed of plagioclase and clinopyroxene with minor olivine in the sill (Figs. S2C–D), and have accessory magnetite, apatite, zircon and baddeleyite. The dykes have traces of chalcopyrite and ilmenite.

Previous K-Ar dating of the dykes and the sill yielded ages of 746 to 631 Ma, respectively, leading to their correlation with the Franklin igneous event (Chandler and Stevens, 1981; Fahrig et al. 1971; Palmer and Hayatsu 1975). Geochemical data show that the rocks are compositionally similar to those of Franklin lavas, dykes and sills, yielding 48–52% SiO_2, 2–5.5% Na_2O+K_2O, 3–6.5% MgO (Dybbol sill is 10% MgO), and 1–2.75% TiO_2 compositions (Dufour et al., 2021). Trace element ratios (Dufour et al., 2021) indicate that the Fury and Hecla intrusions were derived from an enriched mantle source that underwent minor crustal contamination comparable to that seen in the Natkusiak basalts/sills (Beard et al., 2017) and Franklin dykes and sills in northern Canada (Dostal et al., 1986; Shellnutt et al., 2004).

Thule Franklin intrusions

The Thule Basin in northwestern Greenland is the easternmost expression of the Bylot basins (Fig. A2.2). It consists of a 6 km sequence of prehnite-pumpellyite facies sedimentary and mafic volcanic rocks comprising the Mesoproterozoic Thule Supergroup, which overlies ca. 2.91 to 1.92 Ga high-grade metamorphic rocks (Dawes, 2006). The Neoproterozoic, mafic, Thule dyke (TD) swarm and the Steensby Land sill complex (SLSC) cut both the Archean–Paleoproterozoic basement and the Thule Supergroup strata (Fig. A2.3).

The studied sills are located between Moriusaq and Pituffik (Thule Air Base). They range from a few meters to 100 m thick, are consistently cut by the faults of the Thule half-graben system, show columnar-jointing, and intrude the Mesoproterozoic sandstone and carbonate of the Dundas Group (Dawes, 2006). The dykes trend WNW–ESE, cut the SLSC (Fig. A2.4A), and are parallel to and/or exploit the faults of the Thule half-graben system, although one fault is seen to cross-cut the dykes (Dawes, 2006, Fig. 37). The dykes are 1–200 m thick, form prominent ridges, and display dyke bifurcation, minor dykes, and locally, cross-cutting relationships. A U-Pb sample of the Thule dyke was taken on the west shore of Grandville Fjord where it cuts an SLSC sill (Figs. A2.S3 and S4A). A sample of an SLSC sill with a more evolved magmatic phase was collected SE of the Thule Air Base (Figs. A2.S3 and S4B).

The dykes and the sills are fine- to coarse grained gabbros and melagabbro (cumulates at the base of sills) with homogeneous to porphyritic, ophitic textures showing variable degrees of alteration. Mineralogy is mainly plagioclase and clinopyroxene, with local occurrences of K-feldspar and interstitial quartz (Figs. S4C–D), ilmenite, minor biotite, hornblende, chalcopyrite, calcite, and accessory phases including apatite, zircon, baddeleyite, and titanite (Denyszyn et al., 2009a; Dawes, 2006).

The trace element geochemistry is similar to Franklin dykes, sills and volcanic rocks in Canada, however the Thule dykes and sills have the highest TiO_2 composition of the Franklin igneous suite, possibly indicating a greater degree of differentiation and/or differences in the magma sources (Dufour et al., 2021). Previous paleomagnetic data and U-Pb baddeleyite ages of the Qannaaq dyke (721 ± 4 Ma) and the SLSC 'Grandville fjord' sill (712 ± 2 Ma) linked the Thule intrusions to the Franklin event (Denyszyn et al., 2009a). However, the dykes typically cut the sills (Dawes, 2006; Fig. A2.4A), and the new U-Pb zircon ages presented here support the field relationships.

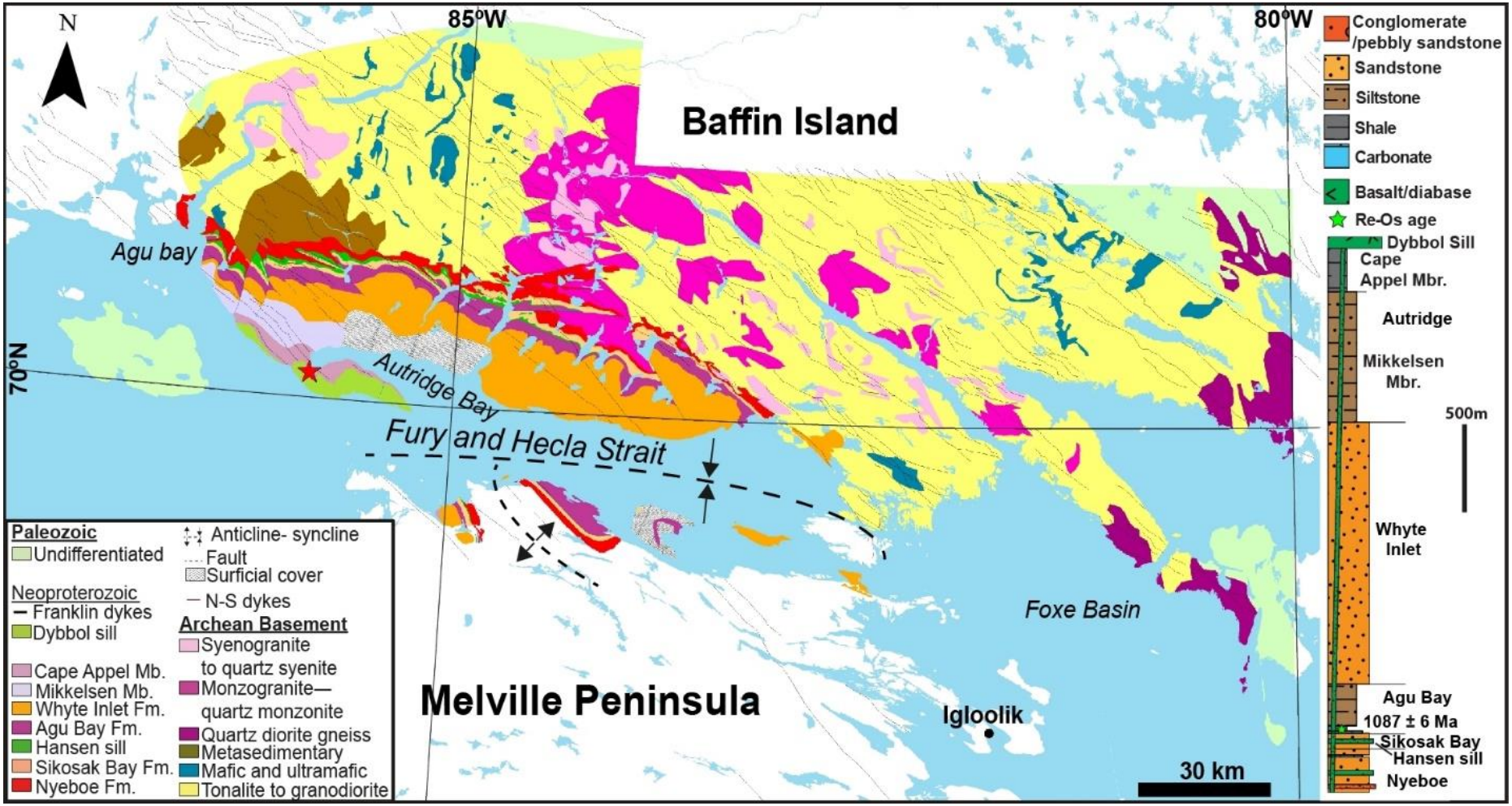

Figure A2.1: Geological map of Fury and Hecla Basin and the Archean basement. The Paleozoic rocks and the Fury and Hecla Basin are adapted from Chandler (1988), Long and Turner (2012) and Greenman et al. (2020). The Neoproterozoic Franklin intrusions and the Archean basement are adapted from Steenkamp et al. (2018) and Dufour et al. (2020). Red star indicates location of the U-Pb ages of the Fury and Hecla dyke and Dybbol sill. Inset figure is the stratigraphy of the Fury and Hecla Basin after Chandler (1988) and Greenman et al. (2021).

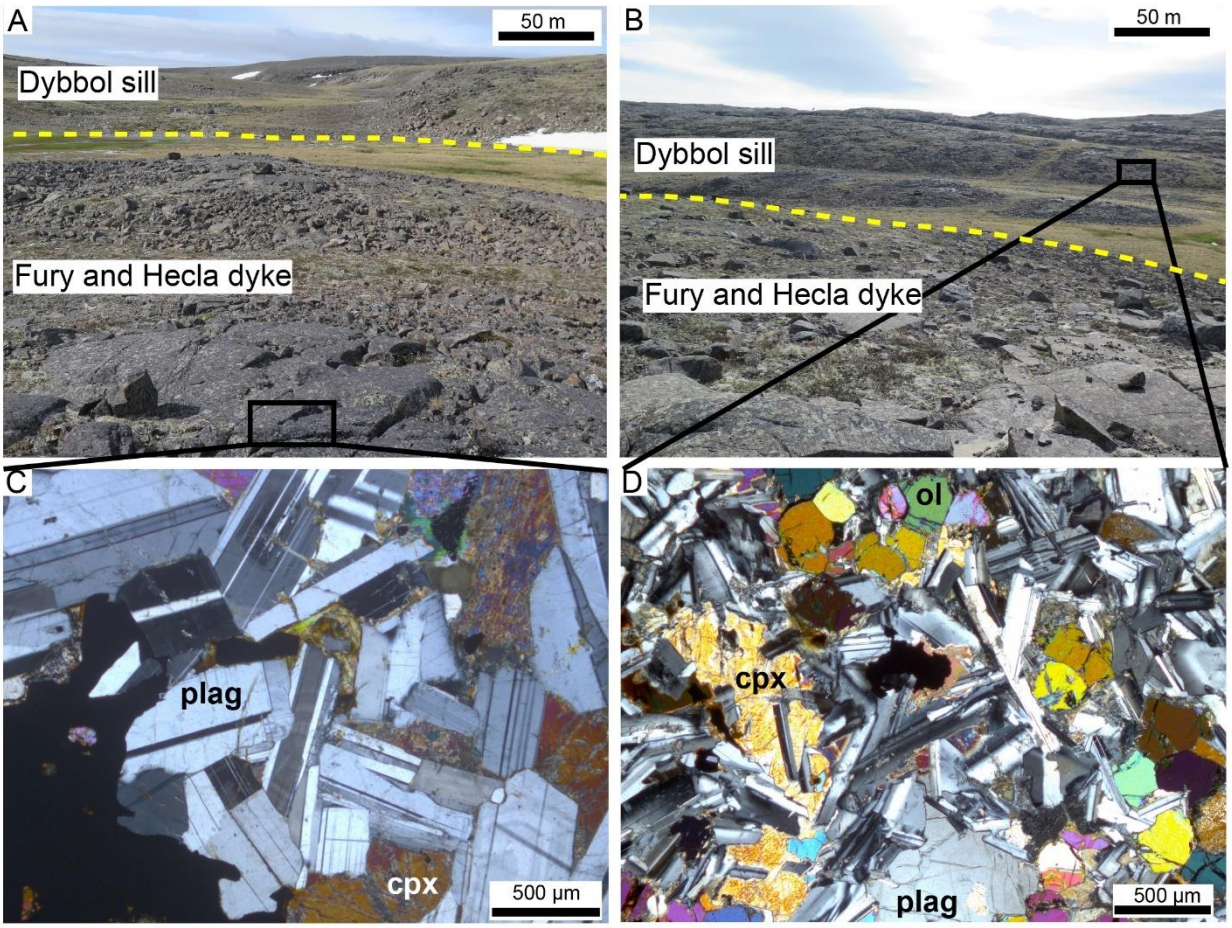

Figure A2.2: Field and thin sections photographs of the Dybbol sill and Fury and Hecla dyke. Outcrops of the gabbro dyke and sill intruding the Cape Appel member. However, cross-cutting relationships are not observed in the field but can be inferred from maps and remotely sensed imagery. (A) View is northwest. (B) View is north. (C) Thin section photomicrograph of the Fury and Hecla dyke; gabbro composed of plagioclase and clinopyroxene (cross-polarized light, 5X magnification). (D) Thin section photomicrograph of the Dybbol sill; gabbro containing plagioclase, clinopyroxene and small amounts of olivine (cross-polarized light, 5X magnification). Plag, plagioclase; Cpx, clinopyroxene.

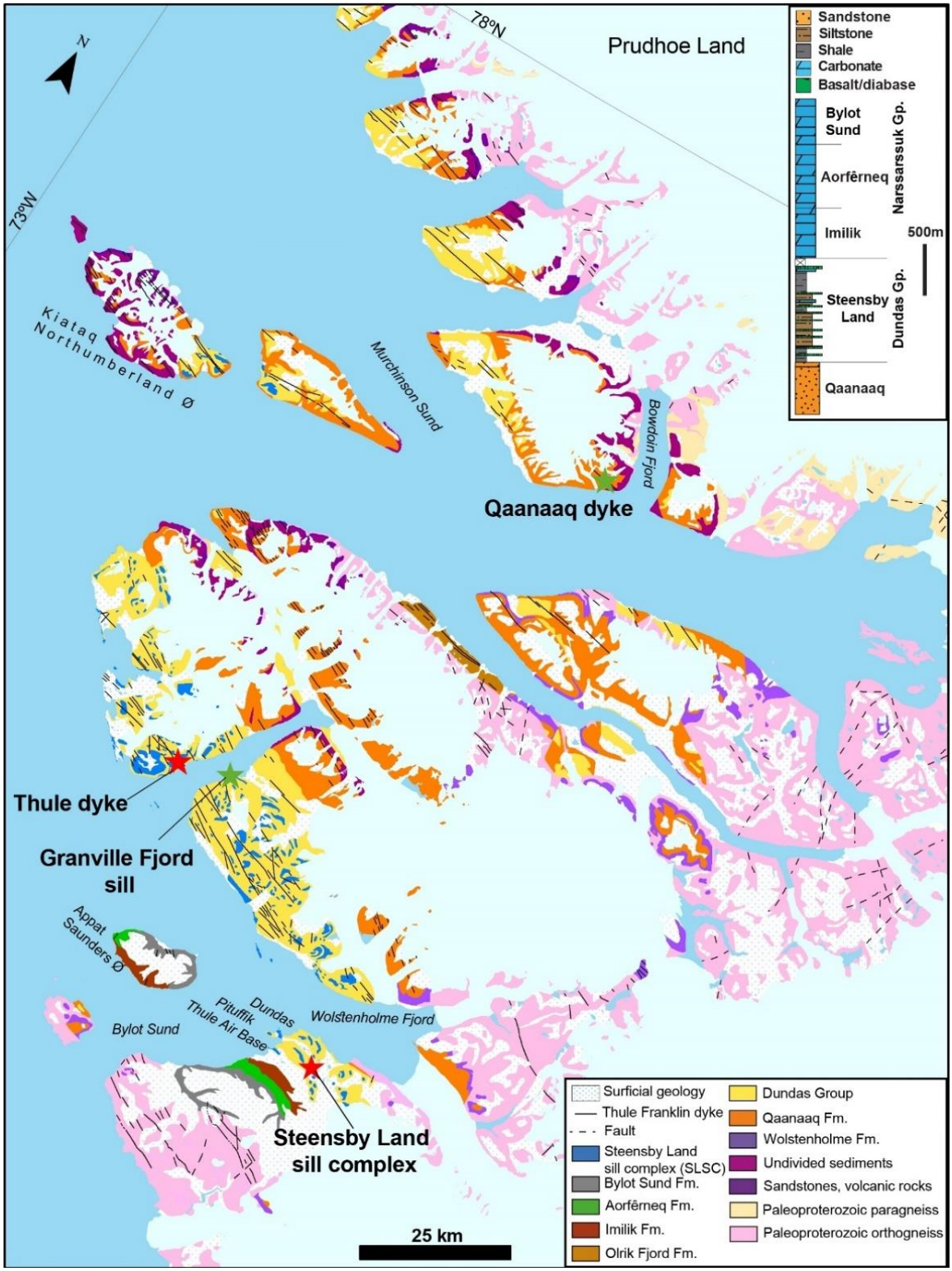

Figure A2.3: Geological map of the Thule area modified from Geological Survey of Denmark and Greenland. Inset figure is the stratigraphy of the Thule Basin after Dawes (1997).

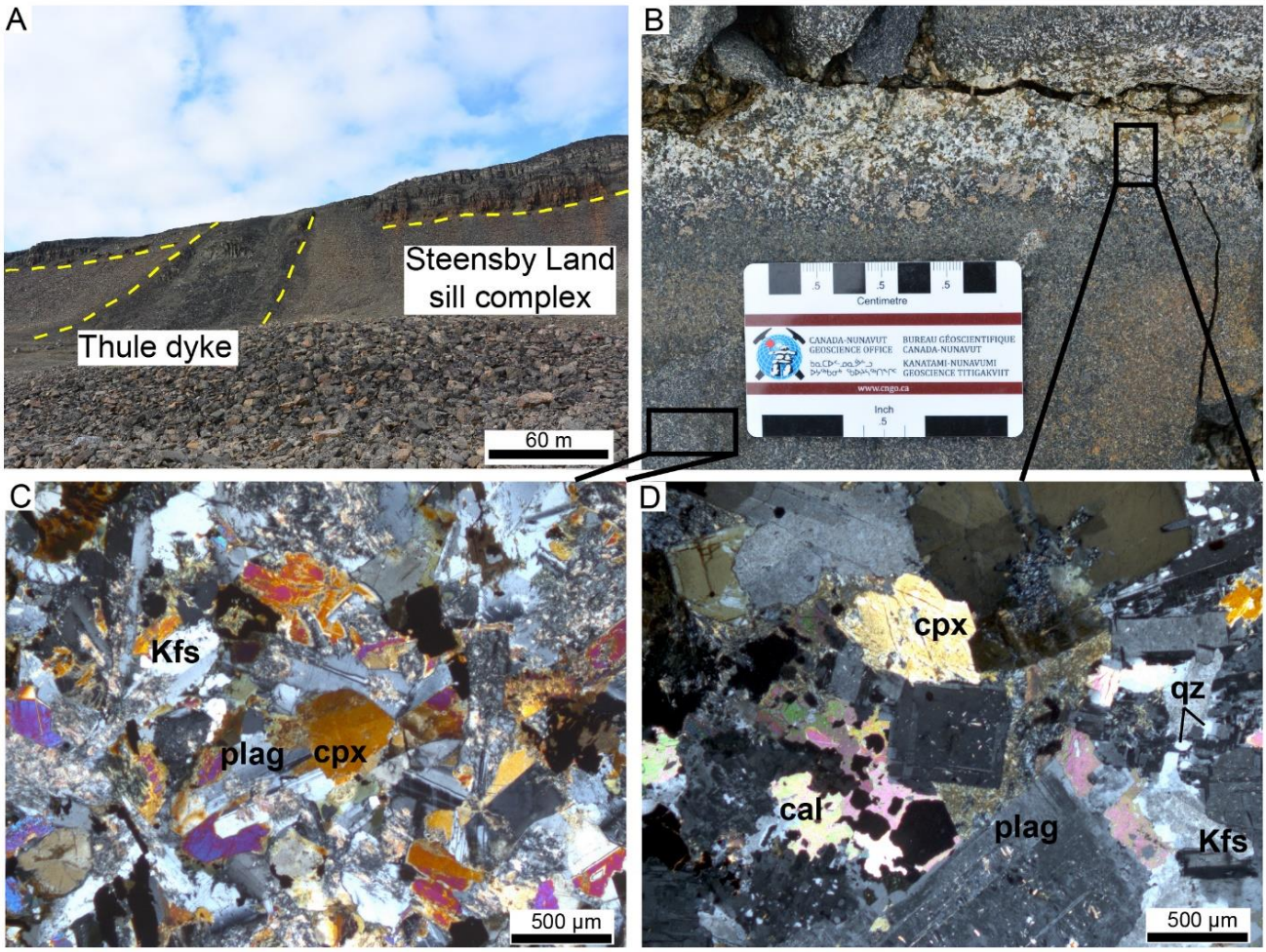

Figure A2.4: Field photograph of the Steensby Land Sill Complex (SLSC) and Thule dyke, and thin section photomicrograph of the sill. (A) A Thule dyke cutting the sill in the west of Grandville Fjord. (B) Outcrop of a more evolved part of the SLSC sill southeast of the Thule Air Base. (C) Photomicrograph showing a melanocratic phase of the SLSC sill containing plagioclase, clinopyroxene, and K-feldspar (cross-polarized light, 5X magnification). (D) Photomicrograph of the leucocratic phase of the SLSC sill containing plagioclase, clinopyroxene, K-feldspar, interstitial quartz, and calcite (cross-polarized light, 5X magnification). Plag, plagioclase; Cpx, clinopyroxene. Kfs, K-feldspar; Qz, quartz; Cal, calcite.

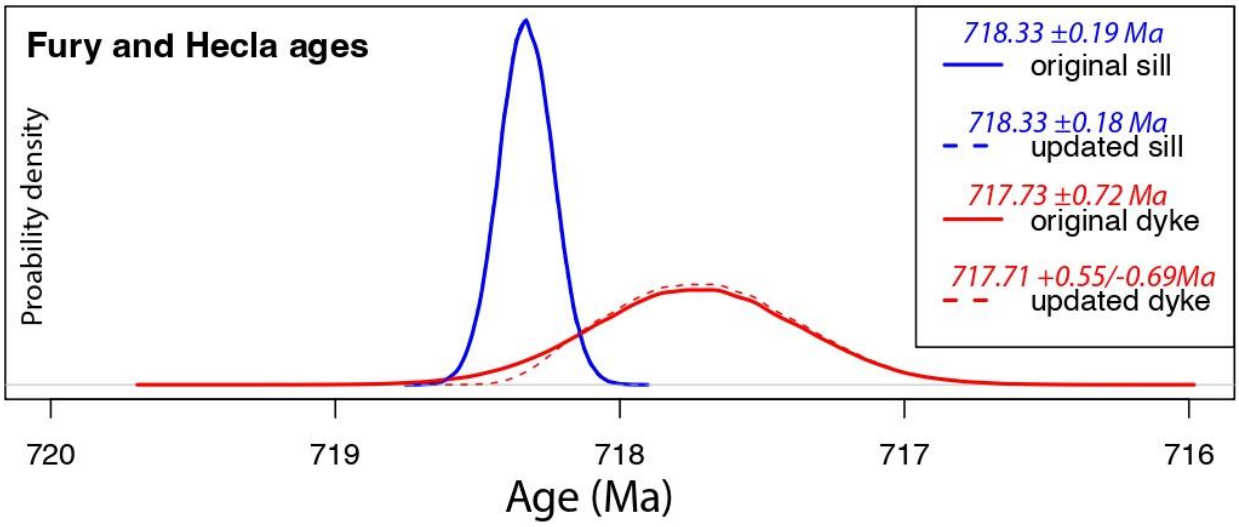

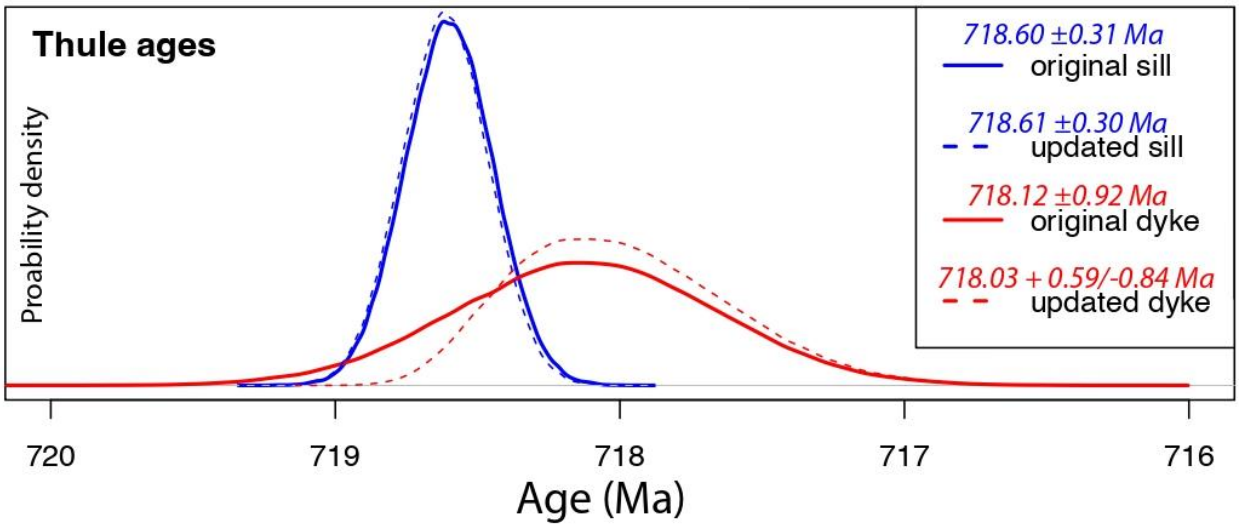

Figure A2.5: Comparison of the updated and original age distributions for the Fury and Hecla and Thule sills and dykes.

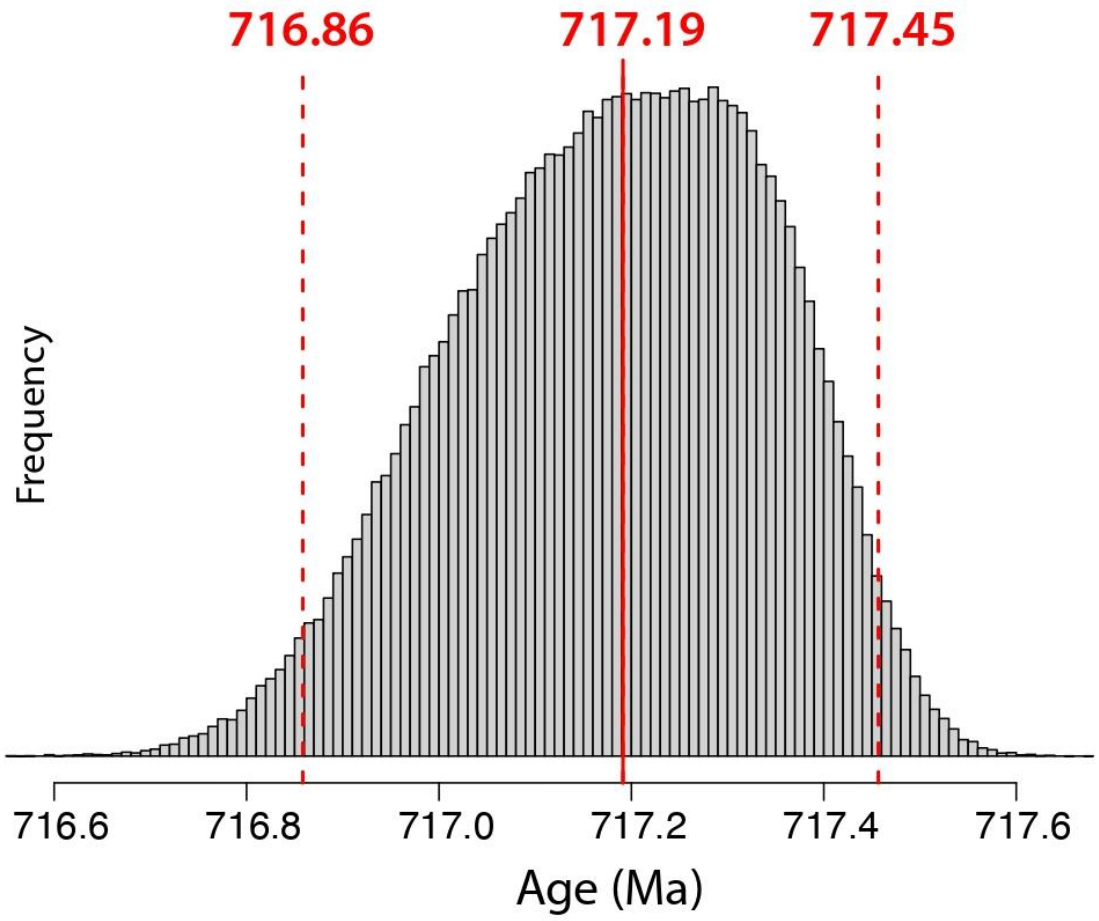

Figure A2.6: Age estimate for the boundary between pre- and syn-glacial strata at Mount Harper in the Ogilvie Mountains. Solid red line is the median age; dashed lines define the 95% confidence interval.

A2.7. R Code for the updated Fury and Hecla and Thule dykes and sills and age estimate for the onset of Sturtian glaciation

This is an R Markdown Notebook. When you execute code within the notebook, the results appear beneath the code.

Execute the code by clicking the *Run* button within the chunk or by placing your cursor inside it and pressing *Cmd+Shift+Enter*.

Add a new chunk by clicking the *Insert Chunk* button on the toolbar or by pressing *Cmd+Option+I*.

When you save the notebook, an HTML file containing the code and output will be saved alongside it (click the *Preview* button or press *Cmd+Shift+K* to preview the HTML file).

The preview shows you a rendered HTML copy of the contents of the editor. Consequently, unlike *Knit*, *Preview* does not run any R code chunks. Instead, the output of the chunk when it was last run in the editoris displayed.

Set up by closing R's graphics windows and clearing R's memory

Next we will install packages we will need and define a few functions used later in the code.

```
library(dplyr)
```

```
##
## Attaching package: 'dplyr'
## The following objects are masked from 'package:stats':
##
##         filter, lag
## The following objects are masked from 'package:base':
##
##         intersect, setdiff, setequal, union
```

```
library(scales)
```

```
# This function generates a median age and the plus and minus uncertainties using quantiles.
  This function generates uncertainties at the 95% level allowing for non-Gaussian distributions.
age_calc <- function(agesamples, prob=0.95){
q <- quantile(agesamples, c(0.5, 0.025, 0.975))
boundarymedian <- q[1]
boundaryplus <- q[3]-q[1]
boundaryminus <- q[1]-q[2]
return(as.vector(c(boundarymedian, boundaryplus, boundaryminus)))
}

# This function generates text describing the age and uncertainty in terms of the familiar +/-
convention typically used in geochronology.
age_print <- function(params){params =
params

age <- paste(round(params[1],2) %>% as.character, "+", round(params[2],2) %>% as.character, "/-",
```

```
round(params[3],2) %>% as.character, "Ma")
return(age)
```

We generate the dataframe used by the code here in order to avoid the issue of co-locating a data file andthis .Rmd file.

```
#all data are from Macdonald et al. (2018, Precambrian Research)

means <- data.frame("Rank"=1:5, "Id" = c("F837A", "F837C", "F837B", "F917-1", "F840A"), age =
c(717.85, 717.68, 717.43, 716.94, 716.47), "age_err95" =
```

```
##   Rank     Id    age age_err95
## 1    1  F837A 717.85      0.24
## 2    2  F837C 717.68      0.31
## 3    3  F837B 717.43      0.14
## 4    4 F917-1 716.94      0.23
## 5    5  F840A 716.47      0.23
```

```
dur <- length(means$age)
# We need to convert 95% uncertainty to 1-sigma for the purpose of this analysis since it
will be done based on standard deviations.
```

Now let's define the likelihood function, assuming the ages are all normal distributions.

```
ln_likelihoods <- function(t){ll <-
matrix(0,dur,1)
for (s in 1:dur){

ll[s] <- dnorm(t[s],mean=means$age[s],sd=(means$age_err95[s])*sd_corr/2, log=T)
}
```

We will also plot the likelihood functions.

```
age_axis <- seq(716,719, by=0.01) # Changes based on data set

len <- length(age_axis) ageAxis <-
matrix(0,dur,len)

for(i in 1:len){

ln_ages <- matrix(0,dur,len)

for(i in 1:len) {

ln_ages[,i] <- 10^(ln_likelihoods(ageAxis[,i]))

}

plot(age_axis,ln_ages[1,], type="l",col=i,xlab="Age [Ma]", ylab="Likelihood", yaxt = "n")
```

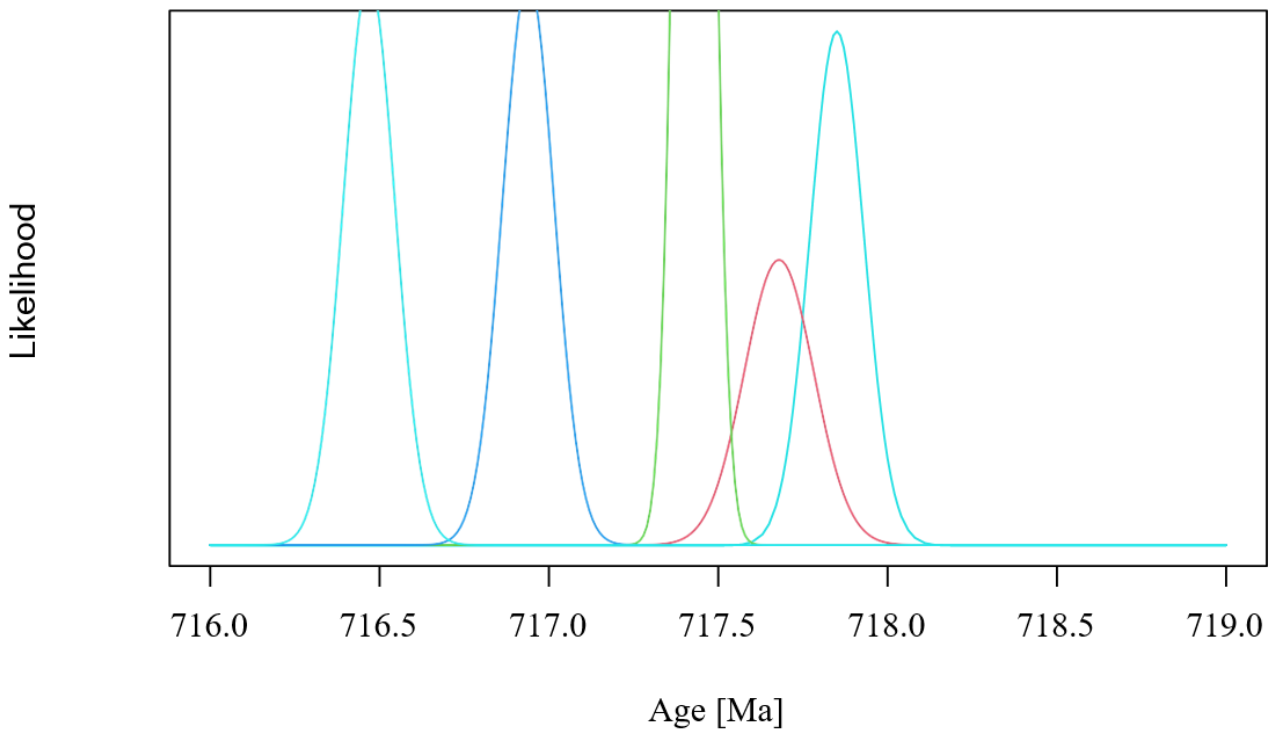

Now we will start to set up our MCMC. First we need to define the likelihood function taking into account all of the ages.

```
ln_likelihood = function(params){ sumll
<-                sum(ln_likelihoods(params))
return(sumll)
}
```

Our prior function (1 if the samples obey superposition, 0 if not)

```
ln_prior <- function(params){

for (i in seq(1,length(params)-
1)){t_prior<- params[i]
  t_next<-params[i+1]if
    (t_prior>t_next){if
       (i==(dur-1)){
      ln_pr <- log(1)
        }else{

t_prior <- t_next
          next

}
```

```
# This is to test whether or not the post function is working.
# ln_post(c(717, 724, 732, 740, 745, 753))
```

```
## [1] 0
```

Next the posterior will be calculated: the posterior = likelihood x prior *(but add them since they are the log values)*

```
ln_post <- function(params){

post <- ln_likelihood(params) + ln_prior(params)
return(post)
```

Create the proposal function.

```
proposalfunction <- function(param){

# The sd values for the proposal function must be calculated depending on the age type#
We will just use 0.05 m.y. for each

sd_vals <- rep(0.05, dur)
```

And now for the MCMC function, which will store the posterior values in chains (1 for each age)

```
run_metropolis_MCMC <- function(startvalue, iterations){chain
= array(dim = c(iterations+1,dur))
chain[1,] = startvalue
for (i in 1:iterations){

proposal = proposalfunction(chain[i,])
probab = exp(ln_post(proposal) - ln_post(chain[i,]))
if (runif(1) <
probab){chain[i+1,] = proposal
}else{
```

Now to set our start values and start the chain. Retry as needed. If it fails, it is because the start samples don't obey superposition.

```
startval <- rnorm(5, mean=means$age, sd=means$age_err95/4)

chain = run_metropolis_MCMC(startval, 30000)

burnIn = 1000
```

#Summary calculations of the posterior distributions:

```
yukon_updated <- data.frame(matrix(nrow=dur,ncol=3))
updated <- vector()
for (i in 1:dur){

yukon_updated[i,] <- age_calc(chain[-(1:burnIn),i])
```

Now to plot the results

```
#histograms
```

```
for (i in 1:dur){
hist(chain[-(1:burnIn),i],nclass=50, main=updated[i], xlab=paste("Updated age for ", means$Id[i]))abline(v =
yukon_updated[i,1], col="red", lwd=2)
}

#chain plots
par(mfrow = c(2,3))
```

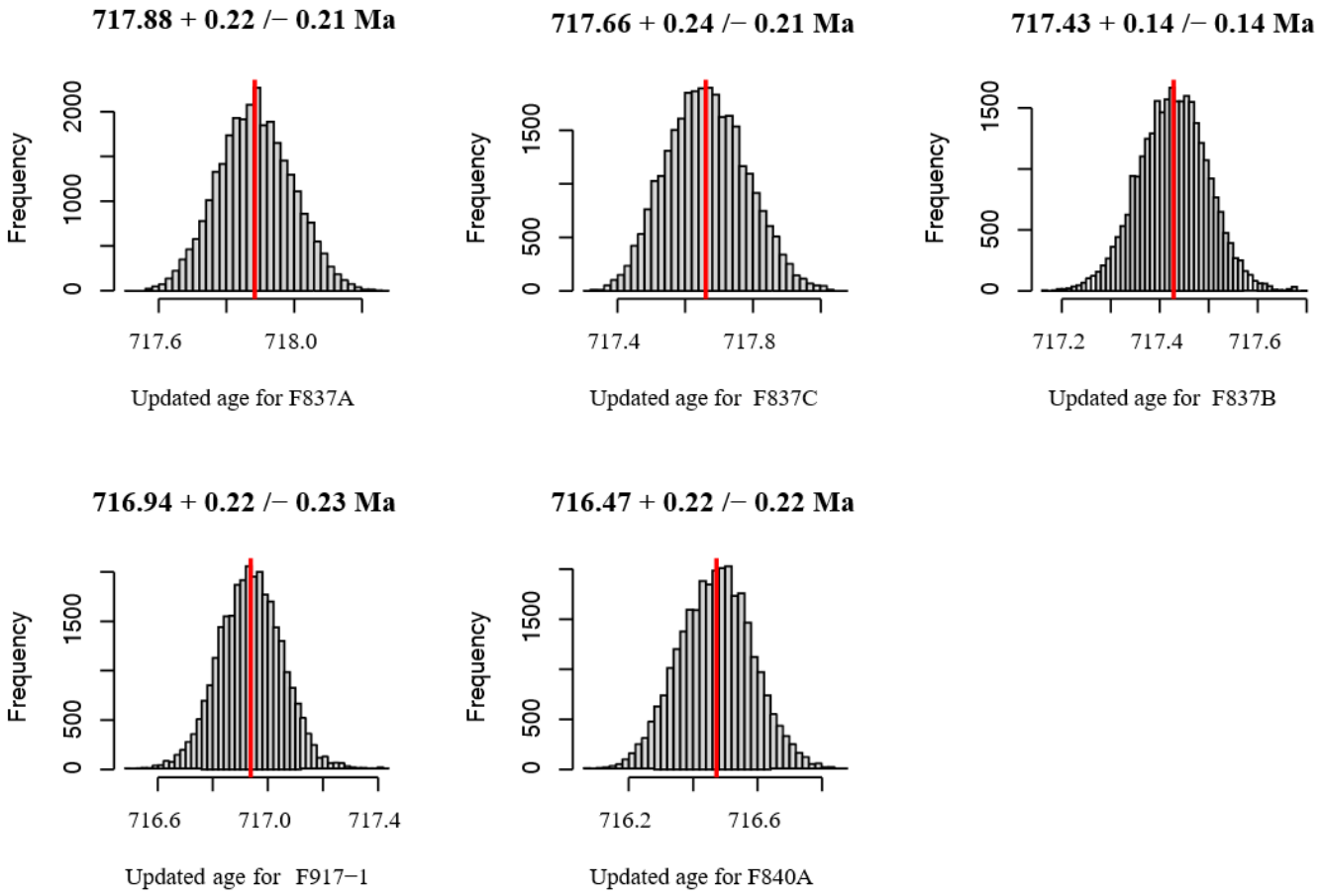


```
for (i in 1:dur){

plot(chain[-(1:burnIn),i], type = "l", xlab="Median is red line" , main = paste("Chain values for ",
means$Id[i]))
abline(h = yukon_updated[i,1], col="red", lwd=2)
}
```

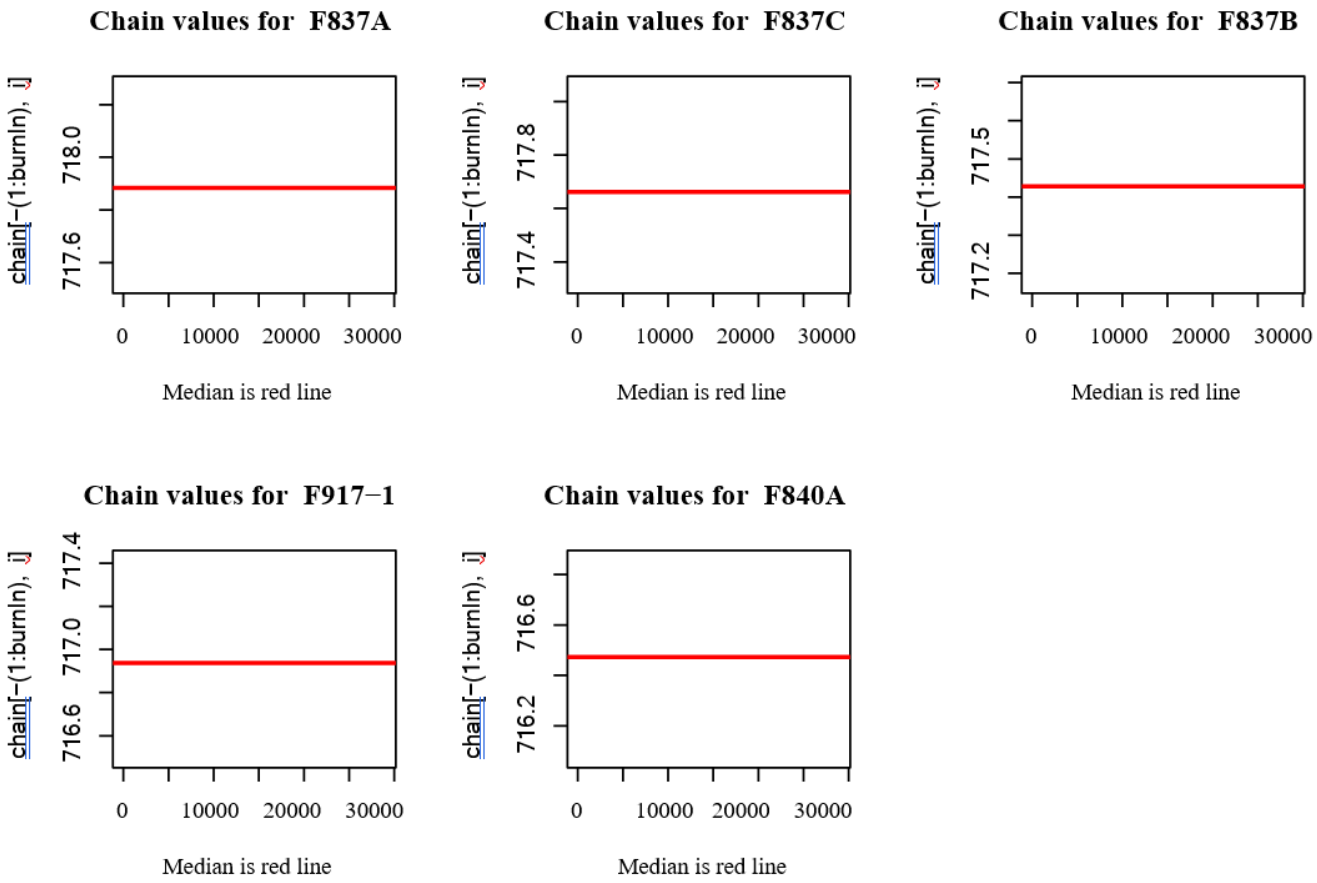


```
for (i in 1:dur){
plot(age_axis, ln_ages[(i),]/max(ln_ages[(i),]), ylim=c(0,1), type="l", col="blue", main=paste("Upda
#dens(chain[-(1:burnIn),step], col="red", norm.comp=FALSE, add=TRUE)
lines(density(chain[-(1:burnIn),i]), col="red")
}
par(mfrow = c(1,1))
```

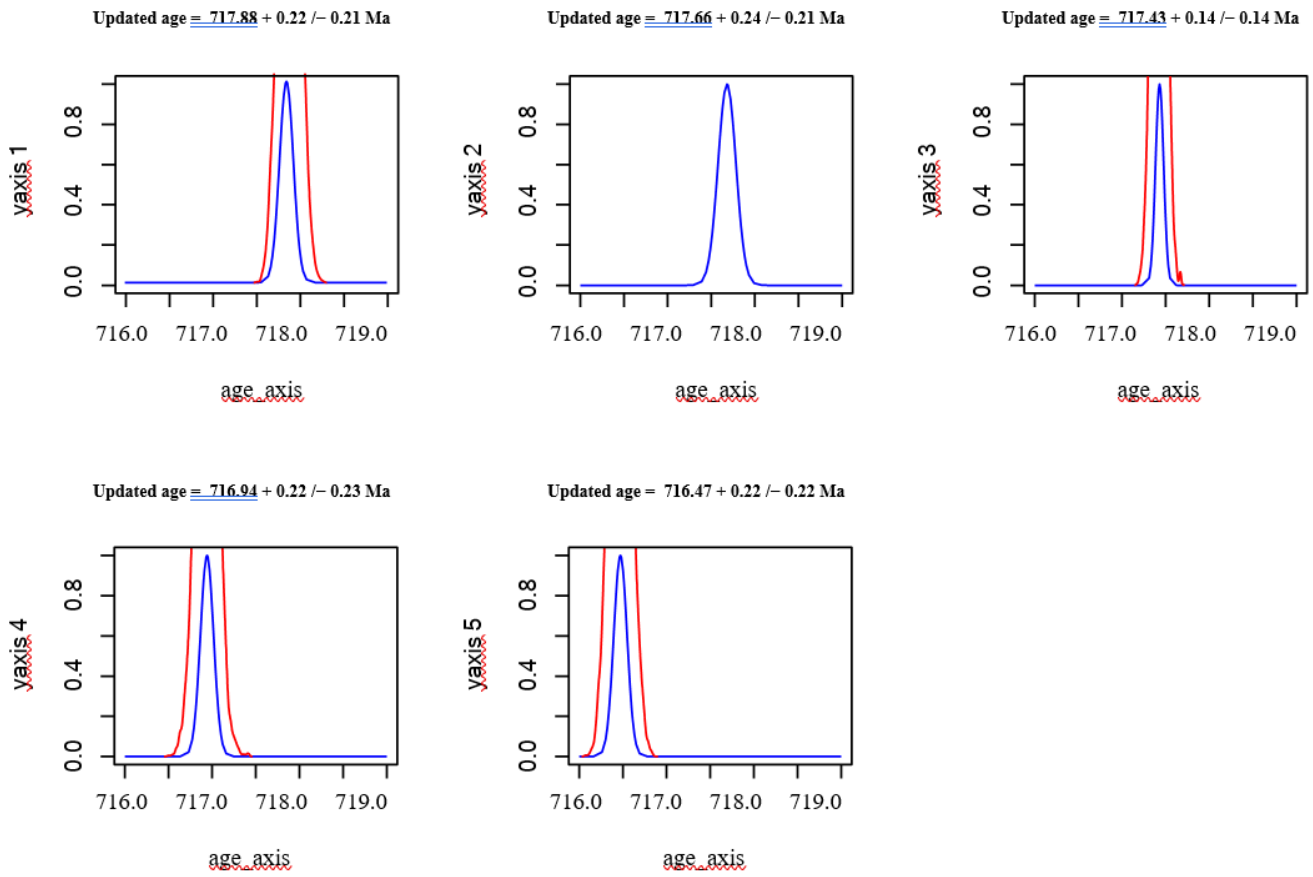

Now we will use the results from the two updated ages above and below the boundary to estimate the age of the boundary. To do this, we will run a MC simulation, sampling from each age distribution n times. Each time we have an age distribution that obeys stratigraphic superposition, we will simply take a random sample from a uniform distribution between the two ages (above and below).

```
#Note that we are assuming a normal distribution for these two update ages for the purpose of resampling because I can generate more numbers.
upperAge <- yukon_updated[4,1] # This is the uppermost pre-glacial age
upperSd <- (yukon_updated[4,2]+yukon_updated[4,3])*sd_corr/4 # And this is its standard deviation
lowerAge <- yukon_updated[3,1] # This is the lowermost post-glacial onset age
lowerSd <- (yukon_updated[3,2]+yukon_updated[3,3])*sd_corr/4 # And this is its standard deviation


sampnum <- 500000 # number of random samples for each age#
Sample from a normal distribution of each
upper_sample <- rnorm(sampnum, mean = upperAge, sd = upperSd) # generate random samples
lower_sample <- rnorm(sampnum, mean = lowerAge, sd = lowerSd)
```

Now to test for superposition and generate a sample of viable ages for the boundary.

```
n <- sum(upper_sample < lower_sample) # calculate number of samples that do not contradict superposition


c <- 1

boundaryage <- vector(mode="numeric", length=n)

for ( i in 1:sampnum ) {

if (upper_sample[i] < lower_sample[i]) {

boundaryage[c] <- runif(1, min=upper_sample[i], max=lower_sample[i])c <- c + 1
```

```
rm(upper_sample, lower_sample)
```

And now we calculate the summary statistics

```
# First, extract the median and the 2.5% and 97.5% quantilesq
<- quantile(boundaryage, c(0.5, 0.025, 0.975)) boundary_median <- q[1]
boundaryminus <- q[1]-q[2]
boundaryplus <- q[3]-q[1]
boundary <- paste(round(boundary_median,2) %>% as.character, "+", round(boundaryplus,2) %>% as.characte
```

And we plot the results

```
hist(boundaryage, nclass=100, xlab="Age (Ma)", main=paste("Age of onset of Sturtian glaciation =", bounabline
(v=q[1], col="red", lwd=2, lty=1)
abline(v=q[2], col="red", lwd=2, lty=2)
abline(v=q[3], col="red", lwd=2, lty=2)
```

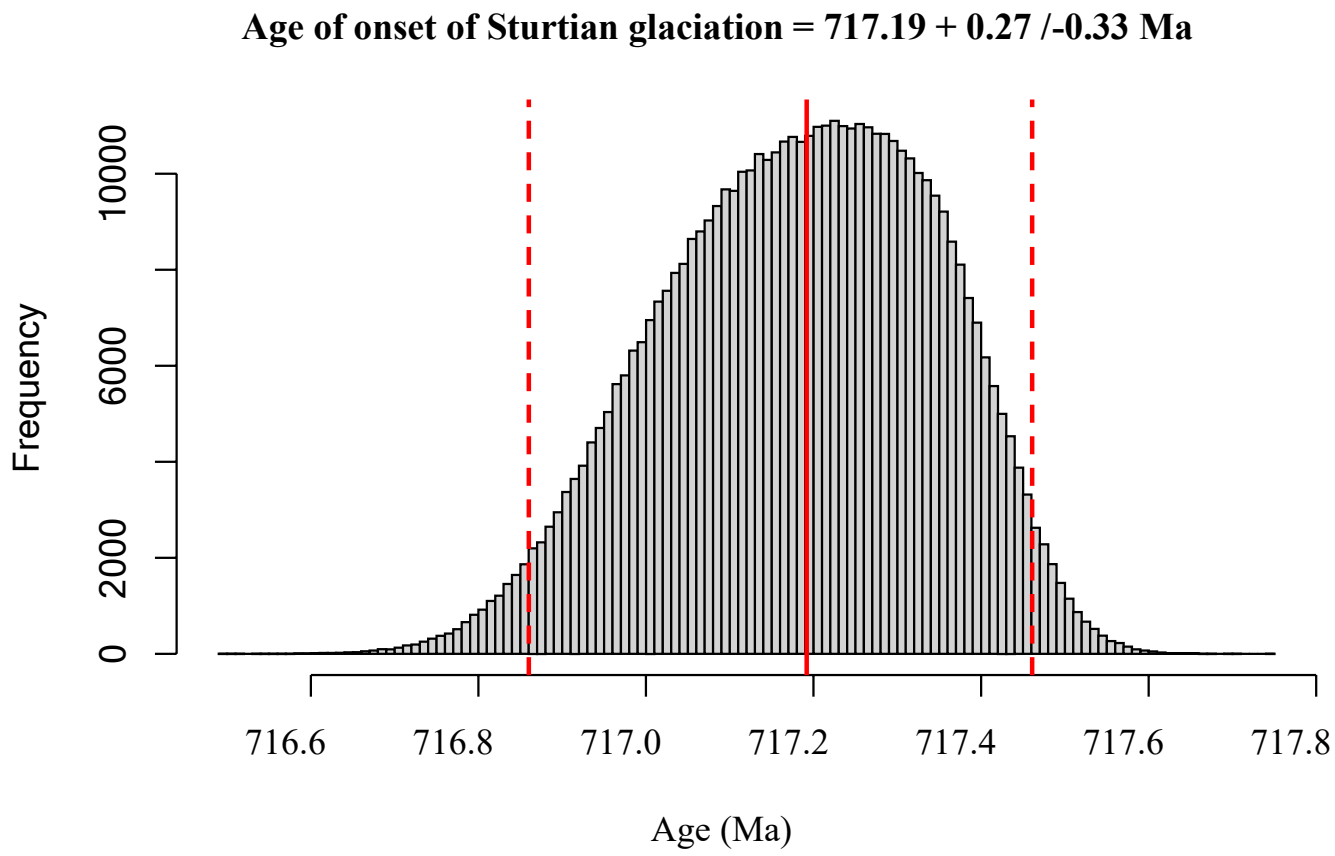


```
plot(density(boundaryage), xlab="Age (Ma)", main=paste("Age of onset of Sturtian glaciation =", boundar
polygon(density(boundaryage), col=alpha("red", 0.2))
abline(v = boundary_median, col="black", lwd=2, lty=2)abline(v =
q[2], col="black", lwd=1, lty=2)
abline(v = q[3], col="black", lwd=1, lty=2)
```

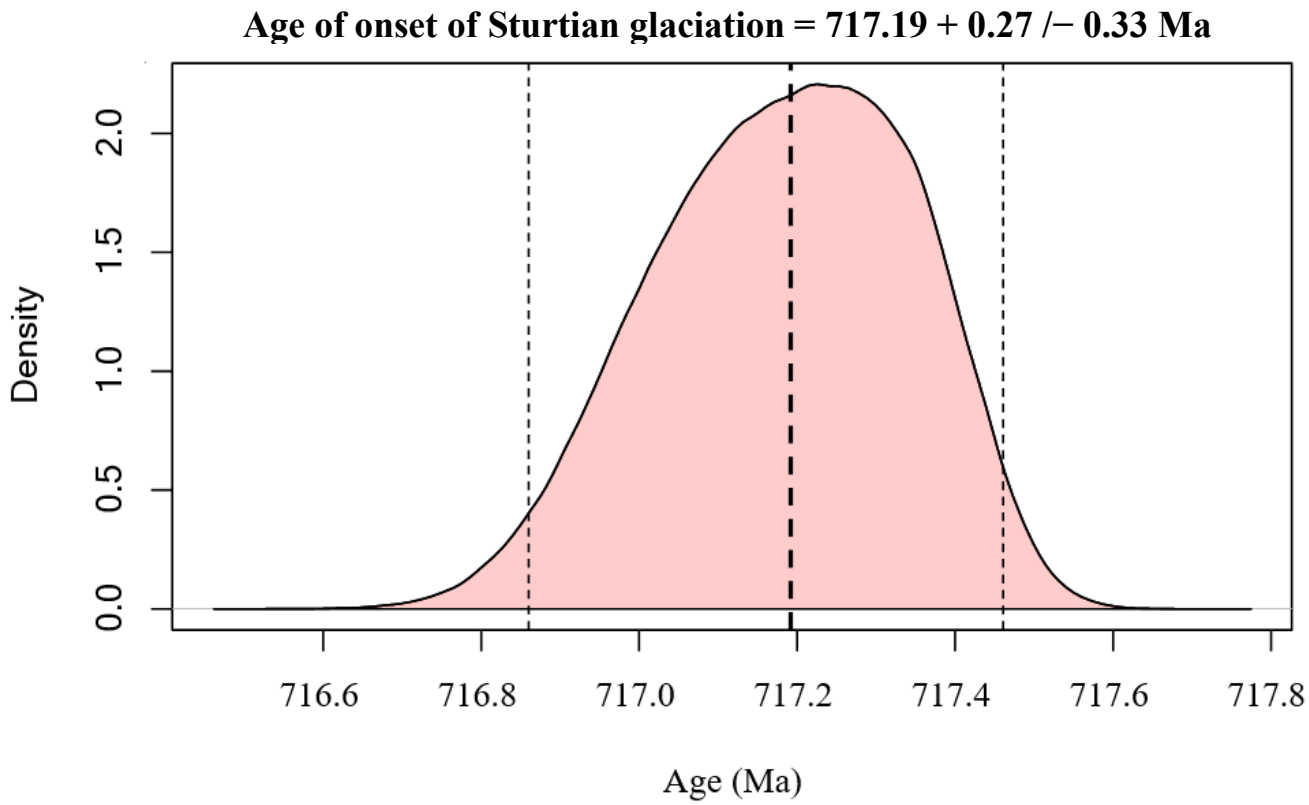

Now to update the ages of the dykes and a sills. This will be done without using MCMC, because it is not in fact required here—it can be done by a Monte Carlo method where we simply eliminate combinations of samples that disobey crosscutting relationships.

We will start by updating the age of the dykes and sills in each location using cross-cutting constraints

```
# First for the Fury and Hecla basin
FHsill_mean <- 718.33
FHsill_sd <- 0.19/2
FHdyke_mean <- 717.73
FHdyke_sd <- 0.72/2
sampnum <- 300000 # number of random samples for each age#
Sample from a normal distribution of each
FHsill_sample <- rnorm(sampnum, mean = FHsill_mean, sd = FHsill_sd) # generate random samples
FHdyke_sample <- rnorm(sampnum, mean = FHdyke_mean, sd = FHdyke_sd)

# now to select those samples that obey cross-cutting constraint
n <- sum(FHsill_sample > FHdyke_sample) # calculate number of samples that do not contradict
superposition
c <- 1
FHsill_new    <-    vector(mode="numeric",    length=n)
FHdyke_new <- vector(mode="numeric", length=n)for  ( i
in  1:sampnum ) {
if (FHsill_sample[i] > FHdyke_sample[i]) {FHsill_new[c] <-
FHsill_sample[i] FHdyke_new[c] <- FHdyke_sample[i]
c <- c + 1
}
}

# And finally to calculate the summary statistics
# And calculate the summary statistics and generate a print label for the figures at the same time
```

```
FHsill_age      <-      age_calc(FHsill_new)
FHsill_label <- age_print(FHsill_age)
FHsill_label <- paste("Fury & Hecla sill: ", FHsill_label)


FHdyke_age    <-    age_calc(FHdyke_new)
```

Now for the Thule basin

```
# First for the Fury and Hecla basin
THsill_mean <- 718.6
THsill_sd <- 0.31/2
THdyke_mean <- 718.12
THdyke_sd <- 0.92/2
sampnum <- 300000 # number of random samples for each age#
Sample from a normal distribution of each
THsill_sample <- rnorm(sampnum, mean = THsill_mean, sd = THsill_sd) # generate random samples
THdyke_sample <- rnorm(sampnum, mean = THdyke_mean, sd = THdyke_sd)

# now to select those samples that obey cross-cutting constraint
n <- sum(THsill_sample > THdyke_sample) # calculate number of samples that do not contradict
superposition
c <- 1
THsill_new    <-    vector(mode="numeric",    length=n)
THdyke_new <- vector(mode="numeric", length=n)for  ( i
in  1:sampnum ) {
if (THsill_sample[i] > THdyke_sample[i]) {THsill_new[c] <-
THsill_sample[i] THdyke_new[c] <- THdyke_sample[i]
c <- c + 1
}
}

# And calculate the summary statistics and generate a print label for the figures at the
same time
THsill_age <- age_calc(THsill_new)
THsill_label <- age_print(THsill_age)
THsill_label <- paste("Thule sill: ", THsill_label)

THdyke_age <- age_calc(THdyke_new)
THdyke_label <- age_print(THdyke_age)
THdyke_label <- paste("Thule dyke: ", THdyke_label)
```

Now we'll plot these up to compare them.

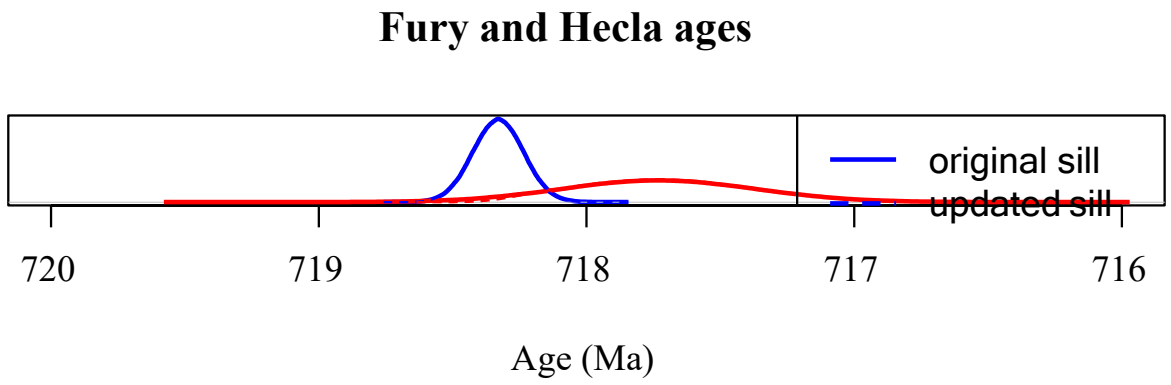

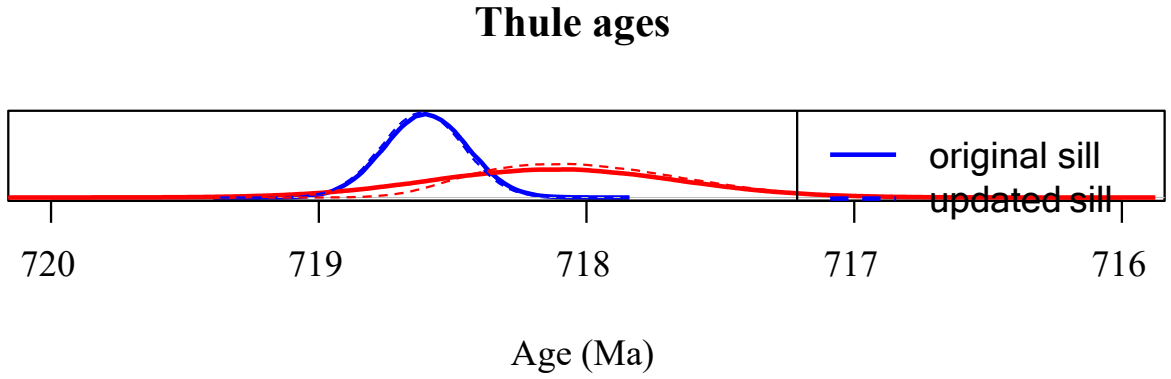


```
par(mfrow=c(1,1))
# first, let's make some labels for the legend
boundary_label <- paste("Glacial onset: ", boundary)

# first, we'll plot the sills


plot(density(boundaryage), col=alpha("black"), lwd=1.5, xlim=c(720, 716), ylim=c(0,5), main="Updated ag
polygon(density(boundaryage), col=alpha("black", 0.1), lwd=1.5)
polygon(density(THsill_new), col=alpha("purple", 0.1))
lines(density(THsill_new), col="purple", lwd=1.5)
polygon(density(THdyke_new), col=alpha("red", 0.1))
lines(density(THdyke_new), col="red", lwd=1.5)
polygon(density(FHsill_new), col=alpha("blue", 0.1))
lines(density(FHsill_new), col="blue", lwd=1.5)
polygon(density(FHdyke_new), col=alpha("orange", 0.1))
lines(density(FHdyke_new), col="orange", lwd=1.5)


# add the median lines
abline(v = THsill_age[1], col="blue", lwd=1.5, lty=3) abline(v =
THdyke_age[1], col="red", lwd=1.5, lty=3) abline(v = FHsill_age[1],
col="blue", lwd=1.5, lty=3) abline(v = FHdyke_age[1], col="red",
lwd=1.5, lty=3) abline(v = boundary_median[1], col="black", lwd=1.5,
lty=3)
legend(x=718.2, y=5, c(THsill_label, THdyke_label, FHsill_label, FHdyke_label, boundary_label))
```

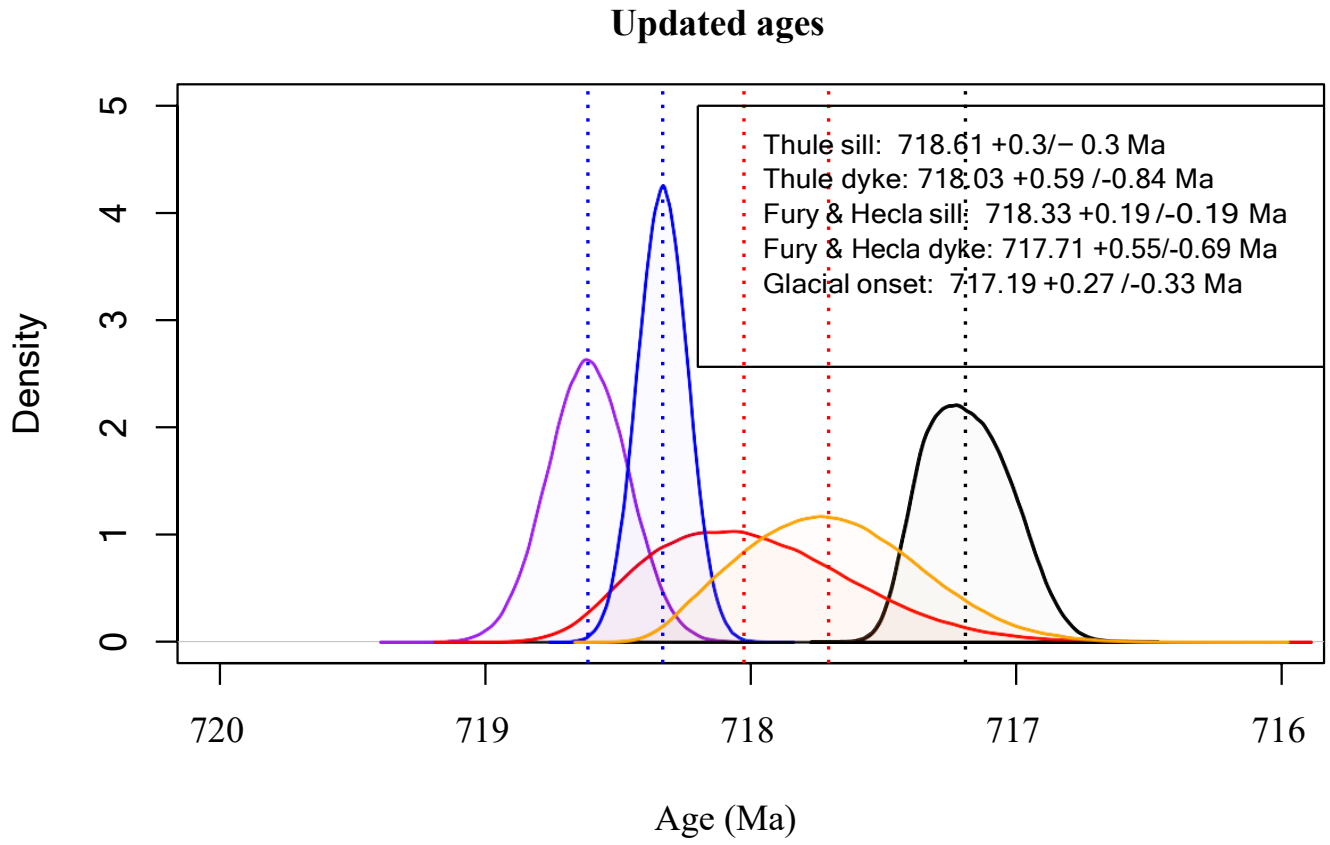

Now we'll compared the combined ages (weighed means) of the dykes and sills with the onset of the boundary.

```
combined_sills_mean <- 718.40
combined_sills_sd <- 0.16*sd_corr/2
combined_dykes_mean <- 717.87
combined_dykes_sd <- 0.56*sd_corr/2

sills_distribution <- rnorm(200000, mean = combined_sills_mean, sd = combined_sills_sd)dykes_distribution
<- rnorm(200000, mean = combined_dykes_mean, sd = combined_dykes_sd) sills_age <-
age_calc(sills_distribution)
sills_label <- age_print(sills_age) dykes_age <-
age_calc(dykes_distribution)dykes_label <-
age_print(dykes_age)
sills_label <- paste("Composite sills: ", sills_label)dykes_label <-
paste("Composite dykes: ", dykes_label)

plot(density(sills_distribution), col="blue", xlim=c(719, 716), ylim=c(0,5), lwd=1.5, main="Combined up
polygon(density(sills_distribution), col=alpha("blue", 0.1))

lines(density(dykes_distribution), col="red", lwd=1.5)
polygon(density(dykes_distribution), col=alpha("red", 0.1))


lines(density(boundaryage), col="black", lwd=1.5)
polygon(density(boundaryage), col=alpha("black", 0.1))

abline(v = sills_age[1], col="blue", lwd=1.5, lty=3) abline(v =
dykes_age[1], col="red", lwd=1.5, lty=3) abline(v = boundary_median,
col="black", lwd=1.5, lty=3)

legend(x="topright", c(sills_label, dykes_label, boundary_label))
```

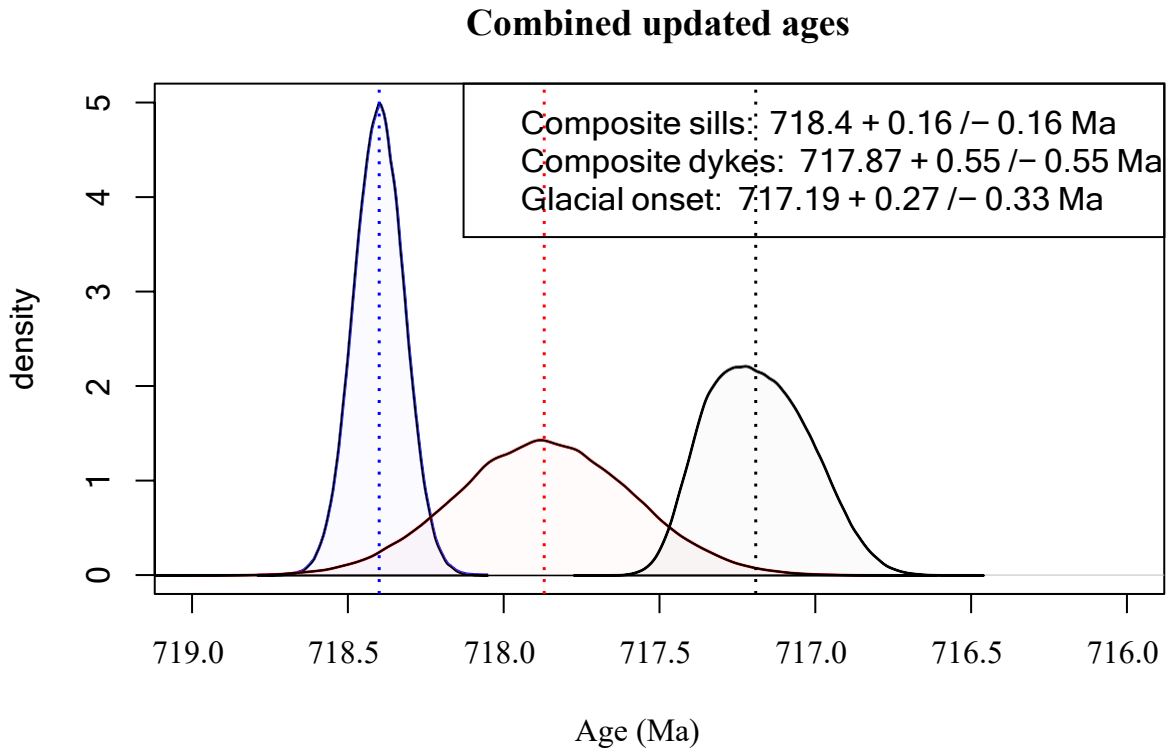

Now we'll with combined ages where we combined the updated sill and dyke ages.

```
sills_age <- age_calc(c(THsill_new, FHsill_new))sills_label
<- age_print(sills_age)
dykes_age <- age_calc(c(THdyke_new, FHdyke_new))
dykes_label <- age_print(dykes_age)
sills_label <- paste("Composite sills: ", sills_label)dykes_label <-
paste("Composite dykes: ", dykes_label)

plot(density(c(THsill_new, FHsill_new)), col="blue", xlim=c(720, 716), ylim=c(0,4), lwd=1.5, main="Comb
polygon(density(c(THsill_new, FHsill_new)), col=alpha("blue", 0.1))

lines(density(c(THdyke_new, FHdyke_new)), col="red", lwd=1.5)
polygon(density(c(THdyke_new, FHdyke_new)), col=alpha("red", 0.1))


lines(density(boundaryage), col="black", lwd=1.5)
polygon(density(boundaryage), col=alpha("black", 0.1))

abline(v = sills_age[1], col="blue", lwd=1.5, lty=3) abline(v =
dykes_age[1], col="red", lwd=1.5, lty=3) abline(v = boundary_median,
col="black", lwd=1.5, lty=3)

legend(x=720, y=4, c(sills_label, dykes_label, boundary_label))
```

Combined updated ages

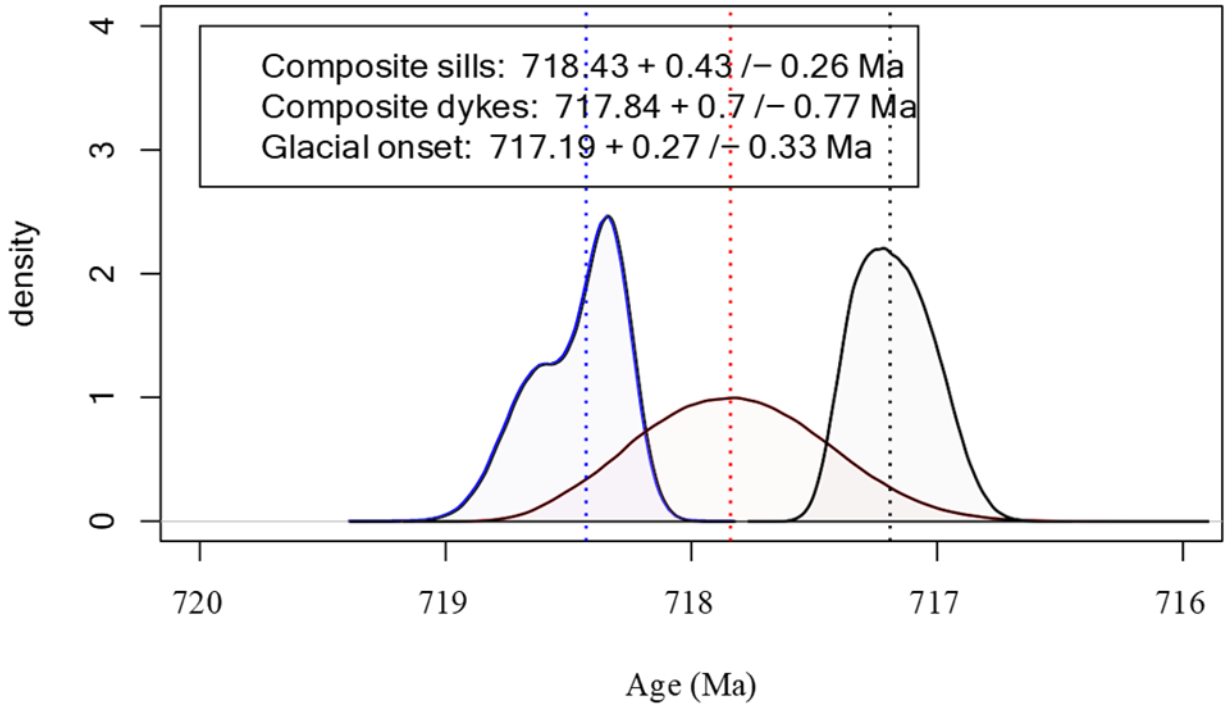

ANNEXE C

DONNEES DU CHAPITRE III

Table A3.1: Whole-rock compositions of Franklin dykes and sills in Baffin Island and Greenland.

Sample	Rock type	Latitude	Longitude	SiO_2	Al_2O_3	Fe_2O_3(T)	MnO	MgO	CaO	Na_2O	K_2O	TiO_2	P_2O_5	LOI	Total
F001	FH dyke margin	69,94	-82,77	50,49	15,67	11,75	0,19	6,35	11,51	2,24	0,80	1,25	0,07	0,41	100,7
F017A2	FH dyke margin	70,22	-84,44	48,59	15,13	14,96	0,22	5,60	9,36	2,18	1,76	1,68	0,14	0,76	100,4
H044A1	FH dyke margin	70,07	-85,86	49,28	13,20	15,58	0,22	6,71	11,02	2,15	0,29	1,65	0,13	0,19	100,4
H046A1	FH dyke margin	70,06	-85,88	48,80	18,11	14,51	0,18	4,05	10,02	2,86	0,27	1,81	0,12	0,02	100,8
H065A1	FH dyke margin	70,10	-83,07	50,08	13,68	14,91	0,21	6,28	11,22	2,23	0,45	1,52	0,12	0,13	100,8
H105C	FH dyke margin	70,24	-80,23	51,03	13,70	11,86	0,20	8,00	7,96	2,16	1,62	0,98	0,09	2,37	99,98
W137B1	FH dyke margin	70,15	-83,69	49,23	13,40	15,73	0,21	6,43	11,14	2,18	0,23	1,82	0,14	-0,08	100,4
F002	FH dyke center	69,94	-82,77	50,28	16,75	13,74	0,17	3,68	9,59	2,91	0,94	1,72	0,17	0,72	100,7
F017A1	FH dyke center	70,22	-84,44	49,05	14,56	14,92	0,18	5,51	9,53	2,32	1,57	1,74	0,16	0,94	100,5
H045A1	FH dyke center	70,07	-85,86	49,16	13,08	15,79	0,22	6,60	10,70	2,10	0,54	1,67	0,14	0,28	100,3
H048A1	FH dyke center	70,06	-85,89	48,02	16,54	16,31	0,17	4,04	9,82	2,79	0,34	2,69	0,11	-0,13	100,7
H064A1	FH dyke center	70,10	-83,07	49,83	17,35	13,94	0,17	3,13	9,44	2,94	1,19	1,83	0,15	0,67	100,7
M147	FH dyke center	69,87	-82,09	49,16	14,15	13,40	0,20	6,40	11,42	2,16	0,37	1,42	0,11	0,24	99,02
W137B2	FH dyke center	70,15	-83,69	48,30	12,32	16,11	0,24	8,33	10,82	1,85	0,42	1,61	0,10	0,34	100,4
H049A1	Dybbol sill center	70,06	-85,88	48,84	14,23	12,57	0,18	9,81	11,66	1,83	0,35	1,07	0,08	-0,12	100,5
W146B1	Dybbol sill margin	70,06	-85,88	50,65	15,26	11,27	0,17	7,17	12,02	2,11	0,43	0,96	0,04	0,31	100,4
SLSC 1	Thule SLSC	76,34	-68,43	47,98	10,38	15,34	0,19	8,10	8,85	2,57	0,44	4,47	0,37	1,50	100,2
SLSC 2	Thule SLSC	76,35	-68,43	48,60	12,12	15,04	0,19	5,37	8,40	2,87	0,97	5,02	0,52	1,18	100,3
SLSC 3	Thule SLSC	76,35	-68,42	48,44	11,50	15,21	0,18	5,55	9,20	2,81	0,51	4,75	0,47	1,27	99,89
SLSC 4	Thule SLSC	76,35	-68,41	48,21	11,62	15,18	0,18	5,53	8,61	2,62	0,67	5,00	0,48	1,42	99,52
SLSC 5	Thule SLSC	76,35	-68,40	48,39	11,34	14,79	0,18	5,62	8,78	2,95	0,68	4,70	0,46	1,40	99,28
SLSC 6	Thule SLSC	76,34	-68,40	49,63	12,83	15,60	0,19	5,76	9,31	2,87	0,50	3,49	0,33	0,32	100,8
SLSC 7	Thule SLSC	76,34	-68,44	49,95	11,54	14,43	0,17	5,14	9,22	2,68	1,06	4,03	0,40	0,66	99,28

Sample	Rock type	Latitude	Longitude	SiO_2	Al_2O_3	Fe_2O_3(T)	MnO	MgO	CaO	Na_2O	K_2O	TiO_2	P_2O_5	LOI	Total
SLSC 8	Thule SLSC	76,34	-68,49	49,89	12,11	15,95	0,21	5,45	9,29	2,82	0,47	3,53	0,35	0,28	100,3
SLSC 9	Thule SLSC	76,34	-68,47	49,69	12,38	16,05	0,19	5,59	9,35	2,67	0,36	3,56	0,34	0,29	100,4
SLSC 10	Thule SLSC	76,33	-68,32	55,78	11,86	13,37	0,17	4,34	5,11	4,39	0,35	2,62	0,47	1,74	100,2
SLSC11	Thule SLSC	76,45	-69,53	49,36	12,51	15,19	0,19	5,31	8,66	2,59	1,28	4,92	0,52	-0,02	100,5
SLSC12	Thule SLSC	76,45	-69,53	48,57	11,97	14,38	0,17	6,62	9,70	2,49	0,84	5,10	0,41	-0,16	100,1
SLSC13	Thule SLSC	76,34	-68,52	48,87	12,23	15,26	0,17	5,38	8,56	2,96	1,00	5,25	0,54	0,50	100,7
SLSC14	Thule SLSC	76,34	-68,49	49,83	12,21	15,01	0,19	5,14	9,01	2,41	1,08	4,23	0,40	0,45	99,95
SLSC15	Thule SLSC	76,56	-68,86	49,43	12,43	16,09	0,21	5,70	9,44	2,72	0,56	3,49	0,33	0,33	100,7
SLSC16	Thule SLSC	76,34	-68,49	50,65	12,69	14,95	0,19	4,84	8,70	2,72	1,10	4,33	0,44	0,15	100,8
TFD1	Thule dyke	76,46	-69,45	48,54	12,01	15,28	0,18	5,07	8,16	3,00	0,82	5,15	0,50	1,18	99,91
TFD2	Thule dyke	76,50	-70,15	49,28	12,28	15,03	0,17	5,17	8,72	2,75	1,00	4,97	0,51	0,47	100,4
TFD3	Thule dyke	76,31	-68,55	49,08	12,13	14,80	0,17	5,58	8,82	2,76	1,01	4,75	0,52	0,64	100,3

FH, Fury and Hecla; SLSC, Steensby Land sill complex; TFD, Thule Franklin dyke.

Sample	Sc	V	Cr	Co	Ni	Cu	Zn	Ga	Ge	Rb	Sr	Y	Zr	Nb	Cs	Ba
F001	35	321	180	45	90	160	80	19	1,4	14	245	16,9	63	2,9	0,3	55
F017A2	35	386	70	46	90	230	100	21	1,5	28	384	24,7	96	4,3	0,5	164
H044A1	44	389	120	53	100	240	100	19	1,7	8	123	25,3	87	3,8	0,4	46
H046A1	26	288	30	43	70	260	100	23	1,4	6	225	22	100	5	0,3	68
H065A1	39	386	130	49	90	220	100	20	1,5	13	172	23,2	91	4,8	0,5	93
H105C	33	271	290	46	130	130	90	17	1,5	70	172	18,9	89	9,9	0,8	194
W137B1	38	383	170	51	100	240	110	21	1,3	7	156	24,9	95	5,1	0,2	58
F002	27	288	30	41	70	290	80	24	1,4	21	287	27,4	117	5,8	0,3	106
F017A1	36	362	70	46	90	210	80	22	1,7	24	302	28,2	109	5	0,4	111
H045A1	43	382	110	51	100	260	110	19	1,6	14	149	25,5	89	4	0,5	243
H048A1	27	739	70	53	110	190	120	25	1,4	10	225	17,3	76	4	0,2	64
H064A1	26	311	< 20	36	40	200	80	25	1,3	34	264	28,7	123	7	0,5	181
M147	40	400	190	47	90	220	100	19	1,6	11	163	22,5	78	4,6	0,3	78
W137B2	40	375	250	65	130	210	130	18	1,8	10	165	21	82	4,1	0,3	95
H049A1	35	284	540	57	240	150	80	17	1,5	11	143	16,5	57	2,8	0,4	69
W146B1	39	359	110	48	100	50	60	17	1,5	16	172	11,9	39	1,8	0,6	82
SLSC 1	34	412	340	61	230	100	120	25	1,7	11	403	36,9	345	23,3	0,2	180
SLSC 2	25	420	80	44	120	300	140	28	1,6	29	608	44,1	427	31,1	0,5	252
SLSC 3	27	420	110	48	130	270	140	26	1,5	14	551	41,1	362	25,5	0,2	208
SLSC 4	27	433	100	47	120	260	140	26	1,6	18	542	40,2	371	26,2	0,3	201
SLSC 5	27	416	120	45	130	240	160	25	1,4	18	554	38,4	361	26,8	0,2	169
SLSC 6	33	469	120	48	110	230	130	24	1,5	13	338	35,5	241	15,5	0,9	134
SLSC 7	28	383	100	45	70	130	90	24	1,4	25	567	37,4	328	22,3	0,4	343
SLSC 8	32	473	100	50	110	320	180	25	1,6	10	329	37,7	255	17,6	0,3	108
SLSC 9	33	482	110	53	110	310	150	24	1,4	7	342	36,7	253	16,5	0,3	94
SLSC 10	23	304	80	30	60	60	110	20	1,4	9	163	37,3	210	14,3	0,1	88
SLSC11	25	435	50	47	130	310	180	27	1,5	31	634	42,7	407	30,3	0,6	314
SLSC12	29	423	160	45	170	170	100	25	1,7	17	583	36,3	328	24,1	0,2	215
SLSC13	24	424	90	45	140	140	120	28	1,7	27	651	44,8	447	34,7	0,6	264

Sample	Sc	V	Cr	Co	Ni	Cu	Zn	Ga	Ge	Rb	Sr	Y	Zr	Nb	Cs	Ba
SLSC14	28	387	110	41	70	160	130	25	1,7	28	527	39,2	328	24,7	0,7	334
SLSC15	33	472	120	48	120	310	150	24	1,5	14	340	35,6	244	16,5	0,2	144
SLSC16	27	387	70	50	70	170	90	26	1,5	24	553	39,3	346	25,7	0,4	337
TFD1	26	445	70	44	120	250	130	26	1,5	23	562	41,2	394	31,6	0,2	220
TFD2	24	454	50	46	140	150	150	28	1,3	24	601	43	408	31,3	0,4	258
TFD3	25	418	70	45	120	260	130	26	1,4	20	606	42,1	400	28,7	0,3	249

Sample	La	Ce	Pr	Nd	Sm	Eu	Gd	Tb	Dy	Ho	Er	Tm	Yb	Lu	Hf	Ta	Th
F001	3,59	9,63	1,53	7,88	2,53	0,997	3,21	0,52	3,34	0,67	1,85	0,253	1,64	0,25	1,7	0,2	0,35
F017A2	6,21	15,2	2,4	11,2	3,72	1,38	4,98	0,82	4,91	0,99	2,88	0,407	2,43	0,348	2,5	0,27	0,81
H041A1	47,5	103	13,7	56,6	12,3	4,14	12	1,75	9,56	1,69	4,41	0,58	3,58	0,503	8,7	1,83	7,81
H044A1	4,83	12,9	2,13	10,7	3,51	1,35	4,87	0,81	5,25	1,02	2,91	0,433	2,78	0,413	2,3	0,24	0,46
H046A1	5,86	15	2,4	11,6	3,53	1,41	4,57	0,73	4,45	0,89	2,54	0,362	2,19	0,345	2,5	0,34	0,59
H065A1	7,49	17,4	2,58	12	3,36	1,26	4,55	0,77	4,69	0,94	2,62	0,374	2,35	0,38	2,5	0,29	1,21
H105C	12,7	25,9	3,36	13,4	3,16	1,04	3,86	0,62	3,82	0,74	2,07	0,304	2,01	0,306	2,2	0,67	2,82
W137B1	6,18	15,8	2,55	12,8	3,89	1,4	4,99	0,84	5,25	1,03	2,78	0,385	2,44	0,364	2,5	0,32	0,68
F002	7,62	19,1	3,06	14,7	4,22	1,65	5,6	0,89	5,54	1,09	3,03	0,46	2,87	0,419	3,1	0,38	0,85
F017A1	7,11	17,3	2,74	13,4	4,28	1,5	5,57	0,93	5,6	1,11	3,21	0,466	2,94	0,446	2,8	0,31	0,94
H043A1	35,9	77,1	10,4	42,4	9,43	3,5	9,27	1,37	7,51	1,3	3,49	0,48	2,92	0,433	6,7	1,49	5,66
H045A1	4,86	13	2,14	10,8	3,48	1,34	4,75	0,81	4,95	1,02	2,98	0,427	2,66	0,402	2,4	0,25	0,47
H048A1	5,3	13,3	2,11	9,82	2,87	1,21	3,57	0,61	3,57	0,69	1,93	0,268	1,72	0,265	2,1	0,28	0,63
H064A1	10,9	24,9	3,46	16	4,68	1,59	5,59	0,89	5,6	1,11	3,12	0,457	2,86	0,422	3,1	0,45	1,71
M147	6,77	16,1	2,24	11	3,19	1,11	3,55	0,63	3,98	0,83	2,29	0,321	2,13	0,322	1,9	0,25	0,95
W137B2	4,85	12,9	2,01	10,3	3,24	1,22	3,91	0,67	4,01	0,84	2,27	0,313	2,05	0,315	2,3	0,28	0,5
H049A1	4,77	10,9	1,66	7,93	2,32	0,887	3,12	0,53	3,28	0,64	1,86	0,255	1,59	0,243	1,5	0,18	0,77
W146B1	5,14	11,3	1,47	6,79	1,73	0,722	1,92	0,33	2,11	0,42	1,16	0,16	1,02	0,157	0,9	0,13	1,22
SLSC 1	27,5	70	9,82	46	11	3,4	10,3	1,51	7,89	1,4	3,61	0,465	2,78	0,402	8,6	1,75	2,89
SLSC 2	38,5	96,6	13,5	61	14,6	4,68	13	1,89	9,73	1,7	4,39	0,549	3,19	0,452	10,8	2,33	3,9
SLSC 3	35,3	88,2	12,4	54,7	13,1	4,23	12,2	1,77	9,21	1,64	3,95	0,479	2,99	0,436	9,1	2,1	3,42
SLSC 4	34,4	86,4	12,2	55,1	13,2	4,34	11,9	1,77	9,21	1,58	4,04	0,478	2,85	0,419	9,3	2,13	3,41
SLSC 5	33,2	83,3	11,8	52,2	12,5	4,07	11,3	1,72	8,62	1,52	3,89	0,462	2,8	0,405	9,2	2,07	3,27
SLSC 6	19	49,3	7,16	33,1	8,77	2,76	8,57	1,36	7,44	1,38	3,57	0,472	2,89	0,442	6	1,17	1,76
SLSC 7	31,8	77,1	10,6	48,3	11,7	3,66	10,4	1,59	8,24	1,45	3,73	0,49	2,92	0,419	8,5	1,72	3,12
SLSC 8	20	53	7,62	36,4	9,25	3,13	9,37	1,47	7,67	1,44	3,76	0,517	3,16	0,458	6,9	1,23	1,81
SLSC 9	19,8	52,1	7,52	35	9,41	3,01	9,39	1,46	7,91	1,45	3,73	0,51	3,12	0,447	6,6	1,21	1,85
SLSC 10	31,8	74,7	9,51	42,1	10,1	2,77	9,6	1,49	7,98	1,47	3,96	0,515	3,15	0,466	5,7	1,16	5
SLSC11	35,6	90,4	12,5	57,4	13,8	4,53	13,1	1,88	9,54	1,66	4,19	0,532	3,19	0,455	10,4	2,19	3,62

Sample	La	Ce	Pr	Nd	Sm	Eu	Gd	Tb	Dy	Ho	Er	Tm	Yb	Lu	Hf	Ta	Th
SLSC12	29,2	74,8	10,6	48,6	11,6	3,7	10,8	1,56	8,16	1,4	3,59	0,435	2,62	0,39	8,5	1,86	2,87
SLSC13	40,4	103	14,2	64,1	15,5	4,73	13,5	1,99	10,1	1,75	4,53	0,554	3,25	0,448	11,4	2,54	4,22
SLSC14	32,5	80,6	11,2	49,6	11,8	3,73	11,1	1,66	8,57	1,51	3,89	0,472	2,99	0,44	8,9	1,78	3,16
SLSC15	18,8	49,9	7,13	34	8,97	2,97	8,76	1,4	7,76	1,42	3,62	0,482	3	0,443	6,3	1,2	1,68
SLSC16	33,4	81,7	11,4	49,5	12,1	3,82	11,2	1,67	8,64	1,53	3,92	0,476	2,92	0,416	8,9	1,85	3,24
TFD1	35,4	89,8	12,7	57,5	13,6	4,32	13,1	1,87	9,51	1,67	4,23	0,511	3,11	0,456	10,1	2,19	3,37
TFD2	35,1	89,2	12,6	58,2	13,8	4,47	12,8	1,88	9,83	1,69	4,26	0,554	3,13	0,443	11,2	2,24	3,76
TFD3	35,5	89,8	12,5	58,2	13,7	4,46	12,5	1,79	9,65	1,69	4,2	0,534	3,17	0,45	10,2	2,08	3,62

Table A3.2: $^{143}Nd/^{144}Nd$ isotopic composition of Franklin dykes and sills

Sample	Rock type	Nd	Sm	$^{147}Sm/^{144}Nd$	$^{143}Nd/^{144}Nd$	2σ	εNd(i)	εNd (718 Ma)	T_{DM}*
F017A2	FH dyke margin	13,27	4,05	0,1846	0,512797	4,62E-08	3,09	4,22	1,86
H041A1	FH dyke margin	56,34	12,17	0,1306	0,512304	3,56E-08	-6,51	-0,40	1,55
H065A1	FH dyke margin	12,12	3,50	0,1747	0,512527	5,77E-08	-2,17	-0,13	2,43
H105C	FH dyke margin	13,74	3,28	0,1443	0,512160	3,35E-08	-9,32	-4,48	2,17
H043A1	FH dyke center	45,04	9,64	0,1293	0,512285	3,78E-08	-6,88	-0,65	1,56
H048A1	FH dyke center	10,45	2,98	0,1722	0,512715	4,48E-08	1,50	3,77	1,60
H064A1	FH dyke center	15,80	4,48	0,1715	0,512533	7,40E-08	-2,06	0,27	2,23
M147	FH dyke center	11,06	3,21	0,1753	0,512583	6,25E-08	-1,07	0,91	2,25
H049A1	Dybbol sill center	8,11	2,38	0,1776	0,512571	1,00E-07	-1,31	0,46	2,44
W146B1	Dybbol sill margin	6,97	1,85	0,1607	0,512253	9,07E-08	-7,52	-4,19	2,57
SLSC 3	Thule SLSC	55,40	12,84	0,1402	0,512563	3,44E-08	-1,46	3,77	1,22
SLSC 5	Thule SLSC	54,37	12,69	0,1411	0,512569	3,17E-08	-1,34	3,81	1,22
SLSC 7	Thule SLSC	49,87	11,62	0,1408	0,512498	3,61E-08	-2,74	2,43	1,37
SLSC 9	Thule SLSC	35,09	8,83	0,1521	0,512675	3,30E-08	0,73	4,86	1,18
SLSC 10	Thule SLSC	42,99	10,03	0,1411	0,512329	3,81E-08	-6,02	-0,88	1,72
SLSC11	Thule SLSC	58,77	13,82	0,1422	0,512577	3,27E-08	-1,19	3,86	1,22
SLSC13	Thule SLSC	63,57	14,50	0,1379	0,512570	3,25E-08	-1,32	4,12	1,17
SLSC14	Thule SLSC	50,37	11,71	0,1405	0,512489	5,00E-08	-2,91	2,29	1,38
SLSC16	Thule SLSC	52,62	12,18	0,1399	0,512492	4,00E-08	-2,85	2,41	1,36
TFD1	Thule dyke	57,31	13,38	0,1412	0,512568	3,59E-08	-1,37	3,77	1,23
TFD2	Thule dyke	58,72	13,73	0,1413	0,512564	3,60E-08	-1,45	3,67	1,24
TFD3	Thule dyke	59,88	13,94	0,1407	0,512564	3,04E-08	-1,44	3,74	1,23

*T_{DM} model is from DePaolo (1981).

Table A3.4: Partition coefficients (Kd) used in the incongruent dynamic melting model are from Shaw (2000) and Salters and Stracke (2004).

	La	Ce	Pr	Nd	Sm	Eu	Gd	Tb	Dy	Ho	Er	Tm	Yb	Lu
Spinel lherzolite														
Olivine	0,0005	0,0005	0,000251	0,00042	0,0011	0,0008	0,0011	0,0021	0,0027	0,005	0,013	0,016	0,02	0,02
Opx	0,0031	0,004	0,00033	0,012	0,02	0,0033	0,0065	0,0067	0,011	0,0127	0,045	0,025	0,08	0,12
Cpx	0,03	0,08	0,137	0,088	0,299	0,329	0,35	0,405	0,4	0,415	0,42	0,409	0,45	0,511
Spinel	0,00002	0,00003	0,0001	0,0002	0,0004	0,0006	0,0009	0,0012	0,0015	0,0023	0,003	0,0038	0,0045	0,0053
Garnet lherzolite														
Olivine	0,0005	0,0005	0,000251	0,00042	0,0011	0,0008	0,0011	0,0021	0,0027	0,005	0,013	0,016	0,02	0,02
Opx	0,004	0,004	0,00033	0,012	0,02	0,0033	0,065	0,0067	0,065	0,0127	0,065	0,025	0,08	0,12
Cpx	0,015	0,038	0,06	0,0884	0,1509	0,21	0,16	0,405	0,17	0,415	0,18	0,409	0,25	0,276
Garnet	0,0007	0,017	0,054	0,064	0,23	0,32	1,2	0,1	2	0,9	3	3	5,5	7

Table A3.4: Whole-rock and $^{143}Nd/^{144}Nd$ isotopic compositions of Paleoproterozoic rocks from Fury and Hecla

Sample	**M152**	**C074A1**	**P043A1**	**P110A1**	**Basement mix**
Rock type	Meta-tonalite	Meta-tonalite	Meta-monzogranite	Meta-sedimentary semi-pelite	Mean
Latitude	69,87	70,19	70,30	70,37	
Longitude	-82,10	-81,86	-82,70	-85,71	
SiO_2	70,14	73,4	63,96	65,99	
Al_2O_3	17,55	15,09	16,16	11,65	
$Fe_2O_3(T)$	1,33	1,53	5,42	12,46	
MnO	0,02	0,023	0,072	0,142	
MgO	0,49	0,28	1,87	3,32	
CaO	2,32	2,22	3,33	0,75	
Na_2O	6,24	5,19	4,32	1,04	
K_2O	1,58	1,86	3,62	3,33	
TiO_2	0,11	0,113	0,629	0,675	
P_2O_5	0,06	0,03	0,23	0,03	
LOI	0,81	0,67	0,83	1	
Total	100,7	100,4	100,4	100,4	
Sc	< 1	1	8	21	
V	8	11	70	93	
Cr	< 20	< 20	20	160	
Co	2	2	12	26	
Ni	< 20	< 20	< 20	80	
Zn	30	< 30	80	110	
Ga	19	15	21	15	
Rb	38	41	94	146	
Sr	619	647	808	106	
Y	1,2	2	16,8	20,7	
Zr	56	62	181	124	

Nb	0,8	1,8	7	6	3,9
Cs	0,6	0,8	3,5	2,3	
Ba	316	849	1974	550	
La	2,2	6,01	59,2	30	24,35
Ce	3,04	10,2	112	57,1	45,59
Pr	0,34	1,05	13,1	6,42	5,23
Nd	1,41	3,83	50,2	23	19,61
Sm	0,27	0,69	8,29	4,36	3,40
Eu	0,248	0,347	1,82	0,742	0,79
Gd	0,25	0,41	5,25	3,46	2,34
Tb	0,04	0,06	0,73	0,59	0,36
Dy	0,2	0,33	3,43	3,5	1,87
Ho	0,04	0,06	0,63	0,76	0,37
Er	0,12	0,19	1,63	2,26	1,05
Tm	0,02	0,029	0,218	0,348	0,15
Yb	0,13	0,21	1,36	2,31	1,00
Lu	0,022	0,036	0,188	0,339	0,15
Hf	1,3	1,3	3,9	2,7	
Ta	0,06	0,11	0,89	0,76	
Tl	0,16	0,19	0,47	0,78	
Pb	16	21	25	14	
Th	0,69	1,79	11,7	14,3	7,12
U	0,67	0,65	2,27	2,36	
Nd	0,89	3,75	47,60	15,28	
Sm	0,18	0,64	7,87	2,82	
$^{147}Sm/^{144}Nd$	0,1259	0,1029	0,0999	0,1117	
$^{143}Nd/^{144}Nd$	0,511124	0,510952	0,510876	0,510975	
2σ	3,26E-07	1,73E-07	5,09E-08	5,33E-08	
εNd(i)	-29,54	-32,89	-34,38	-32,44	
εNd(718 Ma)	-23,04	-24,27	-25,48	-24,63	-24,35
Tdm	3,50	3,01	3,03	3,23	

RÉFÉRENCES

Arndt, N. T., Czamanske, G. K., Wooden, J. L. et Fedorenko, V. A. (1993). Mantle and crustal contributions to continental flood volcanism. Tectonophysics, 223(1–2), 39–52.

Baragar, W. R. A., Ernst, R. E., Hulbert, L. et Peterson, T. (1996). Longitudinal petrochemical variation in the Mackenzie dyke swarm, northwestern Canadian Shield. Journal of Petrology, 37(2), 317–359.

Beard, C.D., Scoates, J.S., Weis, D., Bedard, J.H. et Dell'Oro, T.A. (2017). Geochemistry and origin of the Neoproterozoic Natkusiak flood basalts and related Franklin sills, Victoria Island, Arctic Canada: Journal of Petrology, 58(11), 2191–2220, https://doi.org/10.1093/petrology/egy004.

Bédard, J. H., Naslund, H. R., Nabelek, P., Winpenny, A., Hryciuk, M., Macdonald, W., Hayes, B., Steigerwaldt, K., Hadlar, T., Rainbird, R., Dewing, K. et Girard, É. (2012). Fault-mediated melt ascent in a Neoproterozoic continental flood basalt province, the Franklin sills, Victoria Island, Canada. Bulletin, 124(5–6), 723–736.

Bryan, S. E. et Ernst, R. E. (2008). Revised definition of large igneous provinces (LIPs). Earth-Science Reviews, 86(1–4), 175–202.

Buchan, K. L. et Ernst, R. E. (2021). Plumbing systems of large igneous provinces (LIPs) on Earth and Venus: Investigating the role of giant circumferential and radiating dyke swarms, coronae and novae and mid-crustal intrusive complexes. Gondwana Research, 100, 25–43.

Condomines, M., Gauthier, P. J. et Sigmarsson, O. (2003). Timescales of magma chamber processes and dating of young volcanic rocks. Reviews in Mineralogy and Geochemistry, 52(1), 125–174.

Chandler, F.W. (1988). Geology of the late Precambrian Fury and Hecla Group, northwest Baffin Island, District of Franklin. Geological Survey of Canada, Bulletin 370, 30 p., https://doi.org/10.4095/126938.

Chandler, F. W. et Stevens, R. D. (1981). Potassium-argon age of the late Proterozoic Fury and Hecla formation, northwest Baffin Island, District of Franklin, GSCAN-P-81-1A.

Cherniak, D. J. et Watson, E. B. (2003). Diffusion in zircon. Reviews in mineralogy and geochemistry, 53(1), 113–143.

Coffin, M. F. et Eldholm, O. (1994). Large igneous provinces: crustal structure, dimensions, and external consequences. Reviews of Geophysics, 32(1), 1–36.

Courtillot, V., Jaupart, C., Manighetti, I., Tapponnier, P. et Besse, J. (1999). On causal links between flood basalts and continental breakup. Earth and Planetary Science Letters, 166(3–4), 177–195.

Cox, G.M., Halverson, G.P., Stevenson, R.K., Vokaty, M., Poirier, A., Kunzmann, M., Li, Z.-X., Denyszyn, S.W., Strauss, J.V. et Macdonald, F.A., 2016. Continental flood basalt weathering

as a trigger for Neoproterozoic Snowball Earth. Earth and Planetary Science Letters, 446, 89–99.

Davies, J. H. F. L., Marzoli, A., Bertrand, H., Youbi, N., Ernesto, M., Greber, N. D., Ackerson, M., Simpson, G., Bouvier, A.-S., Baumgartner, L., Pettke, T., Farina, F., Ahrenstedt, H. V. et Schaltegger, U. (2021). Zircon petrochronology in large igneous provinces reveals upper crustal contamination processes: new U–Pb ages, Hf and O isotopes, and trace elements from the Central Atlantic magmatic province (CAMP). Contributions to mineralogy and petrology, 176(1), 1–24.

Davies, J. H. F. L., Marzoli, A., Bertrand, H., Youbi, N., Ernesto, M. et Schaltegger, U. (2017). End-Triassic mass extinction started by intrusive CAMP activity. Nature communications, 8(1), 1–8.

Dawes, P. R. (1997). The proterozoic thule supergroup, Greenland and Canada: history, lithostratigraphy and development. Geology of Greenland Survey Bulletin, 174, 1–150.

Dawes, P. R. (2004). Explanatory notes to the geological map of Greenland, 1: 500 000, Humboldt Gletscher, Sheet 6. Geological Survey of Denmark and Greenland Map Series, 1, 1–48.

Day, J. M., Pearson, D. G. et Hulbert, L. J. (2013). Highly siderophile element behaviour during flood basalt genesis and evidence for melts from intrusive chromitite formation in the Mackenzie large igneous province. Lithos, 182, 242–258.

Denyszyn, S. W., Halls, H. C., Davis, D. W. et Evans, D. A. (2009a). Paleomagnetism and U–Pb geochronology of Franklin dykes in High Arctic Canada and Greenland: a revised age and paleomagnetic pole constraining block rotations in the Nares Strait region. Canadian Journal of Earth Sciences, 46(9), 689–705.

Denyszyn, S. W., Davis, D. W. et Halls, H. C. (2009b). Paleomagnetism and U–Pb geochronology of the Clarence Head dykes, Arctic Canada: orthogonal emplacement of mafic dykes in a large igneous province. Canadian Journal of Earth Sciences, 46(3), 155–167.

Dessert, C., Dupré, B., François, L. M., Schott, J., Gaillardet, J., Chakrapani, G. et Bajpai, S. (2001) Erosion of Deccan Traps determined by river geochemistry: impact on the global climate and the 87Sr/86Sr ratio of seawater: Earth and Planetary Science Letters, 188(3–4), 459–474, https://doi.org/10.1016/S0012-821X(01)00317-X.

Dostal, J., Baragar, W. R. A. et Dupuy, C. (1986) Petrogenesis of the Natkusiak continental basalts, Victoria Island, Northwest Territories, Canada: Canadian Journal of Earth Sciences, 23(5), 622–632, https://doi.org/10.1139/e86-064.

Dufour, F., Stevenson, R., et Halverson, G. P. (2020). Timing of emplacement of mafic rocks of the Fury and Hecla Group and younger mafic intrusions, northwestern Baffin Island, Nunavut, in Summary of Activities 2019: Iqaluit, Canada-Nunavut Geoscience Office, 27–36.

Dufour, F., Stevenson, R. et Skulski, T. (2021). Geochemical comparison of Mackenzie and Franklin igneous mafic rocks in Nunavut, Northwest Territories and northwestern Greenland, in Summary of Activities 2020: Iqaluit, Canada-Nunavut Geoscience Office, 33–46.

Ernst, R. E. (2014). Large igneous provinces. Cambridge University Press.

Ernst, R. E. et Baragar, W. R. A. (1992). Evidence from magnetic fabric for the flow pattern of magma in the Mackenzie giant radiating dyke swarm. Nature, 356(6369), 511–513.

Ernst, R. E., Head, J. W., Parfitt, E., Grosfils, E. et Wilson, L. (1995). Giant radiating dyke swarms on Earth and Venus. Earth-Science Reviews, 39(1-2), 1–58.

Ernst, R. E., Buchan, K. L. et Campbell, I. H. (2005). Frontiers in large igneous province research. Lithos, 79(3-4), 271–297.

Ernst, R. E., Hamilton, M. A., Söderlund, U., Hanes, J. A., Gladkochub, D. P., Okrugin, A. V., Kolotilina, T., Mekhonoshin, A. S., Bleeker, W., LeCheminant, A. N., Buchan, K. L., Chamberlain, K. R. et Didenko, A. N. (2016). Long-lived connection between southern Siberia and northern Laurentia in the Proterozoic. Nature Geoscience, 9(6), 464–469.

Ernst, R. E., Liikane, D. A., Jowitt, S. M., Buchan, K. L. et Blanchard, J. A. (2019). A new plumbing system framework for mantle plume-related continental Large Igneous Provinces and their mafic-ultramafic intrusions. Journal of Volcanology and Geothermal Research, 384, 75–84.

Ernst, R. E., Bond, D. P. G., Zhang, S. H., Buchan, K. L., Grasby, S. E., Youbi, N., El Bilali, H., Bekker, A. et Doucet, L. S. (2021). Large Igneous Province Record Through Time and Implications for Secular Environmental Changes and Geological Time-Scale Boundaries. In: R.E. Ernst, A.J. Dickson, A. Bekker (eds) Large Igneous Provinces: A Driver of Global Environmental and Biotic Changes, American Geophysical Union Geophysical Monograph 255, 3–26.

Evans, D. A. et Mitchell, R. N. (2011). Assembly and breakup of the core of Paleoproterozoic–Mesoproterozoic supercontinent Nuna. Geology, 39(5), 443–446.

Fahrig, W. F., Irving, E. et Jackson, G. D. (1971). Paleomagnetism of the Franklin diabases. Canadian Journal of Earth Sciences, 8(4), 455–467.

Fahrig, W. F., Christie, K. W., Jones, D. L. et Campbell, F. H. A. (1981). Paleomagnetism of the Bylot basins: evidence for Mackenzie continental tensional tectonics. Proterozoic basins of Canada. Edited by FHA Campbell. Geological Survey of Canada, Paper, 81(10), 303–312.

Gaynor, S. P., Svensen, H. H., Polteau, S. et Schaltegger, U. (2022). Local melt contamination and global climate impact: Dating the emplacement of Karoo LIP sills into organic-rich shale. Earth and Planetary Science Letters, 579, 117371.

Geological Survey of Denmark and Greenland (2016). Geological map of Greenland: Geological Survey of Denmark and Greenland, Esri ArcGIS package, scale 1:500 000: https://maps.greenmin.gl/geusmap/?mapname=greenland_portal&lang=en#baslay=baseMapGl&optlay=&extent=-554897.0905608042,8582991.55927224,100482.67878329978,8892760.903376289&layers=grl_geus_500k_geology_map (January 2022).

Gibson, T. M., Shih, P. M., Cumming, V. M., Fischer, W. W., Crockford, P. W., Hodgskiss, M. S., Wörndle, S., Creaser, R. A., Rainbird, R. H., Skulski T. M. et Halverson, G. P. (2018). Precise age of Bangiomorpha pubescens dates the origin of eukaryotic photosynthesis. Geology, 46(2), 135–138.

Goddéris, Y., Donnadieu, Y., Carretier, S., Aretz, M., Dera, G., Macouin, M. et Regard, V. (2017). Onset and ending of the late Palaeozoic ice age triggered by tectonically paced rock weathering. Nature Geoscience, 10(5), 382–386.

Greenman, J.W., Patzke, M., Halverson, G.P. et Ielpi, A. (2020) Updated stratigraphy of the Fury and Hecla Group of Melville Peninsula and northwestern Baffin Island, Nunavut, in Summary of Activities 2019: Iqaluit, Canada-Nunavut Geoscience Office, 37–50.

Greenman, J. W., Rooney, A. D., Patzke, M., Ielpi, A. et Halverson, G. P. (2021). Re-Os geochronology highlights widespread latest Mesoproterozoic (ca. 1090–1050 Ma) cratonic basin development on northern Laurentia. Geology, 49(7), 779–783.

Griselin, M., Arndt, N. T. et Baragar, W. R. A. (1997). Plume–lithosphere interaction and crustal contamination during formation of Coppermine River basalts, Northwest Territories, Canada. Canadian Journal of Earth Sciences, 34(7), 958–975.

Halverson, G. P., Shen, C., Davies, J. H. F. L. et Wu, L. (2022). A Bayesian Approach to Inferring Depositional Ages Applied to a Late Tonian Reference Section in Svalbard. Front. Earth Sci, 10, 798739.

Halls H. C. (1987) Dyke swarms and continental rifting: some concluding remarks. In: Halls HC, Fahrig WF (eds.) Mafic dyke swarms. Geological Association of Canada, Special Paper 34, 483–492.

Heaman, L. M., et LeCheminant, A. N. (1993). Paragenesis and U-Pb systematics of baddeleyite (ZrO2). Chemical Geology, 110(1–3), 95–126.

Heaman, L. M., LeCheminant, A. N. et Rainbird, R. H. (1992). Nature and timing of Franklin igneous events, Canada: implications for a Late Proterozoic mantle plume and the break-up of Laurentia. Earth and Planetary Science Letters, 109(1–2), 117–131.

Hoffman, P. F. (1988). United plates of America, the birth of a craton: Early Proterozoic assembly and growth of Laurentia. Annual Review of Earth and Planetary Sciences, 16(1), 543–603.

Hoffman, P. F., Kaufman, A. J., Halverson, G. P. et Schrag, D. P. (1998). A Neoproterozoic snowball earth. science, 281(5381), 1342–1346.

Hou, T., Zhang, Z., Kusky, T., Du, Y., Liu, J. et Zhao, Z. (2011). A reappraisal of the high-Ti and low-Ti classification of basalts and petrogenetic linkage between basalts and mafic–ultramafic intrusions in the Emeishan Large Igneous Province, SW China. Ore Geology Reviews, 41(1), 133–143.

Jackson, G. D. et Iannelli, T. R. (1981). Rift-related cyclic sedimentation in the Neohelikian Borden Basin, northern Baffin Island. Geological Survey of Canada, Paper, 81(10), 269–302.

Jaffey, A. H., Flynn, K. F., Glendenin, L. E., Bentley, W. T. et Essling, A. M. (1971). Precision measurement of half-lives and specific activities of U 235 and U 238. Physical review C, 4(5), 1889.

Jones, A. P., Price, G. D., Price, N. J., DeCarli, P. S. et Clegg, R. A. (2002). Impact induced melting and the development of large igneous provinces. Earth and Planetary Science Letters, 202(3–4), 551–561.

Jourdan, F., Bertrand, H., Schärer, U., Blichert-Toft, J., Féraud, G. et Kampunzu, A. B. (2007). Major and trace element and Sr, Nd, Hf, and Pb isotope compositions of the Karoo large igneous province, Botswana–Zimbabwe: lithosphere vs mantle plume contribution. Journal of Petrology, 48(6), 1043–1077.

Johnstone, S. A., Schwartz, T. M. et Holm-Denoma, C. S. (2019). A stratigraphic approach to inferring depositional ages from detrital geochronology data. Frontiers in Earth Science, 7, 57 p.

Ju, W., Hou, G. et Hari, K. R. (2013). Mechanics of mafic dyke swarms in the Deccan Large Igneous Province: Palaeostress field modelling. Journal of Geodynamics, 66, 79–91.

Kasbohm, J., Schoene, B. et Burgess, S. (2021). Radiometric constraints on the timing, tempo, and effects of large igneous province emplacement. Large Igneous Provinces: A Driver of Global Environmental and Biotic Changes, 27–82.

King, S. D. et Anderson, D. L. (1998). Edge-driven convection. Earth and Planetary Science Letters, 160(3–4), 289–296.

LeCheminant, A. N. et Heaman, L. M. (1989). Mackenzie igneous events, Canada: Middle Proterozoic hotspot magmatism associated with ocean opening. Earth and Planetary Science Letters, 96(1–2), 38–48.

Long, D. G. et Turner, E. C. (2012). Tectonic, sedimentary and metallogenic re-evaluation of basal strata in the Mesoproterozoic Bylot basins, Nunavut, Canada: Are unconformity-type uranium concentrations a realistic expectation?. Precambrian Research, 214, 192–209.

Macdonald, F.A., Schmitz, M.D., Crowley, J.L., Roots, C.F., Jones, D.S., Maloof, A.C., Strauss, J.V., Cohen, P.A., Johnston, D.T. et Schrag, D.P. (2010). Calibrating the cryogenian. science, 327(5970), 1241–1243.

Macdonald, F. A. et Wordsworth, R. (2017). Initiation of Snowball Earth with volcanic sulfur aerosol emissions. Geophysical Research Letters, 44(4), 1938–1946.

MacLennan, S., Park, Y., Swanson-Hysell, N., Maloof, A., Schoene, B., Gebreslassie, M., Antilla, E., Tesema, T., Alene, M. et Haileab, B. (2018). The arc of the Snowball: U-Pb dates constrain the Islay anomaly and the initiation of the Sturtian glaciation. Geology, 46(6), 539–542.

Marzoli, A., Callegaro, S., Dal Corso, J., Davies, J. H., Chiaradia, M., Youbi, N., Bertrand, H., Reisberg, L., Merle, R. et Jourdan, F. (2018). The Central Atlantic magmatic province (CAMP): A review. The Late Triassic World, 91–125.

Melluso, L., Mahoney, J. J. et Dallai, L. (2006). Mantle sources and crustal input as recorded in high-Mg Deccan Traps basalts of Gujarat (India). Lithos, 89(3–4), 259–274.

Palmer, H. C. et Hayatsu, A. (1975). Paleomagnetism and K-Ar dating of some Franklin lavas and diabases, Victoria Island. Canadian Journal of Earth Sciences, 12(8), 1439–1447.

Pehrsson, S.J. et Buchan, K.L. (1999). Borden dykes of Baffin Island, Northwest Territories: a Franklin U-Pb baddeleyite age and a paleomagnetic reinterpretation; Canadian Journal of Earth Sciences, v. 36, 65–73.

Pohlner, J. E., Schmitt, A. K., Chamberlain, K. R., Davies, J. H., Hildenbrand, A. et Austermann, G. (2020). Multimethod U–Pb baddeleyite dating: insights from the Spread Eagle Intrusive Complex and Cape St. Mary's sills, Newfoundland, Canada. Geochronology, 2(2), 187–208.

Pollard, D. D. (1987). Elementary fracture mechanics applied to the structural interpretation of dykes. In Mafic dyke swarms, 34, 5–24.

Reiners, P. W., Carlson, R. W., Renne, P. R., Cooper, K. M., Granger, D. E., McLean, N. M. et Schoene, B. (2017). Geochronology and thermochronology. John Wiley & Sons.

Rioux, M., Bowring, S., Dudás, F. et Hanson, R. (2010). Characterizing the U–Pb systematics of baddeleyite through chemical abrasion: application of multi-step digestion methods to baddeleyite geochronology. Contributions to Mineralogy and Petrology, 160(5), 777–801.

Rivers, T. et Corrigan, D. (2000). Convergent margin on southeastern Laurentia during the Mesoproterozoic: tectonic implications. Canadian Journal of Earth Sciences, 37(2–3), 359–383.

Schaller, M. F., Wright, J. D., Kent, D. V. et Olsen, P. E. (2012). Rapid emplacement of the Central Atlantic Magmatic Province as a net sink for CO2. Earth and Planetary Science Letters, 323, 27–39.

Schaltegger, U. et Davies, J. H. (2017). Petrochronology of zircon and baddeleyite in igneous rocks: Reconstructing magmatic processes at high temporal resolution. Reviews in Mineralogy and Geochemistry, 83(1), 297–328.

Schoene, B. (2014). 4.10-U–Th–Pb Geochronology. Treatise on geochemistry, 4, 341–378.

Sevigny, J. H., Cook, F. A. et Clark, E. A. (1991). Geochemical signature and seismic stratigraphic setting of Coppermine basalts drilled beneath the Anderson Plains in northwest Canada. Canadian Journal of Earth Sciences, 28(2), 184–194.

Salters, V. J. et Stracke, A. (2004). Composition of the depleted mantle. Geochemistry, Geophysics, Geosystems, 5(5).

Shaw, D. M. (2000). Continuous (dynamic) melting theory revisited. The Canadian Mineralogist, 38(5), 1041–1063.

Shellnutt, J. G., Dostal, J. et Keppie, J. D. (2004). Petrogenesis of the 723 Ma Coronation sills, Amundsen basin, Arctic Canada: implications for the break-up of Rodinia. Precambrian Research, 129(3-4), 309–324.

Simões, M. S., Lima, E. F., Rossetti, L. M. et Sommer, C. A. (2019). The low-Ti high-temperature dacitic volcanism of the southern Paraná-Etendeka LIP: geochemistry, implications for trans-Atlantic correlations and comparison with other Phanerozoic LIPs. Lithos, 342, 187–205.

Steenkamp, H.M., Bovingdon, P.J., Dufour, F., Généreux, C.A., Greenman, J.W., Halverson, G.P., Ielpi, A., Patzke, M. et Tinkham, D.K. (2018). New regional mapping of Precambrian rocks north of Fury and Hecla Strait, northwestern Baffin Island, Nunavut, in Summary of Activities 2018: Iqaluit, Canada-Nunavut Geoscience Office, 47–62.

Swanson-Hysell, N. L. (2021). The Precambrian paleogeography of Laurentia. In Ancient Supercontinents and the Paleogeography of Earth. Elsevier, 109–153.

Torsvik, T. H., Smethurst, M. A., Burke, K. et Steinberger, B. (2006). Large igneous provinces generated from the margins of the large low-velocity provinces in the deep mantle. Geophysical Journal International, 167(3), 1447–1460.

Wang, C. Y., Zhou, M. F. et Qi, L. (2007). Permian flood basalts and mafic intrusions in the Jinping (SW China)–Song Da (northern Vietnam) district: mantle sources, crustal contamination and sulfide segregation. Chemical Geology, 3(243), 317–343.

White, R. et McKenzie, D. (1989). Magmatism at rift zones: the generation of volcanic continental margins and flood basalts. Journal of Geophysical Research: Solid Earth, 94(B6), 7685–7729.

White, W. M. (2005). Geochemistry. An on-line textbook. Cornell University, 701.

Widmann, P., Davies, J. H. F. L. et Schaltegger, U. (2019). Calibrating chemical abrasion: Its effects on zircon crystal structure, chemical composition and UPb age. Chemical Geology, 511, 1–10.

Xu, Y., Chung, S. L., Jahn, B. M. et Wu, G. (2001). Petrologic and geochemical constraints on the petrogenesis of Permian–Triassic Emeishan flood basalts in southwestern China. Lithos, 58(3–4), 145–168.